Numerical Investigation of Rupture Potential of Abdominal Aortic Aneurysm

A thesis submitted to the University of Manchester for the degree of

Doctor of Philosophy

In the Faculty of Science and Engineering

2020

Wisam Jasim Kadhim Al-Obaidi

School of Mechanical, Aerospace, and Civil Engineering

Table of Contents

Words count: 46.190

List of Figures

List of Tables

Abstract

Numerical investigation of rupture potential of Abdominal Aortic Aneurysm
Wisam Jasim Kadhim Al-Obaidi, 2019
Doctor of Philosophy, the University of Manchester

Abdominal aortic aneurysm (AAA) is a life-threatening cardiovascular condition, especially if the rupture occurs. Previous investigations have shown that low wall shear stress, high oscillatory shear index distributions may play a significant role in the formation and progression of AAA. The location of the rupture has been observed to coincide with the location of maximum wall stress. This thesis aims to investigate the rupture potential of the abdominal aortic aneurysm using a comprehensive numerical simulation involving fluid-structure interaction. The main objectives are to (i) Investigate the suitability of using a computational model derived from 3D ultrasound (3D-US) images in the finite element stress analysis instead of Computed Tomography (CT) images which have the risk of ionising radiation; (ii) Develop a numerical model using extended finite element method based on the principles of fracture mechanics to predict the initiation/propagation of rupture in AAA; (iii) Study the effect of minor geometrical differences induced by segmentation process, and their role on the hemodynamic metrics; (iv) Study the effect of different patterns of inlet and outlet boundary; (v) Develop a finite element model to investigate the effect of the surrounding organs on the stress profiles of AAA.

Finite element analyses were conducted by applying a static pressure of 120mmHg on the computational models of AAA derived from 3D-US and CT images, with and without the surrounding organs. The predicted wall stress profiles have been analysed and compared quantitatively and qualitatively. In general, the 3D-US models generated higher wall stress compared to the CT models. However, the difference in magnitude and location is greatly reduced if characteristic stress is considered instead of the maximum stress. The magnitude of wall stress was found to be higher in the absence of surrounding organs. An extended finite element model was developed to investigate the effect of three different levels of pressure and strength. The stress profiles, rupture length, and location were obtained and compared between 3D-US and CT models. Despite the overestimation of stress magnitude, the 3D-US models showed comparable locations of rupture. Two fluid-structure interaction simulations were conducted using STAR CCM+ and ABAQUS by applying boundary conditions of standard velocity/pressure waves, and mass flow wave with 3-elements Windkessel model. The flow patterns, hemodynamic metrics, and wall stress distribution were compared between models obtained from two different segmentation software. In addition, the type of boundary conditions was seen to affect the prediction of hemodynamic distributions. All numerical simulations were validated against experimental works that are available in the literature.

Overall, it was concluded that 3D-ultrasound models are feasible to be used in the stress analysis if the characteristic stress is taken into account in the evaluation of the rupture. The extended finite element method was shown to be suitable for rupture risk assessment. The hemodynamic patterns and wall stress profiles of abdominal aortic aneurysm are sensitive to minor geometrical differences induced by the segmentation process, and the boundary conditions used in the simulation. Finally, the presence of the surrounding organs in the model was shown to significantly affect the magnitude and distribution of the wall stress of the abdominal aortic aneurysm.

Declaration

No portion of the work referred to in the thesis has been submitted in support of an application for another degree or qualification of this or any other university or institute of learning.

Copyright statement

Acknowledgements

All praise belongs to Allah. I would like to express my profound gratitude to my supervisor, Dr Parthasarathi Mandal, for his guidance, unlimited encouragement and supervision throughout the period of this research. I appreciate all his contributions of time, ideas, and support to make my PhD experience productive and exciting. I want to also mention his continuous and patient support during writing my PhD thesis.

For his invaluable encouragement, I am especially grateful for my co-supervisor Dr Alistair Revell. I will remain indebted to him; in particular, his persistent help in learning & running advanced CFD/FSI simulations are really appreciated. I would like to thank Dr Christopher Lowe along with his colleagues for their collaboration. I hope this collaboration is able to continue in the future.

I would like to express my deepest gratitude to Dr Steven Lind, who was the internal examiner of my first and second your reports. His notations and suggestions are highly appreciated. I am so much grateful to the school of mechanical, aerospace and civil Engineering/University of Manchester for the financial support to attend the 14th international symposium on Biomechanics in Vascular Biology and Cardiovascular Disease, London, UK.

I would like also to thank the Higher Committee for Education Development in Iraq (HCED) for the financial support of my PhD scholarship and the University of Al-Qadisiyah for a leave of absence to carry out my PhD study at the University of Manchester.

I would like to thank our IT administrators Dr George Leaver and all IT staff for their efforts to keep the system always running and their support to any problem in the computer systems. My time at Manchester was made enjoyable in large part due to the many study mates, friends and groups that became a part of my life. I am grateful for the time spent with my Mexican friends for being such loyal friends always ready when I am in need. I extend my thanks to all the staff of MACE school.

I am grateful to my beloved parents, sisters and brothers, whose love is more than I can desire. I am deeply indebted to them. And most of all for my loving, supportive, encouraging, and patient wife whose faithful support during the final stages of this PhD was and still so appreciated. Thank you all.

Dedication

This thesis is dedicated to

My beloved parents

My siblings ***Noor, Nagham, Wiaam, Wurud, Husam, Haider and Ali***

My faithful wife ***Shaymaa***

My beloved kids ***Sajjad*** and ***Ruqaya***

All my friends in Iraq especially ***Sayed Hamid***, ***Jaffer, Ali Talal*** and ***Ali***

For their love, endless support and encouragement

List of Notations:

Latin symbols

2D,3D	Two and Three-Dimensional
a_i	The nodal enriched degrees of freedom for the set of nodes whose shape functions supports are fully cut by the crack
b_i^{α}	The nodal enriched degrees of freedom for the set of nodes whose shape functions supports are cut by the crack tip
C	The capacity component in 3-element Windkessel model
C_0, C_1, C_2, C_3, P_1 and P_2	Coefficients correlating with each curve in the Idealised AAA
C_{20} /C_{10}	Constants of polynomial strain energy function
C3D4	3D stress tetrahedral element
C3D4H	3D stress hybrid- tetrahedral element
f	The critical value of the damage
F_{α}	Asymptotic crack-tip functions
FC3D8	Fluid tetrahedral element
H(x)	Jump function
I_0 /I_R	Default time incrimination parameters in XFEM
I_1	The first invariant of the left Cauchy-Green tensor
I_A	Number of increments
ILT $_{thickness}$	Thrombus thickness
L	Length
N_i	Standard FE function of the node (*i*)
P	Static pressure
r	Radial coordinate
R	Artery radius
R_d	Distal resistance in 3-element Windkessel model
Re	Reynold number
R_p	Proximal resistance in 3-element Windkessel model
T	Time length of the cardiac cycle
U	Displacement Magnitude
u	Fluid velocity vector

u_i	Nodal displacement vectors in XFEM
V_{CT}	The volume of AAA computational model based CT images
V_{max}	Maximum velocity of blood
V_{US}	The volume of AAA computational model based 3D-US images
V_z	Velocity component in the Z direction
W	Strain energy function

Greek symbols

α	The second constant of the polynomial strain energy function
α_i	First material constant of Ogden strain function
β	The first constant of the polynomial strain energy function
V	Gradient differential operator
$\lambda_1, \lambda_2, \lambda_2$	Principal stretches
ρ_f	Fluid density
σ_{max}	Maximum stress
σ_n	Local stress
μ_f	Fluid dynamic viscosity
μ_i	Second material constant of Ogden strain function
${}^{F}\Omega(t)$	Fluid domain
$\vec{\tau}_w$	Instantaneous wall shear stress vector in three direction
$\lvert\vec{\tau}_w\rvert$	Instantaneous wall shear stress magnitude

Mathematical accents

$SumWssmag	Summation of wall shear stress magnitude
$SumWssX	Summation of wall shear stress component in the X direction
$SumWssY	Summation of wall shear stress component in the Y direction
$SumWssZ	Summation of wall shear stress component in the Z direction

Acronyms

3D-US	3D-Ultrasound image
AAAs	Abdominal Aortic Aneurysms
CT	Computed Tomography image
CAD	Computer-Aided Design
CFD	Computational Fluid Dynamic
CFL	Courant–Friedrichs–Lewy number
DICOM	Digital Imaging and Communication in Medicine
DP	Diastole Pressure
EVAR	Endovascular Aneurysm Repair
FEA	Finite Element Analysis
FEARI	Finite Element Analysis Rupture Index
FSI	Fluid-Structure Interaction
HU	Hounsfield Units
ILT	Intraluminal Thrombus
MAP	Mean Aortic Pressure
Maxps Damage	Maximum principle stress damage
Mimics	Materialise Interactive Medical Image Control System
MRI	Magnetic Resonance Imaging
NHS	National Health Services
NOR_D	The normalised diameter of the AAA
OSI	Oscillatory Shear Index
RPI	Rupture Potential Index
RRT	Relative Residence Time
SP	Systolic Pressure
STL	Stereolithography file
TAWSS	Time-Averaged Wall Shear Stress
URF	Under-Relaxation Factors
US	Ultrasound
UTS	Ultimate Tensile Strength
WSS	Wall Shear Stress
XFEM	Extended Finite Element Method

1 Chapter One: General introduction

1.1 Aorta and abdominal aortic aneurysms (AAA)

The aorta is the largest blood vessel within the circulatory system of the human body. Although the normal size of the aorta diameter varies locally from 1.5 to 2.5 cm, aortic wall changes its structure due to various ageing processes, and also to adapt to altered hemodynamic forces resulting from cardiovascular conditions. Some of these changes may be permanent and are manifested in abnormal enlargement in aorta diameter due to loss of mechanical stiffness, termed as an aneurysm.

The most common aneurysm is an abdominal aortic aneurysm or AAA, which occurs at the abdomen segment of the aorta between the infra-renal arteries and common iliac arteries, see **Figure *1.1***. Generally, any enlargement in an artery can be categorised as an aneurysm if the expansion goes over 50% of its original diameter [1]. In this case, the normal diameter of the abdominal aorta is 2 cm, the AAA is considered to be present if the aorta becomes of a diameter of 3 cm or above [2]. It is worthy to mention here that one of the most famous scientists, Albert Einstein, had suffered from AAA and died due to AAA rupture[3]. The AAA has been classified as a silent killer [4] owing to its asymptomatic nature and the uncertainty involved in predicting rupture. The most common symptoms of AAA rupture include sudden severe pain in the back/abdomen and vomiting. Clinically, the risk of rupture is evaluated and associated with aneurysm size but remains linked with high morbidity and death [5, 6]. Many risk factors increase the risk of development and rupture of AAA, such as Gender (female) [7], smoking [8], hypertension [9], and family history [10]. The risk of AAA rupture is currently evaluated using one of these indicators: (i) the maximum transverse diameter, (ii) and annual/quarterly growth rate [11]. However, a rupture is hard to predict, and AAA remains a serious life-threatening condition.

The AAAs are thought to develop due to the reduction and degradation of collagen and elastin fibres in the aortic wall [12]. The affected segment of the aorta becomes prone to aggressive enlargement and eventually ruptures [13]. Furthermore, the formation of AAA is significantly associated with hemodynamic forces on the aortic wall. For instance, it has been observed that locations of low wall shear stress are highly correlated with the formation of an intraluminal thrombus [14], which subsequently yields to AAA wall inflammation and weakening [15].

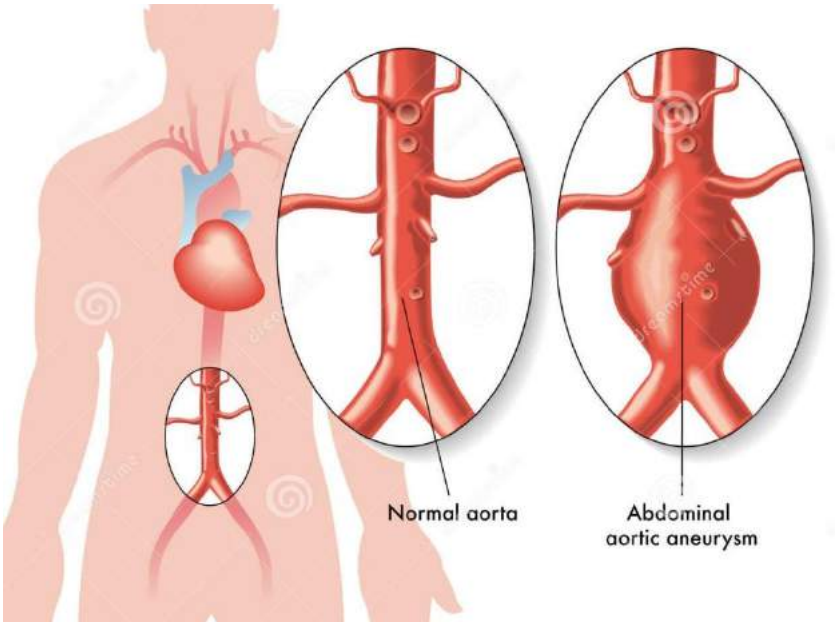

Figure 1.1: Illustrates normal aorta and abdominal aortic aneurysm [16].

1.2 The clinical dilemma of AAA

For a patient with AAA, three main stages are followed by the surgeons to prevent and monitor the risk of rupture, described as follows:

Firstly detailed information of AAA such as sac volume, maximum diameter, inflammation, intraluminal thrombus, and presence of leakage can be obtained using one of the conventional imaging techniques: Computed Tomography (CT), 3D-Ultrasound (3D-US) and Magnetic Resonance Imaging (MRI). Each of the screening methods has advantages and disadvantages. For instance, CT and MRI scans are highly recommended before the urgent surgical interventions of ruptured AAA due to the high resolution of scans. However, the cost of having these scans is expensive and not recommended for routine surveillance due to the high risk of ionizing radiation. Therefore, clinicians recommend 3D-US imaging to monitor the growth rate of AAA, maximum diameter, and other biomechanical factors. Imaging using 3D-US can be described as relatively inexpensive and painless [17]. However, 3D-US does not work very effectively in some cases, such as people with obesity and in the presence of bowel gases [18].

Secondly, the provided information regarding AAAs is evaluated in terms of the maximum diameter (over 5.5 cm [11]) and growth rate (over 6mm/y in men [19] or 10 mm/y in women [11, 20]) to weigh the risk of rupture against the risk of repairing. Consequently, surgeons decide whether the condition of the patient with AAA requires urgent surgical intervention if the risk of rupture is more than the risk of the operation. On the other hand, if

the AAA is observed to be stable and not showing the high potential of rupture, then it is suggested to undergo regular monitoring using 3D-US screening.

Thirdly, if the AAA is highly prone to rupture, AAA must be repaired using one of these two treatment methods:

1) Open surgical treatment: the diseased AAA wall is removed and replaced by a vascular graft stitched to intact walls up/downstream in order to get rid of any recirculation in the blood flow stream. The surgical operation is considered successful in the absence of blood leakage. However, this method of treatment is associated with high morbidity and death rates [21].
2) Endovascular aneurysm repair (EVAR): the AAA wall is repaired by sending an expandable stent-graft through a small cut in the femoral artery to correct the flow stream by excluding the dilated part of the AAA wall [22].

Although the critical threshold of maximum AAA diameter of 5.5 cm represents the golden rule in weighting the cumulative threat of surgical treatment against the potential risk of rupture, small AAAs in the early stages have also been observed to rupture [11, 23]. Hence, the theory of maximum diameter to evaluate the rupture of AAA is questionable. Patient-Specific numerical simulations of the AAA can potentially make a big difference in understanding the mechanism of rupture and improve the assessment method of risk rupture.

1.3 Outputs of numerical simulations as indicators to assess the risk of AAA rupture

It is essential to find alternatives indicators of AAA rupture potential in order to save the lives of people with AAA without relying solely on the maximum diameter. In this study, various computational approaches such as maximum wall stress in Finite Element Analysis (FEA), low wall shear stress in Computational Fluid Dynamic (CFD), and wall stress and hemodynamic metrics based wall shear stress in Fluid-Structure Interaction (FSI) will be employed to understand the biomechanics of AAA [24-29]. These numerical techniques have the ability to characterise blood flow patterns and stress distribution due to the progression of AAA and other parameters that influence the flow configurations within the affected wall. In the standard FEA modelling technique, the presence of blood is ignored; instead, a constant static pressure representing the blood pressure is presumed. The CFD modelling technique assumes that the AAA wall structure is inflexible (rigid). While in reality, the artery's wall deforms spatially and temporally. The FSI modelling technique takes into account the effect of shear forces induced by the unsettled flow that produces stress on the AAA wall.

To improve the rupture risk assessment of AAA using computational techniques, patient-specific AAA models are to be developed from medical scans such as CT, MRI, and 3D-US. Several studies have focused on the effect of geometrical features [30-33] of AAA, using different boundary conditions [34]. Furthermore, intensive work was undertaken to extract realistic mechanical properties [35-37] in order to characterise the mechanical behaviour of the AAA wall numerically. Other researchers have derived new indicators [38-40] of potential rupture based on the strength of the AAA wall that predicted the rupture site. Although the majority of patient-specific AAA models in previous studies were derived either from CT or MRI scans, these are not a feasible option due to the presence of ionizing radiation if one wants to model and validate the growth of the aneurysm. Different imaging modalities also introduce minor geometrical variations for the same patient due to different segmentation packages; the effect of these variations on rupture risk assessment has not been studied yet.

1.4 Objectives of the current work

The present work focuses on enhancing the rupture risk indicators in AAAs by implementing a wide range of numerical solution methods depending on the desired rupture indicator to provide a good understanding of rupture prediction, which would pave the way for subsequent work. Some studies [41, 42] have investigated the feasibility of using numerical patient-specific models of AAA derived from 3D-US images to evaluate the risk of rupture. Multiple red patches indicating overestimation in high-stress values of the 3D-US AAA models compared to CT AAA walls were observed. Therefore, it is important to derive a new indicator that would yield similar results from both CT and 3D-US image-based models. In addition, the current work, for the first time, attempts to model the mechanism of rupture, i.e., the initiation and propagation of rupture based on the principle of fracture mechanics. The effects of minor geometrical differences of AAA models generated using different packages and the impact of assigning different dynamic inlet and outlet boundary conditions on the flow profiles and biomechanics of AAA are currently somewhat imperfectly understood.

Furthermore, the presence of surrounding organs and their role in the stress analysis of AAA will be examined. Brief descriptions of AAA models with different configurations are listed below in five categories, in addition to the key objectives of this work:

1) Conduct a comprehensive literature review for previous numerical studies related to the current work to find the gaps, and to present the originality of the ongoing work. Two main parts will be presented as follow:
    - Clinical indicators of rupture, the conventional treatments, and detecting methods of AAA.
    - Employing of numerical tools in association with different medical imaging modalities to generate rupture indices.
2) Investigate the suitability of using computational models of AAA derived from 3D-US images by comparing the stress profiles to CT based models. The steps below will be followed
    - Conducting standard FEA analysis to obtain the stress profiles in both CT and 3D-US AAA walls.
    - Generate finite element models of AAAs from computed tomography and three-dimensional ultrasound.
    - Define an alternative rupture indicator to the maximum wall stress that has similar value and location for both CT and 3D-US models to avoid any misleading prediction of stress overestimation.
3) Numerical modelling of rupture initialisation and growth in abdominal aortic aneurysm using the XFEM approach. The main steps of this work are
    - Develop a computational model of AAA based on the principle of fracture mechanics represented by extended finite element method for four AAA patients to achieve a better understanding of the mechanism of initiation and propagation of rupture in AAA.
    - Investigate the presence of potential blood leakage induced by the rupture.
    - Extend the investigation of using 3D-US computational models instead of CT models by comparing the rupture length and leakage of blood.
4) Study the effect of minor geometrical differences induced by the segmentation process and their role on the hemodynamic metrics of the abdominal aortic aneurysm. The main tasks include
    - Construct three idealised AAA models from a representative model from the literature and vary the dimensions by ±10% to study the effect of the variation on the hemodynamic and stress distribution.

- To study the effects of including the AAA wall, the lumen (blood), and thrombus in the model.
- Develop a fluid-structure interaction AAA models to compare and evaluate various hemodynamic metrics and wall stress profiles resulting from geometrical differences arising from the segmentation process.

5) Study the effect of different patterns of inlet and outlet boundary conditions on the hemodynamic predictions of abdominal aortic aneurysm. The main steps will include
   - Develop a fluid-structure interaction model of idealised and patient-specific AAA models using standard velocity/pressure waves.
   - Develop a second fluid-structure interaction model of idealised and patient-specific AAA models using mass flow rate at the inlet and 3-elements Windkessel model at the outlet.
   - Explore and compare the flow patterns, hemodynamic, and stress distribution results from the two sets of inlet and outlet boundary conditions.
6) Investigate the effect of the surrounding organs on the stress profiles of AAA. The key steps will be
   - Construct computational models of AAA, Intestine, Colon, and Spine from CT data set for a single patient by using Mimics v.18 [43].
   - Conduct a Finite element analysis with the presence of AAA and the surrounding organs.
   - Conduct a standalone stress analysis on the AAA wall only by excluding the surrounding organs from the simulations.
   - Study the impact of including and excluding surrounding organs on the AAA wall stress distribution by comparing the stress profiles at three different orientations.

All FEA and XFEM simulations were implemented using the commercial software Abaqus v6.14/2016 [44], while the FSI simulations were conducted using two packages: STAR CCM+ v.13.04 [45] and Abaqus 2016 [44].

1.5 Outline of the thesis

Following the introductory part above, **Chapter Two** reviews the previous studies regarding AAA and how numerical techniques could significantly contribute to the assessment of AAA rupture risk. The literature review is divided into two main sections:

(i) clinical indicators of rupture, the conventional treatments and detecting methods of AAA; (ii) the use of numerical tools in association with different medical imaging modalities to generate rupture indices. In addition, omitting parts of the AAA geometry, excluding the surrounding organs around AAA, and the influence of the inlet and outlets profiles are comprehensively reviewed to illustrate the importance of these parameters on the analysis of AAA rupture as well as to present the originality of the current work.

The segmentation process to obtain patient-specific models of the AAA wall and its components using the ImFusion suite [46] and Mimics v.18 [43] packages are explained in **Chapter Three.** Furthermore, the cleaning and smoothing process of 3D computational models of abdominal aorta aneurysms in 3-Matic v.10 [43] are demonstrated.

Chapter Four addresses the use of finite element models of AAA extracted from 3D ultrasound images as well as CT images to predict the risk of rupture. Stress/strain profiles and their locations in both models are compared. In addition, statistical analysis has been carried out to compare the magnitude of wall stress at 50% and 95% confidence intervals in order to resolve the overestimation of stress values produced in the 3D–US models. Stress profiles in an idealised AAA are compared with experimental results. The numerical findings are showing significant agreement with the experimental data.

In **Chapter Five**, the extended finite element method (XFEM), based on fracture mechanics principles, has been employed for the first time to model the rupture process in AAA. Three different values of wall strength and three different levels of pressure were applied to the AAA wall. The detailed procedure on how to implement the XFEM modelling using damage initiation criterion of maximum principal stress has been explained. Stress profiles in both 3D-US and CT models of AAA for different pressures levels have been compared. Finally, a quantitative comparison of rupture length has been carried out. The experimental work of idealised AAA has been replicated numerically for validation. The predictions of the rupture site between the XFEM model and the experimental data have shown good agreement.

In **Chapter Six**, two groups of idealised and patient-specific AAA models have been constructed using two different packages to illustrate the effect of segmentation on the hemodynamic metrics and stress profiles. The effects of mesh density and dynamic time-step on the accuracy of the results have been examined. A good agreement has been achieved

between the numerical velocity profiles and the experimental work from the literature at different time intervals during the cardiac cycle.

Based on the results presented in **Chapter Six**, the effect of using different configurations for the inlet and outlet boundary conditions and their influence on the hemodynamic of AAA has been investigated and reported in **Chapter Seven**. Two sets of boundary conditions (standard velocity/pressure waves) and (mass flow inlet wave/ 3-elements Windkesssel model) were considered to study the effect on the distribution of hemodynamic metrics and wall stress.

Chapter Eight addresses, for the first time, the impact of the inclusion of the surrounding organs in the stress profiles of AAA. Images of adjacent organs to the AAA such as Intestine, Spine and Colon have been extracted from CT data for a single patient using Mimics v.18 [43]. The stress distributions for supported and non-supported AAA wall have been compared qualitatively and quantitatively at three positions to illustrate the effect of surrounding organs. Significant variations were observed on the stress results.

Finally, **Chapter Nine** summarises the key conclusions and contributions of the current work, followed by recommendations for future work.

2 Chapter Two: Literature Review

2.1 Introduction

The term aneurysm means an abnormal localised increase of artery diameter due to the gradual loss of the arterial wall strength with time. The most common aneurysm in the circulatory system is the abdominal aortic aneurysm or AAA, which occurs between the infra-renal arteries and the common iliac branches as a result of reversed flow between them[47]. When the abdominal aorta diameter grows by more than 50% of its original size of approximately 3 cm diameter [1], then it has a high potential for rupture. Rupture risk assessment is the process that is used for identifying patients at potential risk of AAA burst. Clinicians usually make their decision for or against surgical interventions based on empirical statistics, and some of these are not patient-specific. In recent times, numerical analysis using finite-element methods have become a useful tool in the rupture-risk assessment. For these models, using and constructing patient-specific geometries and boundary conditions will significantly improve the risk assessment. The purpose of this chapter is to briefly review the relevant previous studies on AAA and identify the gaps that need further work and implications to improve the rupture assessment in AAA.

2.2 Indicators of potential rupture being used clinically

The prevalence of an aortic aneurysm rises with age profile to reach a rate of 5%-10% for people who are 65-70 years old [48]. Generally, the clinical monitoring of AAA showed that AAA is asymptomatic until the eventual rupture. In the event of AAA rupture, severe symptoms develop very rapidly, causing death for around half of the cases before any clinical intervention could take place, however, if surgical intervention happens quickly, the patients may survive [5]. The following parameters indicate the likelihood of rupture in AAA, and the patient should undergo surgical repair prior to rupture.

2.2.1 Transverse diameter of AAA

The maximum diameter indicator proposes that the size of the transverse diameter of AAA is a key indicator of the potential of rupture. Despite the relative simplicity of this indicator, the key question and the debate surrounds the threshold value of the maximum diameter for surgical intervention [49, 50]. The current threshold of the maximum diameter of 5.5 cm[11] is based on clinical surveillance of AAA. However, some clinical observations

revealed that large AAAs to have a maximum diameter bigger than 5.5 cm did not burst during the life of the patient[51].

In contrast, some small AAAs have been observed to rupture [51-53], specifically in women[54]. Based on the above, the size of the AAA or the maximum diameter is not sufficient to evaluate the risk of rupture. Therefore, finding alternative rupture indicators should be taken into consideration in making the clinical decision[19, 55].

2.2.2 The growing rate of AAA

It has been found that when the growth rate of AAA increases rapidly is correlated with significant potential of rupture [55-58]. Consequently, continuous clinical observations of AAA in the UK have confirmed that an annual growth rate of 6 mm/y[19] in AAAs size indicates elevated potential rupture compared to a stable AAAs. The growth rate of AAA is associated with factors such as hypertension[9, 59], smoking tobacco[8], gender (female)[7] in addition to other factors discussed below.

It is thought that the dilation of the aorta is caused by an increase in collagen production, a substantial decrease in aortic elastin, and inflammation, which leads to biological changes in the aortic wall structure. In addition, family history and genetic factors are linked to the formation process of the AAA disease [10, 60]. **Figure *2.1*** shows the factors that are thought to be potentially conducive to create AAA. The most common risk factors that increase the rupture rate are [59, 61] :

- Atherosclerosis.
- Inflammation.
- Chronic obstructive pulmonary disease.
- Age.

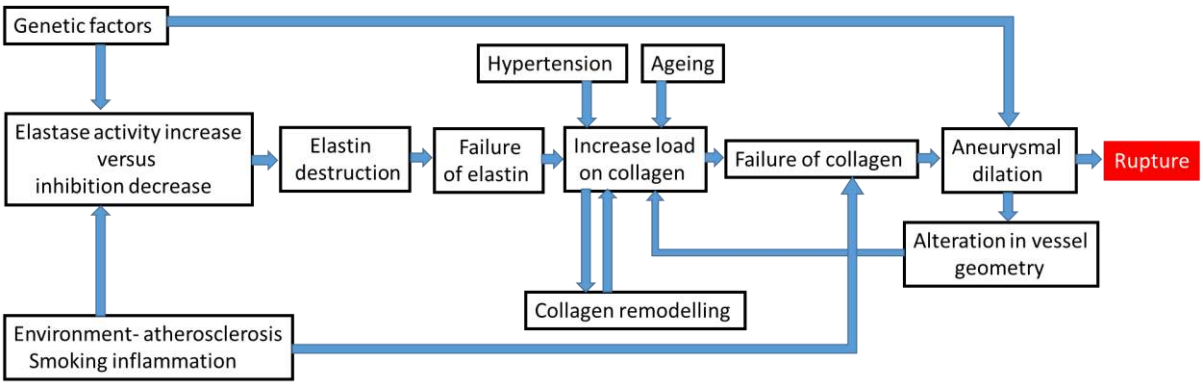

Figure 2.1: Key causes of abdominal aortic wall disease based on medical background.[10]

2.3 Diagnosis of AAA

Some AAAs can only be identified by chance during the physical examination for different illnesses because AAA tends to be asymptomatic. For instance, big AAA may be discovered clinically by carefully feeling the unusual wide pulsation in the abdomen area [23]. On the contrary, the inspection of AAA in obese people can be challenging for physical examination. Despite this, sometimes doctors use the stethoscope to hear the abnormal sound that induces from the turbulence of blood flow inside the AAA. Therefore, medical imaging modalities are being used by surgeons to discover the presence of AAA, which also plays as diagnostic tools to give detailed information about AAA size, diameter, the presence of the thrombus, and any possible leakage in the wall. At present, a number of medical imaging methods are available, and each method has various advantages and disadvantages. There are three most common methods of imaging AAA are:

2.3.1 3D Ultrasound imaging (3D-US)

This type of screening currently represents the most common, affordable, and easiest way to detect AAA for a large group of patients[62]. Using 3D-Ultrasound scans in medicine is considered to be a reliable and significant method since 1977, especially to estimate AAA size in spite of the difficulty in identifying the outside AAA wall, proximal branches, and bifurcation parts. The best feature of the 3D-US examination is that it does not contain ionizing radiation. In most situations, the results can be reported instantly, unless some obstacles block the scanning in the area of interest, such as bowel gas and extreme obesity, preventing sufficient picturing [63]. **Figure *2.2* (A)** represents two images of an AAA in transverse and longitudinal positions, respectively. Graham et al. studied 3D-Ultrasound as a diagnostic tool to detect the AAA and reached the conclusion that 3D-Ultrasound detection has a low probability of misleading results[62]. The predictive quality of 3D-Ultrasound results is high, approximately 100% in AAA screening[64], making it reliable for surveillance of non-complicated AAA. Therefore, the clinical uncertainty of AAA presence should be confirmed by using ultrasound screening in the first place.

2.3.2 Computerised tomography imaging (CT)

In the event of failure of 3D-US of providing necessary information about AAA, CT scans must be used, especially if the risk of rupture is thought to be higher than the surveillance of AAA. The disadvantages of CT imaging can be described as it is more expensive than 3D-Ultrasound and has high-risk ionizing radiation. On the other hand, it

provides comprehensive information about AAA shape, inner and outer diameter, thrombus, calcifications, and relations to adjacent structures and organs such as the renal arteries[65], see **Figure *2.2* (B)**. In addition, CT is widely used prior to surgical-operation if rupture is suspected. Although CT scanning has advantages, sometimes it may fail in providing important detail, more specifically in complex AAAs and the surrounding organs[66].

2.3.3 Magnetic resonance imaging (MRI)

This type of imaging provides outstanding details about AAAs and the nearby soft tissue in case of pre-operative assessment see **Figure *2.2*(C)**. Furthermore, MRI has a powerful capability to capture and identify the AAA, the renal arteries upstream, the bifurcation branches downstream, calcification, inflammation, thrombus[66]. Generally, the pros of MRI imaging compared to CT comprising less exposure to the gadolinium contrast medium and harmful ionizing radiation. The cons of MRI are: very expensive, fear of closed places by some patients, and avoiding the artefact induced by the motion of the patient during the scanning process[67].

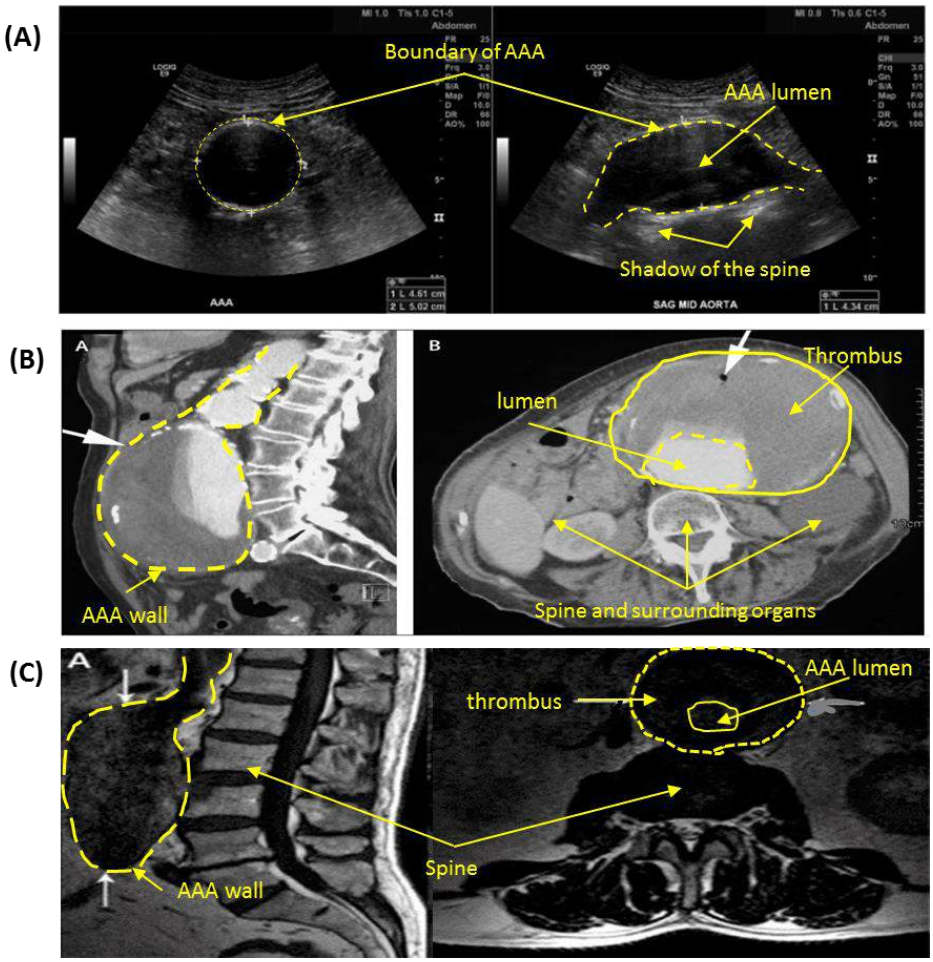

Figure 2.2: Sagittal and cross-section images of AAA represent **(A) 3D ultrasound**, **(B) CT,** and **(C) MRI.**[68]

2.4 Treatment of patients with AAA

The key issue of AAA is that they are usually asymptomatic until it ruptures. In case the patient feels a pulsating mass in the abdomen near the belly button[69], that indicates the presence of AAA. The symptoms below happen when an aneurysm does rupture:

- Sudden cruel pain in the abdominal or back.
- The pallor of colour from the face.
- Feeling of thirst and dryness of the mouth or skin.
- Vomiting, and nausea.
- Shaking, fainting, dizziness, sweating, and fast heartbeat.

In the event of small AAA, the only treatment is to have a periodic observation to monitor the growth rate and other biomechanical factors. However, when the AAA increases in size rapidly, then the AAA has a high potential of rupture. Thus surgical action is highly recommended and essential, which itself is risky as it has a mortality rate of between 2% and 5% [70, 71]. Two surgical interventions are available:

2.4.1 Open surgical repair

It is recommended for large, non-ruptured AAA. During this operation, the surgeon cuts the affected (dilated) area of the aorta. Then, a synthetic graft is placed inside an aneurysm in order to connect the two ends of the normal aorta by sutures, as shown in the right of **Figure *2.3***. The surgical operation of fixing AAA may be life-threatening than a stable aneurysm. Thus, observation management is the first option for any new patient with elective surgery and should only be taken when the risk of rupture is high[21].

2.4.2 Endovascular repair

The surgeon sends an endovascular graft inside an aneurysm through the femoral artery; the purpose of that is making a new lumen (the graft) for the blood, as shown in the left of **Figure *2.3***. Endovascular repair needs more accurate morphological data and thorough measurements than open repair[22]. Endovascular repair is associated with a high incidence (17-26%) of blood leaking into an aneurysm and outside the graft lumen with the possibility of rupture during the 18 month follow-up period. Spotting a leakage requires significant effort, which dramatically increases the cost of endovascular repair treatment[72].

At present, the measurements of the maximum diameter and the annual percentage of the growth rate of the AAA are the available choices for doctors to decide when to make a surgical treatment is made. For instance, when the diameter of the AAA exceeds 5.5 cm, it is recommended that the intervention is urgently performed. In addition, the surgical treatment is also recommended for AAAs that are less than 5 cm in diameter in case of the average growth rates are more than 0.5 cm/year [23, 30]. AAAs can be either stable, growing slowly, or they can enlarge rapidly. The need for an accurate identifier of patients with a high-risk of AAA rupture would consequently decrease medical costs and protect lives [73, 74].

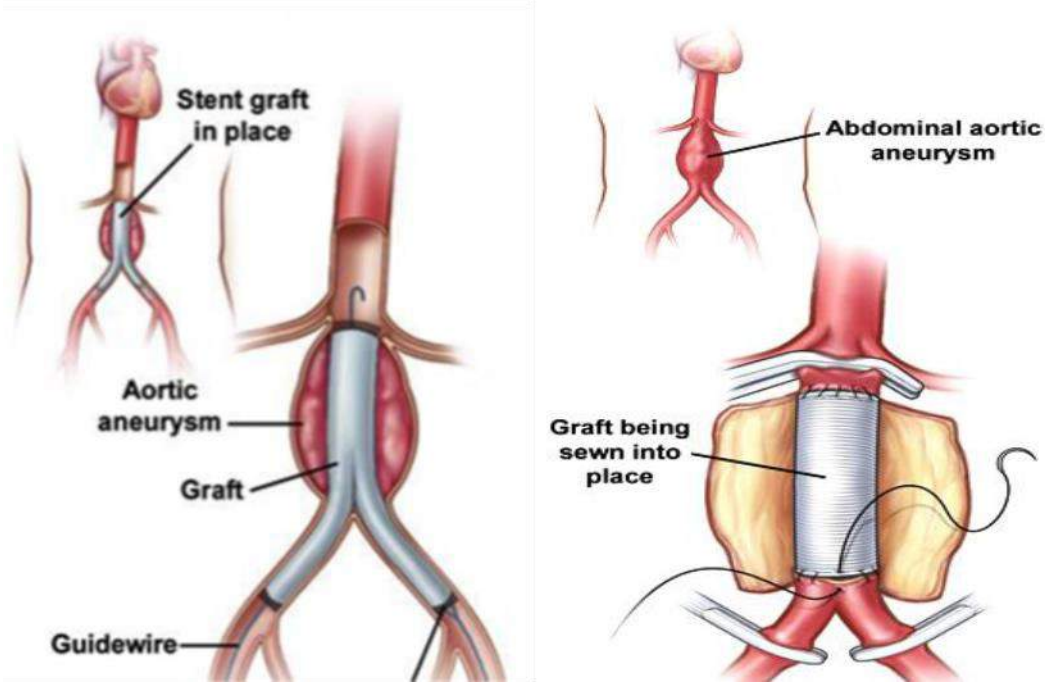

Figure 2.3: illustrates (Left) an endovascular repair, and (Right) an open surgical AAA repair.[75]

2.5 Indicators of potential rupture predicted by biomechanical analysis

The potential rupture of AAAs has been evaluated and studied using three common computational methods: finite element methods (FEA), computational fluid dynamic (CFD), and fluid-structure interaction (FSI) besides performing experiments on replicas of AAA made of silicone. The most common analytical solution in analysing the potential rupture is FEA because it does not need a qualified person to perform the risk analysis, and the results can be obtained in a relatively short time. Retrieving of realistic AAAs from patients is linked to ethical considerations, which makes setting up experiments challenging.

Each of the numerical modelling techniques provides different information that helps the clinicians to make decisions regarding surgical interventions on AAA patients and avoid rupture. For instance, FEA analysis offers detailed information regarding stress distribution at the AAA wall for a chosen level of pressure to the internal wall on the patient-specific AAA geometry. The location and magnitude of wall stress above 0.4 MPa refer to the location of potential rupture and the urgency of repairing AAAs. FEA analysis ignores the fluid domain from the calculation. Researchers have been trying to understand the correlation between the fluid forces such as wall shear stress/formation of vortices and the rupture site or progression of AAA. Therefore, the requirement to include fluid (blood) flow parameters in the analysis of rupture is paramount, which can be obtained by CFD analysis. The outcomes of CFD analysis have shown that the location of low wall shear stress is highly linked to the location of rupture and formation of intraluminal thrombus. Recently, a multi-physics solution such as FSI overcame the limitations of the FEA and CFD solutions by combining both structure (wall) and blood domains of AAA in the same simulation. The deformation induced in the AAA wall due to blood pressure interacts directly with the blood volumes, which forces the blood to change its flow profiles to accommodate with variation in the wall deformation. Performing the FSI solution is time-consuming, despite the valuable information provides. So, in the case of repairing or critical AAA, it may not be feasible to carry out promptly. Generally, the numerical approaches provide a good understanding of the mechanism of rupture by linking the outcomes of these tools to the failure in the AAA.

2.5.1 The maximum wall stress indicator

The outcome of the FEA approach in the AAA wall is to obtain and evaluate the stress distribution and linking it to the failure (rupture). It was first used in predicting the rupture site for idealised AAAs by Stringfellow et al. [76] in the late 1980s. Following this research, other researchers [77-79] started to explore and evaluate the effect of AAA geometry on the stress distribution by conducting stress analysis for 2D complex idealised AAA models. For example, Inzoli et al. [78] utilised axisymmetric AAA models to show the role of the thrombus on the wall stress distribution, which concluded that thrombus acts on reducing the wall stress. Two other studies [80, 81] reached the same conclusions given by Inzoli regarding the role of thrombus on the wall stress distribution. Whereas Mower et al. [79] and Elger et al. [77] employed the FEA solution method to observe the association between the AAA size and the predicted wall stress and the significant effects of AAA geometry profile on the estimation and site of maximum stress in the AAA wall. Earlier stress studies of AAA

had provided useful information about the stress distribution using idealised AAA geometries and simple mechanical properties (Linear). However, these distributions cannot be interpreted into realistic AAA geometries[82]. For instance, Raghavan et al.[83]studied the effect of using linear and hyper-elastic material properties on stress distribution. It was observed noticeable differences in the predicted stress distributions (linear vs. hyper-elastic materials), see **Figure *2.4***.

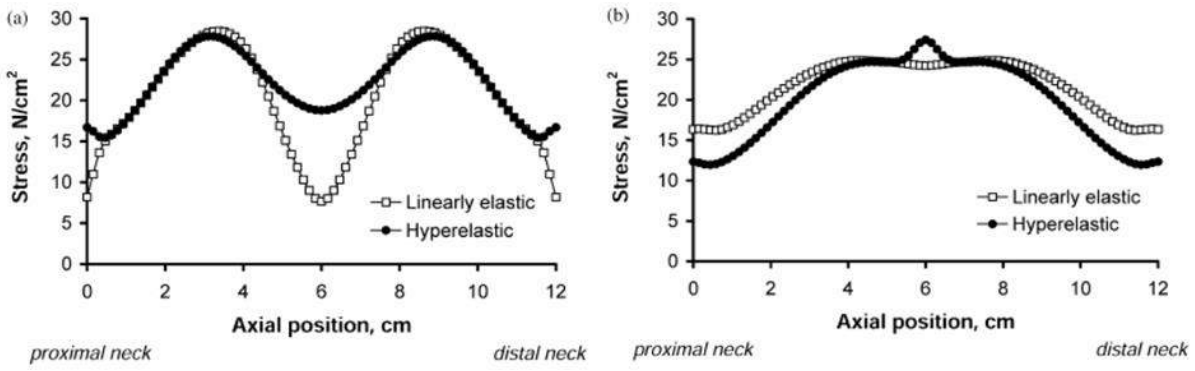

Figure 2.4: illustrates the variation in the predicted stress profiles between linear and hyperelastic material properties: (a) Anterior surface, (b) Posterior surface of idealised AAA.[83]

In recent years, it has been observed that the inclusion of patient-specific AAA models derived from the medical imaging modalities such as CT[84, 85] and 3D-Ultrasound[42] remarkably improves FEA outcomes regarding the potential of rupture assessment. A large number of stress analyses were conducted on 760 AAAs in order to compare the predicted maximum wall stress for patients who had symptoms (ruptured) and those who elected for AAA repair (non- ruptured)[26, 73, 84-93]. The reported findings of these studies revealed that the maximum wall stress was observed to be prominently higher in the ruptured group, as well as, both ruptured and maximum wall stress locations were identical [73, 84, 85], see **Figure *2.5***.

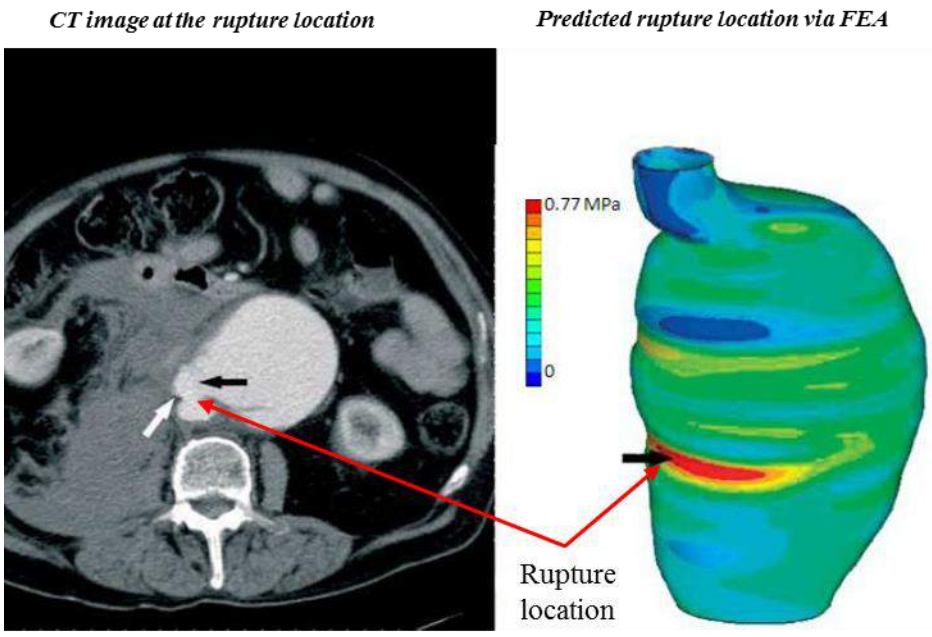

Figure 2.5: Demonstrates the site of rupture in a cross-sectional CT scan **(Left)**; predicted high wall stress via the FEA model**(Right)**. [84]

Truijers et al. [26] included in his study ruptured AAAs and intact AA geometries for relatively comparable diameters. The observation from their study showed that the predicted maximum wall stress in ruptured AAA models was higher compared to the maximum stress of the intact aorta. Another group of researchers, such as Fillinger et al.[85], Gasser et al.[87], Maier et al.[90] and Raghavan[93] divided patients of AAA into groups based on matching their diameter to find out the role of the AAA diameter on the predicted maximum wall stress. The conclusion they have reached confirms that ruptured AAAs models possess higher maximum wall stress than the un-ruptured AAAs. To enhance the comparison of maximum wall stress between ruptured and non-ruptured AAAs, Erhart et al. [89] established one condition to involve a ruptured AAA in their study if their data (CT scans) were available before and after the occasion of rupture. In addition, a control group of intact AAA models, with diameters matching the diameters of pre ruptured AAAs, was comprised in the study for comparison. Then, 3D models of AAA pre/post-rupture were created from the obtained CT images and employed for stress analysis. The comparison of maximum wall stress of AAAs models based on the control group showed that the ruptured AAA models did not significantly predict higher wall stress than the pre-ruptured AAA models. By looking deeply at the AAA groups that have been included in the previously mentioned studies, it was observed that there is a time gap between the obtained CT scans in AAAs before and after the

state of rupture. Subsequently, the presence of this short or long gap may lead to unfavourable outcomes which can be catastrophic for the patients sometimes. For instance, there were five stress analysis studies [84, 87, 89-91] in AAA that used urgent CT scans just before undergoing the surgical intervention to fix the rupture. Likewise, a similar number of studies [73, 85, 86, 92, 93] used CT images for elected AAAs groups who later extremely dilated and ruptured. By contrast, only two analyses used 3D models of AAAs derived from CT images obtained pre-and post-rupture, one with a very short time between the pre and post images[26]; however, the time gap in the second study was unknown[88]. Interestingly, Erhart et al. [27] in his study included representative models of AAAs created from the CT images that were obtained on the same day before and after rupture. The peak wall stress in the non-ruptured group predicted the future potential rupture accurately in many AAA cases, see **Figure *2.6***.

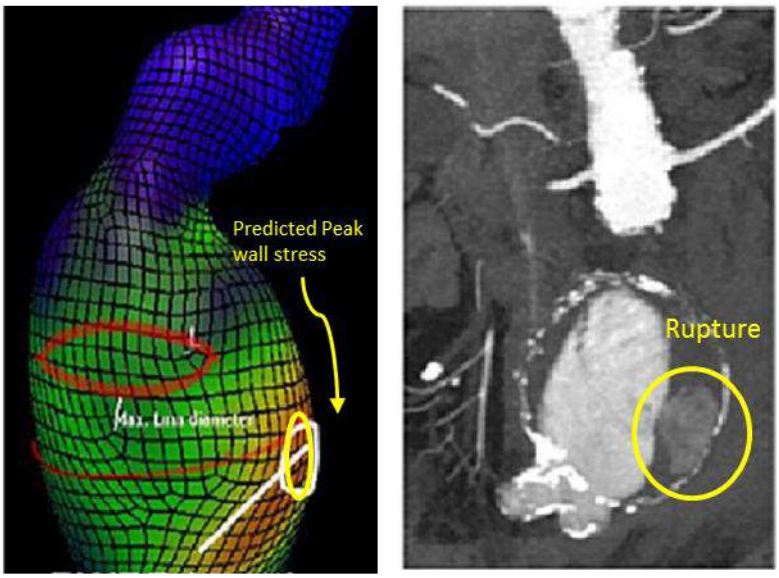

Figure 2.6: Peak wall stress (FEA/Left) predicted the rupture location (CT image of rupture/Right).[27]

It is recommended that CT scans should not be used for frequent AAA surveillance due to the direct exposure to ionizing radiation. In contrast, the use of 3D-Ultrasound as an alternative source of creating 3D models is promising because AAA patients can have regular scanning to monitor the growth of AAA and conduct regular FEA analysis. Kok et al. [42] performed stress analysis to demonstrate the possibility of using 3D-Ultrasound as an input

source to create 3D AAA models. Despite the similarities between the segmented 3D-Ultrasound and CT models, 3D-Ultrasound AAA models predicted higher maximum wall stress magnitude compared to CT models, see **Figure *2.7***.

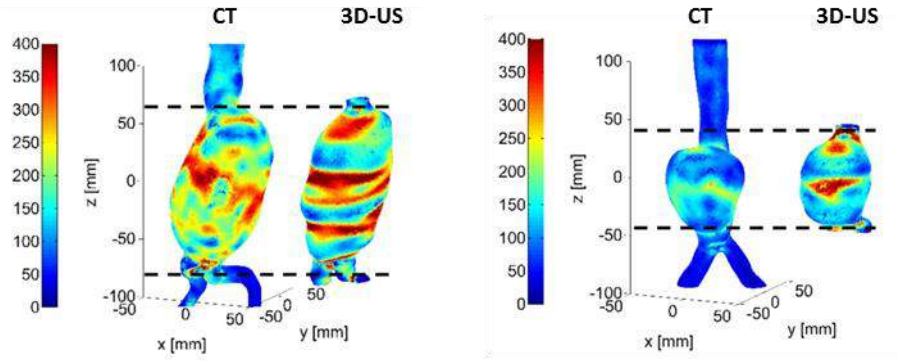

Figure 2.7: Comparison of predicted wall stress distributions in (kPa) between CT and 3D-US AAA models.[42]

2.5.2 Potential rupture indicators derived from the maximum wall stress and strength

The mechanism of AAA rupture from the engineering aspect is due to the overcome of the stress to the wall strength at a certain point. Stress analysis in AAA assumes that the final state of the wall after applying an internal load (dynamic or static) provides relevant information concerning the likelihood of rupture and its site. The predicted maximum wall stress in AAA, as a standalone rupture indicator, does not achieve the rupture (failure) unless accompanied by patient-specific wall strength and geometry. Consequently, engaging all patient-specific failure parameters in the stress analysis increases the reliability of the AAA rupture assessment significantly. The following two rupture indicators were established based on the ratio between the predicted wall stress and AAA strength.

2.5.2.1 Rupture Potential Index (RPI)

The mathematical definition of the Rupture Potential Index (RPI) can be described as the ratio of the predicted (calculated) maximum wall stress at a certain point to the strength of the vessel wall. Therefore, the scale of RPI has a range from 0 (low risk of rupture) to 1 (extreme risk of rupture), which can be used as a diagnostic tool to evaluate the AAA rupture. Firstly, the maximum wall stress can be obtained from the last frame of the AAA vessel produced by the FEA analysis. Secondly, patient-specific strength of the AAA wall was non-invasively predicted by Vande Geest et al. [94], by creating a mathematical model relying on

the available clinical data or parameters such as gender, thrombus thickness ($ILT_{thickness}$/ cm), family history and normalised diameter (NOR_D) of the AAA, see the equations **(2.1)** and **(2.2)** below:

$$Strength_{statistical} = 719 - 379 \times \left(\sqrt{ILT_{Thichness}} - 0.81 \right) - 156 \left(NOR_D - 2.46 \right) - 213 \times History + 193 \times Gender \quad \textbf{(2.1)}$$

$$RPI = \frac{Predicted\ maximum\ wall\ stress}{Strength_{statistical}} \quad \textbf{(2. 2)}$$

The term (History) can be substituted by 0.5 or -0.5 if the presence of AAA in the first-degree relative or not, respectively. Similarly, values of gender are 0.5 = men or -0.5 = women. A large number of studies, approximately seven, used the current empirical equation to measure the strength and evaluate the RPI in rupture/non-ruptured AAAs. Consequently, RPI was observed to be significantly higher in the ruptured group compared to non-ruptured/eligible for repair AAAs in all studies [27, 38, 87-89, 95, 96], see **Figure *2.8***. Furthermore, the findings of these studies found that the predicted rupture locations in 7 cases with high RPI in pre-ruptured AAAs group were fairly identical with real rupture site. It is also demonstrating that predictions of the RPI scale and location may be beneficial to predict future rupture sites [97].

Although the predictions of RPI were, to some extent, good, some limitations are associated with measurements of AAA wall strength. The lack of availability of clinical data is the biggest issue facing strength calculations, which makes the statistical model inadequate and may be unreliable. More importantly, it was also observed that the strength of the AAA wall varies locally within the vessel [35, 94]. Thus, the next rupture indicator will be addressing this issue.

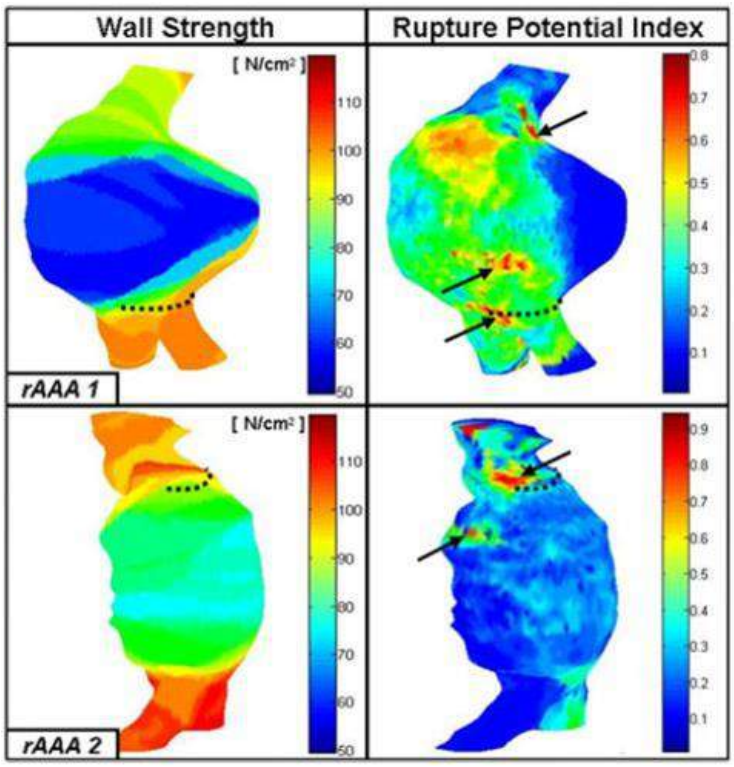

Figure 2.8: Demonstrates the distribution of RPI and strength in ruptured AAA, the dotted lines refer to the actual rupture sites which coincided with at least one site of the potential rupture. [95]

2.5.2.2 Finite Element Analysis Rupture Index (FEARI)

This index uses a similar mathematical definition of RPI. However, rather than using a statistical strength model, values of strength here had been obtained by averaging and combing the tensile test data [35-37], see equation **(2.3)** below. These three studies provide full details regarding the conducted experimental work to determine the AAA local strength. For instance, Raghavan et al. [36] performed a tensile test for 52 AAA specimens to find that the average ultimate tensile strength (UTS) is approximately 0.942 MPa. Following this study, Thubrikar et al. [37] collected 49 aneurysmal tissue specimens in different orientations and locations in order to investigate any changes in mechanical behaviour with the location of the specimen. It was observed, in the longitudinal orientation of AAA, that the wall strength was small in the Posterior compared to the Anterior and Lateral sites. While AAA wall strength increased from the Posterior towards Anterior and Lateral in the circumferential orientation. The measured averaged ultimate AAA wall strengths were found regionally as follow: Anterior = 0.45 MPa, Posterior = 0.46 MPa and lateral = 0.62 MPa. Subsequently, Raghavan et al. [35] conducted a further tensile experiment to involve 48 samples, which were gathered from different regions and orientations of the AAAs. The conclusion was that

the strength of AAA varies locally to a range from 0.336 MPa to 2.35 MPa. The local strength of AAA obtained from these three studies can be used in conjunction with predicted maximum wall stress, corresponding to the same location of the strength, to obtain FEARI and scale of the potential of rupture.

$$FEARI = \frac{Predicted\ maximum\ wall\ stress}{Strength_{Experimental}} \qquad \textbf{(2. 3)}$$

Two studies by Doyle et al. [39, 40] used the FEARI concept to evaluate the rupture in 10 ruptured AAAs group and 42 eligible for repair AAAs group, where the acquired CT scans have been used to construct 3D AAA models. The predicted maximum wall stress was obtained by applying a uniform, static pressure of 120 mmHg on the internal wall of the AAA for validation purposes. **Figure *2.9*** demonstrates the methodology of using the FEARI method. The results of this study showed that the FEARI scale in the ruptured AAAs group was higher (1.03) compared to FEARI of (0.62) repaired AAAs. The FEARI assessment can be improved by tensile testing of the excised AAA fresh samples to obtain regional patient-specific strength, which in turn increases the applicability of using FEARI as a diagnostic rupture tool.

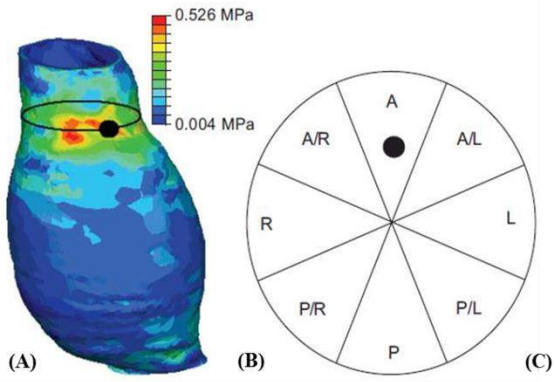

AAA region	Ultimate tensile strength (MPa)
A : Anterior	0.7744
P : Posterior	0.8658
L : Left	0.9221
R: Right	0.9187
A/L : Anterior/Left	0.8482
A/R: Anterior/Right	0.8465
P/L : Posterior/Left	0.8939
P/R : Posterior/Right	0.8922

Figure 2.9: Demonstrates the scheme of using FEARI as rupture predictor: (A) represents the location and value of the predicted maximum wall stress, (B) represents the local AAA strength that corresponds to predicted maximum wall stress, and (C) regional ultimate tensile strength [36, 39, 40].

2.5.3 Hemodynamic factors in AAA

Stress analysis using the FEA approach does not involve frictional forces induced by the blood flow and their role in the progression of AAA disease. Hemodynamic indices in AAA

can be observed by performing Computational Fluid Dynamic (CFD) analysis, which is able to predict the distributions of the frictional forces exerted at the aortic wall. Unfortunately, the wall stress distribution is not obtainable in this approach as it ignores the mechanical interaction between the fluid domain (blood) and the solid domain (wall) by assuming the aortic wall is rigid (un-deformable). Thus, if researchers are interested in investigating both wall stress and hemodynamic metrics in AAA, it is recommended to use the comprehensive numerical method of fluid-structure interaction modelling, FSI.

The general blood flow feature within an intact aorta is laminar with an absence of adverse flow, while diseased abdominal aorta (AAA) is significantly correlated with the adverse flow conditions that lead to creating dynamic vortices (recirculation) and strong fluctuations, which can be represented by wall shear stress WSS, oscillatory shear index OSI and relative residence time RRT[67, 98-100]. In the first place, the researchers thought that the maximum wall shear stress is correlated with damage of AAA[101]. However, Caro et al. [102] have shown that low wall shears stress can cause initiation, remodelling and damage in the blood vessels. Consequent work by Ku et al. [103] and Tarbell et al. [104] confirmed the role of low WSS that leads to damage of the arterial wall in combination with the role of blood flow oscillation vectors. Therefore, the hemodynamic parameters oscillatory shear index OSI was first defined by Ku et al. [103, 105] that combine the effects of both shear stress value and the changes in its direction. Their observations were as follow:

1- The healthy carotid artery was found to carry bloodstreams in one direction (no-oscillation) of relatively high wall shear stress.
2- The diseased carotid artery was observed to have dominant recirculation zones, in which the blood flow changes its direction (oscillatory) with low wall shear stress

The OSI has a scale from 0 to 0.5, where zero OSI value means the blood flow has one direction with no disturbances. In contrast, 0.5 OSI value indicates the blood flow encounters multi-directional flow (recirculation) see **Figure *2.10***. The wall shear stress vectors can be time-averaged over the cardiac cycle or cycles, which is known as Time-Averaged Wall Shear Stress, TAWSS. It is used to observe the cumulative effects of wall shear stress vectors during the cardiac cycle and linked with rupture location or AAA growth. Another important hemodynamic metric that is derived based on the wall shear stress is called Relative Residence Time, RRT, which quantifies the time that blood particles spend within the AAA

sac during the cardiac cycle. The RRT index also reflects the combined effects of wall shear stress and oscillatory shear index adjacent to the arterial wall.

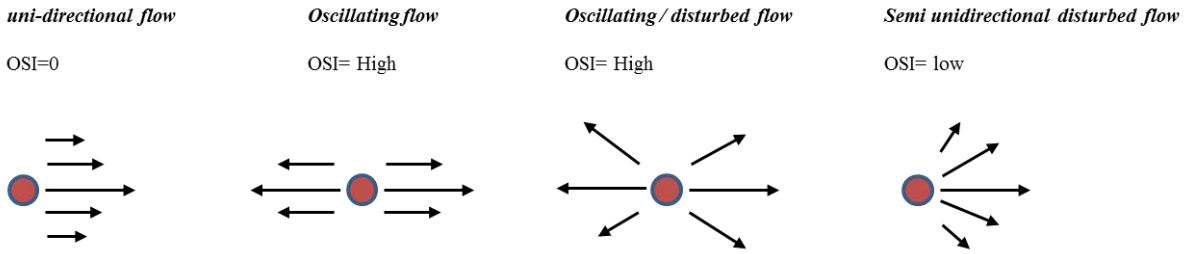

Figure 2.10: Schematic representation illustrates the correlation between OSI and flow features[106].

Boyd et al. [107] performed a CFD analysis for 7 ruptured AAA group to evaluate wall shear stress distribution with the location of rupture. It was found that there is no association between ultimate wall shear stress and rupture site. Remarkably, significant low wall shear stress/ low velocity (recirculation) in six AAAs out of seven was observed on or near the location of rupture, see **Figure *2.11***. It was also found by Dalman et al. [98] and Papaharilaou et al. [108] that the magnitude of wall shear stress is proportional to the size of the AAA. In other words, when the AAA size increases, subsequently, blood flow at the AAA sac encounters low velocity and, therefore, low wall shear stress, see **Figure *2.12***. Another group [41] used wall shear stress to assess and compare the predictability of AAA derived from 3D-Ultrasound and CT. It was found that wall shear stress distributions and profiles were fairly similar between 3D-US and CT models. Hence, 3D-US images can be used to construct 3D models of AAA to perform numerical analysis to assess the rupture and AAA pathology as an alternative to CT scans. Further work by Chisci et al. [109] investigated and compared hemodynamic metrics TAWSS, OSI, and RRT of a large group involving ruptured/non-ruptured AAAs and normal intact aortas. They observed that these hemodynamic indices were considerably varied among the three groups. Doyle et al. [110] studied the effect of TAWSS on AAA progression and rupture. CT images were acquired four times from the date of revealing AAA to pre-rupture. It was found that the location of low TAWSS was identical with the location of AAA expansion, thrombus formation, and rupture.

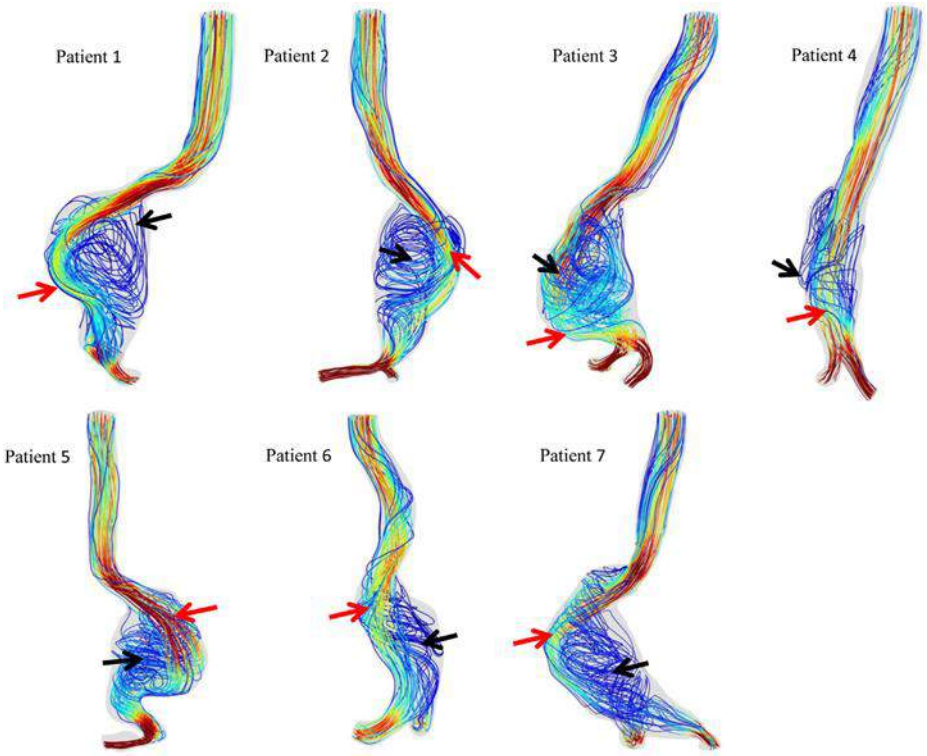

Figure 2.11: illustrates the correlation between rupture site and low wall shear stress / recirculated flow in ruptured AAAs (red arrows refer to high wall shear stress/ high velocity), whereas (black arrows refer to low wall shear stress/ recirculated flow)[107].

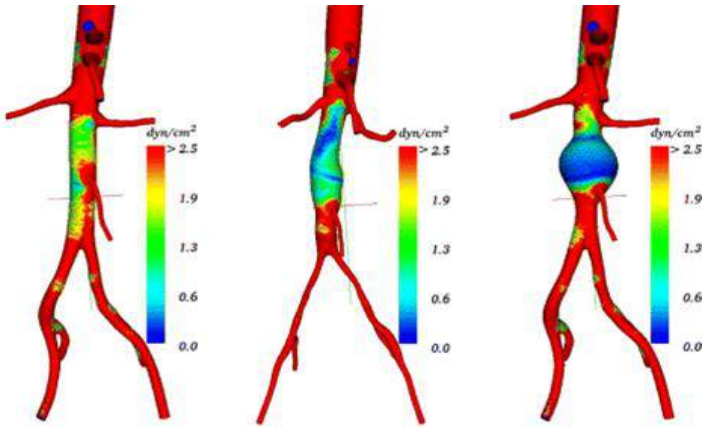

Figure 2.12: Demonstrates the relationship between the progression of AAA and the magnitude of wall shear stress. [98]

More recently, many studies have been conducted to quantify the changes in AAA hemodynamic during physical exercise (rest, mild exercise, extensive exercise) by obtaining patient-specific geometries and boundary conditions from MRI scans[28, 67, 99, 100]. Les et al. [100] and Suh et al. [99] have collected MRI scans, flow waves, and pressure for a number

of AAAs in order to conduct CFD simulation to describe the alteration in hemodynamic indices TAWSS, OSI and RRT on the AAA growth. The observations from all the studies showed that AAA hemodynamic determinants hugely affected by the intensity of the exercise; for instance, extreme exercise increases the TAWSS level considerably, and decreases OSI/ RRT. Therefore, they hypothesised that hard exercise works on decreasing the progression of AAA and the contrary is right, see **Figure *2.13***.

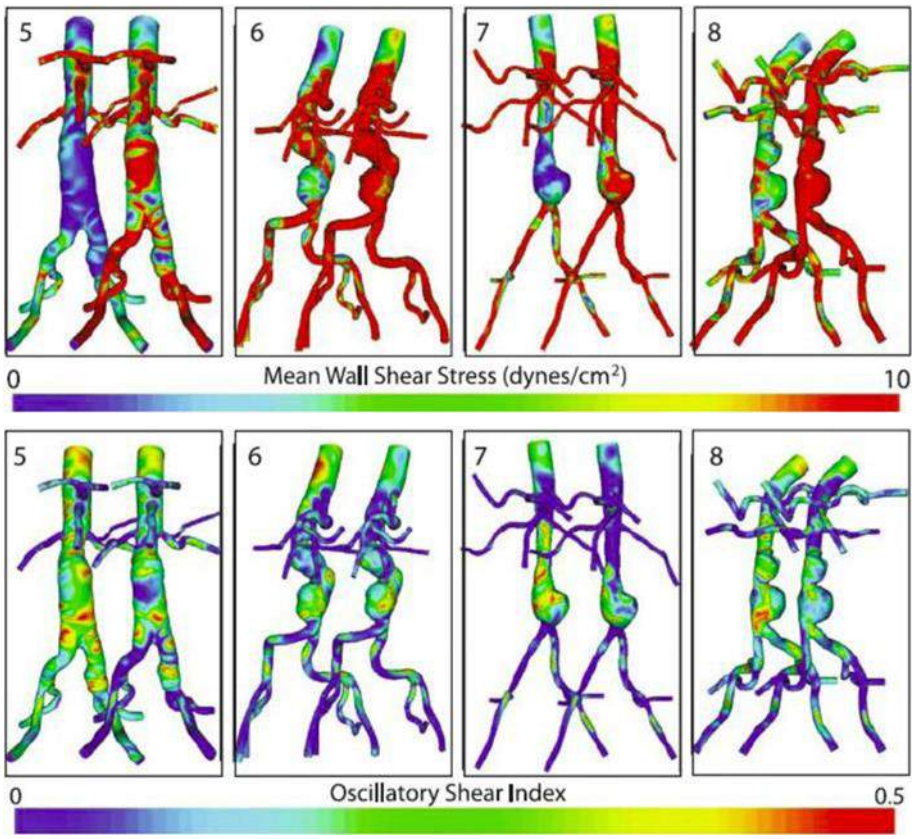

Figure 2.13: Effects of exercise intensity (left/ rest) (right/ exercise) on the AAA hemodynamic TAWSS and OSI of four patients adopted from[100].

2.6 The role of geometrical features on the rupture assessment

Configurations of AAA geometry such as symmetry, asymmetry, curvature, tortuosity, including common iliac branches and geometrical irregularities, seem to have a direct role in the mechanism of rupture. Therefore, some considerations should be given to the general shape of the AAA in the construction and smoothing process [30, 31, 111, 112]. Vorp et al. [113] performed stress analysis on 10 virtual AAAs to investigate the correlation between the asymmetry/diameter of AAA and predicted stress distribution. The investigation of this study reached an important conclusion; the predicted wall stress profiles are highly dependent on

two parameters the asymmetry and diameter of the vessel. Later, Doyle et al. [114] proposed a method to measure the asymmetry in the front-back plane of the AAA vessels in order to clarify the link between the asymmetry and maximum wall stress. The study revealed that the association between back surface AAA wall stress and asymmetry of AAA showed that extreme inflation in the front or backside of AAA predicts high stress on the reverse side, see **Figure** ***2.14***.

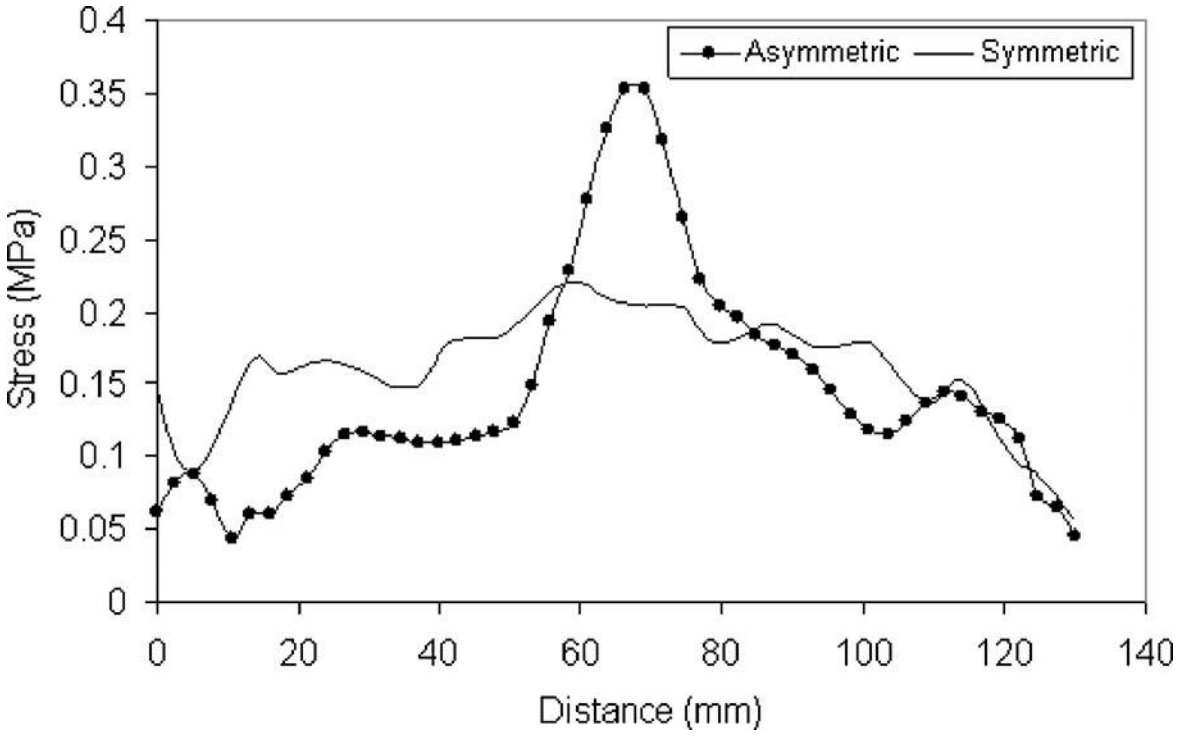

Figure 2.14: Comparison of stress profiles between symmetric and asymmetric AAA. [114]

Giannoglou et al. [115] studied the impact of the centreline curvature of the AAA geometry on the maximum wall stress, where it was found that mean curvature has a linear relationship with maximum wall stress and potential risk of rupture. Doyle and McGloughlin [116] also used the asymmetry as a CAD tool parameter to identify the potential of rupture. The observations found that the predicted maximum wall stress in the ruptured AAA group was 157% higher compared to the stress of repaired AAAs, despite the maximum diameters in both groups were comparable. In addition, the asymmetry of ruptured AAA lumen was 125% higher than the repaired AAAs, see **Figure** ***2.15***.

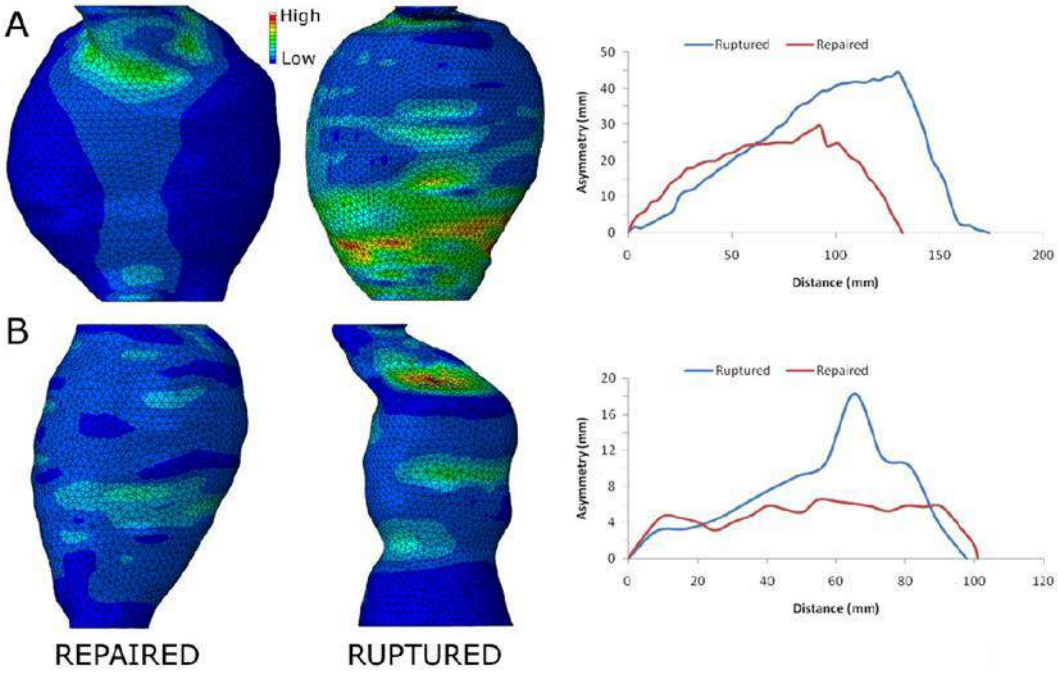

Figure 2.15: Comparison of wall stress between ruptured and repaired AAAs (Left). Comparison between the measured asymmetry of ruptured and repaired AAA lumen[116].

The presence of AAA is usually associated with intraluminal thrombus (ILT). Its role is believed to reduce the wall stress profile and value significantly, which may alter the prediction of rupture if it is excluded from the analysis. Although Venkatasubramaniam et al. [84] and Fillinger et al. [73, 85] ignored the presence of thrombus in their computational analysis, the three studies predicted accurately rupture site, see **Figure *2.5***. On the contrary, few stress studies [78, 80, 81] performed on idealised AAAs showed that predicted maximum wall stress was reduced by 30% when the ILT inclusion was taken into consideration. Consequent further works were done by Wang et al. [117, 118] and Bluestein et al. [119] to investigate the role of ILT on wall stress but this time using patent specific AAA geometries, their results confirmed that the involving ILT works on decreasing the wall stress, see **Figure *2.16***.

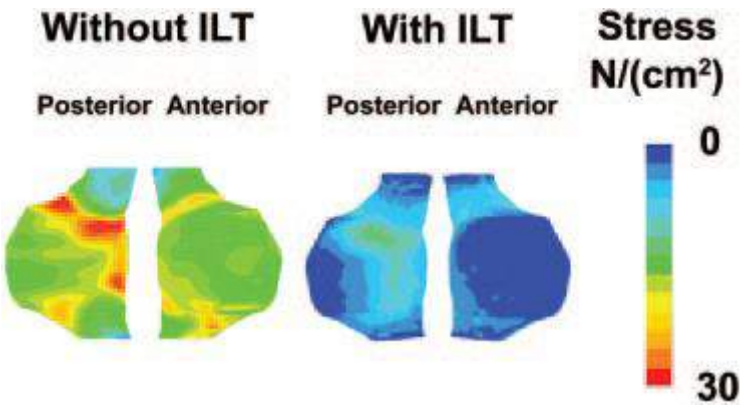

Figure 2.16: Influence of ILT inclusion on the AAA wall stress distribution for a representative AAA.[118]

Sometimes the construction of patient-specific AAA geometry encounters missing key parts of the AAA such as the neck, bifurcations branches, and renal arteries owing to poor quality of the input medical images. Influences of these important parts on the wall stress distribution and other hemodynamic metrics have been addressed numerically. In terms of including the common iliac branches in the 3D AAA model, Xenos et al. [32] conducted a parametric FSI study on idealised and patient-specific AAAs models to evaluate AAA formation and progression by taking into account two parameters: bifurcations and neck angulations. The observations based on their results indicated that predicted maximum wall stress and wall shear stress distributions in AAA sac and iliac branches significantly intensified with the increase of neck and bifurcations angles. Therefore, they should not be ignored or omitted out of the simulations, see **Figure *2.17***. Similar subsequent work was done by Drewe et al. [33] attempting to explore the impact of proximal neck and bifurcation angles on the hemodynamic of AAA by performing FSI simulation on idealised AAAs. The conclusion was similar to Xenos work: AAAs with fairly large bifurcation angle had fewer recirculation areas and high WSS; hence, the low potential of rupture.

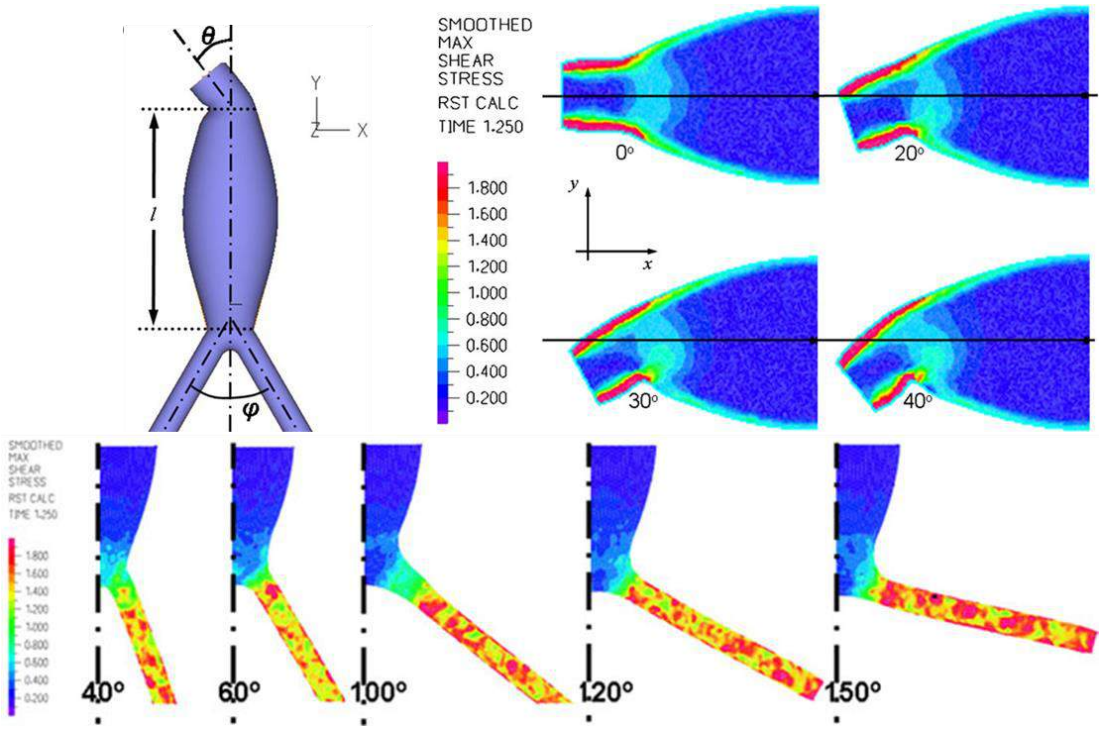

Figure 2.17: Illustrates the influence of neck and bifurcations angles on the shear stress profiles.[32]

2.7 The role of boundary conditions on AAA ruptures studies

In order to run a stress/rupture analysis of AAA, whatever the numerical approach being used, needs either advanced or straightforward boundary conditions to be defined at the inlets, outlets, and the aneurysmal wall depending on the required outcomes of the study. However, it was found that the types of boundary conditions significantly influence the flow patterns, pressure distributions, wall shear stress, and maximum wall stress within the AAA.

Most of the FEA studies [26, 78, 113, 115, 120] on AAA used a standard uniform static pressure, more specifically 120mmHg, representing the systolic pressure during the cardiac cycle. However, some studies suggested mean aortic pressure (MAP)[7, 87], the average pressure over the time of the cardiac cycle ought to be applied instead at the internal wall of the AAA. The mathematical representation of MAP links the steady and pulsatile components of the aortic pressure (mean aortic pressure=MAP), (systolic pressure=SP and diastole pressure=DP), respectively, see the equation **(2.4)** below.

$$MAP = P_{diastolic} + \frac{1}{3}\left(P_{systolic} - P_{diastolic}\right) \qquad \textbf{(2. 4)}$$

On the other hand, investigating the hemodynamic of AAA using computational fluid dynamics CFD and fluid-structure analysis FSI requires dynamic boundary conditions (velocity and pressure waves) as the blood flow is pulsatile. Although it can be performed using the ordinary boundary conditions steady flow (Poiseuille flow) at the inlet and zero pressure at the outlet[41]. Unfortunately, in order to conduct an accurate hemodynamic analysis in AAA requires a lot of information. This information is unobtainable owing to lack of experimental data of blood flow/pressure of the aorta of a human. Therefore, many researchers had to impose or simplify the inlet and outlet flow conditions in order to express a well-posed rupture problem. For example, waves of velocity and pressure in arteries are exposed to dispersing, reflecting, and damping owing to the variations in the AAA volume, mechanical properties of the vessel, and bifurcation angle[100]. The most common choices of outlet boundary conditions for periodic flow are either pressure wave being defined at the outlets, or a Windkessel model that represents the distal and proximal resistance besides the capacitance [121-124]. Hundreds of published articles regarding AAA did not use patient-specific boundary conditions at the inlets and outlets, which makes the accuracy of these works questionable. Madhavan and Kemmerling [34] examined how the blood flow is sensitive to the assumption of inlet velocity profiles (plug, parabolic, linear shear, skewed cubic, and Womersley) and outlet conditions (2-D, 3-D Windkessel and outflow) of the human aorta, see **Figure *2.18***. It was concluded that the inlet velocity profiles and outlet boundary conditions significantly affect the flow patterns adjacent or in the vicinity of the inlet and outlet surfaces. The distal flow patterns were shown to have insignificant influence. The most used patient-specific pressure-velocity waveforms in many studies [31, 111, 112, 125] are those used by Mills et al. [126], who collected flow/pressure data of the main arteries from 23 patients using a velocity probe. Moreover, a mass flow rate wave[127] was extracted from 39 patients using MRI scanning to characterise flow patterns at the ascending and descending aorta. The outlet surface is prescribed as a 3-element Windkessel model[121], representing the downstream resistance of blood flow.

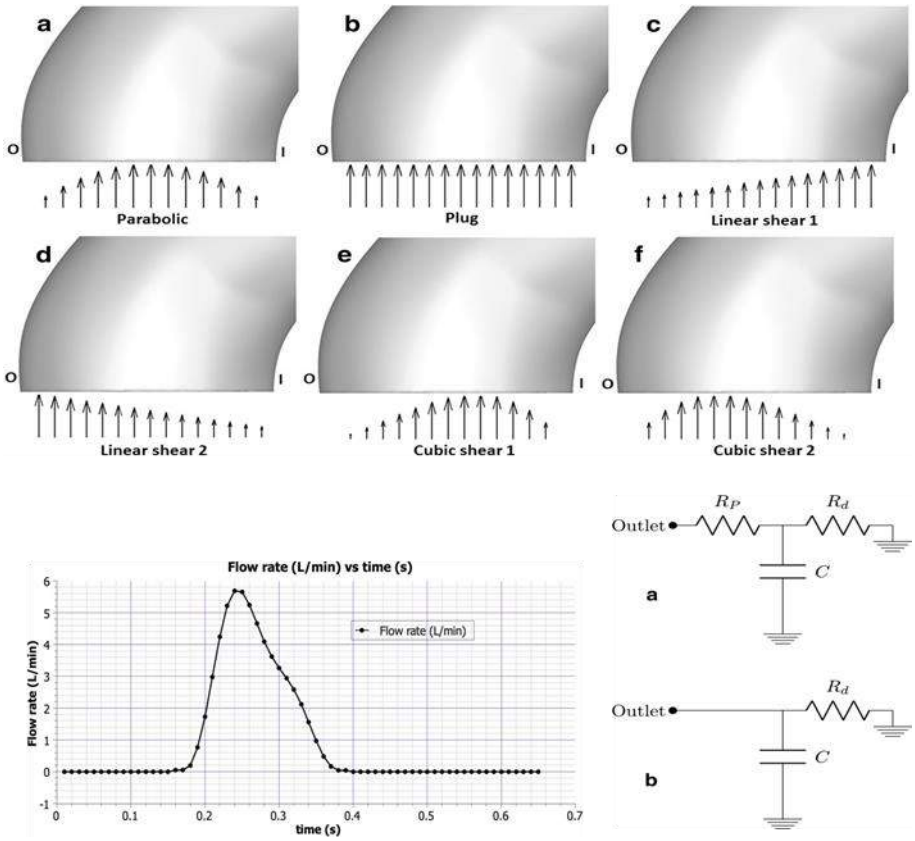

Figure 2.18: Illustrates the inlet velocity profiles (up), the inlet flow rate at the inlet (left down corner), and the Windkessel models at the outlets (right down corner).[34]

2.8 The role of surrounding organs

The anatomy of AAA reveals that it is surrounded by soft tissues and organs such as muscles, ligaments, Spine, Colon, Intestine, and fat. However, similarities in contrast between these organs make it too hard for the imaging operator to capture them during the segmentation process. Thus, to date, the majority of stress analysis studies excluded the surrounding organs from their simulations. Di Martino et al. [128] conducted the first explicit fluid-structure interaction simulation taking into consideration the presence of descending aorta, AAA, and inclusion of surrounding organs in order to add a realistic environment to the simulation. The numerical model was imported from the human anatomy library that included AAA wall, AAA lumen, thrombus, retroperitoneum, and a thick layer represents the abdominal cavity part to provide supportive pressure on the AAA wall, see **Figure *2.19***. Later, Józsa and Paál [129] studied the impact of the spine on the flow patterns of AAA. They concluded that the spine does not significantly influence the flow patterns inside the AAA. A subsequent study done by Kwon et al. [130] incorporated the spine besides the AAA wall to understand its effect on the wall stress states. Their conclusion was that the

surrounding organ remarkably influences the geometry of AAA, which in turns affects the wall stress. Therefore, involving the surrounding soft tissues and spine will increase the accuracy of the predicted wall stress. Farsad et al.[131] conducted an FEA analysis to study the interaction between the spine and the AAA. It was found that the Spine behaved as a constrained by preventing the growth of the AAA, while the AAA growth was faster in the Anterior region.

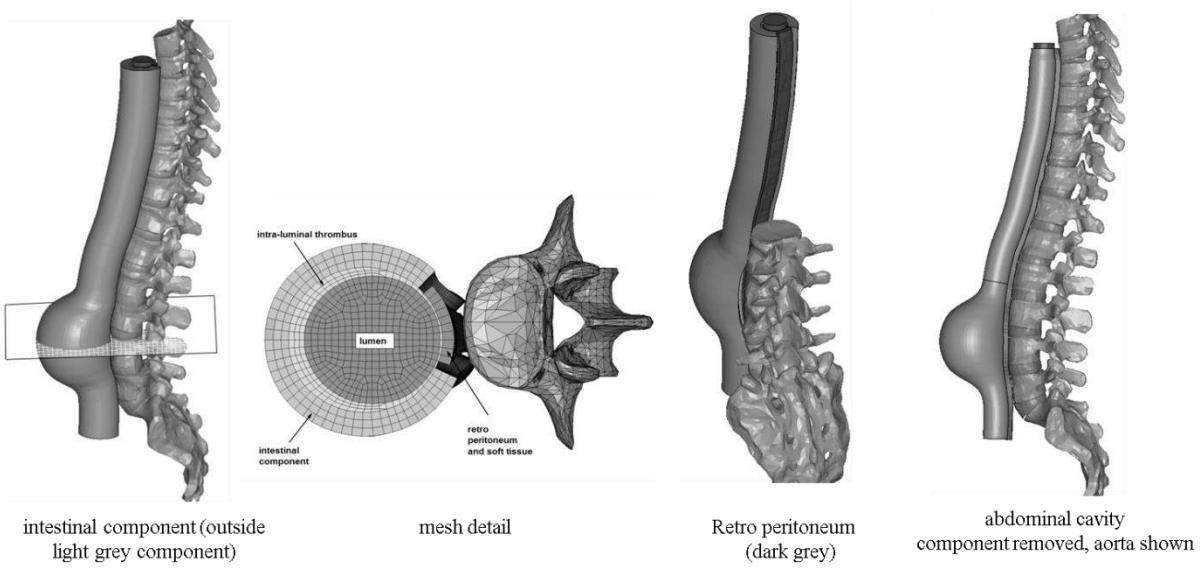

Figure 2.19: FEA model used by Di Martino that included the AAA and surrounding organs.[128]

2.9 Modelling of blood in human arteries

The presence of aneurysms in the cardiovascular system is associated with the changes in the behaviour of the blood flow passing through the arteries[132]. The formation, progression, and rupture of AAA are attributed to the direct interaction between the wall shear stresses and the corresponding variations in the AAA wall induced from blood flow [133].

Blood behaves as a Non-Newtonian fluid in the circulatory system of the human body. However, blood behaves as a Newtonian fluid when the shear rate increases above 100 s^{-1} [134, 135]. The non-Newtonian influence of blood also significantly decreases in large vessels such as in the Aorta because the shear rate is high[136]. Therefore, the assumption of Newtonian behaviour can be considered as satisfactory in AAA modelling [134, 137, 138] as no significant differences were observed in Newtonian/non-Newtonian velocity[139] or wall shear stress profiles[140], see **Figure 2.20**. Gijsen et al. [139] studied the variances in the flow resulted from the Newtonian and non-Newtonian assumptions through 90˚ curved tube

between. Recently in 2017, Kumar D et al.[141] has studied the variances in velocity and pressure distributions due to modelling blood as Newtonian and non-Newtonian in transient flow for specific patient AAA. Their results showed a considerable similarity between the velocity and pressure distribution in terms of maximum and low magnitude, as well as the location. Thus, the assumption of modelling blood as a Newtonian fluid in the current work is acceptable.

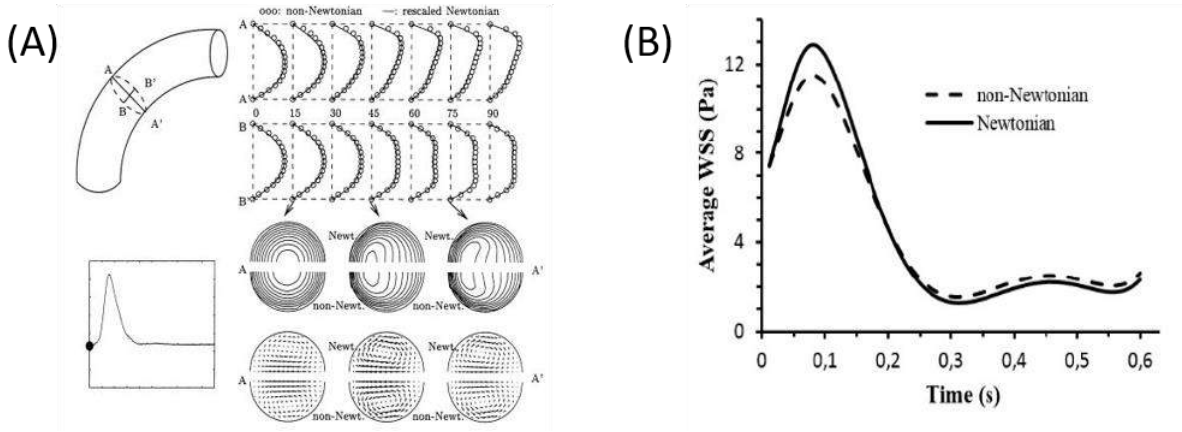

Figure 2.20: (A) Comparison of Numerical velocity profiles and contours in planes (Ā-Ā) and (B̄-B̄) for Newtonian and Non-Newtonian fluid at end diastole[139]. **(B)** Average wall shear stress in AAA bifurcations during one heart cycle for Newtonian and non-Newtonian cases[140].

2.10 Summary, Work methodology, and originality

The current chapter contains a brief review of previous studies on AAA that have been classified into two main parts:

- The medical background addressing the way of evaluating rupture risk clinically using maximum diameter and growth rate as rupture indicators, treatment, and diagnosis of AAA.
- Summarising of the numerical techniques that been used to establish new rupture indicators besides those mentioned in the medical section.

The main goal of this chapter is to identify the current gaps in the AAA knowledge base so far in order to work on them extensively to provide new original work that enhances the rupture risk assessment of AAA. These gaps are listed below:

1. Although only two numerical works [41, 42] have been conducted to evaluate the viability of using 3D-ultrasound images in constructing 3D numerical models of AAA. It is found no single work has addressed the significant overestimation of wall stress produces by 3D-US models compared to CT AA models making unreliable rupture assessment. Therefore, an alternative indicator of rupture potential rather than the maximum wall stress should be used that would produce similar results for both CT and 3D-US AAA models of a single patient.
2. The two most common rupture indicators based on AAA wall strength in FEA models are FEARI and RPI. However, these two parameters may indicate multiple locations of high stress and potential rupture sites. They do not show the initiation and propagation of rupture. The present work employs for the first time the extended finite element method XFEM (failure approach) to investigate the initiation of rupture in AAA involving the main three failure parameters ultimate strength, maximum wall stress, and maximum wall strain. In addition, the potential of using 3D-US AAA models in the rupture risk assessment will be further examined.
3. The segmentation process employed by different software such as the ImFusion suite [46] and Mimics v.18 [43] may create models with minor geometrical differences despite the source CT image being the same. This study will extensively address the overall impact of these geometrical differences on the accuracy of predicting the hemodynamic metrics and wall stress of AAA using the Fluid-Structure Interaction (FSI) method.
4. The effects of using different boundary conditions at the inlet and outlets were discussed briefly in the literature. During the skimming process of the previous studies and owing to the lack of measuring patient-specific boundary conditions, it was noticed that the researchers have been using different lengths and shapes of velocity/ pressure waves, hence generating questionable data. Therefore, two sets of boundary conditions (velocity/pressure waves) and (mass flow rate wave/3-elements Windkessel model) will be applied and investigated for a number of patients using the same FSI methodology. Hemodynamic indicators such as TAWSS, OSI, and RRT will be examined and thoroughly compared.
5. Almost all the previous stress analyses studies on AAA have excluded surrounding organs that support AAA and ignored their impact on the stress distribution, which would inevitably affect the accuracy of subsequent rupture analysis. In this study, the AAA wall and the key surroundings organs (Spine, Intestine, and Colon) will be

segmented for a single patient using CT images and Mimics v.18. Further, FEA analyses will be conducted to compare stress distributions and profiles in the presence and absence of the surrounding organs by applying static pressure and appropriate material properties for each organ obtained from the literature.

3 Chapter Three: Construction of AAAs from the acquisition of images to the segmentation process

3.1 Introduction

Earlier in the introduction and literature chapters, the criterion of maximum AAA diameter is observed to be a controversial threshold in evaluating the risk of rupture. Alternatively, a number of numerical rupture risk indicators based biomechanics and hemodynamic of AAA such as maximum wall stress, rupture potential index, finite element analysis rupture index, low wall shear stress, and low-velocity zone were proposed in order to pursue patients that require an urgent repair. In the earlier rupture studies of AAA, it was used idealised computational geometries based on the recommendations of the surgeons [142, 143] to illustrate AAA wall stresses and flow patterns [144, 145]. It has been observed that the distribution of wall stress was extremely relying on the real shape of the AAA and its maximal diameter [113, 146] because the complexity of AAA shape in-vivo alters the stress distribution significantly [147].

Certainly, it was evident that providing 3D models of AAAs that were built from patient-specific images demonstrate complicated wall stress distributions [25, 85], which can be highly influenced by many factors such as the presence of the thrombus [118]. Detailed information of AAA, such as the maximum diameter and presence of thrombus, can be collected during the examination and diagnostic procedure using one of the imaging techniques such as computed tomography, 3D ultrasound, and Magnetic resonance imaging. Nowadays, these two-dimensional cross-sectional images data can be converted into 3D patient-specific models of AAA, which can be helpful to understand the biomechanics and hemodynamic of AAA computationally. Moreover, engaging 3D patient-specific models of AAA in various numerical solutions may provide a reasonable justification behind the vague of rupture in small aneurysms. Segmentation software such as Mimics v.18 [43] has a high ability to import medical images and create 3D smooth patient-specific geometry of the AAA is employed in this work. Then, the final 3D model of AAA will be exported to one of the validated engineering codes such as Abaqus v6.14 [148]/2016 [44], STAR CCM+ v.13.04 [45] to investigate the biomechanics and hemodynamic of AAA [25, 84, 85, 149, 150]. Engineering codes provide colour coded contours showing stress distribution on the AAA wall that calculated based on the patient-specific AAA models constructed from the medical images, which make the predictions of rupture assessment more understandable and precise.

This chapter covers the methodology of the segmentation process of patient-specific AAA from importing the medical DICOM images to the final 3D CAD utilising two packages:

1- Mimics v.18 [43], ***M**aterialise's **I**nteractive **M**edical **I**mage **C**ontrol **S**ystem*, is a medical image processing software developed by Materialise that is being broadly utilised among researchers and doctors to extract 3D models of the internal organs of the human body. This software has a powerful platform to import CT and MRI images to construct and process highly detailed 3D geometries of AAAs for rupture risk assessment using various computational numerical solutions.

2- Vascular Suite ImFusion [46] is a medical image analysis software used by clinicians that provides high-efficiency in time and cost in rendering and processing of CT and 3D-US medical images of patients with AAA and converts them into 3D geometries of for the research purposes.

Furthermore, this chapter offers a full understanding to the readers about the capabilities of each platform in capturing even the minor details of the AAA. In addition, engage these models of AAA in different approaches that contribute to enhancing the rupture risk assessment of AAA.

3.2 Imaging

3.2.1 Acquisition of computed tomography images

Each set of CT images was implemented using a 128-slice Siemens SOMATOM Perspective scanner (Siemens Medical, Munich, Germany). Patients were positioned supine, and images at 1mm slices were acquired from the aortic arch to the femoral heads. Arterial phase images were acquired using a bolus dose of 100 mL of the iodinated contrast medium Omnipaque 240 (GE Healthcare, UK) administered at a flow rate of 3 mL/s.

3.2.2 Acquisition of 3D Ultrasound images

3D US data was acquired using a Phillips IU22 ultrasound console (Phillips, Amsterdam, Netherlands) using a C5-1 curved array transducer. An electromagnetic tracking system (Ascension, Vermont, USA) that consists of a magnetic field generator and two tracking sensors that attach to the ultrasound probe were used along with 3D guidance software that provides the rotational and positional precision of 0.5o and 1.4 mm root mean square respectively. The positional information generated by the movement of the sensors in the magnetic field allows the system to orientate the US-probe in time and space. Then, a

high accuracy grabber was utilised to collect the 2D US frames that can be displayed on an ultrasound device, which then be assembled into a 3D volume.

3.3 Segmentation of AAA in Mimics

CT images were imported into Mimics v.18 research software [43] to construct a 3D model of AAA. The construction process of an AAA starts with using a global thresholding technique, dynamic region growing, and manual or semi-automatic editing for masks, where the whole process is called segmentation.

Global thresholding is the first step to produce initial 3D masks of AAA lumen and thrombus by assigning a specific range of pixel intensity values measured in (HU) Hounsfield units on the CT images. Threshold values were carefully set by using Mimics v.18 [43] predefined threshold values, which can be adjusted manually to capture the AAA lumen and thrombus see **Figure *3.1***. However, in some cases, the threshold intensity of the AAA could be similar to the adjacent organs such as the spine, which can be problematic, therefore, further user intervention needed to split the spine out of the AAA.

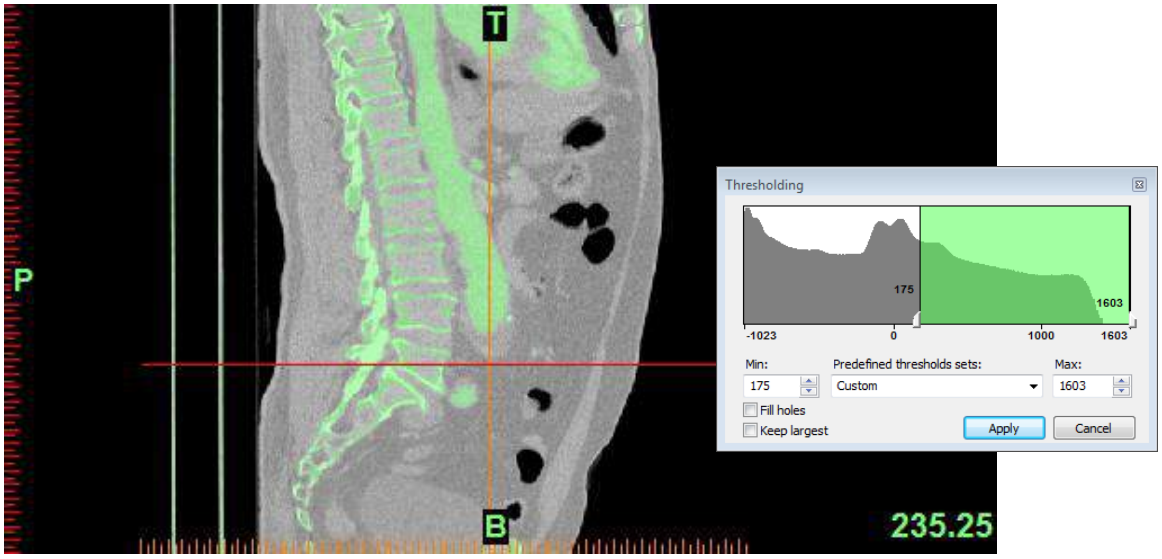

Figure 3.1: Shows good thresholding for AAA in Mimics v.18 [43].

The spine and rib cage were separated out of the AAA mask by using the morphology operations tool. Firstly, applying [Erode operation] in order to remove the pixels connecting the AAA mask and any unwanted adjacent organs. Then, a [region growing tool] was applied to create a new separated AAA mask without the spine. After doing the separation of AAA mask, it is necessary here to compensate the pixels that have been removed by the user.

Therefore, dilation operation was set, and the compensate number of pixels was similar to that one used in the eroding process. The final AAA mask was regenerated to rebuild the original perimeter of the AAA mask as well as to fill the gaps automatically to obtain a precise and homogeneous mask that match the AAA boundaries see **Figure *3.2***. Now, the mask of AAA is ready to calculate a 3D model of the aorta, where the final shape of the segmented aorta is shown in **Figure *3.3***.

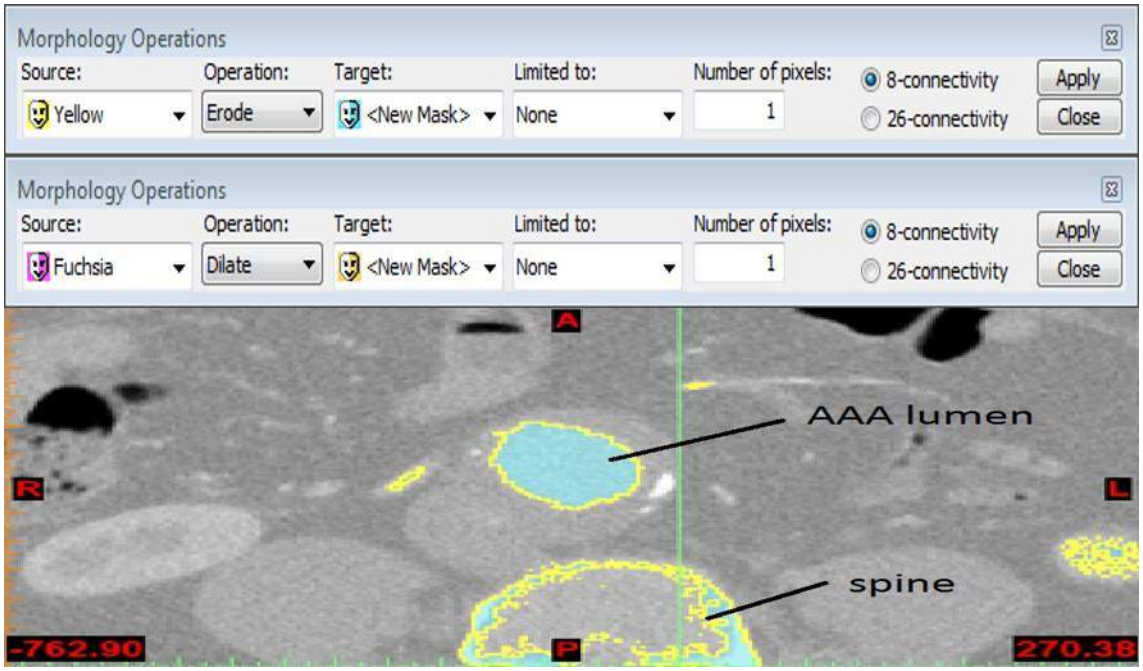

Figure 3.2: Illustrates the morphological operations to isolate the aorta out of the spine.

Concerning the segmentation of the Intra Luminal Thrombus (ILT), a good threshold should be set to capture the whole volume of both ILT and the lumen of AAA. Then, one of these two options is recommended for the user to create the ILT mask. The first option is how to get rid of the blood volume throughout editing the slices manually and create a separated ILT model. The'' multiple slice edit'' tool was used to locally threshold the blood in order to remove AAA lumen mask from the ILT mask, starting from the first slice that contains the thrombus to the last slice. An interpolation process was conducted among these slices to fill any forgotten slices during the editing process; eventually, the ILT mask was subtracted from AAA mask to obtain the ILT 3D model see **Figure *3.3***. The second option is using the Boolean subtract tool in the morphology operations, where the improved and separated AAA lumen mask was subtracted from the mask of AAA (lumen + ILT) to produce a new precise

mask just for the ILT. The use of the second option is highly recommended because it is more accurate, saves time, handy, and produces a smooth, precise ILT mask.

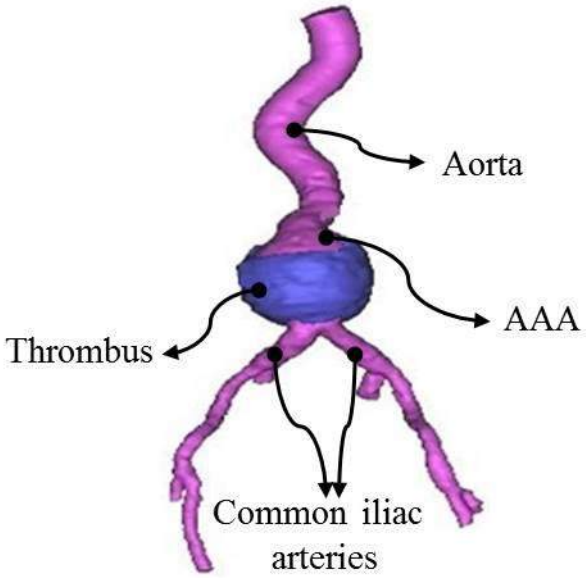

Figure 3.3: Shows a 3D representative model of the AAA segmented in Mimics v.18 [43].

3.3.1 Editing AAA models in 3-Matic v.10

The final model of the AAA produced in Mimics v.18 [43] is relatively rough and need to be smoothed before creating the aortic wall. So, in this case, the AAA model was imported to 3-Matic v.10 [43] in order to perform a smoothing process to the rough areas on the surface of AAA using the local smooth tool. Then, the AAA model is now ready to create the aortic wall by using the ‘’Hollow’’ tool that allows the user to expand the luminal surface to the outside for a certain thickness, in this case, the luminal surface was expanded 2 mm outside see **Figure *3.4***.

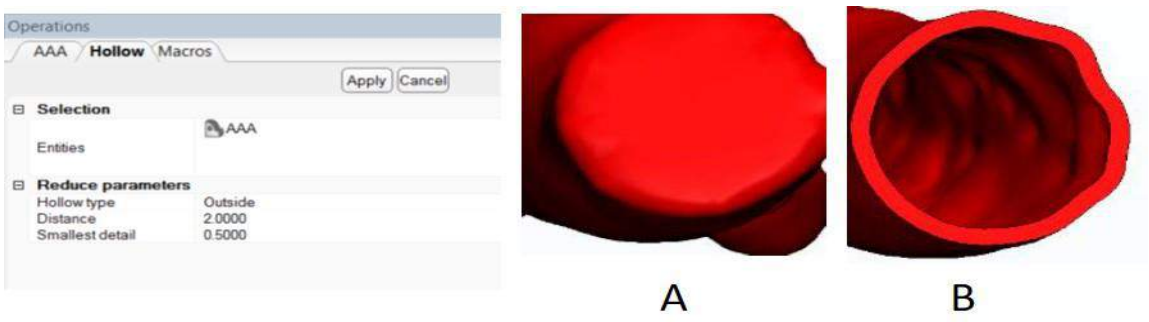

Figure 3.4: Steps of creating AAA wall in 3-Matic v.10 [43].

Due to adding a thickness of 2 mm around all the AAA part, see **Figure *3.4*/A**, the wall is totally closed. Therefore, the ‘’Trimming’’ tool was used to cut the ends of the inlets and outlets of the aortic wall to obtain a smooth hollow wall see **Figure *3.4*/B** and **Figure *3.5***. Finally, additional diagnostic tools such as Fix and Mark are used to identify and fix the geometrical errors induced by the segmentation process of the AAA. For example, removing the overlapped triangles, filling the gaps, and delete the noise shells to obtain the final 3D model of AAA, as shown in **Figure *3.5***.

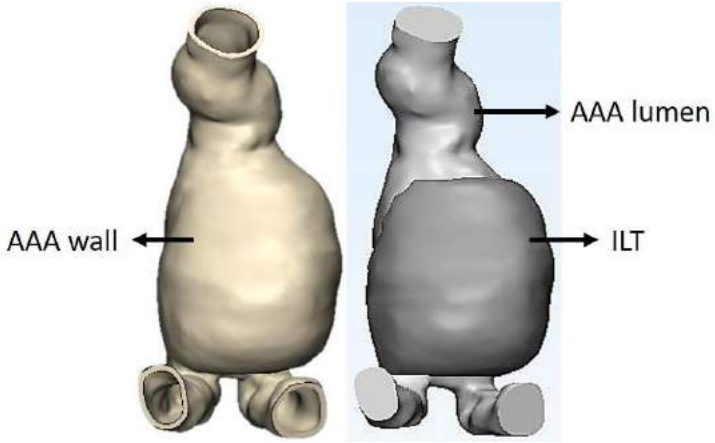

Figure 3.5: Final 3D model of AAA (lumen & ILT/ right) vs. (wall/ left) segmented and smoothed in Mimics v.18 [43].

3.4 Segmentation of AAA in ImFusion

As mentioned earlier, ImFusion suite [46] has the capability of converting the medical images into 3D models of the desired organs. In the first step of segmentation, the obtained images of AAA are imported in order to extract 3D patient-specific models of AAA, which can be employed to conduct biomechanical simulations (FEA, CFD, and FSI) to predict the biomechanics of the AAA numerically. Second, the images are partitioned into a number of segments (slices) to produce and form the outlines of the AAA lumen, wall, and thrombus. Next, the initial AAA models are transformed by interpolation algorithms to construct a 3D model of AAA as a surface mesh called STL geometry.

In fact, the ImFusion software prototype [46] was initially employed to measure the volume of carotid plaque. However, a research team at Wythenshawe hospital[151], who first discovered the potential of using the ImFusion suite [46] as a tool to construct patient-specific models of AAA from CT and 3D-US images. Collaboration between the team [151] and the software developers was reached for the purpose of developing and improving the software to

make it suitable for constructing the AAA. The ImFusion software [46] and a number of segmentation approaches[152, 153] utilise an algorithm called "interactive image segmentation'' which allows the user to define two sets of points as input, known as seeds. The first set of seeds is targeting the entire inside object (green) and the second set of points targeting the whole outside region (red), for instance, the outside and inside of the aneurysmal wall see **Figure *3.6***.

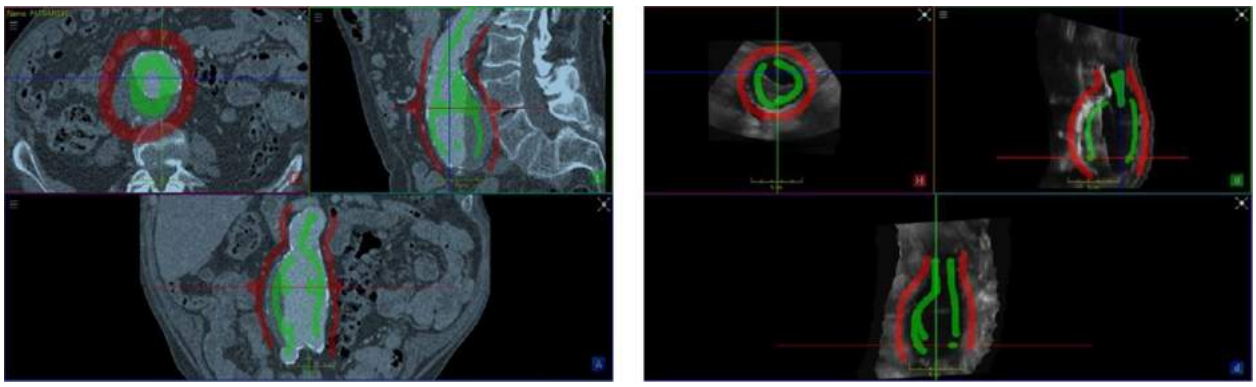

Figure 3.6: Shows the seeds defined by the user on the AAA wall: green (inside) and red (outside) for CT images (left) and 3D-US images (right)[151].

The role of the seeds (green and red) is to initially predict the inner and outer boundaries of the AAA wall as well as constrain the software, in other meaning; the green region will stay inside until the final results of the segmentation and the same concept for the outer region. The next step is producing initial boundaries of the AAA, see **Figure *3.7*** created by the ImFusion software [46].

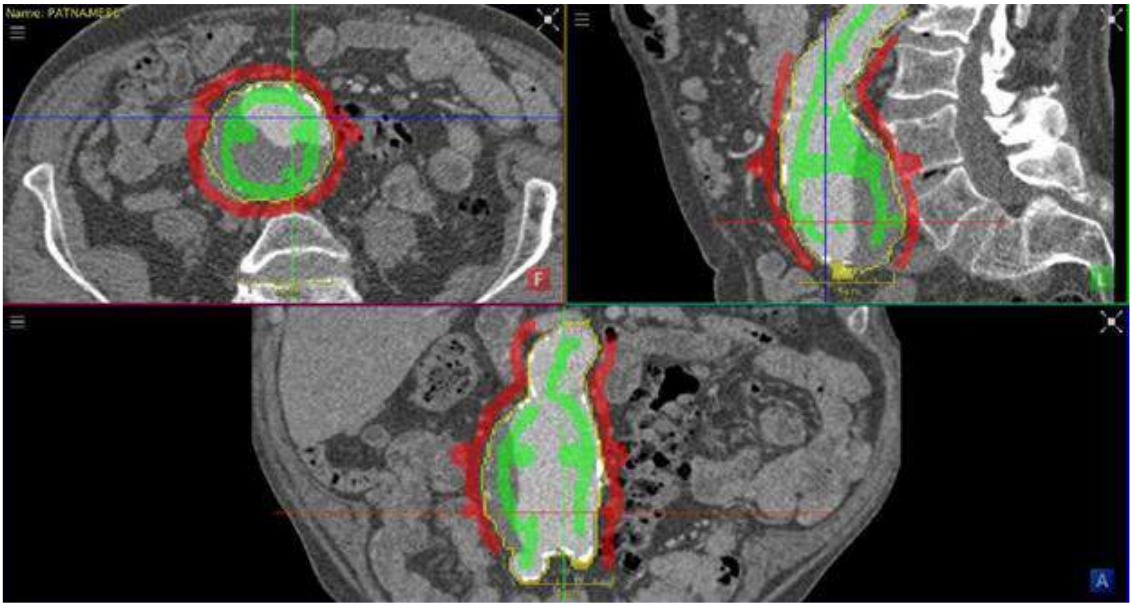

Figure 3.7: Initial segmentation process on CT images showing the boundaries of the AAA wall (yellow line) that will be segmented.**[151]**

If the predicted boundaries of the AAA wall do not match the boundaries on the CT images, which means there is an error that should be corrected manually by hiring additional seeds by the user. At that time, the segmentation process must be repeated and re-assessed to ensure capturing the real boundaries of the AAA wall. It has been observed that if the border that splits the AAA wall out of the surrounding organs is not well-defined, this means further corrections are required, see **Figure *3.8***. It can be seen from **Figure *3.8*** (*left image*) the suggested boundary (*yellow line*) does not capture the outer wall of the AAA. This is attributed to the surrounding organs (blue arrow= inferior vena cava) have similar pixel intensity to that one of the intraluminal thrombus of AAA. Therefore, extra seeds must be placed (*centre image*), and outer the boundaries must be redefined to obtain improved segmentation result (*right image*).

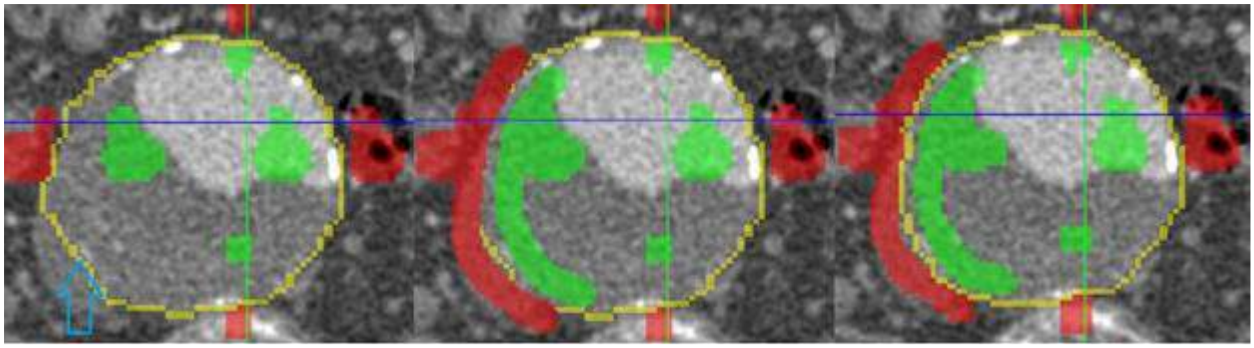

Figure 3.8: Manually correcting the boundary of AAA (**left image**) in segmentation by redefining the new set of seeds (**centre image**) to produce an improved result of AAA wall (**right image**).[151]

To obtain the initial 3D geometry of AAA, the corrected and improved regions (inside and outside) are spread into the whole images[154]. Any undefined pixels neither green nor red will be captured and added to the segmentation process by the neighbour pixels (inside or outside) depending on which one is the faster to reach them. It is also observed that the pixel location affects the propagation speed of the green and red regions. For instance, if the pixel locates on the edge of the CT image, which slows the speed of propagation at this pixel. Once the segmentation process reaches user satisfaction, two main masks will be created: the green mask represents AAA, and the red mask represents the outside (surrounding organs) see **Figure *3.9*/top**. Then, a marching cube algorithm [155] is applied within the ImFusion software [46] in order to convert the masks created by the segmentation process into a 3D surface such as the STL file. Finally, the resolution of the output AAA geometry can be refined to obtain a smoother surface by increasing the mesh resolution to the maximum level. **Figure *3.9*/bottom** shows three different smoothing stages were applied to reach the optimum anatomical features of AAA geometry. Regarding other parts of the AAA (e.g. thrombus, calcification and lumen) can similarly be segmented.

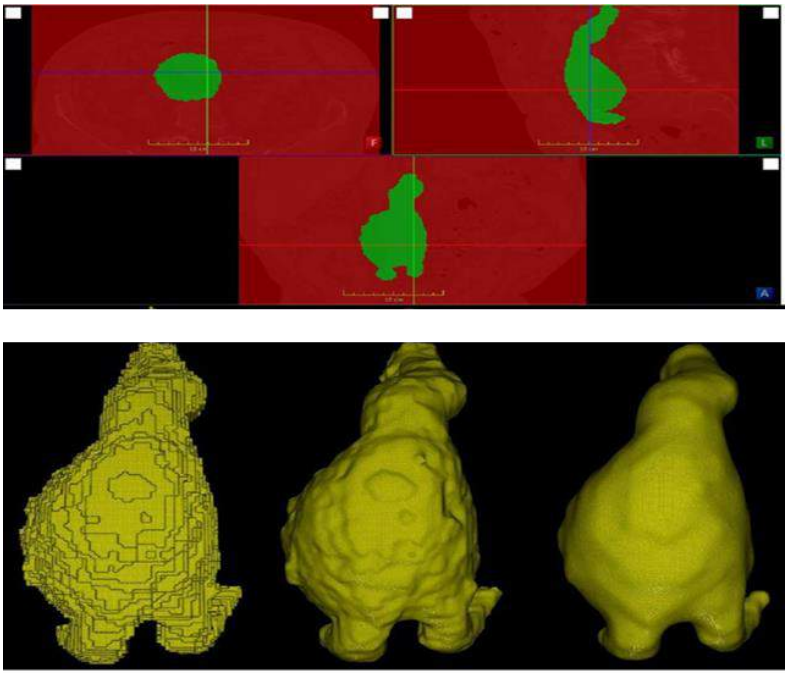

Figure 3.9: Masks generated by the segmentation process (**Top image**). Three different stages of smoothing: no smoothing/ left and high smoothing/right (**Bottom image**).**[151]**

Despite the fact that the output STL file of AAA looks smooth, it needs more smoothing in some rough areas such as bifurcation and neck angle. ImFusion suite [46] would have limited capabilities in CAD processing if another smoothing level applied to the AAA geometry that will reduce the actual size of the aneurysm. Then, the segmented AAA models in the ImFusion suite [46] will be imported to 3-Matic v.10 [43] to inspect any geometrical errors and perform further smoothing because whatever smoothing level being used it will be compensated automatically by 3-Matic v.10 [43].

3.5 Results

The AAAs of Patient1 were selected to show the geometrical differences between CT and 3D-US models. Both AAA models have the same origin and orientation, imported into MATLAB [156] and overlaid over each other, see **Figure 3.10**. The differences in the geometrical features can be observed, which depend on factors such as the experience of the person who implemented the segmentation process, and the contrast of the CT and 3D-US images. In addition, the AAA images being influenced by systolic (high volume of AAA) and diastolic pressure. Finally, the tools that have been used in Mimics v.18 [43] and ImFusion suite [46] to create the AAA wall, thrombus, and lumen can be summarised in **Figure 3.11**.

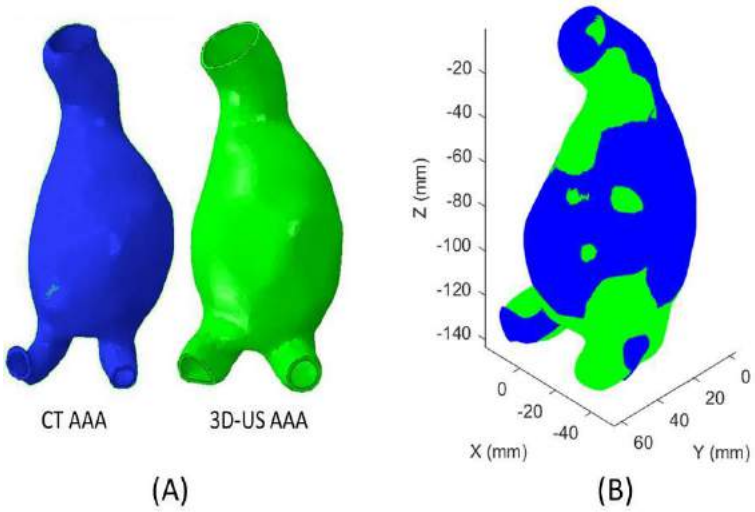

Figure 3.10: (A) AAA CT and 3D-US wall created of Patient1, (B) Juxtaposed images of CT (blue), and 3D-US (green) for Patient 1.

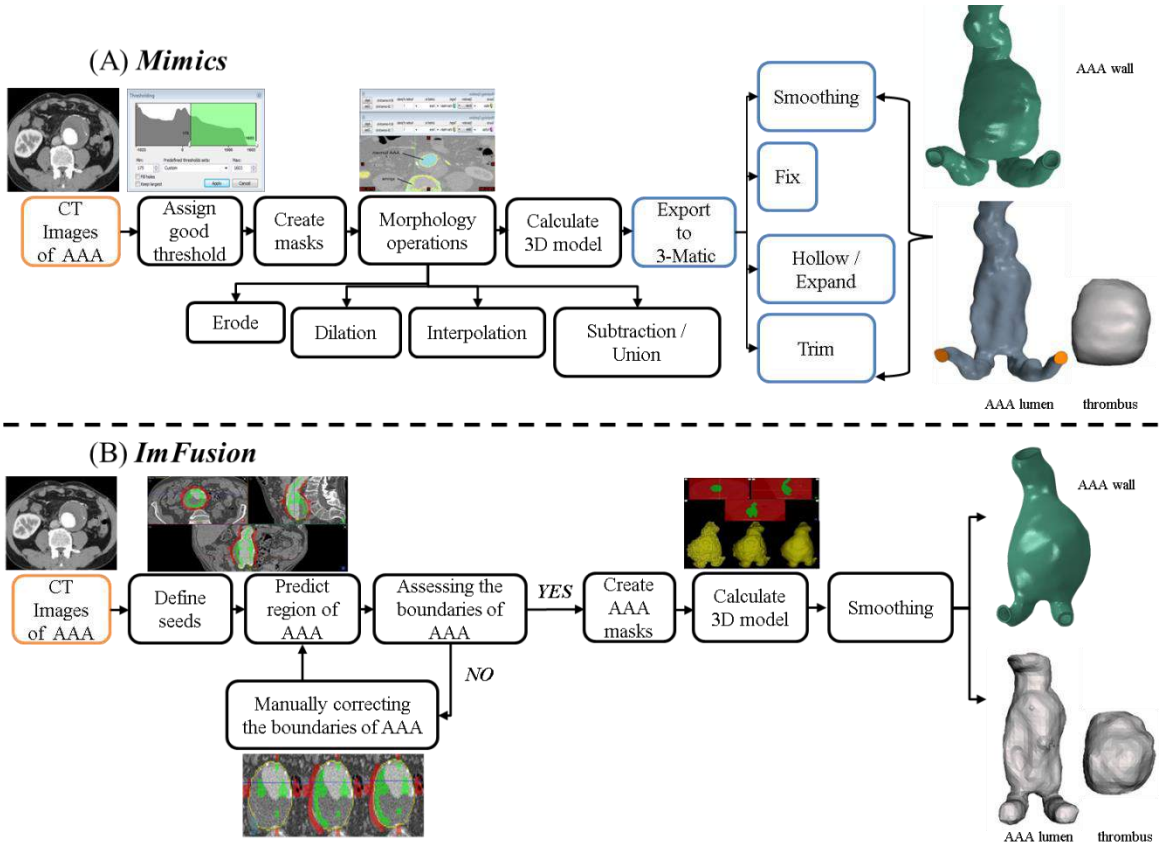

Figure 3.11: Workflow of segmentation process in: (A) Mimics v.18 [43] and (B) ImFusion suite [46] for a single AAA patient.

3.6 Conclusion

Computational modelling of AAA disease has become a vital diagnostic tool in the clinical evaluation of the risk of rupture against the risk of operating. Huge improvements on the AAA rupture risk assessment were developed by engaging patient-specific models of AAA derived from medical images CT, MRI, and 3D-US instead of using idealised geometries. Therefore, two segmentation software Mimics v.18 [43] and ImFusion suite [46] are employed to construct AAA models from CT and 3D-US in order to achieve the objectives of the current work. Detailed workflow from importing the images to the final step of creating a 3D model of AAA is fully described for each software. Furthermore, fixing the computational model of AAA from any expected errors during the construction is achieved in 3-Matic v.10 within Mimics v.18 [43] package in order to avoid any negative influences that reflect poorly on the results of numerical solutions. Most importantly, the ImFusion suite [46] is being widely used in clinical work to construct AAA models; thus, the accuracy of its construction against reliable and well-known software academically and clinically such as Mimics v.18 [43] should be taken into consideration.

4 Chapter Four: Comparisons of finite element models of abdominal aortic aneurysms generated by computed tomography and three-dimensional ultrasound.

4.1 Introduction

The abdominal aortic aneurysm (AAA) in its nature represents a fatal risk due to the unpredictable rupture [157]. Recently, NHS practices run screening programs for patients with AAA to be undergone for routine surveillance using 3D ultrasounds (3D-US) imaging technique to evaluate the progression of AAA growth and, subsequently, the risk of rupture. In contrast, when the AAA ruptures, therefore, Computed tomography (CT) scans are considered urgent to give full details about the damaged AAA wall and size of blood leakage. These pre-operation CT images of AAA are being used to construct 3D patient-specific models of AAA in order to be analysed numerically using the finite element method FEA to understand the mechanism of rupture. However, CT imaging is expensive and exposes patients to both ionizing radiation and intravenous contrast that is potentially nephrotoxic [158, 159]. As a result, if 3D-US could be used to provide patient-specific geometries for FEA analysis, a study of the relationship of wall stress and AAA growth will be obtained for a huge number or group of patients as well as routine FEA analysis can be undertaken to evaluate the development of AAA wall stress.

From the material-failure point of view, AAA rupture occurs when the maximum wall stress exceeds the strength of the AAA wall [150]. In general, FEA analysis can be conducted to investigate the stress distribution and deformation (strain) in the AAA wall due to the luminal pressure of blood. This process currently requires the construction of a numerical, patient-specific geometry of the AAA derived from CT, as well as appropriate boundary conditions and material properties. Generally, the AAA models are derived from CT data using specialized software to perform *segmentation*. Most of the recent researches using CT images have utilized a thresholding method of segmentation, e.g., that used by Mimics v.18 [43]. The CT data have proven to provide a highly detailed model of AAAs, including the intra-luminal thrombus (ILT), wall and lumen, but its use is not suitable for repeated scans for aneurysm monitoring due to the reasons mentioned above[160, 161].

The goal of this chapter was to conduct a comparative analysis of AAA finite element models generated from CT and 3D-US images for four patients. The locations and

distributions of wall stress/strain were investigated using 3D coloured contours. In terms of stress magnitudes, the weighted mean values, as well as the characteristic value (95% of the wall volume having stress value lower than this), were compared.

4.2 Methodology

Four patients with AAA were selected in order to demonstrate the potential and the limitations of using 3D-US to capture the stress and strain in the AAA wall using FEA analysis. The patients had undergone CT for the planning of AAA repair at University Hospital South Manchester and were identified via the radiology department records. All patients gave informed consent, and ethical approval was granted by the National Research Ethics Committee (13/NW/0468).

4.2.1 CT scanning

CT angiography was performed using a 128-slice Siemens SOMATOM Perspective scanner (Siemens Medical, Munich, Germany). Patients were positioned supine, and images at 1mm slices were acquired from the aortic arch to the femoral heads. Arterial phase images were acquired using a bolus dose of 100 mL of the iodinated contrast medium Omnipaque 240 (GE Healthcare, UK) administered at a flow rate of 3 mL/s. via an 18 gauge intravenous cannula in an upper limb vein. The scanner is configured such that detection of contrast in the aortic arch initiates the scan, which follows the contrast bolus from the arch of the aorta down to the femoral vessels.

4.2.2 3D-US scanning

3D-US data was acquired using a Phillips IU22 ultrasound console (Phillips, Amsterdam, Netherlands) with a C5-1 curved array transducer. An electromagnetic tracking system (Ascension, Vermont, USA) comprising of a field generator and two tracking sensors attached to the ultrasound probe was used together with 3D guidance software. The positional information generated by the movement of the sensors in the magnetic field allows the system to orientate the US probe in time and space. This positional data allows the 2D US frames to be assembled into a 3D volume. Patients were positioned in a supine position on an examination couch and asked to remain as still as possible. The scan was initiated from the most proximal section of the aorta that could be visualised, and the transducer moved slowly down the aorta until the bifurcation (or until the aneurysm could no longer be seen).

4.2.3 3D Reconstruction and geometry preparation

CT and 3D-US data were imported to a prototype analysis software (ImFusion Suite [46]) that was able to execute segmentation on both datasets. An interactive segmentation algorithm was utilized where the researcher briefly places seeds inside and outside the relevant structure in a number of slices. The 'outside' and 'inside' sections are then deployed and defused in the whole image, defining the blood (lumen) from the surrounding aortic wall or thrombus [154]. Other structures of the AAA (e.g., wall, thrombus) can also be segmented in the same way. ImFusion software[46] then utilizes a marching cubes algorithm to change the contours created by the segmentation into a surface mesh[155] that can be exported as a stereolithography (STL) file.

The STL files were then imported into 3-Matic .10 [43], which is able to combine CAD tools with pre-processing (meshing) capabilities. Any distinct unimportant points were smoothed using the 'local smoothing' tool. The outer surface of (lumen and thrombus) was expanded, *outwards* by 2mm for the 3D-US model and *inwards* by 2mm for the CT model, to create the aneurysmal wall using the 'hollow' operation see **Figure 3.10 (A)**. This was done as the 3D-US segmentation captures the inner wall of the AAA, and the CT segmentation captures the outer wall of the AAA. A final operation was conducted to cut the inlet of AAA and the bifurcations so that a regular boundary is created for subsequent stress analysis. The method of expanding the AAA surface to create the aneurysmal wall and the assumed wall thickness of 2mm was taken from the literature as no imaging modality has yet been proven to be able to measure AAA wall thickness accurately [42]. The presence of intraluminal thrombus in this study was ignored because its role remains controversial. Studies have suggested it could decrease, increase or have no impact on the wall stress [80, 83, 162-164]. The immediate aortic bifurcation was included in the model but not considered further downstream as it was poorly imaged on 3D-US, and removal of the iliac vessels from FEA simulations does not significantly influence the wall stress distributions[73].

4.2.4 Mesh generation

Once the STL (CT and 3D-US) AAA models were imported into Abaqus v16.4 [148] for stress analysis, an appropriate mesh for AAA geometries was generated. A plug-in within Abaqus v.16.4 [148], 'Mesh to Geometry' was used to convert the STL models into native Abaqus parts in order to mesh them utilising mesh module and reducing the pre-processing time. A re-meshing procedure to create a tetrahedral (C3D4) volume mesh on each of the AAA models was performed. A mesh-sensitivity study was conducted to determine the

optimal number of elements by doubling the seeds point at each mesh to increase the number of elements. The maximum wall stress values were calculated and examined by increasing incrementally the number of elements, in order to obtain suitable mesh size. **Table *4.1*** shows details of mesh-sensitivity study for Patient 1 (CT and 3D-US). The second mesh was chosen as stress values did not grow by more than 2%.

Table 4.1: Mesh study conducted for Patient 1 (CT and 3D US) parts.

AAA CT geometry		AAA US geometry	
Number of elements	**Max wall stress values (MPa)**	**Number of elements**	**Max wall stress values (MPa)**
173 172	0.502	124 000	0.955
355 471	0.593	344 854	1. 178
855 154	0.6	908 456	1.2

4.2.5 Boundary conditions

A static uniform blood pressure of 0.016 MPa (120 mmHg) was applied to the inner surface of AAA geometries [150]. The AAA wall was modelled as a nonlinear, homogenous, isotropic, hyperplastic, and incompressible material based on validated experimental and numerical data [25, 165]. The mathematical form of the strain-energy that used to characterise the nonlinearity of the AAA wall is:

$$W = \alpha\left(I_1 - 3\right) + \beta\left(I_1 - 3\right)^2 \qquad \textbf{(4. 1)}$$

Where W = *strain energy*, I_1= *the first invariant of the left Cauchy-Green tensor*, and α=0.174 MPa β=1.881 MPa are constants that represent the mechanical wall properties of AAA. These properties have been used in a number of previous studies [25, 73, 85, 118, 166]. The AAA was constrained proximally and distally to simulate the fixation of the aorta at the renal arteries and aortic bifurcation.

4.2.6 Post-Processing and data analysis

Volumes of CT and 3D-US AAA numerical models were measured (V_{CT} and V_{US}), respectively, in which the volume of the CT model was considered as the reference for comparison. Next, to quantify the differences between CT and 3D-US models, the percentage of variation was calculated by:

$$Percentage\ of\ \ difference\% = \left[\frac{|V_{CT} - V_{US}|}{V_{CT}}\right] \times 100 \qquad \textbf{(4. 2)}$$

In order to easily visualise and identify the locations of high stress/strain in each AAA pair, contours of strain and maximum principal stress were extracted and compared for both sets of models: CT and 3D-US. The FEA simulation and post-processing were performed in Abaqus v.16.4 [148] to produce detailed stress distributions on the AAA wall. In this study, maximum principal stress was considered first for comparison, similar to other research in the literature [167-171]. The maximum principal stress theory of failure supposes that the AAA wall material fails when the maximum principal stress reaches the failure threshold of the AAA wall; in other words, the strength of the aneurysmal wall. The strain in the AAA wall was obtained to show the wall deformation due to a static peak pressure of 0.016 MPa (120 mmHg). Simulation steps were briefly summarized in **Figure 4.1** from segmentation until the post-processing.

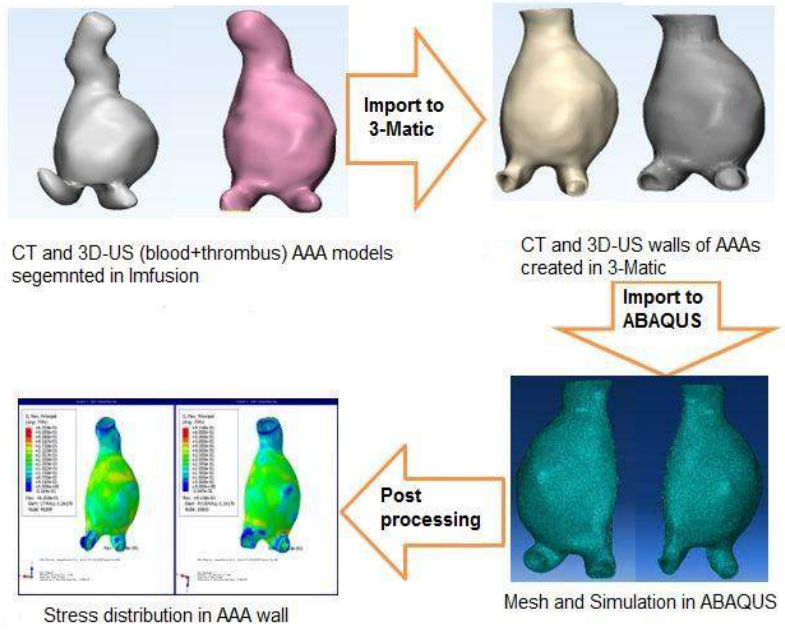

Figure 4.1: Summarised workflow of image processing and FEA simulation.

However, it should be emphasized here that a high value of stress in a single element - possibly an artefact of stress-concentration resulting from unrealistic smoothing - is unlikely to lead to rupture of the whole aneurysmal wall. Hence a statistical approach was undertaken by plotting frequency plots of stress values corresponding to element volumes to observe whether the maximum stress occurs in a single element or a set of elements. The volume-weighted mean (50%) and characteristic wall stress above and below (95%) were calculated for a more meaningful comparison for rupture potential. This part of the analyses was carried out in Origin [172] and MATLAB [156] using kernel distribution function to capture the histogram trend and using the normal distribution for obtaining the mean and characteristic values of stress. The correlation between CT and 3D-US plots was evaluated using a correlation coefficient.

4.3 Results

4.3.1 Validation of FEA solution

Usually, the results of FEA analysis can be validated by performing experimental work using a similar physical model and boundary conditions. Indeed, for AAA, it was hard to carry out detailed experimental analysis due to the geometrical complexity of patient-specific AAA models. Moreover, two broadly manufacturing techniques such as casting and 3D printing are being used to create physical AAA models. Commonly, these techniques are associated with high time consuming, a high cost of manufacturing, material waste, expensive 3D printers [173]. Thus, the validity of the current FEA model was examined, and the results were compared against the experimental/numerical work conducted by Doyle 2009/2010[165, 174]. An identical numerical idealised AAA model, similar to the silicone AAA model used in the experimental work in Doyle 2009/2010 and many other works [165, 174-178], was created in Solidworks v.2016 [179] to represent the realistic dimensions of the aneurysms which being recommended by the EUROSTAR data registry[180]. In this section, the physical conditions utilised in the experimental work[174] was repeated numerically employing the FEA approach in Abaqus v.16.4 [148] to investigate the stress distribution and the relation between the exerted pressure on the AAA wall and the deformation in AAA. The idealised AAA has a maximum diameter = 50 mm, and an inlet proximal diameter = 24 mm with a uniform thickness = 2mm. In addition, the iliac bifurcations and the neck were constrained from moving at all directions (zero displacements and velocity) representing the physical structure of the experiment, see **Figure 4.2**. The mechanical properties of the silicone AAA replicas (Sylgard 160 and 170) were modelled within Abaqus v.16.4 [148] as

hyperplastic material using 1st order Ogden strain energy function, see the equation **(4.3)** ,with material coefficients presented in **Table 4.2**.

$$W = \sum_{i=1}^{N} \frac{\mu_i}{\alpha_i} \left(\lambda_1^{\alpha_i} + \lambda_2^{\alpha_i} + \lambda_3^{\alpha_i} - 3 \right) \quad \textbf{(4. 3)}$$

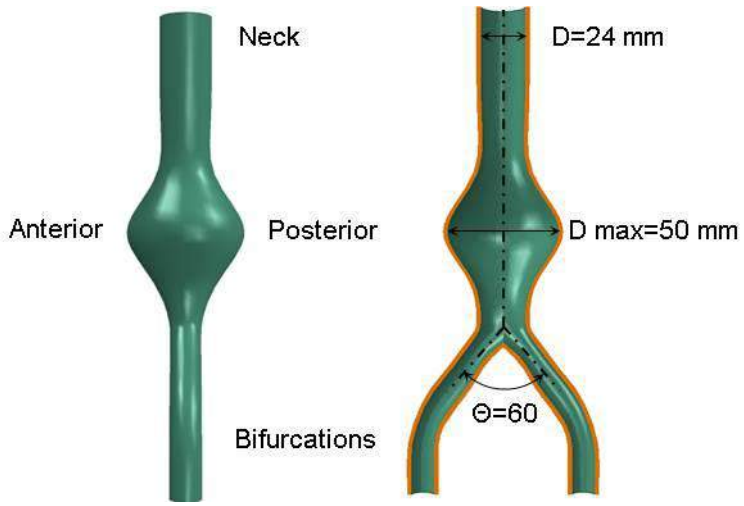

Figure 4.2: An idealised AAA model used in the current study (**left**); dimensions used to create the model (**right**).

Table 4.2: Material coefficients of 1st order Ogden (SEF) for Sylgard 160 and 170.

Silicone mixture type	μ	α
160	1.6525	3.2395
170	0.6988	2.9741

The inner surface of the finite element AAA model was exposed to the same boundary conditions (static pressure), in which the stress distribution and the displacement at the maximum AAA diameter were obtained at each applied load. Most importantly, a mesh and mesh independency study were implemented using linear-hybrid, 3D-stress, tetrahedral elements (C3D4H) and the number of elements to measure the maximum stress was increased gradually until achieving less than 2% error between the final mesh (275343 elements) and the previous mesh (159098 elements).

4.3.1.1 Stress distribution

Stress distribution in the AAA phantom (Sylgard 170) was presented in **Figure 4.3**. AAA replica was exposed to a range of internal loads from 120 mmHg, which represents the

physiological pressure in human arteries to 410 mmHg, which is the mean experimental rupture pressure and then compared against the numerical results of Doyle 2009 [174]. In terms of high and low-stress locations, the variation of stress distribution was fairly consistent with the increase of pressure; however, it was noticed a significant increase in the stress magnitude.

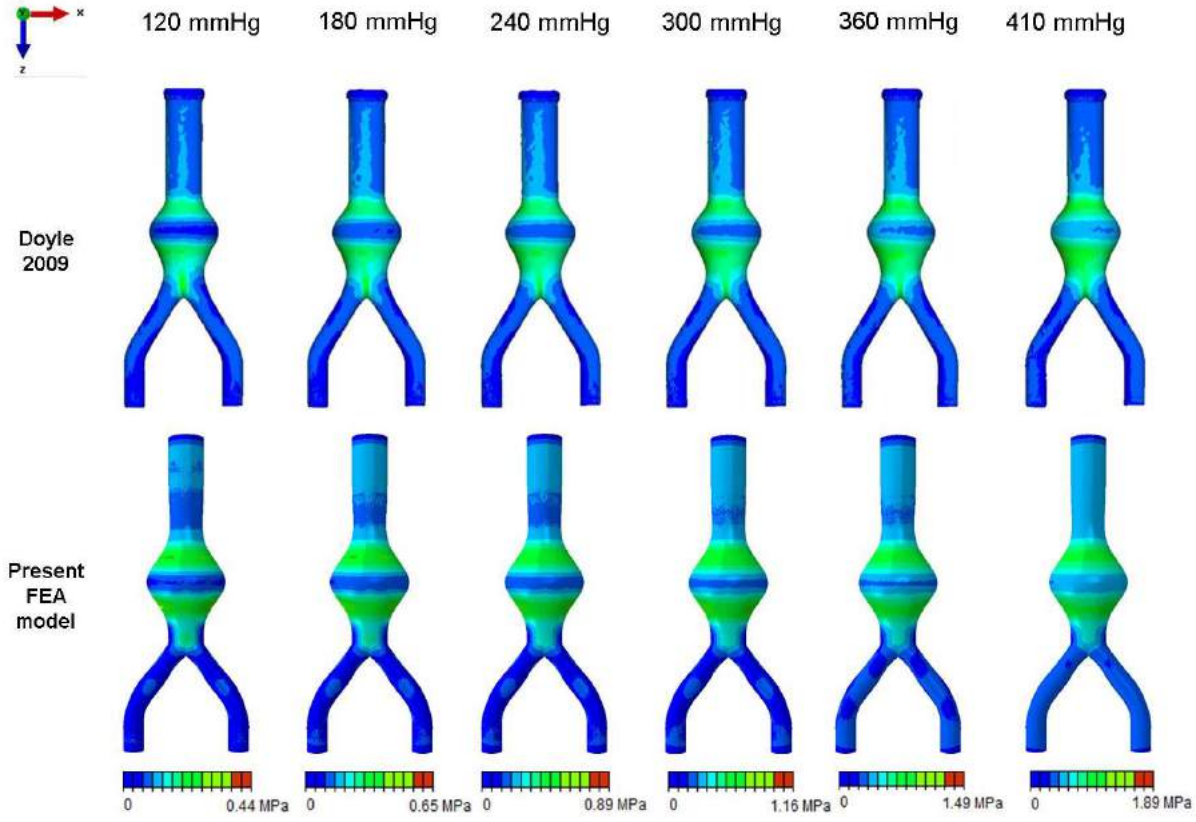

Figure 4.3: Stress distribution of the idealised AAA model obtained from the current FEA work and compared to the numerical results of Doyle 2009[174].

4.3.1.2 Maximum diameter against a pressure load

The trends of changing in the maximum diameter of the AAA replica with the increased pressure load were extracted at each load for both silicone material type (SYL 160 and 170); then, the results were compared with experimental and numerical results of Doyle 2009 [174], see **Figure 4.4**. It was observed that the current FEA model predicted very well the trend of changing in the maximum diameter compared to the experimental results. Besides, the percentage difference between the experimental Doyle 2009 [174] and the numerical results of the current FEA model was measured to be 0.0034% and 0.0129% for models Sylgard 160 and 170, respectively. In summary, the comparisons of stress

distributions and trends of the increased maximum diameter between the current FEA model and the experimental/numerical Doyle 2009 [174] show high agreement; this demonstrates the capability and validity of the current FEA model to be used in the rupture risk assessment of AAA.

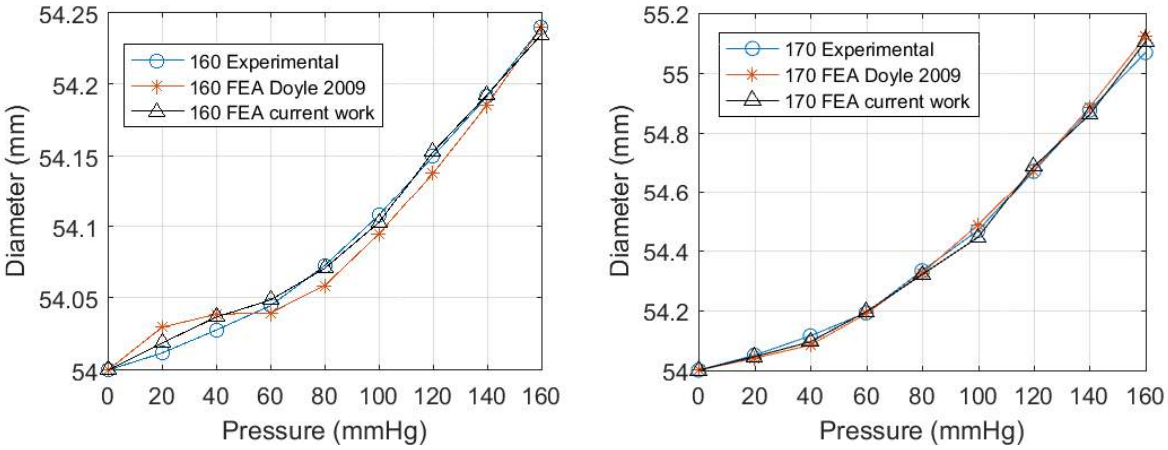

Figure 4.4: Comparison of the results (maximum AAA diameter vs. Static load) for both the silicone model (Sylgard 160/ left and Sylgard 170/ right) of the numerical/current FEA model, numerical and experimental Doyle 2009.[174]

4.3.2 Differences between CT and 3D-US geometries

The quantitative results of the geometry differences between AAA based CT and 3D-US models are presented in **Table *4.3***. Worthy to mention here that the images were obtained via one operator. The percentage differences were determined for the aneurysm part (excluding neck and bifurcations parts) as well as for the whole model. A good similarity was found between CT and 3D-US models in Patient 1 (0.21% whole model, 0.85% for the aneurysm part). Whereas the 3D-US finite element model of Patient 3 showed the highest difference in shape (29.3% whole model and 26.59% aneurysm part), However, as per the literature, the acceptable range is up to 30% difference[181]. The values of maximum wall stress/strain were different, in which the 3D-US models showed high values of stress compared to CT models. However, maximum wall stress locations are comparable between the two models despite the fairly large difference in AAA geometries.

Table 4.3: Quantitative differences in shapes between CT and 3D-US AAA models.

Patients	Percentage of differences Whole Model	Percentage of differences Aneurysm Part
Patient 1	0.21%	0.85%
Patient 2	19.34%	16.88%
Patient 3	29.3%	26.59%
Patient 4	8.93%	6.36%

4.3.3 Wall stress and strain analysis

In terms of providing an index to assess the risk of AAA rupture, wall stress distribution along the AAA is considered to play a vital role, as mentioned in previous studies [24, 84, 150]. **Figure 4.5** and **Figure 4.6** show a comparison of wall stress/strain distribution between CT and 3D-US AAAs for four patients. From **Figure 3.10 (B),** it is evident that the basic geometries from the two methods of scanning (CT and 3D-US) are similar but with noticeable differences. Areas of red colour are shown in various locations indicating locations of high wall stress/strain while the blue regions in the wall represent locations of the lowest wall stress/strain.

The values of maximum wall stress were found as follows: Patient 1 (CT=0.6 MPa, US=0.12 MPa), Patient 2 (CT=0.39 MPa, US=0.54 MPa), Patient 3 (CT=0.41 MPa, US=0.5 MPa) and Patient 4 (CT=0.46 MPa, US=0.58 MPa). Whereas, the values of maximum strain were found as: Patient 1 (CT=0.113, US=0.173), Patient 2 (CT=0.064, US=0.072), Patient 3 (CT=0.067, US=0.065) and Patient 4 (CT=0.061, US=0.08). For better comparison, the colour values in the contour plots have been the same for each patient's CT and US models. Locations of maximum wall stress/strain are in similar areas for both models in all patients except Patient 4 where the location of high wall stress shifted from the bifurcation region in the 3D-US model to the right lateral region in the CT model, as shown by the arrows (see **Figure 4.5**/**Figure 4.6**). However, 3D-US models showed more red patches at different locations besides the area of peak wall stress. Peak wall stress sometimes occurs at the inner surface of the AAA wall (black arrow), while in some cases occurs at the outer surface of the AAA wall (white arrow). It appears that the peak wall stress has no

relation to maximum diameter due to irregular shapes of AAAs geometries, as most of the sites of maximum stress are located at or close to the bifurcation region.

Although the exact locations of high wall stress/strain regions varied among the patients, they were broadly in similar zones (see arrows) in each patient. On the other hand, the differences in the values of stress and strain among patients are due to differences in the AAA shapes; see **Table *4.3*** source of images and CAD processes such as smoothing to get rid of rough spots. Therefore, a further investigation needed to make sure that the obtained maximum wall stress values are not resulting due to the reasons mentioned above; otherwise, the resultant stress will be challenging and misleading the facts.

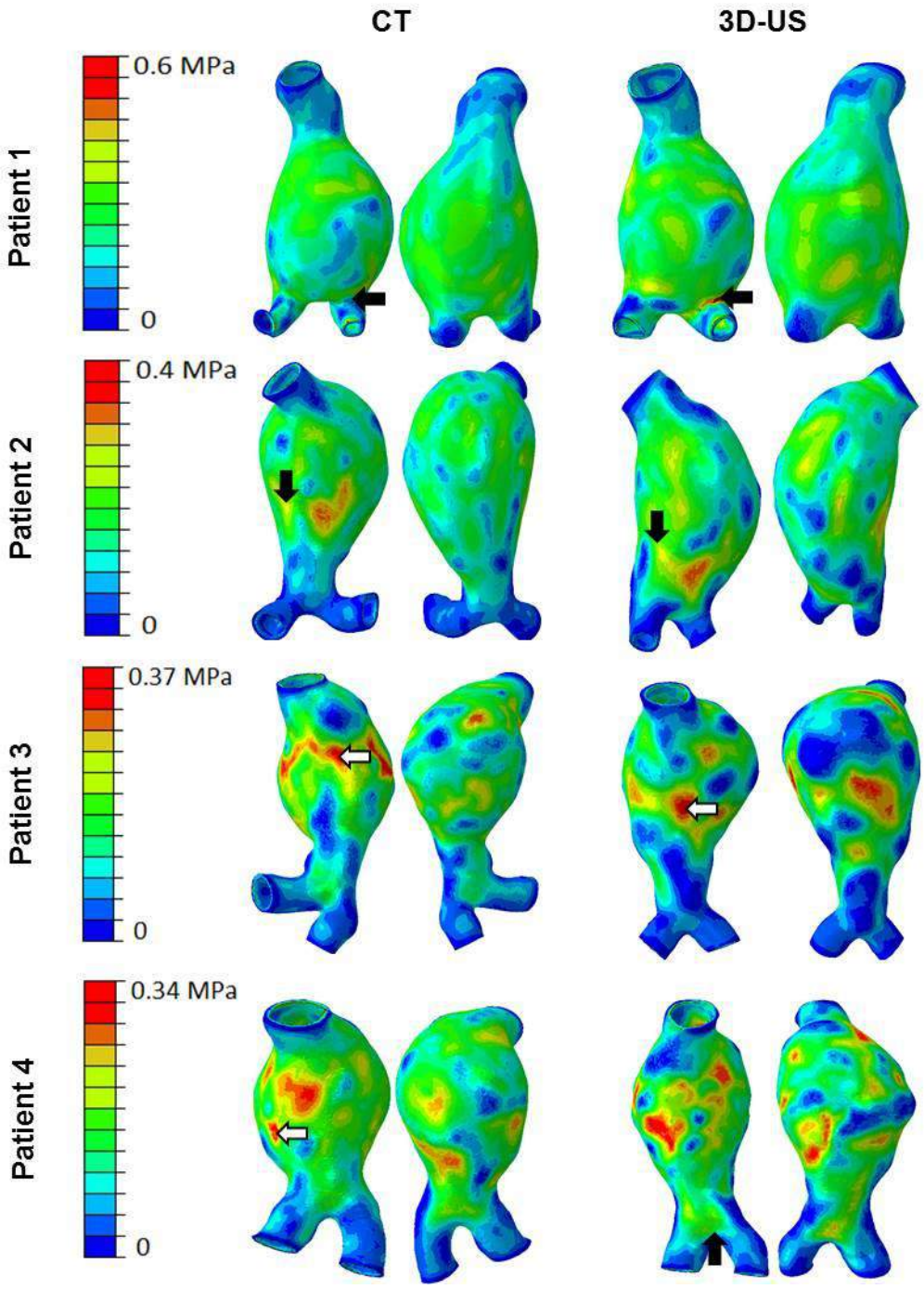

Figure 4.5: Front and back view of wall stress distribution (MPa) in CT (**left**) and 3D-US (**right**), where (**Black and White**) arrows refer that stress occurs at the inner and outer layer of the AAA.

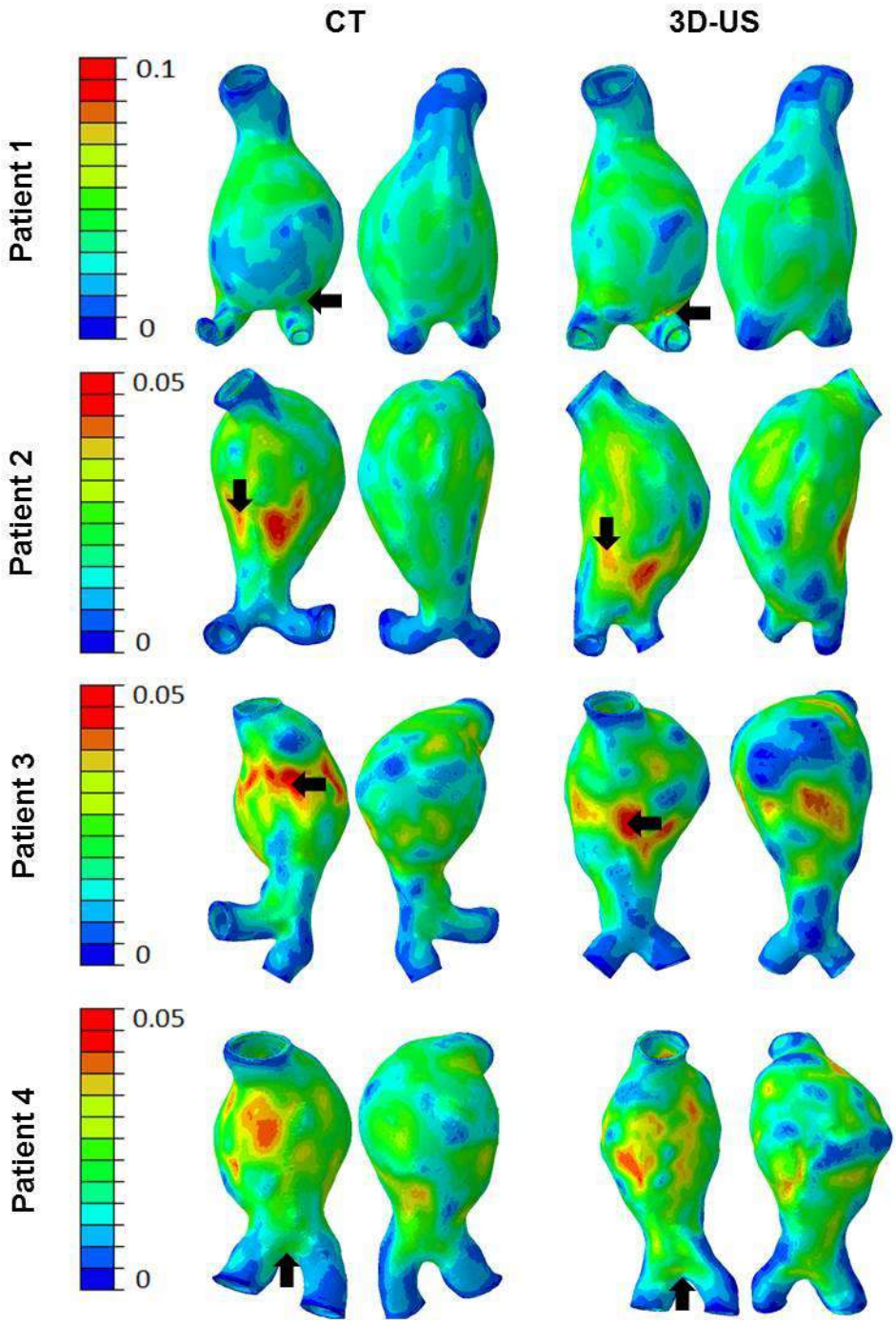

Figure 4.6: Front and back view of strain distribution in all patients CT (**left**) and 3D-US (**right**), where (**Black and White**) arrows refer that strain occurs at the inner and outer layer of the AAA.

4.3.4 Wall stress trends

In order to analyse stress distribution further, the maximum wall stress should be examined to see whether it occurs in an individual element or a set of elements by plotting frequency plots of stress values obtained from each element. The stress varies depending on

the discretisation method of the AAA. The frequency plots of stress values were normalized by equalising the area under the curves for better comparisons.

Typical results are presented in **Figure 4.7**. In general, it can be observed that the stress almost follows the same trend in both CT and 3D-US AAA models in patients (1,2,3 and 4) with correlation coefficients of similarity of (0.96, 0.95, 0.93 and 0.95) respectively. The plots of stress distribution also showed the stress axis started with a negative value of stress (compression). Then, the stress values keep growing with an initial peak of a range of (0.14-0.17 MPa) in Patient 1, and (0.05 – 0.1 MPa) in Patients 2, 3 and 4, followed by a secondary peak of range (0.25-0.26 MPa) in Patient 1, and of range of (0.15- 0.18 MPa) in Patients 2, 3 and 4 in the stress trend for both modalities. Finally, the stress distribution ended with the maximum wall stress on the axis of stress values, which means one or two elements have the maximum wall stress value. Therefore, the characteristic stress value should be taken into consideration instead of maximum wall stress to avoid misinterpretation of stress concentration. The relation between the two peaks and the location of elements was investigated on Patient 4. It was found that the initial peaks of stress distribution in CT and 3D-US model, **Figure 4.8**, occurred nearly in the same location of elements concentrated in the neck and branches area. However, the top peaks of stress were found to be in the site above the maximum radius of the aneurysm.

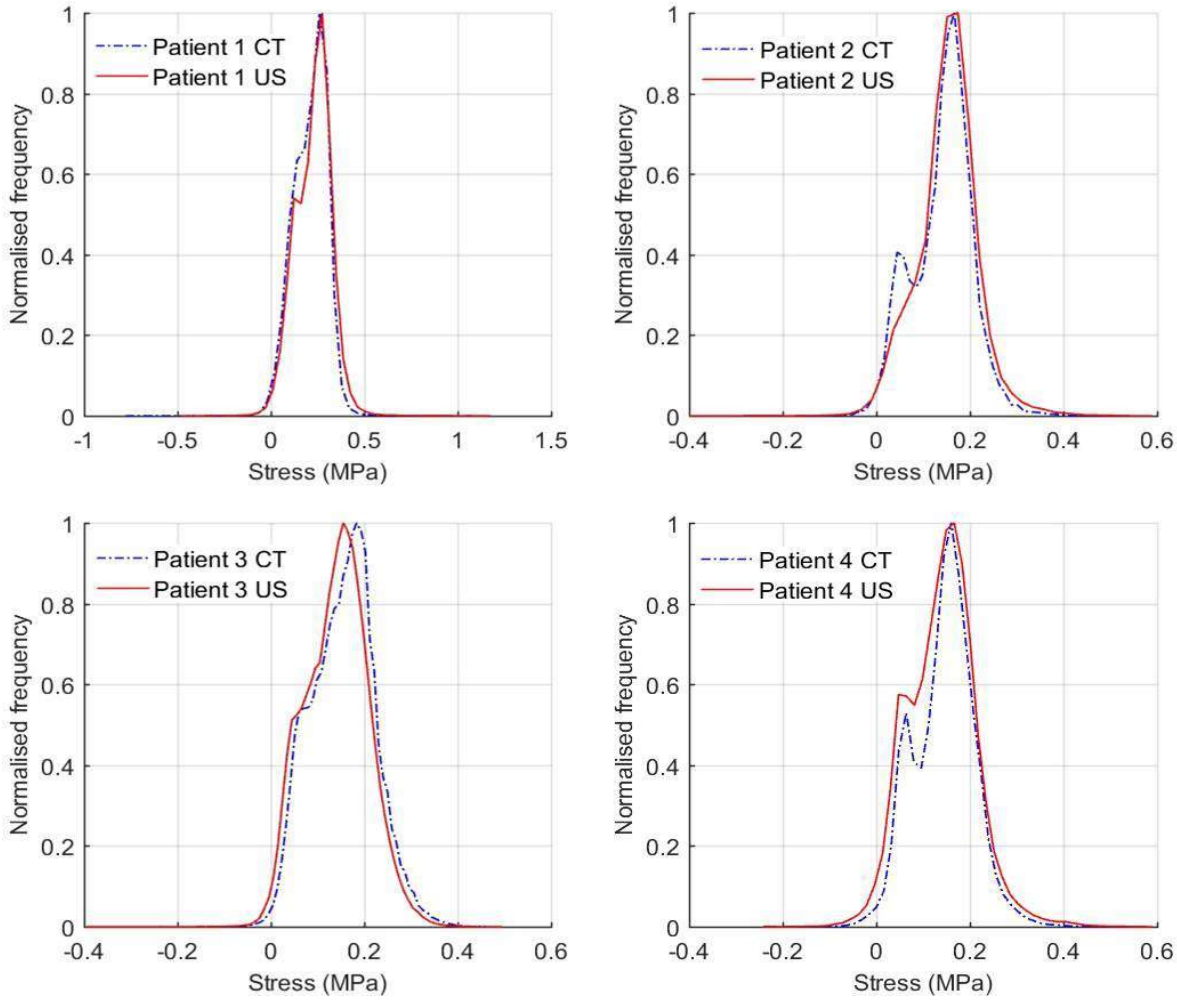

Figure 4.7: Trends of wall stress distribution in AAAs (CT vs. 3D-US).

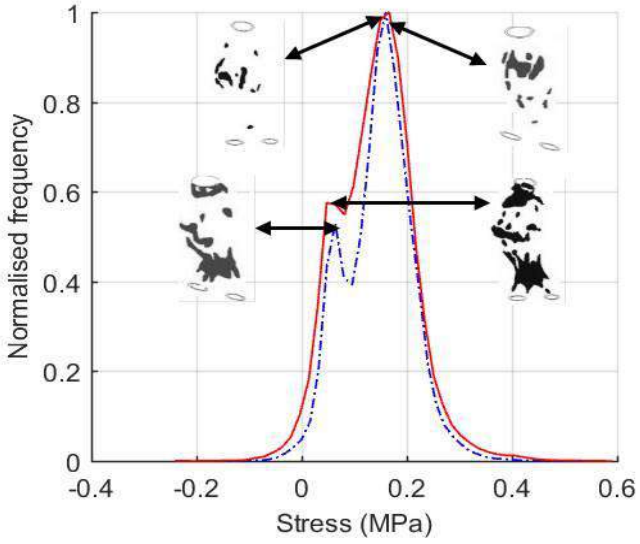

Figure 4.8: The correlation between the stress peaks and elements locations in Patient 4.

4.3.5 Characteristic stress of AAA wall

It ought to be emphasized here that a high-stress value in a single element arising as an artefact of image segmentation cannot be representative of the whole aneurysm site. The peak stress can also be an outcome of irregular meshing. Therefore, instead of maximum/peak stress, we used *characteristic* stress, which corresponds to a 5% probability of exceedance. The characteristic stress is commonly used in the literature and testing codes of engineering materials. In the present case, it means that 95% of the model geometry will have a stress level lower than the characteristic stress. The *confidence interval* of 95% also relates to about 2 times standard deviation from the mean, 1.96 to be exact. The characteristic value of stress was determined from the stress versus normalised element-volume frequency plots shown earlier in **Figure 4.7**. The mean stress, which is equivalent to a 50% probability of exceedance, is shown in **Table *4.4*** for all the patients. For comparison, stress values for 91% to 99% confidence interval, along with the mean stress values, are given in appendix A. It can be observed that that the stress value corresponding to 95% confidence interval compares well between CT and 3D_US models. The mean value, although a good indicator of the overall stress state, but is not representative of the failure stress. Therefore, in this work, we used 95% characteristic stress for comparison between different models and to assess the rupture potential of AAA.

It is suggested that characteristic stress will be a true indicator of the stress state in the aneurysm rather than the maximum wall stress; this is the approach taken in the engineering system where the load or the strength of materials are specified using probabilistic methods. The mean values of wall stress in CT models (0.22, 0.15, 0.15 and 0.14 MPa) were similar or with no significant differences compared to 3D-US models (0.24, 0.15, 0.14 and 0.14 MPa) in Patient 1, Patient 2, Patient 3 and Patient 4 respectively. Similarly, the characteristic stress (95% probability threshold) was consistent and identical of 0.25 MPa in Patient 2 and Patient 4, respectively. However, insignificant differences around or less 0.05 MPa in 95% characteristic stress occurred in Patient 1 and Patient 3 see **Table *4.4***. These results were shown to be highly consistent in terms of the mean and characteristic values of the wall.

Table 4.4: A comparison shows mean and characteristic wall stress probability in each pair of (CT and 3D-US) AAAs.

Stress (MPa)	Patient1		Patient2		Patient3		Patient4	
	CT	US	CT	US	CT	US	CT	US
Maximum	0.6	1.2	0.39	0.54	0.41	0.5	0.46	0.58
Mean (50%)	0.22	0.24	0.15	0.15	0.15	0.14	0.14	0.14
Standard deviation	0.09	0.1	0.06	0.06	0.07	0.6	0.06	0.06
Characteristic (95%)	0.38	0.4	0.25	0.25	0.26	0.25	0.25	0.25

4.4 Discussion

The present work provides a comprehensive comparison of stress/strain distribution and the characteristic wall stress of AAA finite element models derived from CT and 3D-US images. The 3D CAD AAA model construction, AAA wall creation, and stress analysis were performed using three different packages – ImFusion suite [46], 3-Matic v.10 [43], and Abaqus v.16.4 [148]. The key findings of characteristic wall stress were encouraging and consistent for both derived models (CT and 3D-US). Further work was also conducted to examine the suitability of 3D-US AAA models using the CFD approach presented in Appendix B.

The 3D contours of AAA stress/strain of the US model show the locations of high wall stresses (red area), which are similar to the CT models. The minor differences in stress /strain distribution can be attributed to the differences in geometric parameters such as inlet angle, inlet, and outlet diameter, the angle of bifurcations, and the maximum diameter [42, 61].

Although there are minor differences in wall stress distribution and location, the source of imaging was observed to have a significant effect on the predicted value of wall stress/strain. The black arrows in **Figure *4.5*** and **Figure *4.6*** represent the location of high wall stress areas in the interior wall of AAA geometry, which are similar or relatively close in both CT and US models. On the other hand, when the region of high wall stress occurs in the external surface of the AAA wall, represented by the white arrows, is in good agreement with the literature[182]. As well as signifies the high wall stress region occurring adjacent to the inflection point of the wall surface curvature[77]. Generally, the predicted wall stress/strain

locations obtained from the 3D US models were in correspondence with those obtained from CT models. It is also observed that the location of maximum wall stress was unrelated to the maximum diameter of the AAA; see **Figure *4.5*** and **Figure *4.6***, which is in agreement with many previous studies [73, 170, 183-185].

Finally, the plots of stress frequency shown in **Figure *4.7*** demonstrate good agreement between the models obtained from the two scanning methods. The frequency plots avoid the spurious results of high stress/strain values occurring in a small number of elements arising due to automated segmentation and smoothing processes. The mean and characteristic stresses, as defined earlier, from the 3D-US and CT finite models are in good agreement with the literature [42, 85, 186], despite observable geometries differences see **Error! Reference source not found.**. Therefore, consideration of the characteristic stress instead of the maximum stress in assessing the risk of rupture is more appropriate. The likelihood of rupture in AAA can be reduced using characteristic stress by conducting frequent FEA analysis using 3D-US in constant intervals (every month or two) to examine the evolution in characteristic stress value. If the inspection of the new characteristic stress value shows increasing compared to the previous value, that means the risk of rupture is high, and there is a need for surgical intervention. However, in case the characteristic stress is showing slight or no differences between the previous and the current value, that means the AAA is more likely stable.

One of the limitations of this study was ignoring the influence of ILT as contentious what the role is. Interestingly, Patient 2 did not contain any thrombus (ILT) formation, which means that the stress values and distribution are more likely to have this limitation in the results obtained. The neck and bifurcation parts were included in this model, which affects the location and value of maximum wall stress [42, 73]. Also, the systolic pressure was assumed to be constant and had a uniform distribution from the literature [183]. In terms of wall thickness, it was considered constant (2 mm); however, the AAA wall thickness is known to vary in different regions of AAAs and between patients [187]. Lastly, the influence of initial stress was neglected here due to the lack of information (patient-specific pressure) from the source of the images. In mitigation, there is no reliable imaging method to-date that is able to measure AAA wall thickness accurately. It is to be noted here that there is no ‘gold standard’ method to follow when modelling AAA wall stress [188].

4.5 Conclusion

In summary, a comparative FEA analysis of computational models obtained from CT and 3D-Ultrasound images was conducted to examine the effect of imaging methods on the peak values and distribution of AAA wall stress/strain. The results showed that wall stress/strain distributions are largely independent of the imaging methods, whereas the peak values are different for the two imaging methods, as small changes in the geometrical features highly influence the peak stress/strain values. Therefore, two new parameters: weighted mean wall stress and characteristic wall stress are proposed in this study, which has been observed to be independent of small unavoidable geometric differences. Finally, the prediction of the rupture of abdominal aortic aneurysm (AAA) can be reliably obtained by evaluating the characteristic wall stress rather than the peak wall stress.

5 Chapter Five: Developing a numerical model using XFEM approach to predict the rupture initiation and propagation in AAA

5.1 Introduction

Aortic wall condition is affected by many factors such as smoking, hypertension, age, and gender, etc.[67, 189, 190], which may cause irreversible localised inflation (an aneurysm) leading to ruptures [157]. One of these life-threatening aneurysms, especially in the event of rupture [191], is called Abdominal aortic aneurysm (AAA). Abdominal aortic aneurysms can be surgically treated, but it is an expensive procedure associated with a high rate of mortality [192, 193]. Therefore, periodic surveillance of AAA to predict the risk of rupture and its location prior to surgical intervention is vital for saving lives. The current guideline for considering a surgical intervention is when the maximum diameter of AAA reaches 5.5 cm [23, 192]. However, it has been reported that some cases of aneurysms [11, 194] ruptured before reaching the threshold value of 5.5 cm. The rupture process of an aneurysm can be interpreted from a mechanical point of view when the maximum wall stress of AAA induced from the blood flow exceeds the ultimate strength of the AAA wall [150]. To obtain the information on the state of stress and strain realistic 3D AAA geometries and mechanical properties of materials such as aortic wall strength and ultimate strain are necessary requirements.

Recently, good-quality patient-specific models of AAAs are being created from medical images CT, MRI, or 3D ultrasound, which can be provided by the hospitals. The mechanical properties of AAA can be obtained from direct physical tests such as uniaxial or biaxial tensile tests, and also from the published literature on previous test data. This information is being increasingly utilised in the process of rupture risk assessment using numerical approaches such as finite element method (FEM) [25, 42, 89, 195], computational fluid dynamic (CFD) [196-199] and fluid-structure interaction (FSI) [2, 200-202]. The finite element method is able to successfully predict the rupture site in a number of studies [27, 84]. For instance, a computational model was developed by Vorp et al. [38] to compute the rupture potential index (RPI) as a rupture indicator to determine the possibility of rupture in AAAs. The mathematical formula of RPI combines the predicted maximum wall stress obtained from FEA results with a standalone statistical model used to compute the aneurysmal wall strength [90, 94]. The findings of RPI have identified the risk of rupture better than the ordinary way of maximum diameter criterion [38, 90].

Doyle et al.[40] developed a similar computational model to analyse the risk of rupture called Finite Element Analysis Rupture Index (FEARI). This indicator can be defined as the ratio between the predicted maximum wall stress of a finite element analysis to the local AAA wall strength[35, 37] that corresponds to the predicted location of the maximum stress of AAA wall, where FEARI values range between 0 (low risk of rupture) and 1 (high potential of rupture) [166].

Based on the above, it has been noticed that the following three elements: maximum strength, maximum stress, and maximum strain of the AAA wall should be taken into consideration in the rupture evaluation analysis. In other words, when these three failure factors (stress, strength, and strain) meet at the same place in the diseased wall, this will lead to initiate the rupture in the wall. Interestingly, the Extended Finite Element Method (XFEM), a computational method based on the principles of fracture mechanics being used to evaluate the failure of materials (cracks or rupture[203]), can be employed to achieve numerical modelling of rupture in AAA by engaging the three elements of failure mentioned earlier.

The purpose of this study is to develop a numerical model using XFEM approach to understand the initiation/propagation of potential rupture and predict its location in abdominal aortic aneurysm wall by involving the parameters of failure: the wall stress, wall strength, and strain, as well as, investigating the use of 3D-US AAA models instead of CT models.

5.2 Methodology

5.2.1 Image acquisition and construction of AAA geometry

Four patients previously diagnosed with AAA had undergone for CT and 3D US scanning test prior to AAA repairing or urgent evaluation at the University Hospital South Manchester were included in this research. National Research Ethics Committee (NREC) (13/NW/0468) has granted the ethical approval of using the scanning data. A similar procedure of segmentation using the ImFusion suite [46], see Chapter Four, was followed in this work to create the 3D computational models of AAA derived from 3D-US and CT scans. Subsequently, all the AAA geometries had been exported into Abaqus 2016 [44] for stress and rupture initiation analysis.

5.2.2 eXtended Finite Element Method in Abaqus

Extended Finite Element Method (XFEM) is a numerical solution technique based on the fracture mechanics that combines the ordinary finite element approach and the principle

of partition unity to model crack initiation and propagation independently of the mesh size[203]. This approach can handle high discontinuities of displacement in a solution domain by assigning a specific displacement function to enrich and readjust degrees of freedom for a finite element. Equation **(5.1)** represents the conventional finite element with the partition of unity method; in other words, the extended finite element method[203]:

$$u = \sum_{i=1}^{N} N_i(x)\left[u_i + H(x)a_i + \sum_{\alpha=1}^{4} F_\alpha(x) b_i^\alpha\right] \quad \textbf{(5. 1)}$$

Where u: Displacement vector; N_i: standard FE function of the node (i), u_i: Nodal displacement vectors; $H(x)$: jump function; a_i : Nodal enriched degree of freedom vector; F_α: Asymptotic crack-tip functions; b_i^α : Nodal enriched degree of freedom vector.

The following two steps must meet altogether at one time and one place in order to achieve the initiation and propagating of rupture (crack) within the AAA wall. Firstly, the ratio of the predicted wall stress to the assigned wall strength (0.33, 1.34 and 2.35 MPa) should reach the critical value of a failure factor (f =1) [203] which can be represented by the maximum principal damage criterion as in the following equation:

$$f = \left|\frac{AAAstress_{predicted}}{AAAstrength}\right| \quad \textbf{(5. 2)}$$

Secondly, a damage evolution parameter, maximum strain, corresponds to displacement at failure should be defined and reached. Then, the aneurysmal wall starts to rupture. In the event any one of these two steps or both does not fulfil the damage criteria, the rupture does not occur. Contours of maximum principal stress and virtual 3D rupture are to be requested, see **Figure *5.1***.

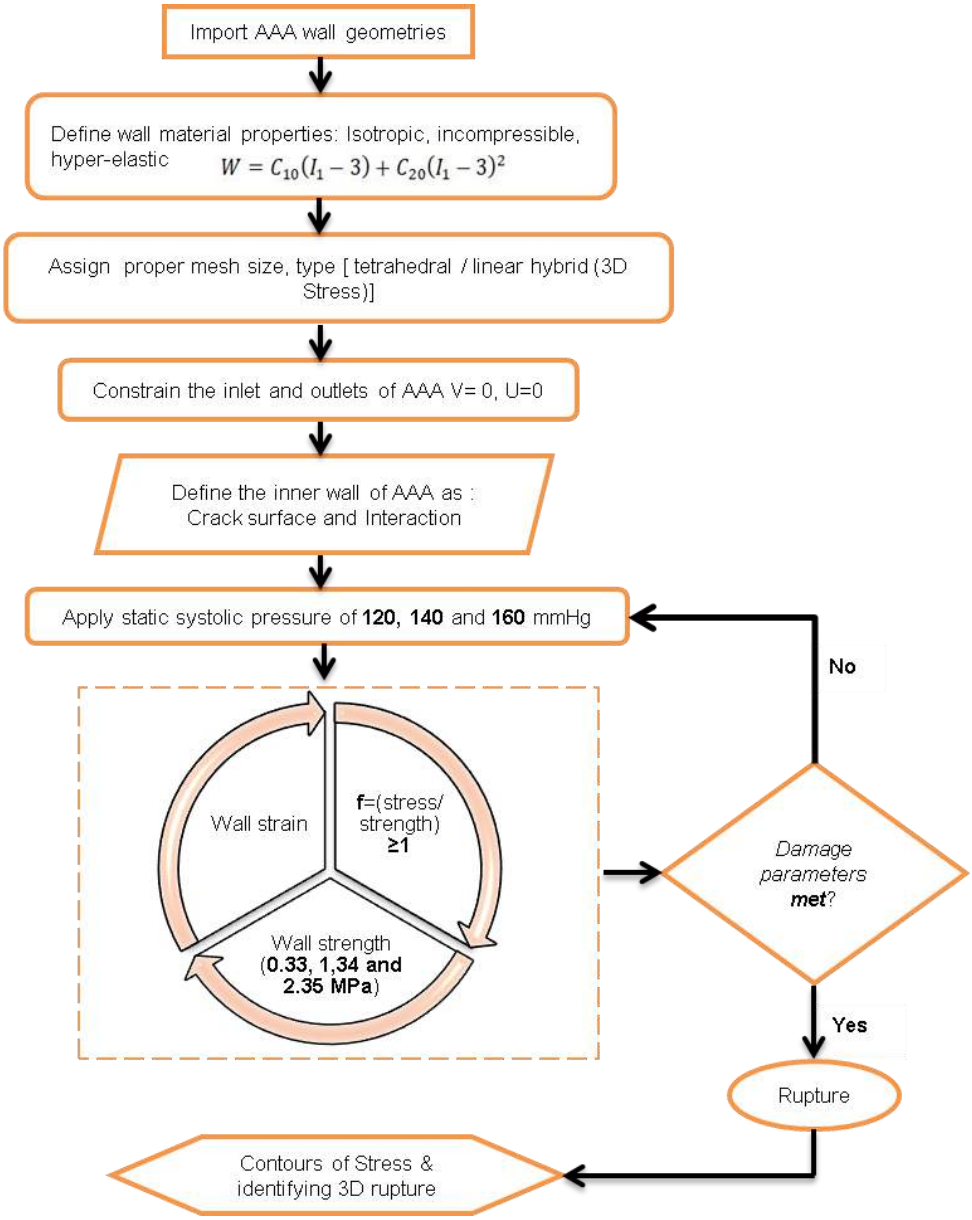

Figure 5.1: The process of damage criteria and damage initiation in extended finite element simulation used in this work.

5.2.3 Mechanical properties of the blood vessel

Non-linear mechanical properties of blood vessels (AAAs) previously extracted from the uniaxial tensile test [83] that have been widely used in several studies [2, 73, 84, 108, 204] were employed. The material library within Abaqus 2016 [44] provides a variety of mathematical models to express the nonlinear behaviour of aneurysmal tissues. In this case, a 2nd order polynomial strain energy mathematical model was utilized:

$$W = C_{10}\left(I_1 - 3\right) + C_{20}\left(I_1 - 3\right)^2 \qquad \textbf{(5. 3)}$$

Where W = strain energy, I_1= the first invariant of the left Cauchy-Green tensor *and* C_{20}= 1.881 MPa / C_{10}= 0.174 MPa are constants that represent the mechanical wall properties of AAA. The vessel was imposed to behave as isotropic, incompressible, hyperelastic-structure [83, 205]. Further material properties are required by XFEM solution to reach the rupture (crack) initiation and propagation in AAA, such as ultimate strength and strain. Regarding ultimate strength, Raghavan et al.[35]showed that the ultimate regional strength of the AAA wall ranged from 0.336 to 2.35 MPa. Damage criteria of maximum principal stress within Abaqus 2016 [44] was employed to involve the following failure strength of (0.336,1.343 and 2.35 MPa) of the aortic wall in the simulation. In addition, the damage evolution factor is presumed to be the maximum strain of 0.15[35].

5.2.4 Mesh study and improving the convergence analysis

XFEM approach in Abaqus 2016 [44] is supposed to be independent of the element's size. However, it has been observed that mesh refinement affects the length of the rupture slightly. In this analysis, geometries of AAA walls were meshed in Abaqus 2016 [44] using a hybrid 4-nodes tetrahedron (C3D4H) volumetric element. A systematic mesh independence was performed on AAA1 3D-US, and CT models with low strength, which exposed to a static pressure of 160 mmHg as other pressures of 120 and 140 mmHg will be within the range. The purpose of mesh verification is to investigate the mesh refinement sensitivity against the length of rupture, see **Table *5.1***.

Table 5.1: *Mesh independency performed on AAA1*.

	CT model		3D-US model	
Mesh No.	***No. of elements***	***Rupture length (mm)***	***No. of elements***	***Rupture length (mm)***
1	163091	9.7	148040	12.5
2	231007	9.8	207375	12.8
3	364585	9.9	342055	13
4	415025	9.9	399279	13.3
5	684552	10	515631	13.3

No significant change has been observed in terms of the rupture length between mesh 4 and 5 in both CT/3D-US models. Therefore, settings of mesh 4 were applied to all geometries. Furthermore, the following settings parameters had to be modified to aid convergence the rupture (crack) initiation analysis successfully:

a) *Analysis control:* in most of FEA simulations (continuous domain), default time incrimination parameters $\mathbf{I_0}$ = 4 and $\mathbf{I_R}$ = 8 are utilised to conduct a good performance[206]. However, in rupture (crack) initiation (discontinuous displacement), using default time settings may lead to cutbacks and abortion of the analysis. Thus, the values of I_0 and I_R in this work were changed to 8 and 10, respectively, to increase the number of attempts of each increment and avoiding the cutbacks[207].

b) *Damage initiation tolerance:* The initiation of damage sometimes may cause convergence issues[208]. In particular, when the value of the calculated stress at a specific element is higher than the specified magnitude, then the increment size will be reduced by Abaqus 2016 [44]. Subsequently, the specified value of initiation stress cannot be reached in an iterative process, damage tolerance of 0.05 (default) should be defined to initiate the damage in this case. However, to avoid the convergence issues in this study, damage tolerance of 0.001 was prescribed.

c) *Modifying the number of increments*: the number of increments I_A was modified to be 50 for the same reason mentioned above.

5.2.5 Boundary Conditions

All aneurysms were constrained upstream and downstream at all directions[209] to simulate the fixed position of the aorta. The presence of intraluminal thrombus and flow forces (shear stresses) were excluded from this simulation because the thrombus can effectively decrease the wall stress[118, 209], and the shear stresses were considered negligible due to no blood flow [14, 78]. In addition, the surrounding organs were imposed, not causing a load at the outer wall of blood vessels, which means the residual stresses in the AAAs wall assumed to be zero[118]. The local variances of the blood vessel thickness cannot be captured by the CT scan; hence, it was presumed to be 2 mm [108, 210-212] and uniformly distributed at all regions of the AAA wall. Hypertension contributes to the formation of AAA and a key factor causing the rupture[213]. Therefore, the AAA geometries were pressurised uniformly to the maximum systolic pressure of 120, 140, and 160 mmHg[42] assuming the patients had hypertension.

5.3 Validation of XFEM simulation

It is worth to mention here that the use of extended finite element method XFEM in predicting the rupture site in abdominal aortic aneurysms AAAs is a new idea; therefore, there is no numerical data available in the literature to examine the reliability of the current results. On the other hand, due to the complexity of the patient-specific AAAs geometry; seeking for experimental work to rupture an idealised AAA was ideal for examining the validity of the XFEM model. Interestingly, Doyle et al.[178] performed an experimental work to observe the relation between the rupture site and the location of the maximum stress obtained from the FEA simulation for the same AAA silicone model. Therefore, Doyle et al.[178] work was chosen to validate and compare the XFEM results in terms of predicting the rupture site and stress distribution.

5.3.1 Creating of idealised AAA geometry and Silicon Sylgard 184 material properties

The geometry of the idealised AAA replica was widely used in previous studies [165, 174, 176, 177] and created previously in the validation section in Chapter Four, see **Figure *4.2***. The experimental rig was replicated numerically using the same boundary conditions and material properties. The mechanical properties of Sylgard 184 silicone were extracted mechanically from tensile test data. It was found that the 3rd Ogden strain energy function within Abaqus 2016 [44] material library captures and fits quite well the hyper-elastic behaviour of this material. **Table *5.2*** shows the material coefficients used to characterise the 3rd Ogden strain energy function, see equation **(4. 4)**, of the Sylgard 184.

Table 5.2: Material coefficients of 3rd Ogden strain energy for Sylgard 184.

	μ	α
1	-304.235	1.2667
2	148.232	1.5962
3	157.156	0.9075

5.3.2 Boundary conditions and Mesh generation

Two values of static pressure were used in the current numerical simulation. The first pressure was 120 mmHg, represents the average systolic pressure in the cardiac cycle, subject to the internal wall of the idealised AAA with a uniform thickness of 2 mm. The purpose of applying this load was to compare the stress profile between Doyle et al.[178] and the XFEM model along a path starts from the beginning of the AAA sac to a point above the bifurcation.

The second load 364.5 mmHg was applied until the AAA reaches the threshold of rupture initiation in order to compare the location of rupture initiation and stress distribution in the idealised AAA between the experimental, FEA, and XFEM results. The numerical model was constraint from moving and rotating at proximal and iliac part representing the experimental rig. Idealised AAA was meshed in Abaqus 2016 [44] using linear and hybrid-tetrahedral of type 3D stress-element (C3D4H). Later, mesh independence study was implemented as reported in section *Mesh study and improving the convergence analysis;* by increasing the number of cells and investigate whether it influences the length of rupture. The number of elements that found to be satisfactory the accuracy of numerical results were 362705 elements.

5.3.3 Predicted stress distribution and rupture locations

Figure *5.2* shows a comparison of the predicted stress distributions and rupture initiation location between the XFEM approach and the Experimental/ FEA simulation of Doyle et al.[178]. The red spot at the very left hand of **Figure *5.2*** refers to the initiation of rupture observed experimentally (proximal inflection) which is in correspondence with the predicted rupture site (proximal inflection) by the XFEM model (very right hand of **Figure *5.2***) at the same load of 364.5 mmHg. In regards to stress distribution, the overall tendency was consistent between the FEA and XFEM results with an insignificant difference due to using two different numerical approaches. These comparisons showed that the XFEM results in good agreement with experimental results[178] and previous numerical studies[113], as well as showed the ability of the XFEM model in predicting the rupture site numerically.

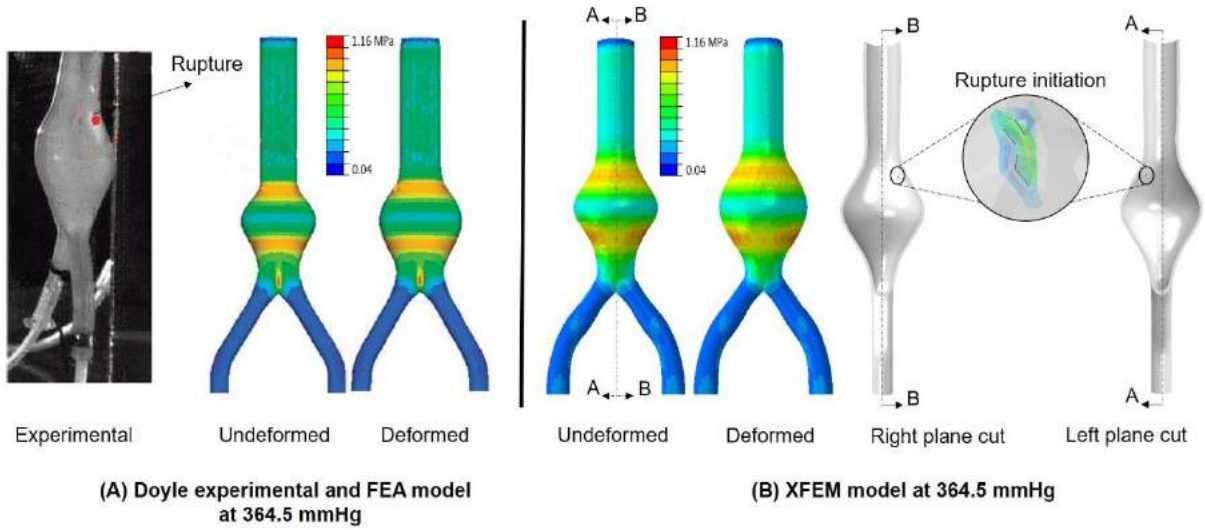

Figure 5.2: Comparison of the present rupture locations and stress distribution with the experimental work of Doyle et al.[178].

5.3.4 Stress trends comparison (FEA vs. XFEM) results

The FEA results of Doyle et al.[178] investigated the effect of wall thickness on the stress trends at 120 mmHg. For the purpose of validation of this work, stress profile from the FEA solution of Doyle et al. [178] for idealised AAA with 2 mm thickness was nominated for comparison with stress profile of the same geometry of 2 mm thickness obtained in XFEM solution. **Figure *5.3*** shows a comparison of the AAA wall stress trends between FEA [178] and the XFEM work. It can be seen that the wall stress profiles were fairly comparable, in which the inflection areas (proximal and distal) observed to have high stresses (first peak/ second peak). However, the maximum diameter region was noticed to have lower stress (between the peaks).

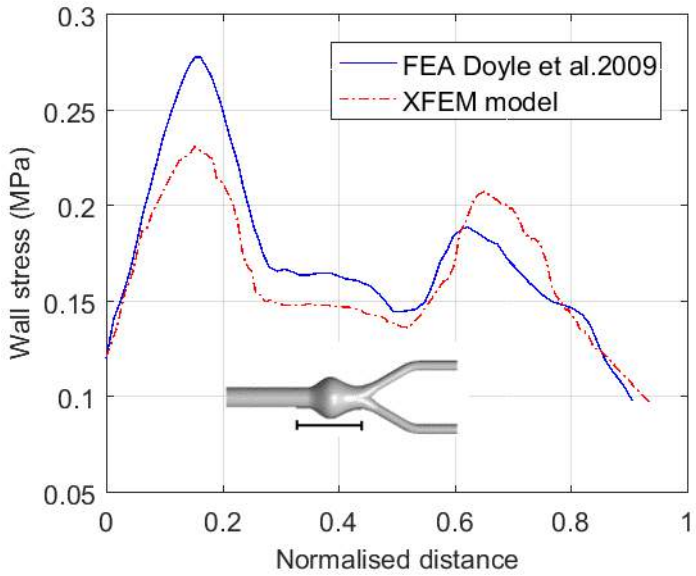

Figure 5.3: Comparison of wall stress profiles between FEA Doyle et al. and XFEM model.

5.4 Results

Rupture risk indicators, RPI and FEARI, mentioned in the introductory part, used the finite element method to predict the site of rupture, which did not involve the strength and strain in the rupture analysis. In this study, three failure parameters (stress, strength, and strain) were taken into consideration by developing a numerical model of AAA in the extended finite element approach. Comparison of wall stress distribution and rupture initiation/propagation between 3D-US and CT models were obtained to examine the eligibility of using 3D-US AAA models in the rupture analysis.

5.4.1 AAA wall stress

Comparisons of wall stress distribution in all patients are presented in colour-coded contours in which areas of maximum and minimum stresses are symbolised by red and blue colours respectively. **Figure *5.4*, Figure *5.5*, Figure *5.6*,** and **Figure *5.7*** show different orientations of AAAs: front, left side, right side, and back in order to facilitate the comparison process. Values of AAA wall stress ranged from the lowest 0 MPa dark blue to the highest 0.4 MPa dark red in AAA1, AAA2, AAA3, and AAA4 sequentially. In general, it can be observed noticeable differences in the stress distribution between CT and 3D-US models of AAA, to be more specific in the high-stress areas. Low-stress regions of zero MPa in CT and 3D-US AAA models can be simply observed in the bifurcation areas showing no significant influence by increasing the pressure. However, regions of high stress 0.4 MPa in all patients are observed to grow with the increase of the applied pressure significantly. It is also noticed that the location of maximum wall stress remains unaffected by the increase of the load magnitude. AAA4/3D-US in **Figure *5.7*** attracts the attention because it shows high sensitivity to pressure magnitude by producing high wall stress of 0.4 MPa, where the red colour almost covers all the aneurysm. In contrast, it is apparent that the stress distribution in CT models increases in a consistent way. The red patches are seen in many places in all patients CT and 3D-US AAA models, but which one of these spots is more likely to rupture? The functionality of using XFEM approach comes to reduce the potential sites of rupture by picking the weakest red spots in the AAA wall where the failure parameters meet together and representing the failure as a 3D crack in the aneurysmal wall.

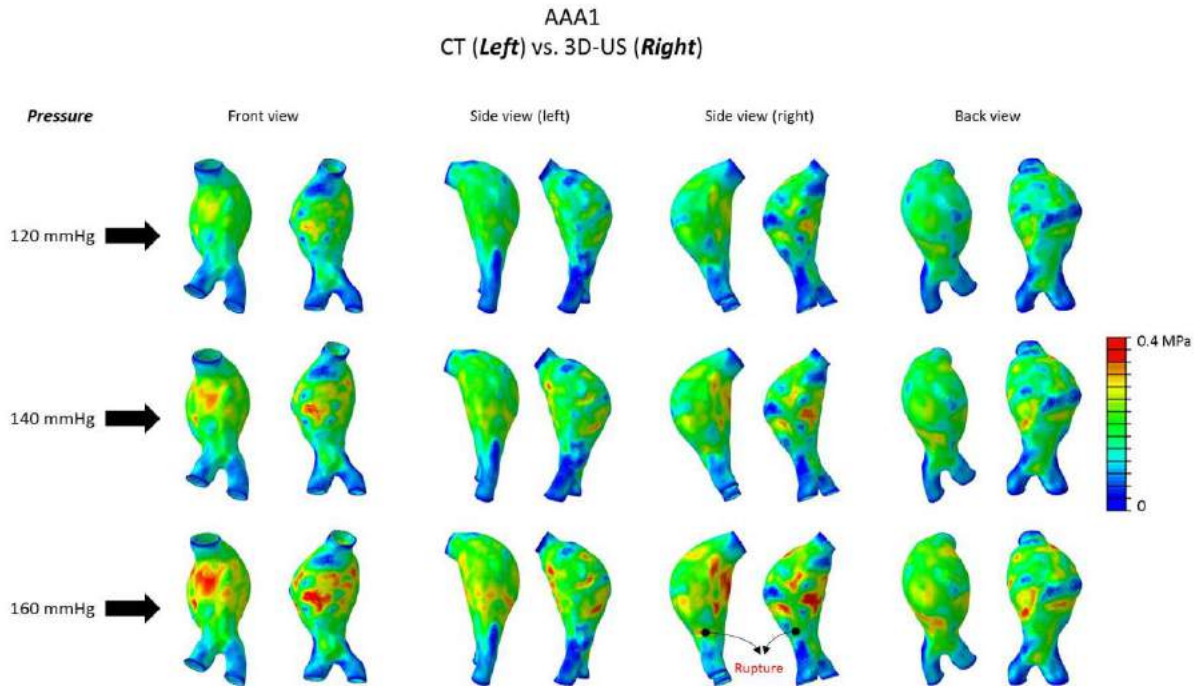

Figure 5.4: Shows predicted wall stress distribution in AAA1 obtained by XFEM.

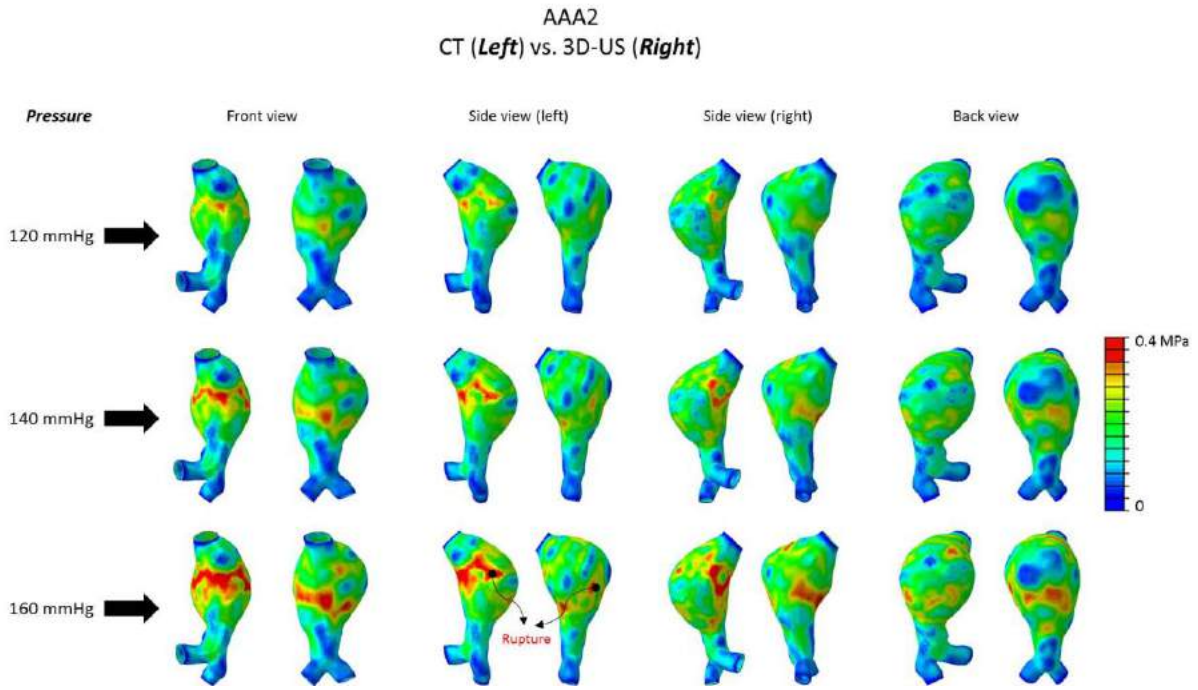

Figure 5.5: Shows predicted wall stress distribution in AAA2 obtained by XFEM.

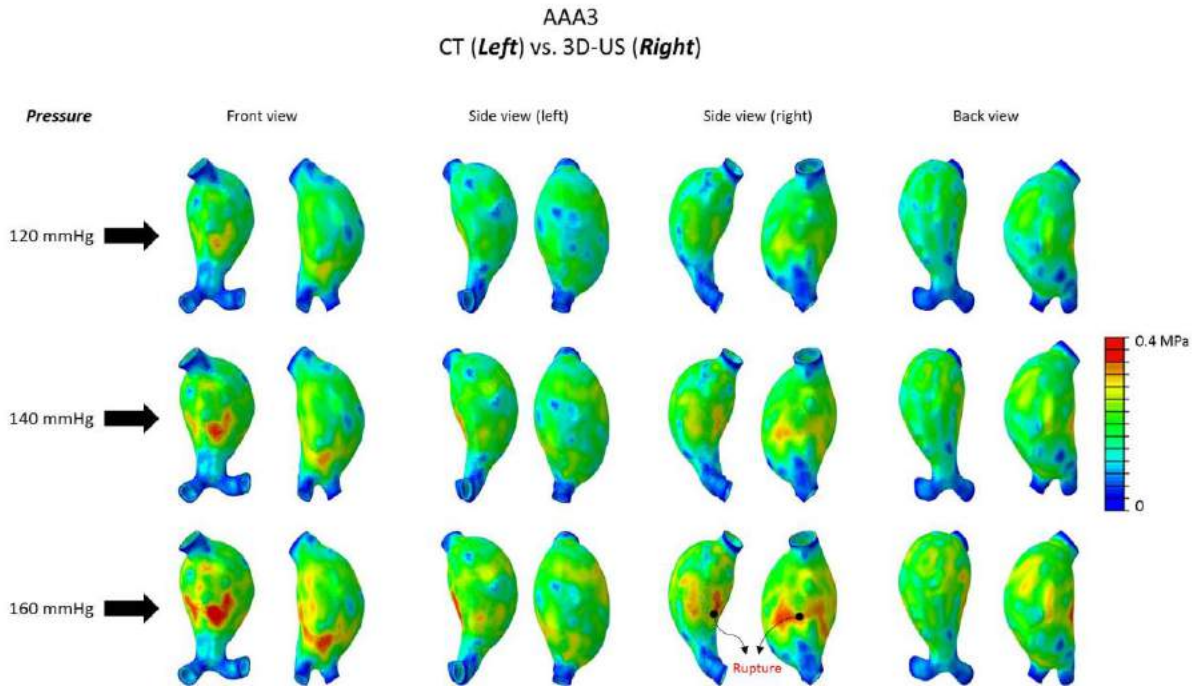

Figure 5.6: Shows predicted wall stress distribution in AAA3 obtained by XFEM.

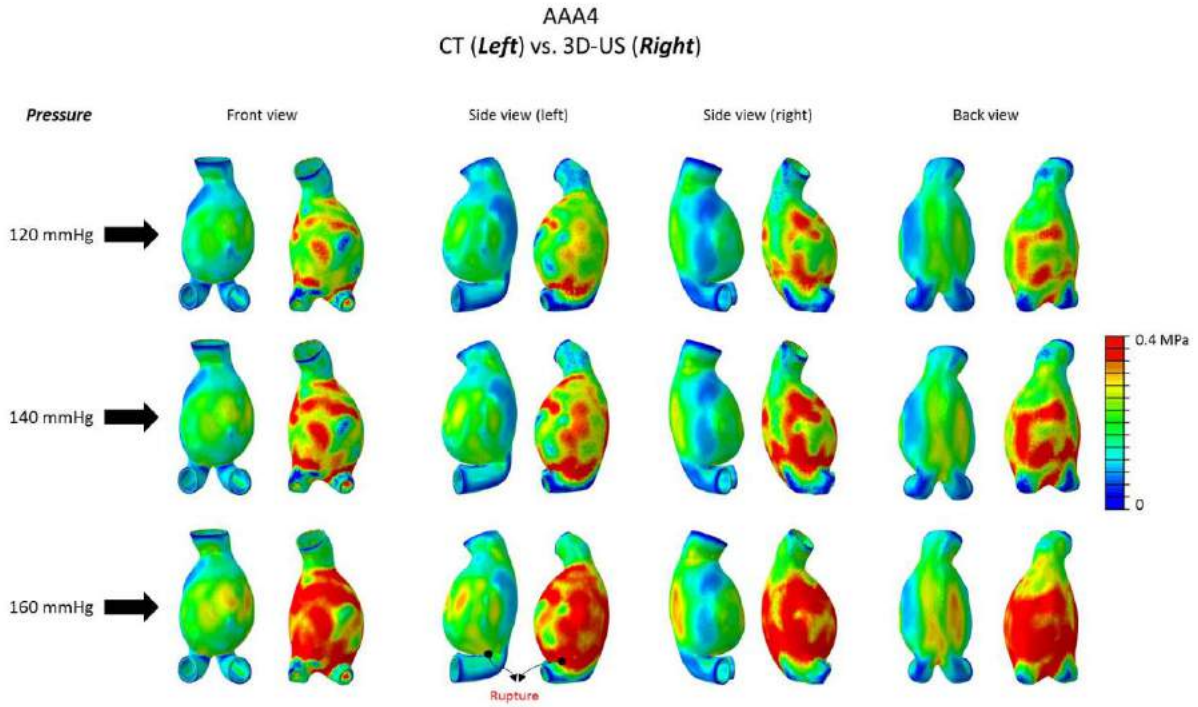

Figure 5.7: Shows predicted wall stress distribution in AAA4 obtained by XFEM.

5.4.2 Initiation and propagation of rupture:

The initiation and propagation of rupture were successfully examined for three different values of pressure and strength by employing the XFEM approach in CT and 3D-US AAA

models. A measurement analysis was conducted to measure rupture length in each model of AAAs, based on the increasing of luminal static pressure and wall strength. Most interestingly, the initiation of rupture is not observed for the average 1.35 MPa and the maximum 2.35 MPa wall strength, even for the 160 mmHg pressure. In contrast, the rupture is observed that begins initiating almost in all aneurysms (CT and 3D-US) when the AAA wall assigned to a low wall strength of 0.33 MPa, then propagates with intensifying of pressure. **Figure *5.8*** illustrates a comparison of rupture length between CT and 3D-US models of AAAs at different pressures and AAA low wall strength. Evidently, in **Figure *5.8,*** 3D-US AAA models show high tendencies to rupture than the CT models. For instance, the rupture in CT models of AAA1 and AAA3 did not initiate when it pressurised at 120 mmHg, unlike 3D-US models that start rupture. Furthermore, the rupture is observed to propagate with the increase of the pressure and, of course, the source of models, where the 3D-US models of AAAs showed high propagations in rupture than the CT models for the same pressure loads. Furthermore, in **Figure *5.8,*** the rupture length of AAA4 /3D-US at 160 mmHg is 26 mm, while the CT model is 13 mm.

Strengthening the AAA wall by assigning mean and high wall strengths of 1.34 and 2.35 MPa respectively reveal that the rupture did not occur in both CT and 3D-US models despite the increase of pressure magnitude. The length of rupture is not showing whether a full (rupture) penetration occurs in the AAA wall or not. Therefore, failure (rupture) in the AAA wall can be virtually demonstrated by presenting 3D contours of rupture to show the threatening of bleeding in the AAAs wall. **Figure *5.9*** shows the rupture in the CT and 3D-US AAA models for 160 mmHg and low wall strength in all patients. In terms of rupture locations, it is observed to be fairly identical in CT and 3D-US models. For instance, in **Figure *5.9,*** the rupture tends to happen in the right and left lateral very close to the bifurcation area in AAA1 and AAA4, respectively. However, AAA2 and AAA3, rupture occurs in the left and right lateral far of the bifurcation regions. In terms of full rupture in AAA wall, AAA1 and AAA3 show that the rupture occurs in the internal layer of the AAA wall, whereas the rupture in AAA2 happens in the external layer see **Figure *5.9***; which did not lead to full failure in the AAA wall. However, both CT and 3D-US models of AAA4 show full damage in the external and internal layer of the AAA wall, which means full penetration (blood leakage) happens in this patient, see **Figure *5.9***. In other words, this patient AAA4 has a high likelihood of rupture and death than other patients because of blood leakage.

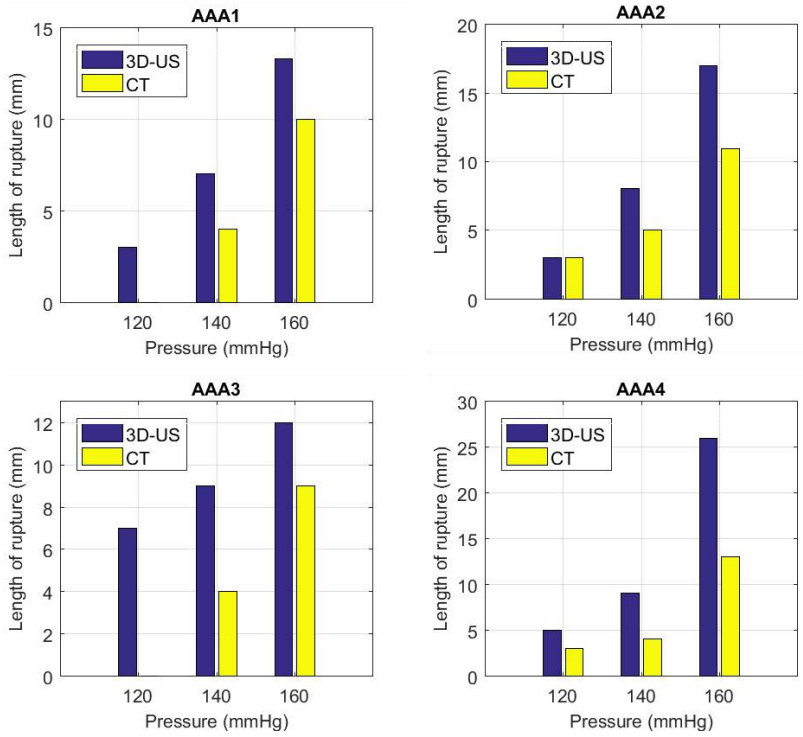

Figure 5.8: Comparison of rupture length in all AAAs (CT vs. 3D-US) at three different pressures (120, 140, and 160 mmHg) for the lowest wall strength of (0.33 MPa).

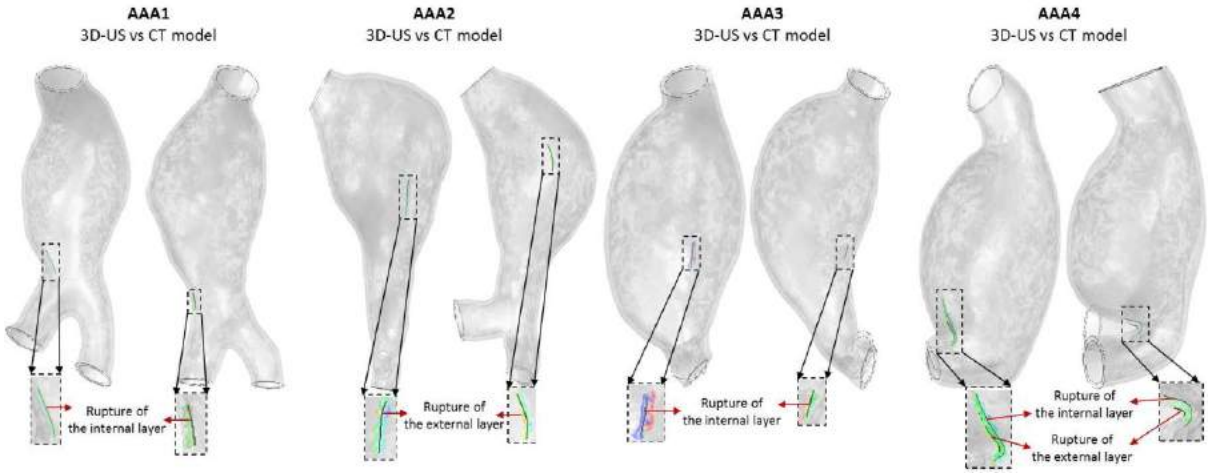

Figure 5.9: Predicted rupture initiation and location in AAAs wall at160 mmHg and 0.33 MPa wall strength.

5.5 Discussion

Prior researches about rupture risk assessment in abdominal aortic aneurysms have well documented the efficiency of employing finite element analysis in predicting the location of rupture [24, 25, 42, 61, 73, 84, 187, 214] by identifying the location of maximum stress in the AAA wall and reducing the life-threating of unpredictable rupture. Applying non-patient-

specific simplified boundary conditions such as linear (isotropic) wall material properties and uniform static pressure were good enough to successfully implementing wall stress analysis [78, 113, 215, 216]. However; this study needed to involve patient-specific AAA models from two different sources and non-linear material properties to obtain more precise results [35, 83].

The current results of wall stress distribution presented in **Figure *5.4***, **Figure *5.5***, **Figure *5.6*** and **Figure 5.7** showed that the increase of internal pressure on the AAA wall led to a significant increase in the area of maximum wall stress as well as the magnitude, whatever it would be the wall strength. Stress distribution varied throughout the patients owing to many factors such as geometrical differences like tortuosity, the inflection of the AAA surface, irregular shapes [61, 217], and asymmetric [61, 113, 217]. Moreover, using different sources of images (CT and 3D-US) and the segmentation process play an important role in the stress distribution as well. It was observed that the distribution of wall stress highly influenced by the pressure value (hypertension hypothesis)[218], numerical solution, and model source, where 3D-US models showed overestimation in the wall stress distribution as reported in FEA work by Kok et al. [42]. AAA4/3D-US in **Figure *5.7*** undoubtedly overestimated wall stress (red area) compared to the CT model of the same patient. However, it did not have multi- rupture despite the wall stress 0.4 MPa overcame the wall strength 0.33 MPa in many locations. This proves that the rupture site needed the three elements of rupture to meet together in one place in order to damage the aneurysmal wall.

It was observed that the strength of the AAA wall did not affect the stress distribution; however, it affected the rupture initiation and propagation in both CT and 3D-US models of AAAs, for instance: The weak AAA wall that had low wall strength of 0.33 MPa was shown high trendies to rupture than other values of strength 1.33 MPa and 2.35 MPa. More interestingly, locations of maximum wall stress did not change with increasing pressure in both CT and 3D-US models. In addition, no relationship was found between maximum wall stress location and the maximum diameter of the aneurysms [73, 214, 219].

XFEM approach used in this analysis provides detailed information regards the predicted stress distribution, rupture length, and shape, unlike the FEA method that provides only stress contours. It was observed that the AAA models regardless the source of imaging did not show any chances of rupture when the wall assigned average and high strength values, because these models of AAAs despite exposing to relatively high pressure 140 and 160 mmHg, it was not sufficient to generate high stress in the AAA wall that overcomes the average and high strength values of 1.35 and 2.35 MPa. Bar charts in **Figure *5.8*** showed a

comparison of rupture length that propagates with the increase of the internal pressure when the AAA wall has a low strength of 0.33 MPa. 3D-US models of AAAs firstly started rupture of a length ranged between 3 mm to 7 mm at low 120 mmHg, which then started propagating with the increase of the rupture to reach a range between 12 mm to 26 mm at 160 mmHg. On the other hand, CT models of AAAs showed fewer chances of rupture despite the exposure to the same boundary conditions. For instance, AAA1 and AAA3 did not rupture at 120 mmHg, whereas AAA2 and AAA4 tend to have rupture of length varied from 3 mm to 4 mm at the same pressure. Then, CT models of AAAs that ruptured and those who did not; started initiating and growing the rupture when the internal pressure increased. It is evident from the bar charts that 3D-US AAA models predicted the rupture earlier than the CT models, as well as, the rupture site was fairly identical in both.

Although the comparison of rupture propagation in **Figure *5.8*** was helpful in terms of providing the relation between pressure and length of rupture in both CT and 3D-US models, the rupture shape and blood leakage is still vague. 3D representation contours of rupture obtained from the XFEM approach in **Figure *5.9*** were vital to understanding whether the rupture led to full penetration in the AAA wall or not. The failure in the AAA wall was evident to happen in the internal wall, firstly where the stress intensity is maximum in the AAA wall, as observed in AAA1 and AAA3 in **Figure *5.9***. However, the rupture occurred at the external layer of the wall in AAA2. The 3D-US/CT AAA4 predicted failure in both layers of the wall, which means blood leakage, and would have required urgent surgical intervention. The rupture contours can be used to give a good indication of whether the patients need urgent surgery or not. As there is no thrombus formation in AAA3, the predictions of stress and rupture initiation are likely to be more accurate. In other words, the potential of rupture risk in AAA3 may be very close to reality. **Figure *5.9*** also shows that the AAA walls fail in the longitudinal directions rather than the circumferential, which is in good agreement with the literature [37]. The XFEM model can be developed for patients regularly to examine the failure/penetration in the AAA wall by comparing the crack length, stress, and penetration to decide which AAA has more potential rupture.

This work has some limitations, such as: ignoring the thrombus in this work was based on findings of Venkatasubramaniam et al.[84] that successfully predicted the rupture site without including the thrombus in his work. Furthermore, other studies [118, 160, 220] have found that the thrombus acts as a mechanical cushion and working on reducing the wall stress. Supposing the aneurysmal walls have one value of strength is the second limit of this study, which, in fact, the wall strength is varying locally in the whole wall[35].

5.6 Conclusion

XFEM, being based on the principles of fracture mechanics, is shown to be suitable for the assessment of rupture potential in the abdominal aortic aneurysm. The good agreement of rupture predictions between the XFEM method and the experimental work in the abdominal aortic aneurysm was found to be applicable for biological materials. The findings of this method provide detailed information about the rupture, such as stress distribution on the aneurysmal wall, length of rupture, site of rupture, and potential of blood leakage, unlike the conventional FEA method that just predicts the rupture site. In addition, the XFEM approach picks only the weak red patches among others that overcome the maximum wall strength, stress, and strain, which reduces the chances of potential rupture in other sites despite having maximum wall stress.

In terms of using 3D-US images instead of CT in rupture analysis, it is found that the 3D-US models of AAA show good similarity in predicting the rupture site and predicting the leakage of blood. However, US image-based models show a higher risk of rupture than CT based models. In other words, XFEM findings show that 3D-US is eligible for periodic rupture analysis during the monitoring process of AAA patients due to the availability, no radiation, and affordability of the 3D-US. Accordingly, the approach used here plays as a diagnostic tool for surgeons that may help them to determine if the AAAs require for surgical interventions

6 Chapter Six: The role of minor geometrical differences induced by the segmentation process on the hemodynamic metrics of the abdominal aortic aneurysm.

6.1 Introduction

Many hemodynamic and genetic factors play a significant role in AAA formation [221]. The most common hemodynamic factor is called Wall Shear Stress (WSS), which represents the frictional forces exerted on the AAA wall due to blood flow [222]. The direction of wall shear stress influences various cardiovascular conditions [28, 222, 223]. For instance, the healthy and intact blood vessel is related to unidirectional steady wall shear stress. However, the low magnitude of oscillatory wall shear stress due to flow circulation is linked with atherosclerosis [224]. Normally, the shape of an intact abdominal aorta (AA) can be idealized as a uniform cylinder, and the blood flow within the AA remains laminar. However, the patterns of blood flow change owing to the transformation of the abdominal aorta (AA) shape from nearly cylindrical to aneurismal one (AAA). Formation of abdominal aortic aneurism AAA alters the direction of the blood flow which then produces an oscillatory wall shear stress, which may subsequently cause rupture [225, 226]. Advanced 3D image processing software packages such as Mimics[43], Simpleware[227] and ImFusion suite [46] are widely used to extract 3D patient-specific models of bones, AAA and biological soft tissues from the medical images obtained by different scanning techniques such as CT, MRI, and 3D-US. Creating a 3D model for any part in the human body using one of these packages will invariably produce minor geometrical differences compared to the actual organ itself. For AAA, this may lead to significant variations in flow patterns and misleading implications in the rupture analysis. Therefore, the role of these geometrical differences in the hemodynamic metrics of AAA geometries segmented in the ImFusion suite [46] and Mimics v.18 [43] will be investigated. The main aim of this study is to run and develop a fluid-structure-interaction model of same AAAs segmented in Mimics v.18 [43] and ImFusion suite [46] in order to measure and compare the hemodynamic parameters (TAWSS, OSI, and RRT) to see any noticeable difference in the flow patterns.

6.2 Methodology

6.2.1 Construction of AAA geometries

6.2.1.1 Idealised Abdominal Aortic Aneurysm

A representative idealised abdominal aortic aneurysm called "Default" and two other geometries were created by increasing and decreasing the lateral dimensions of the "Default" AAA by ±10%. These idealised AAAs were created in Solidworks v.2016 [179] and recommended by experts in AAA anatomy [142, 143]. The CAD geometry of AAA is generally asymmetric in the lateral view and symmetric in the anterior view see **Figure *6.1***.

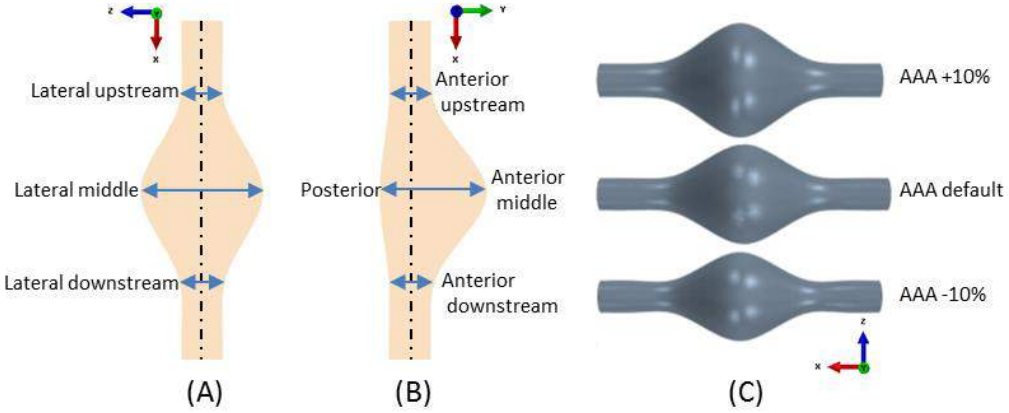

Figure 6.1: AAA default fluid domain geometry (A) anterior view and (B) lateral view; (C) fluid domains of AAA default and AAA ±10%.

For all AAA parts, the axial flow direction was represented by X position, which varies from 0 to 0.19 m, other positions of the AAAs Y and Z were extracted based on the exponential equation below:

$$Y \text{ or } Z \text{ position} = C_0 + \left(\frac{C_1}{\sqrt{\pi C_3}} \right)^{P_2} \left(e^{-\left(x^2 / c_2 \right)} \right)^{P_1} \quad \textbf{(6. 1)}$$

Where C_0, C_1, C_2, C_3, P_1, and P_2 are coefficients and exponents correlating with each curve in the AAA adopted from [29], their values can be seen in **Table *6.1*** which used to create the default AAA geometry.

Table 6.1: Coefficients used to define positions of curves of the default AAA model shape.[29, 142, 143]

Positions	C_0 (m)	C_1 (m)	C_2 (m^2)	C_3 (m^2)	P_1	P_2
Lateral upstream/downstream	0.0102	0.1	7E-6	8E-7	0.009	0.85
Lateral middle	0.1	0.1	1E-5	8E-7	0.007	0.75
Anterior upstream/downstream	0.0097	0.1	8E-6	8E-7	0.0095	0.95
Anterior middle	0.0105	0.1	9E-6	8E-7	0.006	0.81
Posterior	0.0104	0.1	8E-6	8E-7	0.008	0.39

The up- and down-stream diameters of the three AAA fluid parts are assumed to be constants and equal to (0.0216 m), further details of maximum inner diameter along the anterior-posterior and lateral direction of each AAA geometry were showed in **Table 6.2**. Due to insufficient contrast that needed to capture the density of the arterial wall in CT scan or any other available imaging techniques makes the segmentation process of creating the artery wall quite difficult. Therefore, it was assumed to be a uniform thickness of 0.002 m and generated by expanding the fluid parts outwards by 0.002 m.

The inlet and outlet surfaces were extruded by (10*D) [228, 229] for two reasons: (i) to let the velocity profile reaching the fully developed flow profile before entering the aneurysm region [230], and (ii) to get rid of any non-physical behaviour such as backflow near the outlet surface and to ensure that the flow within the AAA does not interfere with the reversed flow at the outlet boundary [229].

Table 6.2: Diameters of AAA default and AAA ±10% at different positions.

Diameters	**AAA +10% (m)**	**Default AAA (m)**	**AAA -10% (m)**
Upstream/ downstream diameters	0.0216	0.0216	0.0216
Maximum inner diameter/lateral	0.07128	0.0648	0.05832
Maximum inner diameter/anterior-posterior	0.06006	0.0546	0.04914

6.2.1.2 Construction of Patient-specific AAA models

In order to cover the objectives of this work, patient-specific models of AAA extracted from Computed tomography CT datasets in the DICOM (Digital Imaging and Communication in Medicine) format obtained from the university hospital of south Manchester Wythenshawe for a number patients who had AAA. The DICOM files contain information about the patient, such as the type of the image, patient name, age, and position of the image (anterior,

posterior, lateral left, and right). Four patients with age above 55 years were chosen because of the high quality of the obtained images. CT scanning was performed using a 128-slice Siemens SOMATOM Perspective scanner (Siemens Medical, Munich, Germany). Patients were positioned supine, and images at 1 mm slices were acquired from the aortic arch to the femoral heads. Arterial phase images were acquired using a bolus dose of 100 mL of the iodinated contrast medium Omnipaque 240 (GE Healthcare, UK) administered at a flow rate of 3 mL/s.

6.2.1.2.1 Construction AAA in Mimics

The CT images were imported into Mimics v.18 [43] research segmentation software to build a 3D model of AAA for all patients. The construction process has segmentation structures that comprise the global thresholding technique, dynamic region growing, and manual or semiautomatic editing for masks, see Chapter Three for further information. Global thresholding is the first step that produces 3D masks showing AAA lumen with yellow colour, and thrombus with blue colour see **Figure *6.2* (A)**. This method assigns pixel intensity values measured in (HU) Hounsfield units. The AAA threshold could be the same for organs close to it, such as the spine; therefore, it is necessary to choose an optimal threshold. Threshold values have been carefully set by customising Mimics[43] predefined threshold values, such as the bone threshold was used with manual adjustments to capture the AAA lumen and thrombus.

6.2.1.2.2 Construction AAA in ImFusion

CT images were exported into the ImFusion suite[46] prototype analysis software that has the ability to implement segmentation on the CT dataset. The operator used the interactive segmentation algorithm, where the seeds briefly are placed inside and outside the blood fluid part in a number of slices with green and red colour respectively, see **Figure *6.2* (B)**. Then, the ‘inner’ and ‘outer’ regions are propagated in the whole scan, describing the blood lumen from the adjacent aortic wall or ILT thrombus [231]. Regarding other parts of the AAA (e.g., thrombus, calcification, and wall) can similarly be segmented. The operator can correct the errors in the segmentation by using the algorithm re-run to increase the precision, see Chapter three for further details. A marching cube algorithm was used then by ImFusion suite [46] to transform the contours created by the segmentation into an (STL) stereolithography file.

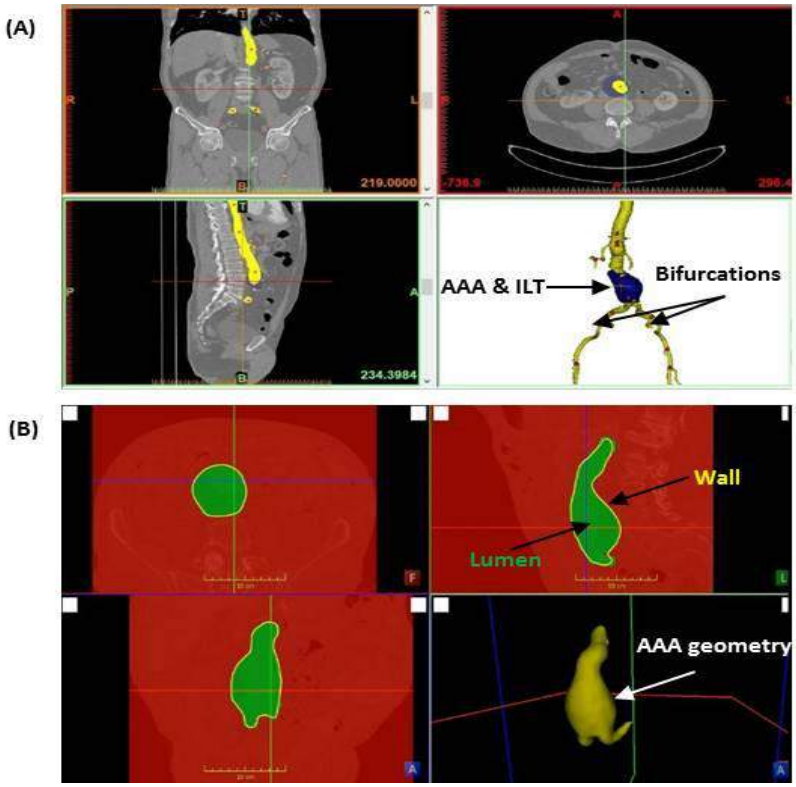

Figure 6.2: CT images in positions of (coronal, sagittal, and axial) of a patient with AAA: (A) Mimics v.18, (B) ImFusion suite.

6.3 Hemodynamic metrics of AAA

Numerical approaches such as Fluid-Structure Interaction (FSI) has been broadly utilised to show a better understanding about the significant correlation between the hemodynamic metrics/forces and the formation and rupture of the AAA, such as wall shear stress (WSS), time-averaged wall shear stress (TAWSS), oscillatory shear index (OSI) and finally relative residence time (RRT) [223, 232]. The reason behind defining these hemodynamic parameters in this study is to provide a good characterisation of blood flow based on the differences between the numerical and anatomical models of the AAA structure [233]. Moreover, a single hemodynamic indicator may have not able to capture the multi-directionality of the blood flow [234]. The following are the most commonly used metrics in vascular diseases analysis:

6.3.1 Wall Shear Stress and Time-Averaged Wall Shear Stress

The frictional and tangential forces resulting from the blood flow exerting directly on the AAA wall are called wall shear stress. It is a very common hemodynamic indicator that has been extensively used in the AAA rupture studies, where the site of low wall shear stress

WSS in the AAA wall corresponds to a high potential of AAA growth or thrombus formation [235]. The components of wall shear stress in the directions of x, y and z can be time-averaged over a number of cardiac cycles to obtain the time-averaged wall shear stress TAWSS parameter. TAWSS represents the cumulative effects of the wall shear stress over during the required cardiac cycles and defined as:

$$TAWSS = \frac{1}{T}\int_0^T |\vec{\tau}_w| dt \quad \textbf{(6. 2)}$$

Where T is the time length of the cardiac cycle, $\vec{\tau}_w$ is the instantaneous wall shear stress vector in three directions of flow. The TAWSS can be determined by using the field mean monitor provided in STAR CCM+ v.13.04 [45] to collect and average the wall shear stress magnitude at regular samples or time intervals of the interested cardiac cycle/cycles.

6.3.2 Oscillatory Shear Index (OSI)

Oscillatory Shear Index is a dimensionless hemodynamic parameter that is associated with oscillatory blood flow. It was proposed [236] to measure the directional variation of the wall shear stress vector during the pulsatile flow. It can be represented mathematically as:

$$OSI = \frac{1}{2}\times\left(1-\frac{\left|\frac{1}{T}\int_0^T \vec{\tau}_w dt\right|}{\frac{1}{T}\int_0^T |\vec{\tau}_w| dt}\right) \quad \textbf{(6. 3)}$$

Where T is the time length of the cardiac cycle, $|\vec{\tau}_w|$ is the instantaneous wall shear stress magnitude and $\vec{\tau}_w$ is representing the vectors of wall shear stress. The purpose of finding the OSI is to identify the regions in the fluid domain where the wall shear stress vector varies in its direction considerably from its axial direction during a single or a number of cardiac cycles. From the equation above, it can be observed that the OSI values change in the range between 0 and 0.5, where 0 means that the wall shear stress vector does not vary its direction during the flow (uni-directional flow) whereas 0.5 means the flow keeps oscillating [233].

In order to measure the OSI in STAR CCM+ v.13.04 [45], a field sum monitor is employed to sum the wall shear stress magnitude ***($SumWssMag)*** and its three vectors ***($SumWssX)***, ***($SumWssY)*** and ***($SumWssZ)*** in the directions (X, Y, Z) over the same cardiac cycle that the TAWSS monitor is set. Then, the following user-defined OSI field-function is utilised:

$$OSI = 0.5 \times \left(1 - \frac{mag\left(\left[\$SumWssX, \$SumWssY, \$SumWssZ\right]\right)}{\$SumWssMag} \right) \quad \textbf{(6. 4)}$$

6.3.3 Relative Residence Time

The purpose of using this parameter is to measure the amount of time of the blood particles reside adjacent to the arterial wall or within the AAA volume. The presence of more circulation and low wall shear stress in the AAA wall is confronting longer residence time. The RRT metric can be defined as:

$$RRT = \frac{1}{\left(1 - 2 \times OSI\right) \times TAWSS} \quad \textbf{(6. 5)}$$

6.4 FSI simulation

6.4.1 Modelling of blood

The following approximations were used to solve Navier-Stokes equations in the fluid domain ${}^{F}\Omega(t)$ of abdominal aortic aneurysm using segregated flow solver in STAR CCM+ v.13.04 [45]:

$$\nabla u = 0 \qquad in\ {}^{F}\Omega(t) \quad \textbf{(6. 6)}$$

$$\rho_f \frac{\partial u}{\partial t} + \rho_f \left(u.\nabla\right) u = -\nabla p + \mu \nabla^2 u \qquad in\ {}^{F}\Omega(t) \quad \textbf{(6. 7)}$$

Where u =velocity vector, ρ_f = fluid density, μ =dynamic viscosity p = pressure scalar and t = time. The blood in this simulation was treated as Newtonian, incompressible fluid with a density and dynamic viscosity equal to 1035 kg/m^3 and 0.0035 Pa.s, respectively owing to a large shear rate in the aorta [136]. As it is known, blood flow is unsteady (time-dependent); therefore, implicit, laminar (based on ***Re*** number at the inlet of the AAA) and unsteady segregate solver were chosen. The flux at each element faces is calculated using the 2nd upwind convection scheme that exists within the segregated flow solver in STAR CCM+ v.13.04 [45]. A sufficient number of inner iterations should be involved to assist the solution to converge at each time step [237]. A SIMPLE algorithm was also utilised to allow the segregated flow solver controlling and updating the solution as well as enforcing mass conservation at every single time step.

6.4.2 Dynamic time-step

The general nature of blood flow is unsteady, time-dependent, which means the velocity magnitude varies accordingly with the time of the cardiac cycle. Therefore, a dynamic time-step should be used and adjusted, relying on three main parameters: fluid velocity, Courant Number (CFL) and Cell-size using the following equation:

$$Time\ step = \frac{(Minimum\ Cell\ size \times Courant\ number\ CFL)}{Maximum\ Velocity} \quad \textbf{(6. 8)}$$

Normally, the simulation of blood flow encounters severe fluctuations in the residuals at the beginning; therefore, it requires a small time-step at first. Once the simulation reaches the stable condition, then the time-step can be increased automatically based on the three factors mentioned in equation **(6.8)**. The parameters in the equation **(6.8)** can be obtained using report function in STAR CCM+ v.13.04 [45]as follow:

1) The Courant number is preferable to be ≤ 1 in order to transfer the obtained information from the given element to the next neighbours, at all the time of the simulation to obtain a stable blood flow. However, in this work a segregated flow solver was used and in order to find out the relationship between the CFL number (coupled solver) and the under-relaxation factors URF (segregated flow); the following formula was used:

$$URF = \frac{CFL}{(1+CFL)} \quad \textbf{(6. 9)}$$

   The required CFL number in this work is≈ 1; then, the equivalent under-relaxation factors would be = 0.5 [238].
2) The velocity magnitude is changing incrementally with the increased time of the cardiac cycle; therefore, it is required to measure the maximum velocity at each time increment by defining the maximum value of the field function Velocity/ magnitude.
3) Finally, obtaining an approximate minimum cell size by creating and using a user-defined field function equation below to collect the information for each cell in the solution domain. Then, a minimum value should be set to measure the minimum cell size [239].

$$Cell_{size} = \sqrt[\frac{1}{3}]{volume_{Minimum}} \quad \textbf{(6. 10)}$$

It is important to mention a vital point before running the simulation; the solution must be initialised first to avoid the error of getting zero time-step. Then, FSI simulation is allowed to develop until obtaining the time-periodic flow by letting the flow runs for 3 cardiac cycles to get rid of the effect of the high residuals that may affect the flow features in the AAA. Therefore, the third cardiac cycle was chosen to extract the data of the fluid-structure interaction simulation.

6.4.3 Modelling of AAA wall and Thrombus

The mechanical properties of the abdominal aortic aneurysm structure can be characterised within Abaqus 2016 [44] to represent the hyper-elastic, incompressible, and isotropic behaviour [83, 240]. The constitutive model of strain energy that was used in this part is similar to strain energy function used in Chapter Four, see equation **(4.1)**. The intraluminal thrombus was modelled as an elastic material that deforms linearly with the following properties: Young modulus=0.11 MPa and Poisson's ratio=0.45 [108, 164].

6.5 Enhancing Implicit Co-simulation settings

Fluid-structure interaction (FSI) modelling couples implicitly both structure domain (AAA wall) and fluid domain (blood) through a common interface (inner wall surface of AAA) which allows exchanging information of the solution (traction vector: static pressure *P* and wall shear stress WSS) of the fluid model and (the displacement: U) of the solid model between each other during the solution [241]. In this particular work, Abaqus 2016 [44] and STAR CCM+ v.13.04 [45] were employed to conduct a fluid-structure interaction simulation of AAA. Some of the important settings in both models needed to be modified as described later in order to allow the software to communicate with each other and reach the convergence stage smoothly [237].

Firstly, it is so important here to reset the fluid model to change the following features of the wall surface (stationary state =solid wall, i.e., no movement) and the shear stress specification (no-slip) into morphing state (moving wall) and slip shear stress in order to allow the wall deformation corresponding to the imported displacement U measured by Abaqus 2016 [44] at the interface surface. In other words, the mesh in the fluid domain deforms correspondingly to suit the deformation in the aortic wall in order to preserve a reasonable quality of the grid in both domains.

The following settings must be modified in order to obtain a stable solution:

1- The traction and displacement data exchange multiple times during each time step, which leads to a strong coupling between both domains as well as optimizing the convergence. Therefore, the inner iterations per single exchange represent the iterations of the fluid domain between two exchanges with the structure domain, which was then set to ***3 iterations***. The minimum number of exchanges represents how many exchanges the co-simulation engine performs with Abaqus in one time-step, which was set to ***15 exchanges***. As a result, the maximum inner iterations should be ***45 iterations or more***, which must not be less than the (***inner iterations * minimum exchanges***).
2- Modifying and creating new stopping criteria: three main stopping criteria were established based on the ***continuity, momentum, and co-simulation displacement***. The purpose of these criteria is to stop the iterations once they are satisfied during the solution. Therefore, the logical rule for all stopping criteria should be set to ***AND***. The criteria option should be set to the ***MINIMUM*** of the value ***1.0E-4***, which means both solvers exchange data during the time-step until they meet the minimum convergence threshold specified above [242].
3- Time Coupling Negotiations: this option determines the coupling time between the two codes or data exchanges. In this work, as a small-time step is needed; therefore, the ***export*** option was set, which allows both simulations to exchange data at a time interval equivalent to the STAR CCM+ time step.
4- Time marching specifies whether Abaqus 2016 [44]or STAR CCM+ leads the FSI simulation in sequence or simultaneously. However, implicit coupling allows running simulations sequentially only, and in this case, ***Star CCM+ leads*** the co-simulation.
5- Adding co-simulation keywords to the input file: in this option, either the user can write the co-simulation definition manually, or it can be added automatically by STAR CCM+ by activating the following node: ***write Abaqus keywords***.
6- Specifying Abaqus version: in this node, the user can specify which version of Abaqus that is being coupled with STAR CCM+; in this work, it is set to ***Abaqus v6.16***.
7- Loading dynamic libraries in Abaqus: this option allows the co-simulation engine to communicate between Abaqus and STAR CCM+ by showing the path of the co-simulation libraries, ***ABQSMACseModules.dll***.

6.6 Inlet and outlet boundary conditions

In this study, the current set of boundary conditions was applied and used for the purposes of comparison and validation. The FSI simulations were performed and run for 3 cardiac cycles to reach a stable simulation, in which the result extracted from the third one. First, a mass flow rate [127] was applied at the inlet surface of each AAAs **Figure *6.3*(a)**. Secondly, a 3-Elements Windkessel model has the following parameters: proximal, distal resistance and capacitance (Rp, Rd, and C) respectively, representing the downstream impedance [121](see **Figure *6.3*(b)**) was coupled to the AAAs outlets via a java macro [243, 244], see Appendix C. The values of Windkessel parameters were modified to achieve the in-vivo flow and pressure pulsatile waves.

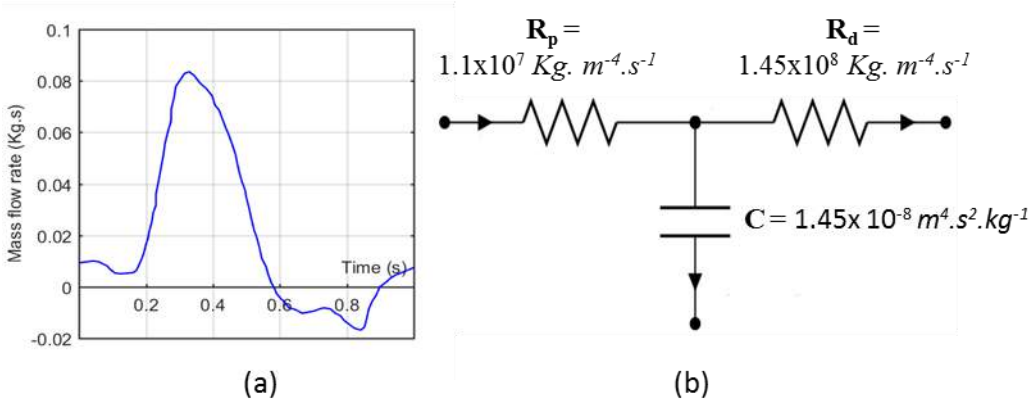

Figure 6.3: Boundary conditions used in the current FSI model (a) Mass flowrate inlet wave and (b) 3-elements Windkessel model.[127] [245]

6.7 Grid convergence study

In any numerical simulation, whatever the solution method is being used, such as CFD, FEA, or FSI, it is important that the solution domain (fluid or solid) has sufficient computational elements to ensure obtaining an accurate solution with minimal errors. Thus, a mesh convergence study was conducted starting with coarse mesh, which was then refined by dividing the base size by two. Four meshes were examined on AAA default and Patient4 (fluid and solid domain) to analyse the wall shear stress/displacement convergence at the systolic flow and pressure. The aneurysmal wall was assigned to the tetrahedral hybrid element configuration (C3D4H), see **Figure *6.4*** (**a**). After running the simulation for each set of mesh, the location and value of displacement were investigated and measured to find the deviation between displacement values and the increase in the number of elements. In terms of displacement location, it was observed that no correlation exists between increasing the

number of elements and the location of the displacement. It was also found that the percentage of deviation in the magnitude of the displacement value is less than 2%; therefore, mesh convergence is considered satisfied see **Table *6.3*.**

On the other hand, the fluid domain comprised polyhedral cells at the core of the AAA and a number of prism layers at the circumference to capture flow features near the wall see **Figure *6.4*(b)**. The wall shear stress profile was studied to observe the effects of changing the cells at the systolic flow see **Figure *6.5***. Mesh 3 was adequate to capture the shear stress profile with no significant changes compared to the wall shear stress profile obtained from mesh 4. Mesh generation and refinement were implemented using mesh modules within commercial codes of Abaqus 2016 [44]and STAR CCM+ v.13.04 [45]as can be seen in **Table *6.3*** below:

Table 6.3: Parameters used in the mesh convergence study for AAA default.

Mesh No.	No. elements (Fluid)	No. prism layers	Prism layer thickness(mm)	No. elements (Structure)	Magnitude displacement (mm)
M1	61088	10	2.97	30206	5.22
M2	109437	13	3.5	63081	5.601
M3	175913	15	3.5	92474	5.789
M4	291548	15	4	130826	5.904

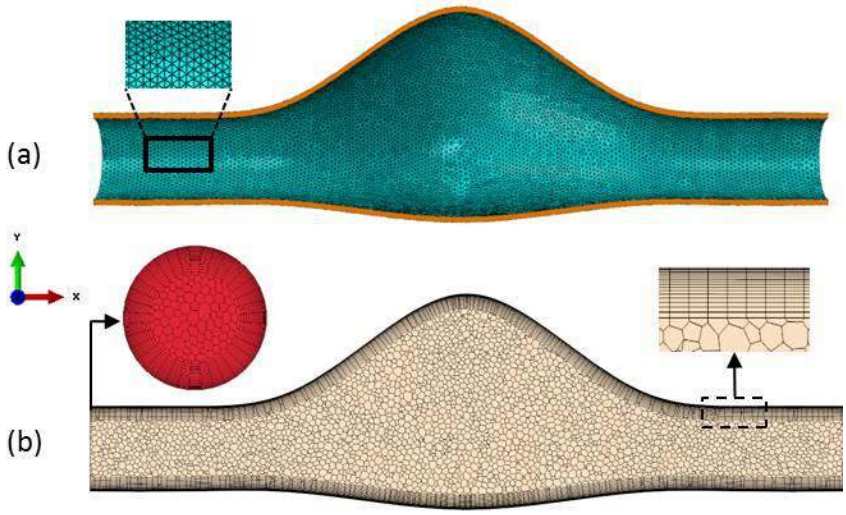

Figure 6.4: Mesh configurations used in this study (a) AAA wall with tetrahedral elements, (b) fluid part with polyhedral elements.

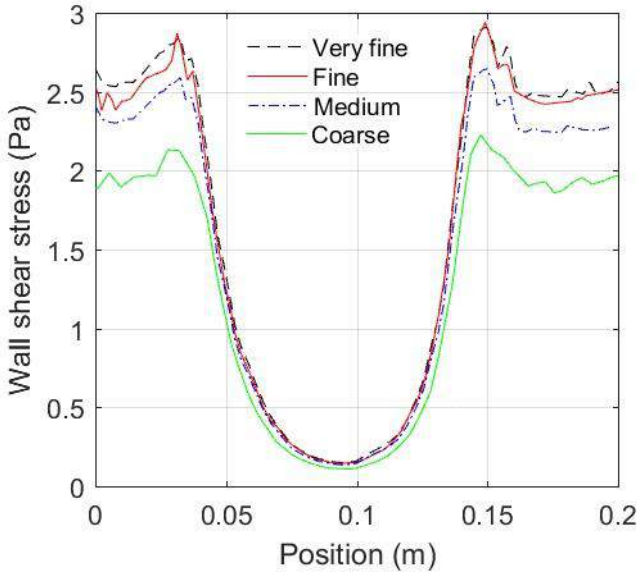

Figure 6.5: Mesh sensitivity study measuring wall shear stress profile at the peak flow of 0.32 sec, default AAA.

Concurrently, changing the mesh configuration in the solution domain also needs to adjust the time step that is compatible with the mesh size to obtain a stable and accurate solution. Therefore, the dynamic time step model was selected to control the desired local convective Courant Number of 1 in the fluid domain at each time step and each element, as explained in the section of ***Dynamic time-step***. Briefly, local convective Courant Number represents the proportion between the physical time step and the mesh convection scale of a certain element. In this work, the area of interest (AAA) should have an averaged convective Courant Number of one to consider the solution is time accurate. In other words, per time step, the fluid is approximately convected one element length. **Figure *6.6*** below explains the mesh and time step convergence study applied to Patient 4. It is apparent from **Figure *6.6*(left hand)** that the wall shear stress profile of M4 does not significantly differ from wall shear stress of M3, despite the huge variation in cell number and long computing time; see **Table *6.4***. In addition, **Figure *6.6*(right hand)** shows the strong relationship between the time step and cell size in the solution domain, as the size of the time step decreases with the decrease of element volume and vice-versa. Then, M3 is considered adequate to run a stable simulation; therefore, settings of M3 were applied to other AAAs.

Table 6.4: Mesh study applied to Patient 4.

Mesh No.	Element cells AAA fluid	Element cells AAA wall	Displacement in AAA wall
M1	44438	364078	1.82 mm
M2	132501	457818	2.1 mm
M3	363383	705709	2.5 mm
M4	452460	1351871	2.53 mm

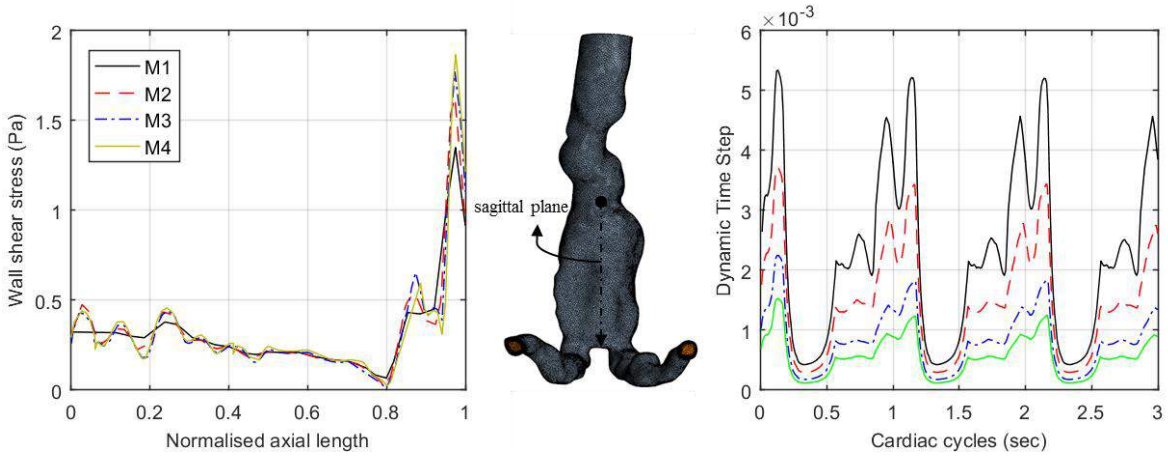

Figure 6.6: Mesh convergence study conducted on Patient4. Left: comparison of wall shear stress profiles / Right: variation of dynamic time step in each set of mesh.

6.8 Validation of FSI simulation

The process of validation of AAA numerical solutions against the AAA clinical data in vivo is quite difficult due to the complication of measuring the mechanical properties of the AAA wall and obtaining the living patient-specific model of the patients. Therefore, it is reasonable to use experimental phantoms of AAAs that are generally utilised to evaluate the accuracy of numerical approaches in the rupture risk assessment. Adding to that, implementing experimental work for a number of AAAs replicas needs a heavy-duty 3D printer and an appropriate material that has similar mechanical behaviour to the AAA mechanical properties, which in turn is fairly expensive and takes time to conduct it. Hence, this work was validated against a published experimental and numerical model developed by Kung. et al. 2011[245], which accommodated to validate the current FSI work.

The experimental and numerical work of Kung 2011[245] consisted of an idealised aorta (deformable pipe) made of silicon, and a pulsatile pump linked upstream to provide a

physiological periodic flow waveform at the inlet of the deformable pipe. On the other hand, the outlet boundary condition was assigned and achieved by using a 4- element Windkessel model with the following parameters in **Table *6.5***.

Table 6.5: 4-elements Windkessel theoretical and experimental components used by Kung 2011.[245]

Windkessel Variables	Experimental	Theoretical
L ($Kg.m^{-4}$)	7.0 e5	7.0e5
$\mathbf{R_p}$ ($Kg.\ m^{-4}.s^{-1}$)	2.4e7	2.5e7
C ($m^4.s^2.kg^{-1}$)	1.3e-9	1.6e-9
$\mathbf{R_d}$ ($Kg.\ m^{-4}.s^{-1}$)	4.0e8	4.1e8

The fluid used in the experimental rig was produced from a mixture of (40% glycerol solution and 0.5% Gadolinium) to have a similar dynamic viscosity of (0.00461 Pa.s) to that of the blood. The deformable wall was assumed to act linearly, where the elastic modulus was measured analytically using the results of the static and dynamic analysis performed previously on the deformable wall. The elastic modulus of static and dynamic data was 0.91 and 1 MPa, respectively, with no significant difference (less than 10%).

6.8.1 Current FSI model: Geometry, boundary conditions, mesh generation, and simulation settings

In order to validate the present FSI results, a two-way FSI model was developed (coupling STAR CCM+ v.13.04 and Abaqus 2016) of a deformable straight pipe adopted from [245] using physiological boundary conditions at inlet and outlet to examine the velocity patterns at different intervals of time during the cardiac cycle. The FSI model consists of the same components that had been used in the experimental work [245]: a deformable pipe of length 25 cm, an inner diameter of 2 cm and a wall thickness of 0.08 cm. The wall part assumed to behave as a linear elastic wall with Young's Modulus equal to 1 MPa, Poisson's ratio of 0.45, and a density of 1000 kg/m^3. The fluid part was assumed to behave as Newtonian, incompressible fluid of dynamic viscosity equal to 0.00461 Pa.s and density of 876.64 Kg/m^3. The inlet and outlet of fluid and wall parts were extruded perpendicular to the surfaces to obtain a stable and fully developed flow (Womersley profile) before entering the region of interest. The deformable wall (structure model) was constrained at both ends of the stream in Abaqus 2016. An inlet mass flow rate wave [127] and a 3-element Windkessel model adopted from [243, 244] were coupled to the inlet and outlet surfaces, see **Figure *6.7***. The Windkessel model used in the experimental work [245] had 4-

elements. However, in the current simulation, the 3-elements model was used instead, as there is no significant difference between the two models [246]. For the solid and fluid models, each had three sets of meshes (19502, 45289, and 71583) tetrahedral 3D stress elements and (33088, 75266 and 100356) polyhedral elements respectively, where the second mesh was found to be satisfactory in terms of the accuracy of the FSI solution. A second convergence study was performed in terms of choosing an appropriate time-step, in which the simulation was set to be stable and numerically converged once the residuals drop below 10^{-6}. The following dynamic time step in **Figure *6.8*** achieved the desired numerical convergence. A cross-section plane in the middle of the deformable pipe was created to examine the flow patterns at different time intervals against those obtained from the experimental and numerical work. The simulation was run for 3 cardiac cycles to ensure no influence of the residuals on the solution, in which the third cycle was chosen to extract the solution data.

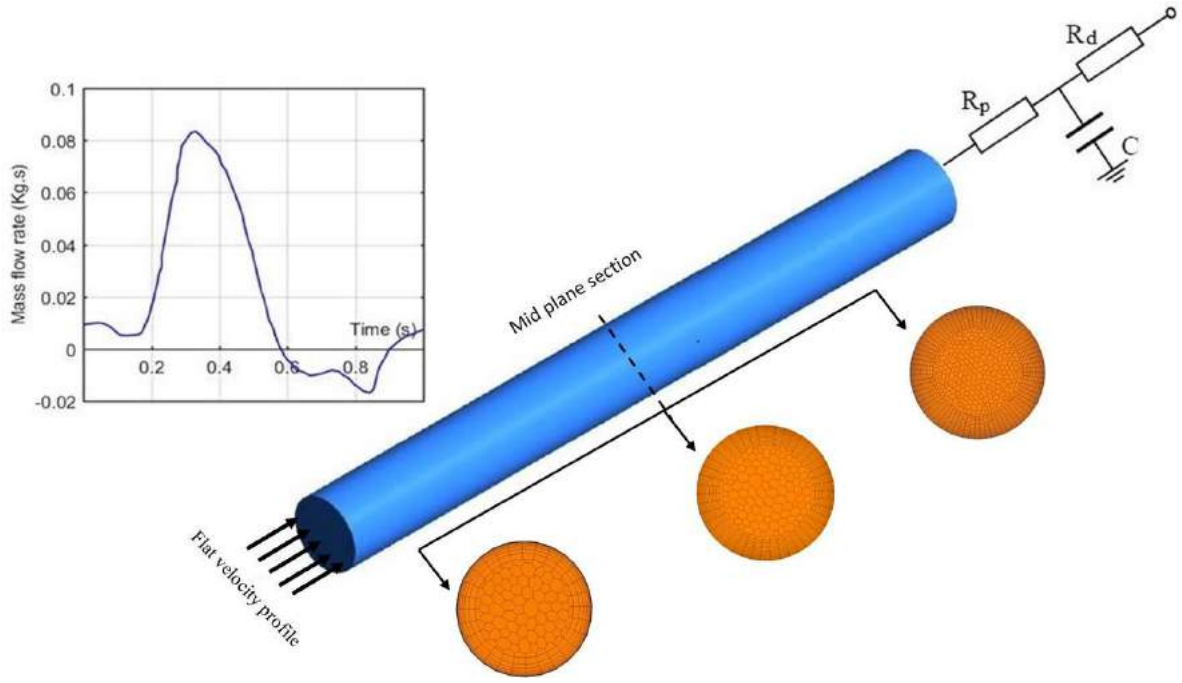

Figure 6.7: Schematic sketch of the fluid domain for a straight deformable pipe shows: (i) the boundary conditions at the inlet and outlet, and (ii) mesh configurations.

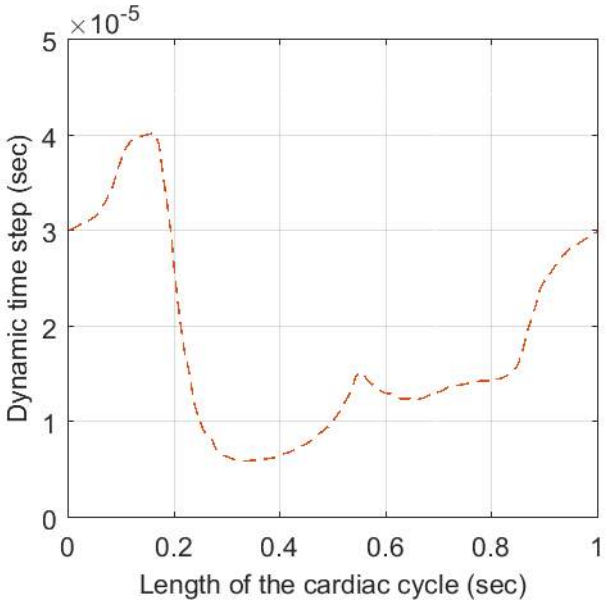

Figure 6.8: Dynamic time step that satisfied a stable FSI simulation in the deformable pipe.

6.8.2 FSI vs. Experimental and numerical results

Velocity patterns through a cross-section plane in the middle of the deformable pipe were obtained. The simulated (current work) and the experimentally measured/simulated velocity patterns were compared at four instances (diastole, acceleration, systole, and deceleration) see **Figure *6.9***. The results showed a good agreement between the experimental and simulated work in terms of the distribution of the velocity in the cross-section plane. It is apparent that the current FSI velocity patterns at acceleration and systole flow are showed to have a forward flow with the high similarity of profiles and magnitudes compared to experimental and numerical results. There is also an obvious thin-layer of low velocities flow (light blue colour) that adjacent to the deformable wall in experimental, simulation from the literature, and the present simulations. Gradually, the domination of the forward flow is restricted in the centre area of the vessel at the diastole and deceleration, adding to that, a noticeable area (dark blue) of backflow at the circumference of the deformable pipe was observed.

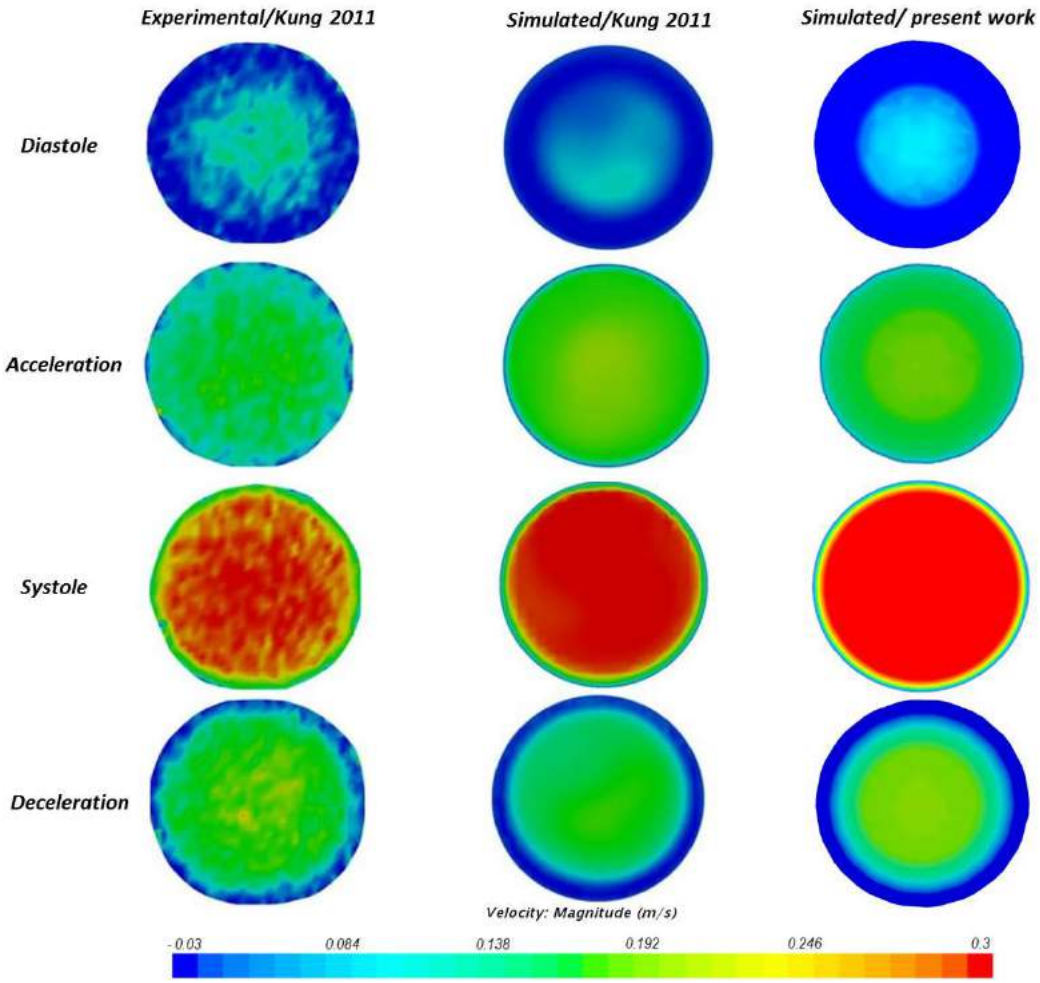

Figure 6.9: Comparisons of velocity profiles (experimental/simulation Kung 2011**[245]** vs. simulated/present work) in the mid-section of straight deformable pipe at four different time points of the cardiac cycle.

6.9 Results

In the following section, the results of fluid-structure interaction simulations in idealised and patient-specific AAA models are presented in two separate parts.

6.9.1 Idealised AAA

6.9.1.1 Velocity streamlines

Figure *6.10* shows a comparison of streamlines distribution of velocity magnitude at four different time points during the desired cardiac cycle in the mid-sagittal plane for idealised AAA default and AAA±10% geometries. It can be seen that for all geometries during the acceleration period, post 0.1 s to the peak systole 0.32 s, flow velocity streamlines remain in stable layers form (laminar), unidirectional, and adjacent to the aneurysmal wall (no vortices). Generally, for any unsteady blood flow, specifically in the acceleration period,

and due to the sudden changes in the cross-section area (expansion) of the abdominal aortic aneurysm, the blood particles experience an increase in the temporal-acceleration (changing with time) which is greater than the convective-deceleration (changing with space).

As a consequence, a positive pressure gradient occurs in the axial flow direction. It is essential to mention that the blood velocity is decreased noticeably (*blue colour*) when it reaches the anterior region of AAA. In contrast, the ultimate velocity flow (*red colour*) stays attached to the posterior of the AAA.

Following the acceleration phase, a period of flow deceleration occurs from 0.32 s - 0.45 s, which results in initiating and forming of moving vortices. As it is observed from the sagittal-plane of the AAA +10% geometry, two dynamic vortices are formed at the entrance of the AAA zone: one at the posterior, and another one at anterior extending almost to the middle of the AAA sac. However, velocity streamlines of AAA default and AAA -10% showed creating one dynamic vortex in the anterior position, as well as. It is noticeable that the intensity of default AAA vortex is fairly larger than the vortex of the AAA -10% geometry. The cause of generating dynamic vortices in the AAA region normally returns to the adverse pressure gradient induced by decelerating blood flow.

Then, the period of diastole blood flow starts from 0.8 s-0.1 s, where the pressure keeps dropping down, and the blood flow velocity stays at a low magnitude. As a result, the dynamic vortices grow and develop in terms of the size and start separating from the aneurysmal wall. For instance, in the AAA +10% geometry, the two dynamic vortices become four (two at the posterior and two massive vortices separated from the AAA wall to reside in the middle of the AAA. On the other hand, three and two vortices formed in AAA default and AAA -10% respectively, depending on the small changes, ±10% of the AAA default geometry. Then, the intensity, size, and number of dynamic vortices decrease gradually with the increase of the flow acceleration, as is shown in **Figure *6.10*** (0.1 s) and completely vanishing in peak systole 0.32 s in all geometries.

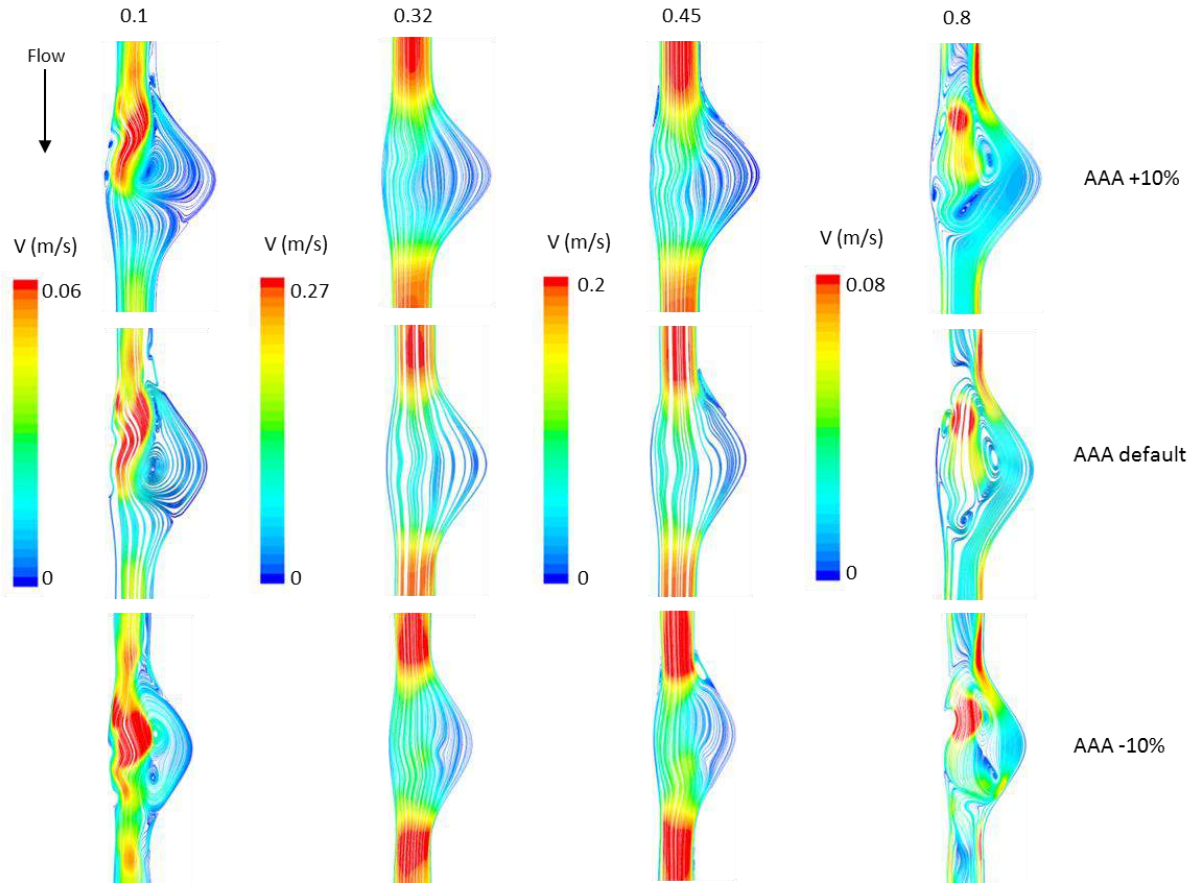

Figure 6.10: Velocity streamlines in AAA default and AAA± 10% at four different time intervals during the third cardiac cycle.

6.9.1.2 Analysis of hemodynamic parameters

A comparison of contours of hemodynamic parameters TAWSS, OSI, and RRT for the whole surface of AAA default and AAA ±10% are presented in **Figure *6.11***. Areas of high TAWSS of 0.3 Pa can be observed consistently distributed in the proximal and distal neck regions in all AAA geometries. However, additional areas of low TAWSS at the peak of the bulge in the anterior is observed in AAA + 10% compared to the AAA default and AAA - 10% cases. Let's turn the attention to the OSI parameter that manifests the total oscillation in the wall shear stress vector during the desired cardiac cycle. A noticeable increase in the high OSI area of 0.5 is observed depending on the geometry dimensions; for instance, AAA +10% shows the highest OSI at the inflection regions in the anterior-distal part. However, AAA - 10% shows the lowest OSI areas in the same regions mentioned above, as well as the posterior; see **Figure *6.11*** in the middle column.

In addition to TAWSS and OSI, **Figure *6.11***, provides a comparison of coloured RRT distribution in AAA default and AAA ±10%. The blue colour Zero (1/Pa) refers that the fluid

particles leave that region rapidly. In contrast, red coloured areas 75 (1/Pa) indicate that the fluid particles reside a long time in these regions before leaving due to the expansion in the cross-section area from the neck to AAA. High RRT in the anterior (from the peak of the AAA to the inflection area of the distal) and lateral sides are observed in AAA +10% comparing to the default and AAA -10% models. The lowest RRT is shown in the AAA -10%, especially in the posterior position.

For further evaluation, trends of TAWSS, OSI, and RRT profiles induced by the variations of AAA dimensions were extracted along a sagittal-plane in the anterior position and plotted against the length of the axial flow axis. It can be seen that all profiles of TAWSS, OSI, and RRT follow the same style with fairly consistent variations that correspond to the variations in AAA geometries, see **Figure *6.12***. Overall, the observations of TAWSS profiles show that AAA +10% experiences very low TAWSS at the centre of the AAA of almost 0.25 Pa, in which gradually increases with the decrease of the AAA dimensions. Moreover, a high TAWSS of an average of 0.42 Pa is observed in the proximal and distal neck regions of AAA -10% because the wall shear stress vector runs in stable condition, and vice versa for the AAA default and AAA +10%.

Similarly, the effect of the varying AAA dimensions can be observed on the OSI profiles in **Figure *6.12*.** Three peaks of OSI of an average 0.48 are observed at locations identical to the dynamic recirculation at the proximal, distal inflections, and centre of the AAA. In addition, OSI profiles revealed that AAA +10% produces more oscillatory flow that AAA default and AAA -10%. Finally, the comparison of RRT profiles shows that blood particles reside a long time in the AAA +10% with RRT of 1193 compared to RRT of 1020 and 700 in AAA default and AAA -10% respectively. In addition, the variations of AAA dimensions have affected the location of the RRT, see **Figure *6.12***.

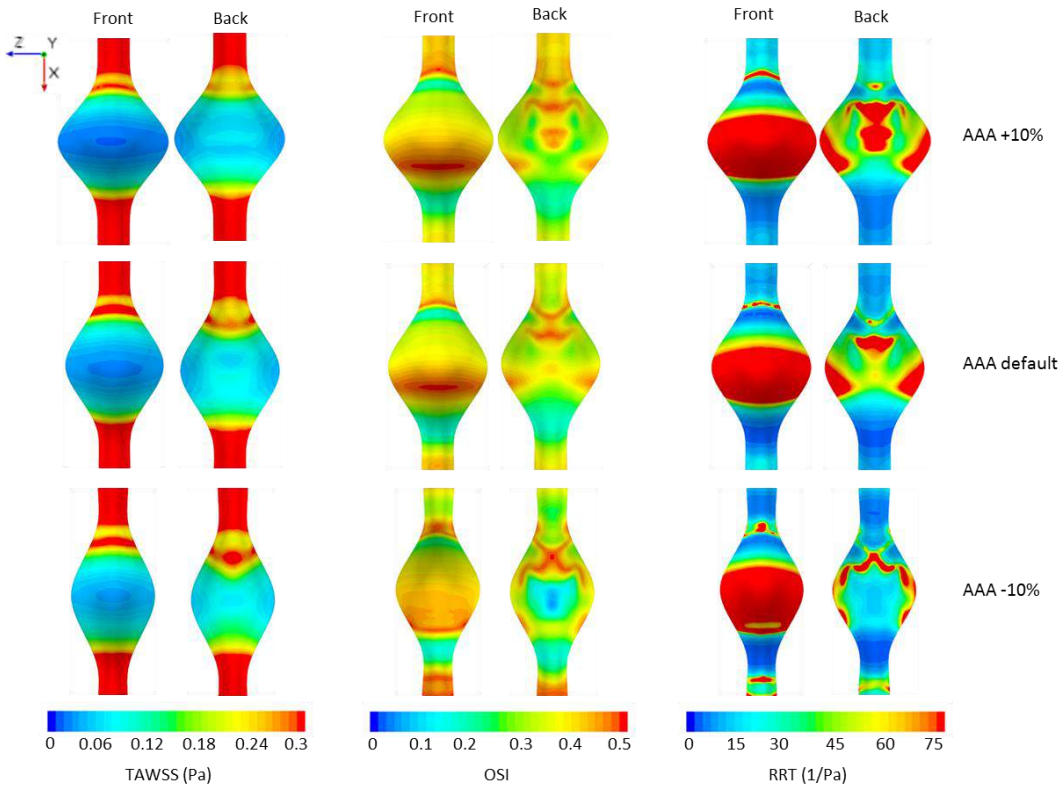

Figure 6.11: Hemodynamic parameters in AAA default and AAA ±10%.

In the top left corner of **Figure *6.12***, it can be seen that the TAWSS values vary between 0.3 and 0.4 Pa and follow straight profile in the proximal neck, which is then followed by a considerable increase over 0.4 Pa in AAA default and AAA -10%. In contrast, TAWSS in the AAA +10% keeps its straight trends. TAWSS values in all AAAs experienced fluctuation and a slight drop between 0.2-0.3 Pa followed by a small peak between 0.3-0.35 Pa. At that point, fluid particles enter the AAA region in which TAWSS encounters a sharp reduction to the lowest value of nearly zero at the zone mid-length of the AAAs. Then, TAWSS gradually rises from the lowest value to another ultimate value between 0.35-0.5 Pa, where the fluid particles leave the AAA to the distal neck, which the TAWSS reaches a stable value between 0.35-0.4 Pa in all AAAs.

Profiles of OSI in AAAs show high fluctuation up and down depending on the changing of the WSS vector and the formation of the dynamic vortices see **Figure *6.10***. Three peaks of OSI are shown in **Figure *6.12*** (Top right corner); the first peak of OSI just over the 0.45 corresponds to the creation of the dynamic vortices at the proximal neck pre-entering the AAA zone. Whereas, the second peak of OSI of just under 0.5 (highest oscillation) is in correspondence with travelling of the dynamic vortices to the middle of the AAA region.

Finally, the vortices now are about leaving the AAA zone to the distal zone induces the third peak in the OSI with a value below 0.4 in the AAA +10% and below 0.5 in both AAA default and AAA -10%.

The trends of RRT show a strong relationship between OSI and RRT, as can be observed in **Figure *6.12*,** the bottom plot. High values of OSI corresponds to high RRT; in contrast, low RRT means low oscillation. The first peak of the OSI just before 0.05 m matches the first peak in the RRT between 100 to 200 (1/Pa), which means that the fluid particles witness relatively low time due to the small size of the vortices. However, an OSI value of just under 0.5 (second peak) at the middle of the AAA link to high RRT value varying from 700 (1/Pa) in AAA -10% to almost 1200 (1/Pa) in the AAA +10%; which then follow low RRT that corresponds to the third peak of OSI.

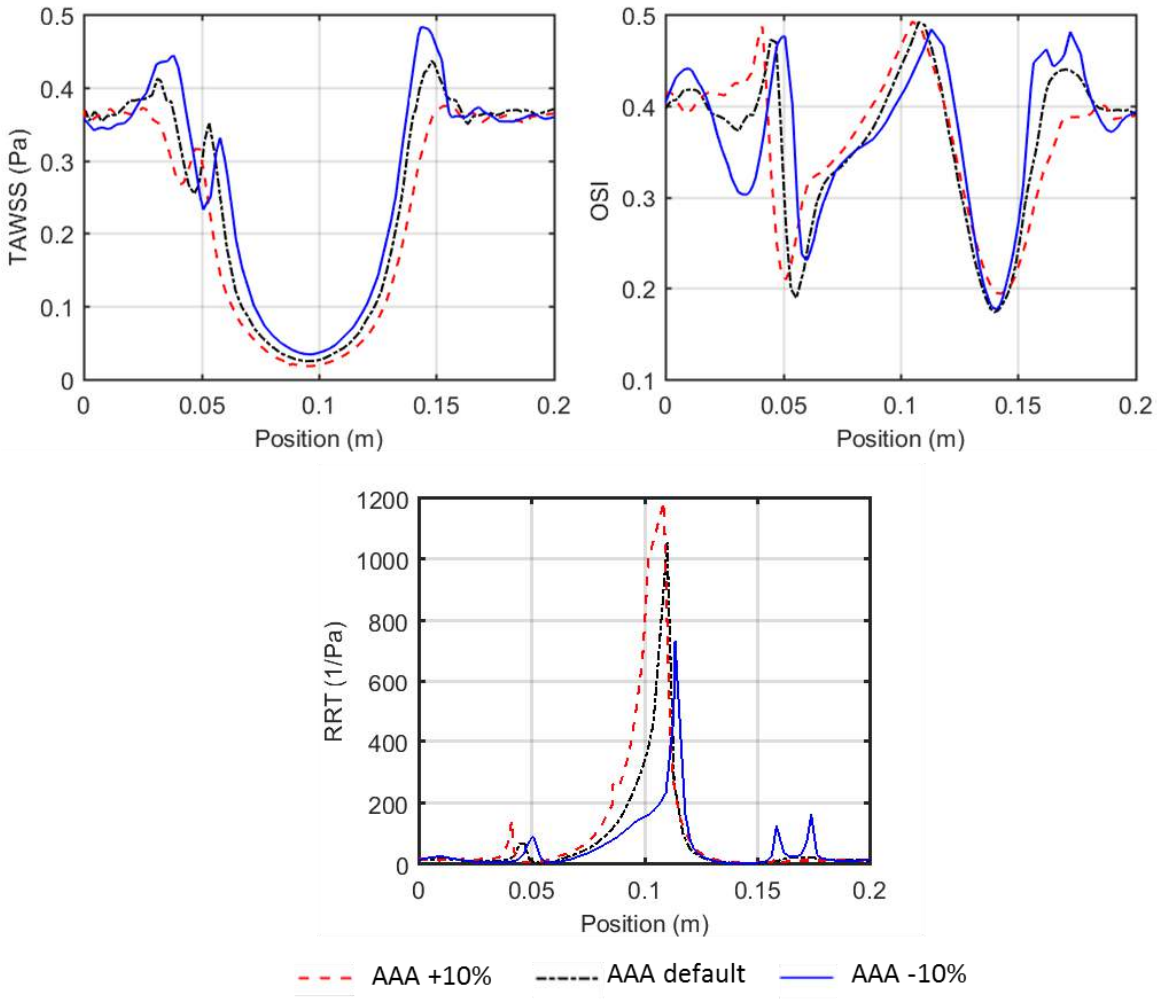

Figure 6.12: Comparison of hemodynamic parameters profiles in AAA default and AAA ±10%, where position represents the x-axis of flow along with the AAA.

6.9.1.3 Stress and displacement patterns

The influence of minor changes of the AAA geometries on the maximum wall stress and displacement distribution is studied and presented for half geometry due to symmetry along the axial axis. **Figure *6.13*** shows a comparison of the maximum AAA wall stress (left hand) and displacement (right hand) induced from the blood flow of idealised AAA: default and AAA ±10% at peak systolic flow. The dashed solid arrow refers to the original (un-deformed) AAA, while the solid black arrow indicates the deformed geometry.

A comparison of the maximum AAA wall stress contours in **Figure *6.13* (A)** has shown that the maximum wall stress occurs at the laterals and inflection points (proximal and distal). AAA -10% shows small areas of high wall stress (just laterals); however, high wall stress area (0.5 MPa) spreads widely to involve the inflection areas besides the laterals in AAA +10%. In **Figure *6.13* (B)**, it can be observed that the displacement magnitude in AAAs shows high influence with the minor changes in AAA structure. It is observed that AAA -10% witness low deformation (low displacement), which develops with the increase of AAA dimensions to produce high deformation of 6 mm (red areas) in both AAA default and AAA +10%.

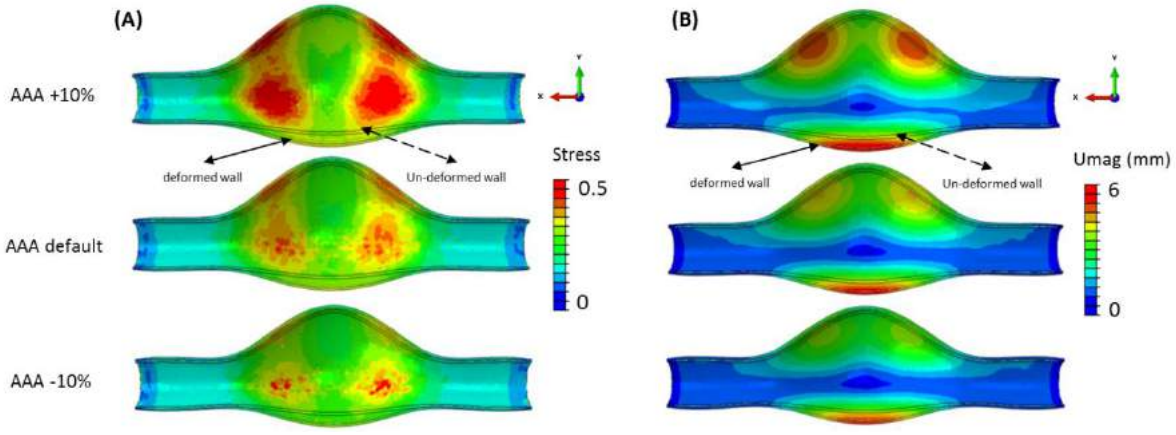

Figure 6.13: Comparison of (A) wall stress; (B) wall displacement in AAA default and AAA ±10%.

6.9.2 Patient-specific AAA models

6.9.2.1 Velocity streamlines

A sagittal plane in the AAA region was created to demonstrate the patterns of velocity streamlines within the AAA zone at four different time intervals (0.2 s, 0.32 s, 0.45 s, and 0.8 s) during the third cardiac cycle. **Figure *6.14*** illustrates a comparison of velocity streamlines in four Patients (ImFusion suite vs. Mimics v.18 models). A navigation compass

at the top left corner shows the orientation of the sagittal plane, where the *left side* of the sagittal plane refers to the *front view*, *right* refers to *back view* and *upstream/ downstream* refers to the *proximal* and *distal* respectively. It can be observed in some patients that the streamlines of velocity magnitude are distributed consistently at a specific time during the cardiac cycle. However, variations are noticed in all patients in terms of the vortex size, number, and separation areas during the desired cardiac cycle. For instance, in **Figure *6.14*** for the peak systole flow at 0.32 s, velocity streamlines are distributed homogeneously in layers form in ImFusion and Mimics AAAs models; however, the variation can be observed in other time points. In **Figure *6.14*** Patient 1 at 0.1 s, ImFusion and Mimics models predict the circulation zone (one big vortex in ImFusion model, two relatively small vortices in Mimics model) at the entrance of AAA as well as the separation in the flow region at inflection surface down the middle of the AAA. In Patient 1 at 0.45 s, ImFusion AAA predicts two tiny vortices in the front and back position at the beginning of the AAA. While, the Mimics model creates two big vortices in the back position at the upper part of AAA, causing separation regions (low velocity) at almost half of the AAA. Velocity streamlines at 0.8 s show good matching, even though the recirculation zone of blood flow at the entrance of the AAA/ImFusion model is shown to be greater than the recirculation zone in Mimics model.

Interestingly, Patient 2 and Patient 4 models show fairly high similarity in velocity streamlines patterns at the examination time points, in spite of noticeable variations in the number and size of the dynamic vortices. At 0.1 s and 0.45 s, the dynamic vortices are almost comparable in terms of number, size, and place in ImFusion and Mimics models. Moreover, the separation regions are noticed to occur in identical places at the front upper inflection point to the middle of the AAAs as well as in the bifurcation region. The consistency of separation regions and dynamic vortices at 0.8 s stays the same between ImFusion and Mimics AAAs, respectively, although AAA Mimics creates relatively more dynamic vortices. However, the position of the big recirculation area has moved to the back position in contrast to the distribution in 0.1 s.

Finally, Patient 3 shows significant variations in the velocity streamlines patterns between ImFusion and Mimics AAAs. For instance, at 0.1 s ImFusion model forms less dynamic vortices (one exactly at the entrance, one in the middle close to the back wall, and one near the bifurcation area) compared to the Mimics model which generates five vortices (one at the entrance, two near the centre of AAA, and two at the bifurcation area) causing high

separation in the flow. At time 0.32 s and 0.45 s, good similarities in the separation and recirculation flow regions are observed. In contrast, it is apparent that the streamlines in 0.8 s are totally altered, where the ImFusion model has three vortices in series starting from the neck towards the middle of the back position, causing a disturbance in the blood flow. While it can be noticed, the Mimics model keeps generating more vortices, which mean disturbance and separation in the flow regions.

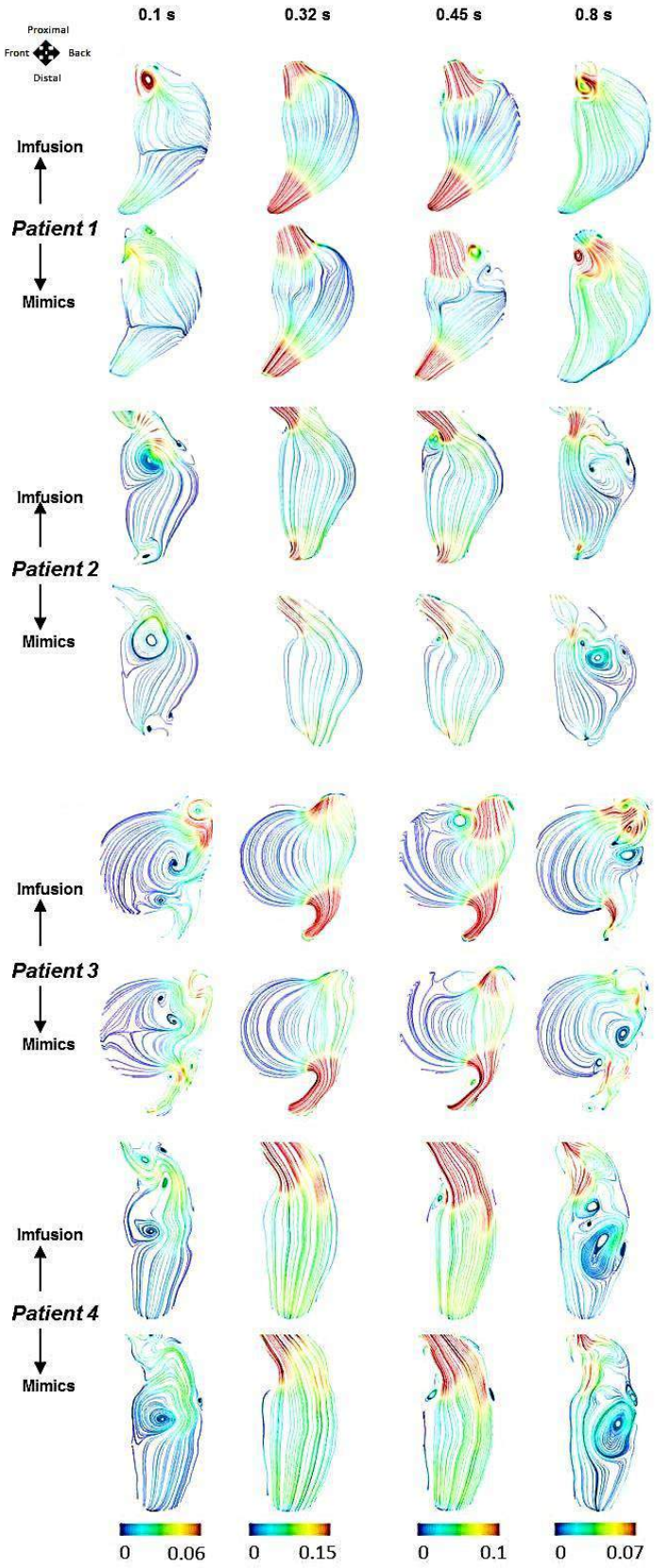

Figure 6.14: Comparison of velocity streamlines of ImFusion and Mimics AAA parts in the mid-sagittal plane at four-time points 0.1, 0.32, 0.45, and 0.8 s.

6.9.2.2 Analysis of hemodynamic parameters

A comparison of hemodynamic metrics contours between AAA ImFusion and Mimics parts is illustrated in **Figure *6.15***. Distribution of TAWSS results can be presented in all patients on the left hand of **Figure *6.15*,** where areas of high TAWSS of 0.5 Pa can be observed in the neck and common iliac branches, however, patterns of TAWSS show that AAA zone is always subjected to relatively low TAWSS of zero or slightly above. In Patient1, both ImFusion and Mimics parts encounter high TAWSS of 0.5 Pa at the common iliac branches, while the neck parts show noticeable variation in terms of high TAWSS. Then, the intensity of TAWSS starts gradually decreasing when the flow approaches the area of the bulge, which encounters relatively low TAWSS. However, low TAWSS in ImFusion AAA tends to be wider compared to Mimics AAA. For Patient 2 and 4, Mimics AAAs frequently exhibited high TAWSS of 0.5 Pa in the common iliac area, unlike the ImFusion AAAs that show high TAWSS in the bifurcations and neck parts. In addition, Mimics AAAs predict lower TAWSS than the ImFusion, almost at the middle of the back of AAA in Patient 2 and at inflection areas and back in Patient 4. The observations of TAWSS distributions show that the magnitude of the low TAWSS in the aneurysmal area varies remarkably with the significant deviation of the aneurysm diameter and the source of the AAA parts. For instance, Patient 3 has a massive aneurysm (ImFusion/Mimics), where the low TAWSS of zero magnitude covers a large area of the aneurysm, especially at the wall far from the flow stream with minor differences in the distribution between the two parts of AAA. However, in Patients 1, 2, and 4 produces TAWSS of almost 0.11 Pa or less depending on the size of the AAA. Patients 1, 2, and 4 show minor differences in TAWSS distribution depending on the source of the parts ImFusion or Mimics, as can be seen in **Figure *6.15***.

Let’s turn the attention to the OSI parameter, which identifies the total oscillation (change) in the wall shear stress vector during the cardiac cycle. The scale of OSI has two main values: low OSI of 0 means the wall shear stress follows one direction, on the other hand, a high value of OSI means the wall shear stress changes the direction due to either stagnant or recirculation flow, see **Figure *6.15*** the mid column. Overall, noticeable variations in OSI distribution between ImFuison and Mimics parts are observed. In **Figure *6.15*,** high OSI values are observed to happen mostly in the bulge area where the wall shear stress changes its direction in various directions to adapt with the flow disturbance induced from changing in the AAA cross-section areas. In Patient 1, ImFusion part predicts high OSI pattern compared to Mimics AAA, where the high OSI of 0.45 occurs in the right side

propagating to the back of the bulge exactly where the separation flow and vortices happen. However, the Mimics part encounters low oscillation of zero OSI on the left side and exactly at the entrance of AAA.

In contrast, the ImFusion part shows more oscillation compared to Mimics AAA. Likewise, differences in high and low OSI distribution can be clearly observed in Patient 2, 3, and 4 despite the ImFusion part predicts the majority of the high and low OSI areas of 0.45 and 0 respectively in the Mimics part. Areas of high OSI 0.45 in all patients are in correspondence to the areas of dynamic vortices or separation flow zone, see **Figure *6.14***. Mimics parts show high OSI compared to ImFusion parts because Mimics can segment a very detailed AAA geometry.

Figure *6.15* left-hand column illustrates as well the distribution of the RRT parameter that describes how long the fluid (blood) particles reside in the AAA zone before leaving. Red areas that have a value of 100 (1/Pa) mean that blood particles spend a long time in these zones due to the recirculation in the flow-induced from the expansion in the AAA diameter. Most of the high RRT areas seem to happen in the AAA domain only. On the other hand, blue areas of low RRT of zero magnitudes indicate that the blood particles are rapidly leaving that part because no disturbance happens in the flow at these zones. Commonly, low RRT is linked with the uniform shape of the blood vessel, such as the neck and common iliac arteries. In all patients, recognizable variations in RRT distribution can be noticed between the ImFusion and Mimics parts. Inflection points beyond the neck, front, and back of the AAA show high RRT value in Patients 1, 2, 3, and 4. Again, the relative residence time is related to recirculation, where regions of high RRT correspond with regions of high OSI and low TAWSS, see **Figure *6.14*** and **Figure *6.15*.**

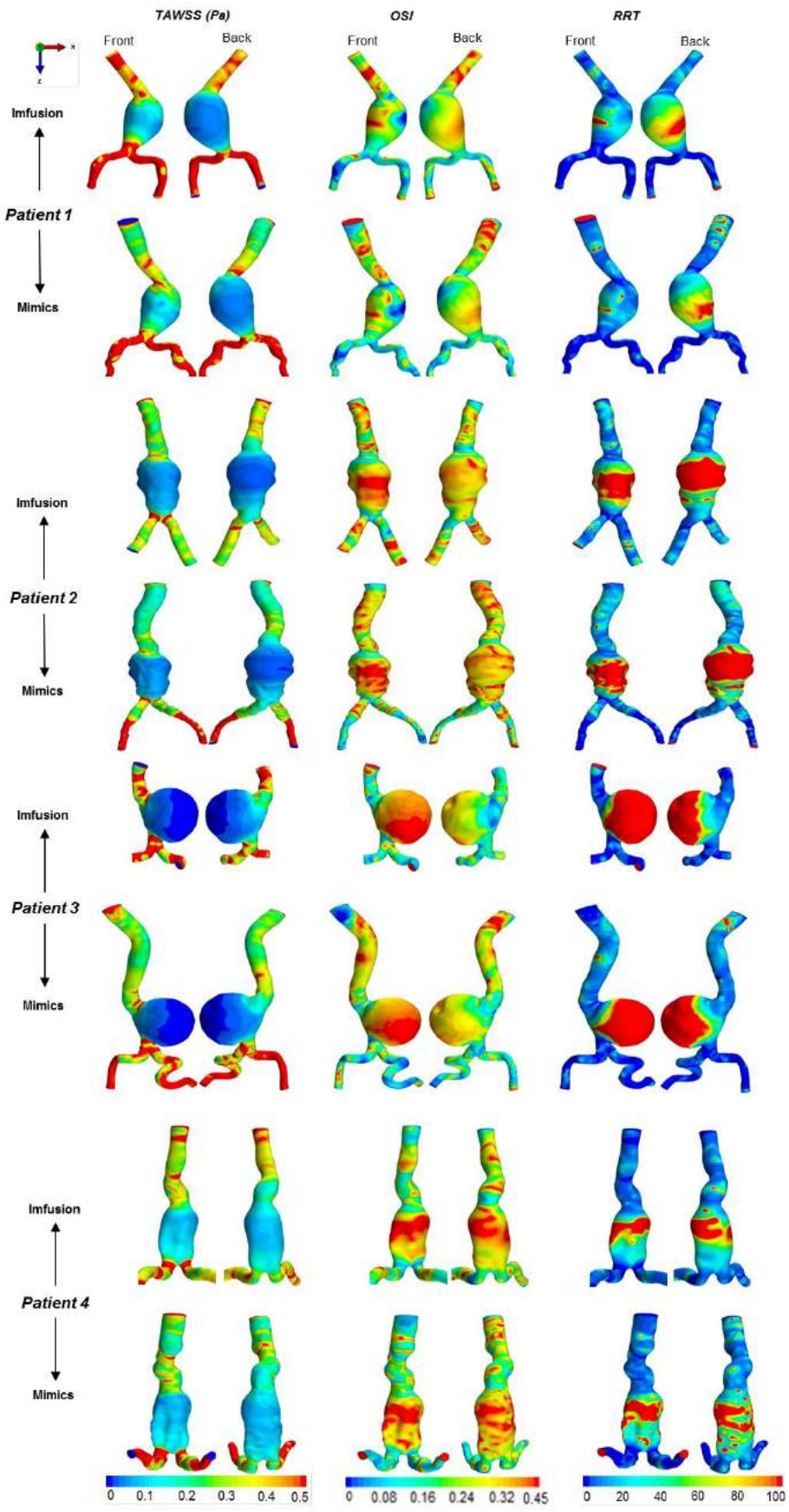

Figure 6.15: Comparison of hemodynamic parameters for ImFusion and Mimics AAA geometries.

The differences in the hemodynamic parameters patterns can be further examined and compared between ImFusion and Mimics AAAs by extracting the trends of TAWSS, OSI, and RRT metrics along a sagittal-plane that was created and explained in **Figure *6.6***. Comparison of TAWSS, OSI, and RRT profiles are presented in the first, second, and third columns in **Figure *6.16,*** respectively, where the red dashed curves refer to ImFusion, and solid blue refers to Mimics. Overall, values and trends of the hemodynamic metrics profiles vary depending on the AAA shape, source of segmentation, and size. In **Figure *6.16*** all Patients except Patient 3 show relatively high TAWSS value occurring at the neck which then drops down with the expansion of the AAA to rise again to reach another peak at the bifurcation areas where the highest value of TAWSS occurs. In other words, the intensity of the recirculation flow (low TAWSS) reaches the maximum when the flow becomes closer to the maximum expansion of the AAA diameter which is 0.5 of the normalised distance of the plane length. **Figure *6.16*(A) left** shows a comparison of the TAWSS profiles (ImFusion vs Mimics) in Patient 1. The values of the first peak of TAWSS in Mimics and ImFusion AAA are 0.4 and 0.49 Pa, respectively. Both models show a decrease in the TAWSS trends of 0.1 Pa till the middle of the sagittal plane, which later rises in both models to reach a second peak of 0.57 and 0.23 Pa followed by a slight drop then another escalation in the TAWSS of 0.4 and 0.89 Pa in ImFusion and Mimics respectively. For Patient 2, the TAWSS profiles show two spikes at the neck of 0.3 Pa ImFusion/ 0.42 Pa Mimics; and at the bifurcation regions of 0.5 Pa ImFusion/ 0.83 Pa Mimics. In between the peaks, the trends of TAWSS are similar to a value of 0.085 Pa in both ImFusion and Mimics, which happens exactly at the AAA zone. Remarkably, the model for Patient 3 predicts fairly identical profiles of TAWSS in ImFusion/Mimics AAAs with a slight difference in the high value of 1.3 and 1.5 Pa at the neck in Mimics and ImFusion and no significant difference in the high value at the bifurcation area. The AAA size has a strong relationship with TAWSS, where massive AAA generates low TAWSS. The lowest value of TAWSS is almost zero due to high recirculation in the flow that can be observed in the AAA zone of Patient 3 ImFusion/Mimics. Finally, TAWSS trends of ImFusion and Mimics AAAs start fluctuating from 0.1 Pa ImFusion/0.2 Pa Mimics to reach the lowest value just below 0.1. Then a sudden growth in the TAWSS pattern is observed at 0.4 Pa ImFusion/0.35 Pa Mimics with notable deviations.

Figure *6.16* provides a comparison of OSI profiles for ImFusion and Mimics AAAs. In general, OSI trends fluctuate up and down and are correlated with the formation of dynamic vortices and separation regions in the AAA zone during the cardiac cycle. An OSI value of

below 0.1 tends to be associated with the neck and bifurcation regions. However, the complexity and intensity of OSI change rapidly in the AAA region to reach the highest value of 0.5 at certain points. Comparison of OSI profiles in Patient1, **Figure *6.16***, revealed that both ImFusion and Mimics parts have four peaks of different values and positions in the OSI. The similarity between the OSI of ImFusion/Mimics AAAs can be observed in the first peaks in terms of the value of 0.35 and with a slight shift in the position. The deviation in OSI trends then begins extensively with the growth of the other three peaks in terms of the value and location. The second peak has an OSI of 0.35 ImFusion/0.42 Mimics corresponds to a location on the sagittal plane of 0.35 and 0.29, respectively. The OSI values fall to reach a reduction of 0.2 ImFusion/ 0.34 Mimics at almost half of the plane. Then, the OSI steadily increases again to the ultimate value of 0.47 ImFusion and Mimics with a location of 0.6 in ImFusion and just over the mid-length of the plane in Mimics AAAs. Following that, OSI profiles collapse twice to the lowest value of 0.2 ImFusion /0.05 Mimics with another peak in between of 0.25ImFusion/0.39 Mimics. The deviation in OSI profiles in Patient 2 can be expressed fluctuating in a consistent manner with slight shifting in the OSI locations. It is observed that a sharp drop in OSI from 0.39 to 0.1 in ImFusion and from 0.25 to 0.085 in Mimics AAAs followed by steady instability in the OSI trends until reaching the ultimate OSI value of approximately 0.5 which is in an adjacent location at almost the middle of the plane. Next, the OSI profiles fall for a second time with noticeable differences to reach the lowest oscillation of 0.05 in ImFusion and Mimics AAAs.

Unlike the other Patients, OSI trends of Pateint3 are almost identical with no significant variations from value and location aspects. Both ImFusion/Mimics profiles begin with a low OSI of 0.05 to increase suddenly to the highest value of just about 0.45. Later, the OSI trends steadily decline to a value just below 0.4, which then suddenly collapse to 0.1 in ImFusion/Mimics parts. Lastly, OSI profiles of Patient 4 show significant variations in OSI distribution (location and value) between ImFusion and Mimics parts. Firstly, the OSI profiles have an initial value at the beginning of the sagittal-plane of 0.16 and 0.22 in ImFusion/Mimics, respectively. Then, OSI profiles gradually approach to the first peak below 0.4 in Mimics and 0.45 in ImFusion corresponding to 0.1 and 0.2 positions in the sagittal plane. A gradual decrease occurs in the OSI in ImFusion/Mimics to meet both trends at the same value of nearly 0.3 and a location of 0.25. After this point, the OSI fluctuates considerably until it approaches the maximum value of almost 0.5 in the same position of 0.6 in the axial plane. Then, the trends of OSI drop remarkably to a very low value of 0.17

Mimics and below 0.05 ImFusion relating to 0.85 and 0.92 on the axial plane. A sudden rise in the OSI to the third peak of 0.32 Mimics and 0.4 ImFusion occurs before falling again at a value of 0.32 ImFusion/ 0.2 Mimics at the end of the plane.

Figure *6.16* illustrates the comparison of RRT trends between ImFusion and Mimics AAAs. Generally, RRT value is considerably higher in the region where the TAWSS decreases and vice versa. Moreover, high values of RRT correspond to high OSI; in contrast, low RRT means low oscillation. The general appearance of RRT patterns shows a wavy distribution specifically in the region of high inflation in the AAA, which occurs mostly at or about the mid-plane length. Evident differences can be shown in RRT trends in Patient1 at the right hand of **Figure *6.16*(A)**. Values and locations of the RRT peaks vary corresponding to the deviations in the TAWSS and OSI profiles. Initially, relatively small RRT values are shown at the beginning of the plane of 5 (1/Pa) Mimics/8 (1/Pa) ImFusion, followed by an increase in the RRT of 20 (1/Pa) Mimics /17 (1/Pa) ImFusion at the axial length of 0.12Mimics/0.15Imfusion. Noticeable growth in the RRT can be observed in Mimics AAAs of almost 70 compared to a value of 20 in ImFusion AAA. The RRT jumps rapidly in both models to reach the maximum RRT in the AAA of 117 (1/Pa) Mimics/ 95 (1/Pa) ImFusion at just over the mid-length of the sagittal plane. Then, the RRT trends fall promptly with another small peak in ImFusion of 20 (1/Pa) while RRT in Mimics keeps dropping to the lowest value of almost zero at the end of the sagittal plane. RRT profiles (Mimics and ImFusion) of Patient 2 in **Figure *6.16*(B)** start with almost zero (1/Pa) which later grows sharply to the ultimate RRT value of 740 (1/Pa) ImFusion and 785 (1/Pa) Mimics with a slight alteration in the position of 0.4 ImFusion and 0.45 Mimics. After this point, the RRT profiles drop with minor instabilities in both models until reaching the zero value of RRT at the end of the sagittal plane. Although profiles of TAWSS and OSI of Patient 3 show little differences, see in **Figure *6.16*(C),** the RRT profiles are different in terms of the highest value and distribution pattern. The RRT trends increase sharply from the zero (1/Pa) at the entrance to the highest value of at around 1000 (1/Pa) ImFusion/1250 (1/Pa) Mimics in the first quarter of the AAA in both ImFusion and Mimics models. Later, a gradual fall with an evident gap between both RRT trends is observed with the progress of flow towards the outlets to reach zero (1/Pa) at the bifurcation point. Similarly, for other patients (Patient4) patterns, values and locations of RRT are clearly influenced by the source of segmentation of AAA. The variation can be clearly seen in the style of RRT distribution along the sagittal-plane, in which small peaks can be observed before reaching the ultimate one of 430 (1/Pa)

Mimics and 489 (1/Pa) in ImFusion which then drop to reach almost zero (1/Pa) at the very end of the Sagittal-plane.

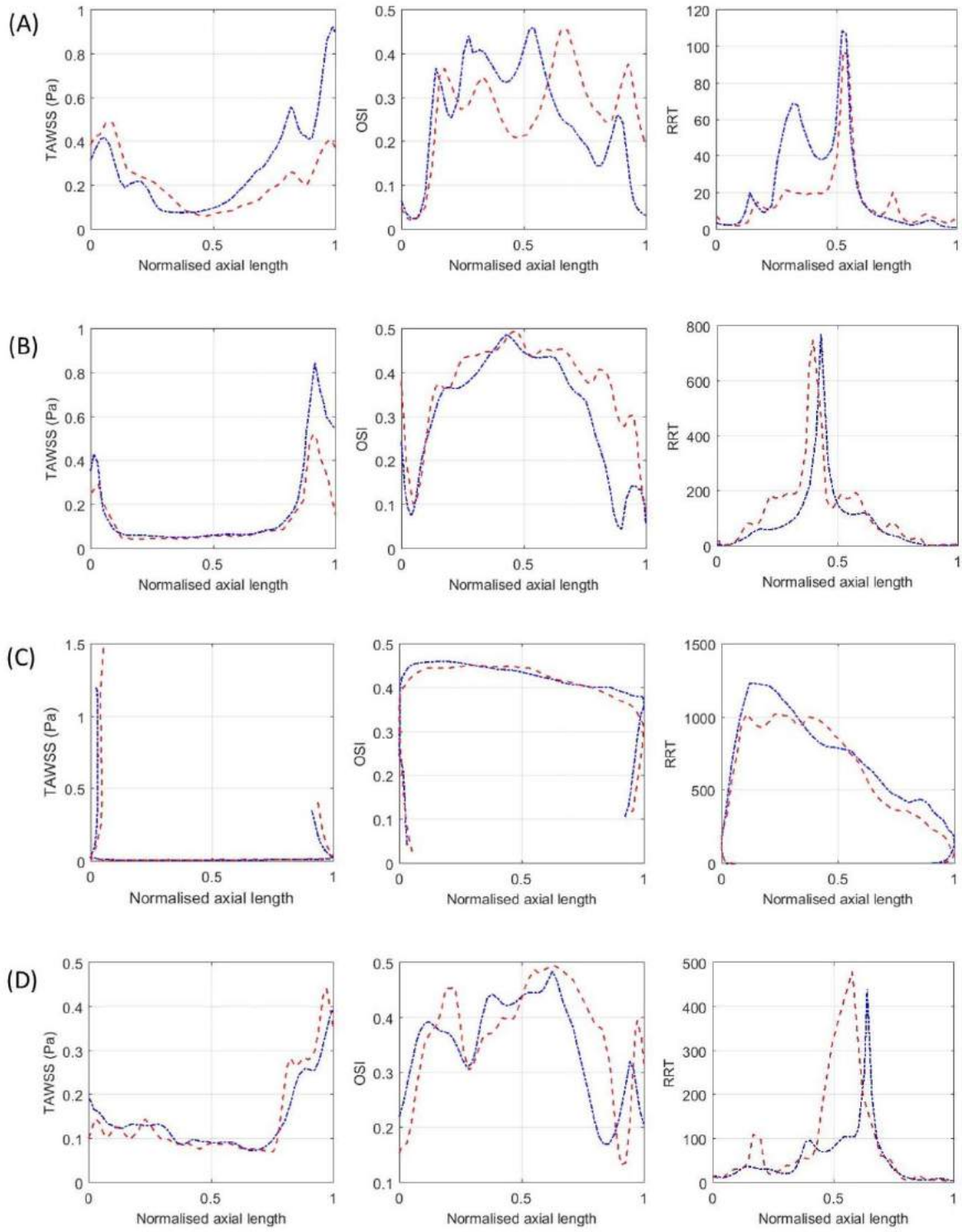

Figure 6.16: Comparison of hemodynamic parameters profiles between ImFusion (*red dashed)* and Mimics (*solid blue)* in Patients A, B, C, and D along the sagittal plane.

6.9.2.3 Stress and displacement patterns

The influence of minor geometrical differences on the maximum wall stress and displacement distribution has been studied. **Figure *6.17*** illustrates a comparison of (**A**) the maximum wall stress and (**B**) displacement induced from the blood flow of AAA (ImFusion vs. Mimics) at peak systolic pressure.

In general, the Mimics AAA wall produced higher value and wider areas of maximum stress and displacement than the ImFusion AAA wall. However, sites of maximum wall stress and displacement were identified as being similar. From the comparison of the maximum AAA wall stress in **Figure *6.17* (A)**, Patient 1 and 3 are observed to have maximum wall stress of 0.28 and 0.3 MPa, respectively. In terms of the locations, maximum wall stress in Patient 1 occurs at the middle of the front view while in Patient 3 occurs at the inflection areas (proximal and distal) and some patches in the front and lateral view. The patterns of wall stress magnitude in Patient1 and 3 vary on the AAA wall with no zero stress magnitude is observed on the wall because of the absence of the intraluminal thrombus.

Moreover, shear forces induced from the recirculation of blood flow act directly on the aneurysmal wall. In contrast, the presence of the intraluminal thrombus can be evidently affecting the stress patterns in Patients 2 and 4, see **Figure *6.17*(A).** Wall stress of zero value can be noticeable in the whole perimeter of Patient 2 with a visible difference between Mimics and ImFusion AAAs. In contrast, the maximum wall stress of 0.28 MPa can be seen at the end of the neck to expand to the AAA proximal inflection. Unlike Patient 2, Patient 4 seems to have zero stress concentration on the front and sides of the AAAs, where the thrombus is formed. Minor geometrical differences can be clearly observed affecting the patterns of wall stress, especially the maximum wall stress of 0.25 MPa, where the back of Mimics AAA produces high stress compared to ImFusion AAAA.

Figure *6.17*(B) illustrates the deformation magnitude in the AAA wall due to blood flow represented by the displacement (mm). The deviation in displacement distributions can be observed in ImFusion and Mimics AAAs because of the minor variances in AAA structure. Generally, Mimics AAAs show high deformation than the ImFusion walls in terms of the maximum and minimum values and location. Patient 1 **Figure *6.17*(B)** ImFusion model shows the displacement with noticeable changes in patterns and locations compared to Mimics AAA in terms of low and high deformation of 4 mm and zero mm, respectively. Although Patient 2 has thrombus covers for most of the AAA circumference reducing the

stress value, the deformation is highly evident in both AAA models with an average value of 1.5 mm. Indeed, the structure of Patient 3 had no thrombus, which makes the AAA undergoing to high deformation of 7 mm in the front view in both AAA models with noticeable deviations. However, the back view of both AAA of Patient 3 shows noteworthy variations in the deformation patterns, see **Figure *6.17*(B)**. For example, ImFusion AAA produces low deformation of almost zero at the back of AAA, whereas the Mimics model generates high deformation at the neck and proximal-inflection of 7 mm. Finally, no correlation is found between deformation distributions in terms of high and low displacement in Patient 4, **Figure *6.17*(B)**, in which Mimics AAA produces higher deformation than the ImFusion AAA. For example, the maximum deformation of 2.5 mm in Mimics model occurs at the end of the neck and shatter in many places at the back, while ImFusion generally produces less deformation and the maximum displacement occurs at the right side of the AAA back. In addition, the presence of thrombus is apparent in ImFusion AAA deformation, which is in contrast to the Mimics model.

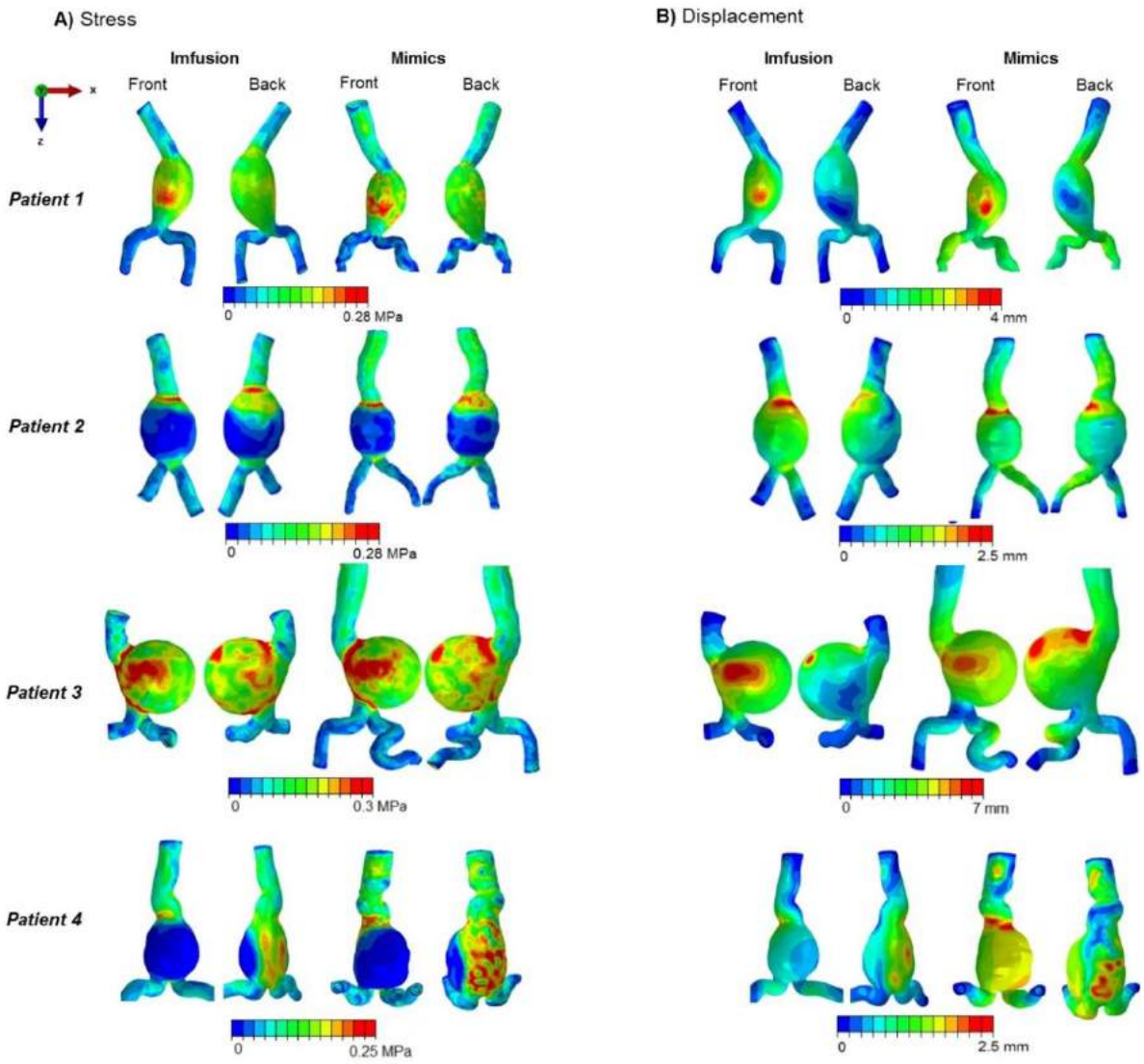

Figure 6.17: Comparison of (A) wall stress and (B) displacement in ImFusion and Mimics AAA geometries.

6.10 Discussion

Nowadays, a good amount of information is available concerning the biomechanics characteristics, medical history, and changes in the tissue properties of abdominal aortic aneurysms AAAs [232, 247-250]. However, surgical intervention relies primarily on the maximum diameter of the diseased vessel [251]. Minor deviations in the segmented Patient-specific models of AAA that being extracted from CT images and constructed using various packages such as Mimics v.18 [43] and ImFusion suite [46] were studied in this work. Numerical Fluid-structure-interaction simulations were executed to evaluate and compare the following parameters TAWSS, OSI, RRT, maximum wall stress and displacement in both models of AAA. In addition, by involving 3-elements Windkessel model at the outlet's

boundaries, it was possible to achieve realistic blood flow features. The validation of the current FSI approach was conducted by comparing FSI velocity patterns in a deformable pipe with the published experimental work [245]. The consistency between FSI and the experimental results were encouraging and in good agreement.

Figure *6.10* and **Figure *6.11*** show the variation in the velocity streamlines and hemodynamic parameters in idealised AAAs induced from decreasing and increasing the original dimensions of the default AAA by ±10%. The significant variations in the velocity patterns, TAWSS, OSI, and RRT distributions are due to the changes that happen in the vessel curvature produced from the reduction and expansion of the AAA dimensions. Moreover, the formation of recirculation or separation flow is another example of the effects of the minor geometrical deviation. In addition, the deceleration in blood flow plays an important role in the forming and progressing of the dynamic vortices. It was also observed in **Figure *6.10*** that the number and size of the dynamic vortices shrank when the vessel has low curvature and vice versa. The current results of idealised AAA are consistent with previous work [143, 252] in terms of creating the vortices in the AAA.

On the other hand, hemodynamic metrics distributions and patterns in **Figure *6.10*, Figure *6.11*** and **Figure *6.12*** were highly affected by the geometrical changes of the dimensions of the AAA, in which TAWSS value decreased noticeably with wide areas in the AAA +10% model compared to AAA default and AAA -10% models. Similar variations in OSI and RRT distributions can be observed affected by the changes in the AAA dimensions. The effects of these geometrical deviations extended to affect the magnitude and distribution of maximum wall and deformation of AAAs. **Figure *6.13*** simply shows the linear relationship between varying the dimensions of AAA and both the maximum wall stress and displacement distribution and value. The maximum wall stress increased with increasing the AAA by 10% compared to the stress distribution of the default AAA model. AAA -10% showed the contrast, where wall stress and displacement values and areas declined remarkably compared to the default AAA.

The general shape of the AAAs differed widely from one patient to another. Moreover, the geometrical variations in a single patient that result from the segmentation process were studied thoroughly. The observations of TAWSS comparisons between ImFusion and Mimics parts in **Figure *6.15*** showed that Mimics models produce lower TAWSS values (zero or slightly above) at the AAA zone more than ImFusion parts with noticeable differences. In

other words, regions of dynamic recirculation in Mimics models are stronger and quite intense compared to those of ImFusion models, as shown in **Figure *6.14***. The sudden expansions of AAA diameter (up/downstream), tortuosity, neck angle, and proximal/distal curvature are key factors that cause dynamic vortices (recirculation) and separation in the flow features compared to the intact aorta.

Furthermore, all low TAWSS areas of zero magnitudes or slightly above correspond either to the thrombus formation location as in Patient 2 and 4 or significantly increase the growth of the AAA as in Patient 1 and 3, see **Figure *6.15*.** Thus, predicting low TAWSS in Mimics models (highly detailed geometry) makes it more reliable than the predictions of ImFusion models because low TAWSS is normally associated with aneurysm growth and atherosclerosis. In contrast, the neck and iliac branches of both AAA models encounter high TAWSS of 0.5 Pa with noteworthy differences because the wall shear stress vector does not considerably change its direction. Comparison of TAWSS profiles in **Figure *6.16*** showed the variation induced by the geometrical deviations in terms of high, low magnitude, and the patterns of TAWSS between ImFusion and Mimics AAAs for the same patient. It was also observed that TAWSS profiles of Patient 3 were not affected significantly by the AAA sources (ImFusion suite or Mimics v.18), because the sagittal plane location could only capture the low TAWSS at the AAA front. However, the variances can be clearly seen on the side views left and right, see **Figure *6.15***. Variations in the neck diameter, angle, and curvature of inflection points in the proximal and distal areas [225, 253-255] are possible reasons to cause the noticeable fluctuation flow patterns and in returns on the TAWSS values. As expected, the widening of the cross-sectional area of AAA reduces TAWSS predominantly in core and curvature regions of the diseased aorta [219].

OSI distributions in the whole AAAs in **Figure *6.15*** were compared between ImFusion and Mimics AAA models. The general observations of OSI distributions showed that Mimics Models of AAA showed higher oscillation regions of 0.45 OSI at different places in the AAA part compared to ImFusion AAA, which reflects the action of the dynamic vortices predominant at these regions, see **Figure *6.14***. By comparing OSI mapping at the neck and bifurcation regions, no consistent distribution was found between ImFusion and Mimics parts. The reason behind predicting Mimics parts even for slightly higher or lower distribution of the hemodynamic metrics corresponds to the high resolution of the AAA parts. However, both AAAs have the same mesh density. Importantly, areas of high OSI 0.45 were in strong correspondence with the area of thrombus location [256] as can be seen in Patient 2

and 4, while, in Patient 1 and 3 as the thrombus was not formed because the oscillation is not stagnant but help on the rapid formation of AAA due to the high recirculation that dominants at AAA zone. OSI profiles at a sagittal plane were compared in **Figure *6.16***. Noticeable changes in the OSI patterns were evident between ImFusion and Mimics AAAs in the same patients, due to the existence of the compound recirculation areas throughout the two parts. The variations comprised of OSI values, shifting in the location of high OSI as well as producing multi-peaks of high OSI. Apart from Patient 3, that presented insignificant changes in OSI patterns because of the sagittal plane location. On the contrary, the inconsistencies in OSI distributions can be evidently observed on the side views left and right of AAAs, see **Figure *6.15*.** In contrast to the TAWSS, the OSI was high within the AAA in areas of low TAWSS (averaged OSI=0.4 over the AAA region from proximal to the distal points).

Relative residence time (RRT) colour maps of blood particles were compared to ImFusion vs. Mimics parts in **Figure *6.15***. The variations in RRT distribution can be observed in Mimics and ImFusion parts in all patients. RRT distributions in Mimics AAAs were very sensitive to the geometrical deviations and source of the AAA. In **Figure *6.16***, a comparison of RRT patterns illustrated that most cases of Mimics AAAs revealed RRT values higher than ImFusion. Definitely, Mimics parts were shown to experience large dynamic recirculation zones that dominate most of the AAA region.

Furthermore, on some occasions, AAA witnesses a high drop in the pressure during the cardiac cycle due to AAA expansion in which recirculation regions can be separated into multi-dynamic regions. These recirculation regions are highly associated with the existence of multi-peaks in the RRT profiles and consequently cause long staying for blood particles in AAA. For instance, Patient1 and 4 have multi-peaks of RRT depending on the intensity of the recirculation during the cardiac cycle, see **Figure *6.16***. Moreover, shifting in the high RRT location can be observed in addition to the high-value deviations.

Finally, the effects of geometrical differences were studied on an important indicator of rupture potential, which is maximum wall stress. This important parameter was shown to be significantly affected by the variations in AAAs induced by the segmentation process, especially those patients with thrombus see **Figure *6.17***. As reported in the literature [257], the presence of thrombus in AAA plays as a mechanical cushion that works on decreasing the wall stress. This finding was matched in Patients 2 and 4 in **Figure *6.17*,** where the zero MPa

stress areas cover the corresponding areas of the thrombus formations. Whereas, in Patients 1 and 3, the opposite behaviour was observed due to no thrombus is being present. Irrespective of the presence of thrombus, it was evident that maximum wall stress and deformation distributions are considerably influenced by the AAA segmentation. Overall, Mimics parts exhibited significantly high wall stress and displacement compared to the ImFusion AAAs.

This study has few limitations, such as using the Newtonian fluid model, assumption of laminar flow, constant aortic wall thickness, and assigning linear material properties to the thrombus. Despite blood is not a Newtonian fluid, it is assumed to behave as a Newtonian fluid in big blood vessels with a diameter larger than 0.5 mm, as well as the viscosity is treated relatively constant in the large vessels because of high shear rates [125]. The flow at the inlet was classified as laminar based on the ***RE*** number and the diameter of the neck at the proximal, which was ≤ 2100. In terms of imposing a constant wall thickness returns to the fact that the aortic wall thickness is difficult to be captured from CT images. Intra-luminal thrombus is assumed to reduce the wall stress [209, 247] regardless of the constitutive model used to represent the mechanical properties of the thrombus.

6.11 Conclusion:

In conclusion, this work highlighted deviations in the hemodynamic metrics distributions, maximum wall stress and deformation patterns in AAAs induced by the minor geometrical variations due to the construction process using ImFusion suite and Mimics v.18 software. It was found that the segmentation process in Mimics v.18 can capture even the small details in the AAA to produce high-quality AAA geometry, in contrast to the ImFusion suite that fails to capture minor details of the AAA that negatively influence the blood flow patterns. It was observed that the imposed variations of ±10% of the idealised AAA default dimensions extremely affected the velocity streamline especially in the AAA +10% model compared to AAA default and AAA -10%, where dynamic recirculation and flow separation were increased and generated with the increase of the AAA dimensions by 10% and vice versa. The values and patterns of hemodynamic metrics in AAA +10% show lower TAWSS, higher OSI, and RRT compared to the AAA default and AAA -10%. Moreover, it is observed that making minor modifications to the idealised AAA dimensions will significantly increase or decrease the value and area of peak wall stress and deformation.

In terms of the patient-specific AAA models, Mimics AAAs are observed to produce a large number of dynamic vortices compared to the ImFusion AAAs. These changes in the flow

patterns reflect noticeably on the hemodynamic metrics and wall stress and deformation distribution, where lowest TAWSS, higher OSI, and RRT are observed in Mimics AAA parts rather than ImFusion AAAA models. Moreover, maximum wall stress and deformation in Mimics AAAs are of higher magnitudes, wider in areas and occur in different locations, in contrary to ImFusion. These variations in the hemodynamic metrics and wall stress /displacement patterns, values, and locations in the AAA should be addressed thoroughly, which may mislead the understanding of the rupture potential, thrombus formation, and AAA growth mechanism.

7 Chapter Seven: Effects of inlet and outlet boundary conditions on the predicted hemodynamic of Abdominal Aortic Aneurysm

7.1 Introduction

Investigating and quantifying flow patterns in a diseased or intact artery are essential to give a good understanding of the reaction of the cardiovascular system to the frictional or biomechanical forces induced by the blood flow[258]. Realistic flow patterns can be predicted numerically by performing unsteady flow simulations to model the blood flow within the AAA by employing numerical approaches such as fluid-structure interaction (FSI). In order to adequately simulate blood flow in arteries; velocity and pressure boundary conditions are needed to reveal the consequences of predicting AAA growth or the potential of rupture [259, 260]. FSI approach can provide contour plots of various hemodynamic metrics which are associated with the formation of the AAA. The most common hemodynamic parameter that has been widely used in many studies[261-264] is called Wall Shear Stress (WSS) which represents the frictional forces exerted on the AAA wall due to blood flow[222], where the direction of wall shear stress may indicate underlying cardiovascular conditions [28, 222, 223]. For instance, healthy and intact blood vessels are subjected to unidirectional steady wall shear stress. However, the low magnitude oscillatory wall shear stress resultant from flow circulation can be linked to the development of atherosclerosis [224]. Incomplete knowledge and assessment of these hemodynamic parameters and other rupture indicators such as maximum wall stress may result in inexpedient decisions leading to potential loss of life.

Appropriate boundary conditions at the inlet and outlet must be provided to run an FSI blood flow simulation. However, obtaining flow measurements in vivo in order to carry out an accurate FSI simulation is quite difficult to be performed on live patients. As a result, many researchers had to impose or simplify the inlet and outlet flow conditions in order to express a well-posed rupture problem. For example, waves of velocity and pressure in arteries are exposed to dispersing, reflecting and damping owing to the variations in the AAA volume, mechanical properties of the vessel and bifurcation angle[100]. On the other hand, the effect of the outlet boundary conditions was shown to have little impact on the flow patterns in AAA [121]. The most common choices of outlet boundary conditions for periodic flow are either pressure wave being defined at the outlets, or a Windkessel model that represents the distal and proximal resistance besides the capacitance [121-124].

Moreover, hundreds of published articles regarding AAA were conducted without using patient-specific boundary conditions at the inlets and outlets, which makes the accuracy of these work very critical. Since numerical approaches are being utilised to help clinicians to make their decision on repairing and diagnosing the AAA, it is very important to verify whether or not the inlet and outlet boundary conditions in a simulation significantly influence the reliability of the numerical solutions. In the present work, simulating blood flow within AAA will be addressing the difference in flow patterns using two sets of boundary conditions. The first set is using pressure-velocity waveforms in the main arteries extracted from 23 patients using a velocity probe[126]. The second set is using a mass flow rate wave[127] extracted from 39 patients using MRI scanning to characterise flow patterns at the ascending and descending aorta. At the same time, the outlet surface is prescribed as a 3-element Windkessel model[121], representing the downstream resistance of blood flow.

The main goal of this work is to investigate the impact of the inlet and outlet boundary conditions on three key hemodynamic parameters (Time-average wall shear stress, oscillatory shear index, and relative residence time) as well as the maximum wall stress distributions of abdominal aortic aneurysm.

7.2 Methodology

7.2.1 Construction of AAA geometries

Representative idealised abdominal aortic aneurysm geometry was created, as reported in detail in Chapter Six, see **Figure *6.1***. The thickness of AAA was assumed to have a uniform thickness of 0.002 m, which was generated by expanding the outer surface of the fluid part outwards. The inlet and outlet surfaces were extruded by (10*D) [228, 229] for two fundamental reasons: the first one is to let the velocity profile reaches the fully developed flow profile before entering the aneurysm region [230], and the second one is to get rid of any non-physical behaviour such as backflow near the outlet surface and to ensure that the flow within the AAA does not interfere with the reversed flow at the outlet boundary[229].

Highly detailed patient-specific models of AAA were extracted from CT images using Mimics v.18 [43] to obtain precise geometries based on the findings on the previous chapters(Three and Six). Four patients with age above 55 years were chosen because of the high quality of images details. The construction process has segmentation structures that comprise the global thresholding technique, dynamic region growing, and manual or semiautomatic editing for masks, see Chapter Three for further information.

7.2.2 Hemodynamic metrics of AAA

The following hemodynamic metrics: time-averaged wall shear stress (TAWSS), oscillatory shear index (OSI), and relative residence time (RRT) [223, 232] were used to study the effects of inlet and outlet boundary conditions. The reason behind defining multiple hemodynamic parameters, and not just one, is to characterise the blood flow depending on different physiological and anatomical structures of AAA [233]. Moreover, a single hemodynamic indicator may not be able to capture the multi-directionality of the blood flow [234].

7.2.3 FSI simulation

Blood was modelled in STAR CCM+ v.13.04 [45] with similar approximations used in Chapter Six. In brief, Newtonian, incompressible fluid with a density and dynamic viscosity equal to 1035 kg/m^3 and 0.0035 Pa.s respectively were assigned to the blood domain. Furthermore, implicit, laminar, and unsteady segregate solvers were employed. Dynamic time-step was used and was adjusted depending on the fluid velocity, Courant Number (CFL), and Cell-size, as mentioned in Dynamic step in Chapter Six. The required CFL number in this work is ≈ 1, with the equivalent under-relaxation factors = 0.5[238].

The AAA wall is characterised as a hyper-elastic, incompressible, and isotropic material [83, 240] within Abaqus 2016 [44] using the same constitutive model of strain energy described in Chapter Four, see equation **(4.1)**. The intraluminal thrombus (ILT) was assumed to behave as linear elastic material with Young's modulus of 0.11 MPa and Poisson's ratio of 0.45[108, 164].

7.2.4 Inlet and outlet boundary conditions

The FSI simulations were run for 3 cardiac cycles to reach a stable simulation, and the results were extracted from the third cycle. In this study, two different sets of boundary conditions were applied for the purpose of comparison and validation as follow:

1. A mass flow rate wave[127] was applied at the inlet surface of each AAAs, reported previously in **Figure *6.3* (a)**. At the same time, a 3- Elements Windkessel model has the following parameters: proximal, distal resistance and capacitance (Rp, Rd, and C) respectively, representing the downstream impedance [121](**Figure *6.3* (b)**) was coupled to the AAAs outlets via a java macro[243, 244]. The values of Windkessel parameters were modified to achieve the in-vivo flow and pressure pulsatile waves in the aorta.

2. Standard boundary conditions adopted from Mills[126]were used at the inlet surface, a pulsatile velocity wave, and at the outlet surface, a pressure pulsatile wave, see **Figure *7.1*.**

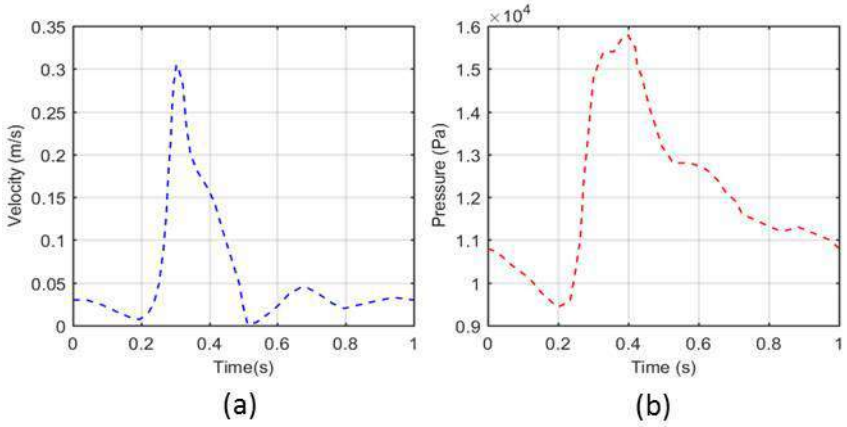

Figure 7.1: Second set of boundary conditions used (a) Inlet velocity wave and (b) outlet pressure wave.**[126]**

7.2.5 Mesh and time-step convergence

A mesh convergence study was conducted similar to the one performed in *Chapter Six*. Four sets of meshes were used for an idealised AAA and Patient 4 (fluid and solid domain) to analyse the wall shear stress/peak wall stress convergence at the systolic flow. The aneurysmal wall of idealised and Patient 4 AAAs was assigned to tetrahedral hybrid elements (**C3D4H**) with a number of elements of **92474** and **705709** for idealised and Patient 4 respectively, while the fluid domains comprised polyhedral cells at the core of the AAA and a number of prism layers at the circumference, Idealised =**175913** elements/ Patient 4 = **363383** elements and **15** prism layers were used in both to capture flow features near the wall.

Concurrently, any changes in mesh configuration in the solution zone required to adjust the time-step that is compatible with the mesh size to obtain a stable and accurate solution. Therefore, the dynamic time step model was selected to control the desired local convective Courant number of 1 in the fluid domain at each time step and at each element, which will be explained in details later. In this work, the area of interest (AAA) should have an averaged convective courant number of one to consider the solution is time accurate. In other words, per time step, the fluid is approximately convected one element length. **Figure *7.2*** below illustrates the desired dynamic time steps that correspond to the number of elements in Patient 4 for ***TWO* sets** of boundary conditions.

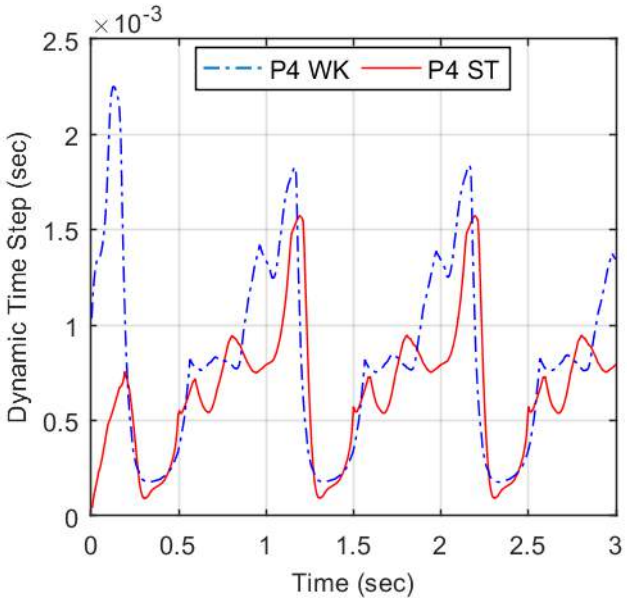

Figure 7.2: Comparison of dynamic time steps used in P4 WK (Patient 4 Mass flow/Windkessel) and P4 ST (Patient 4 Standard) boundary conditions.

7.3 Results

In the following section, results of laminar flow fluid-structure interaction (FSI) in idealised and patient-specific AAA models are presented. Since two sets of boundary conditions were used, comprehensive comparisons of time-averaged velocity, hemodynamic metrics distribution, and their profiles, as well as stress patterns, have been conducted.

7.3.1 Idealised AAA: comparison of time-averaged velocity (Mass flow/Windkessel (Mass/WK) vs. Standard velocity/pressure (ST (V/P))) boundary conditions

Comparison of time-averaged velocity patterns between Mass flow rate/ Windkessel and Standard velocity /pressure boundary conditions, in a sagittal plane in the vertical position of an idealised AAA, is presented in **Figure *7.3***. Inconsistent distributions of the time-averaged velocity are observed to vary gradually from a relatively high value (0.09 m/s) at the centre of the neck (upstream) to a small value of (0.03 m/s) at or near the wall due to the effect of the blood viscosity in both the Mass/WK and Standard velocity/pressure boundary conditions. After blood departing the neck, a jet of blood flow (red area) of a magnitude of 0.1 m/s is shown passing from the neck (upstream) towards the core of the AAA in both boundary conditions sets. However, the area of the jet flow in the Standard B.Cs is observed to be greater than the jet flow area in Mass/Wk. The comparison also shows that the intensity of time-averaged velocity decreased significantly in the anterior region of the AAA of a

magnitude of nearly zero m/s owing to recirculation zones induced from the increase in the cross-sectional area of the AAA and due to the variation of systole and diastole time period in both sets of boundary conditions. Small recirculation zones in the time-averaged velocity at the back of AAA are observed in both B.Cs sets because the radial distance of the AAA in the posterior from the centre line is small compared to the radial distance in the anterior. It can also be observed that the blood flow starts getting rid of low-velocity zones (blue areas) to the relatively high magnitude and inconsistent zonesdue to changing from wide/non-uniform cross-sectional areas to cylindrical uniform cross-sectional areas, in Mass/Wk and Standard boundary conditions.

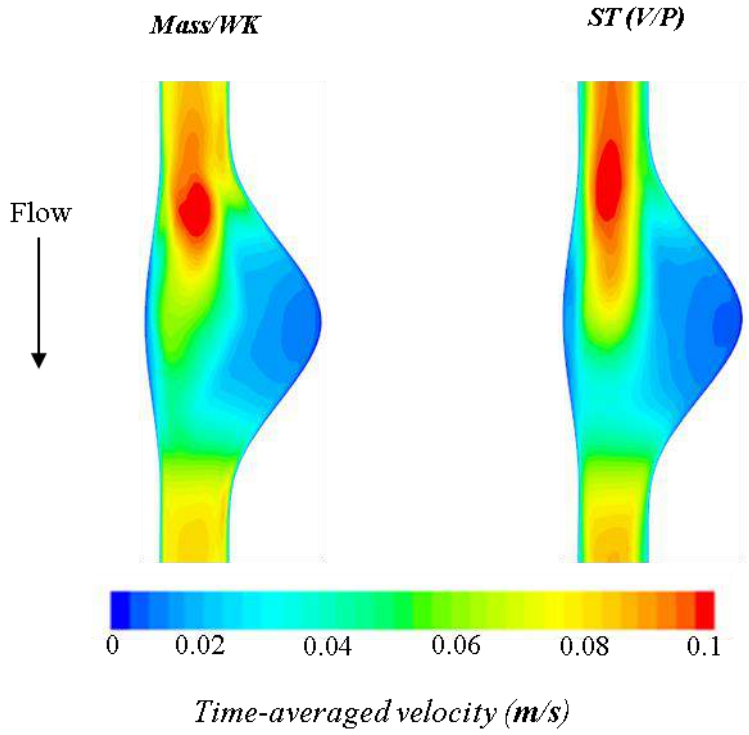

Figure 7.3: Comparison of time-averaged velocity in a vertical sagittal plane of idealised AAA: **(mass flow/Windkessel** against **Standard velocity/pressure relationship boundary conditions).**

7.3.2 Idealised AAA: comparison of hemodynamic parameters: Mass/WK vs. ST (V/P)

Figure *7.4* demonstrates a comparison of TAWSS, OSI, and RRT contours obtained from Mass/Windkessel and standard velocity/pressure boundary conditions for an idealised AAA. For further analysis, trends of TAWSS, OSI, and RRT profiles were extracted along a sagittal-plane in the front position and plotted against the length of the flow axis, see **Figure *7.5*.** The shaded grey area between the dashed-dot blue/Mass/WK and dashed-black/Standard boundary conditions curves correspond to the variations in the profiles.

For mass/WK conditions in **Figure *7.4***, large areas of high TAWSS value (red areas) of 0.3 Pa can be observed in the proximal and distal necks of AAA and part of the proximal curvature compared to TAWSS distribution of Standard B.Cs. Slight deviations in the low TAWSS distributions between both B.Cs sets are observed at the AAA zone. In **Figure *7.5***, the differences between the TAWSS profiles (Mass/WK vs. ST (V/P)) can be easily seen at the proximal/distal and at the AAA zone represented by the grey area.

In terms of the comparison of OSI distributions, both Mass/WK and Standard B.Cs AAAs show a high OSI of almost 0.5 at the inflection regions in the front-distal zone and the back of the AAA with slight variations, see **Figure *7.4***. Furthermore, the slight differences (a grey area) between OSI patterns can be observed by plotting the OSI profile for each set of boundary conditions see **Figure *7.5***.

Figure *7.4* also provides a comparison of coloured RRT distribution in AAA for the two sets of boundary conditions. Red coloured regions of 75 (1/Pa) imply that the fluid particles reside a long time in these regions before departure out of the AAA due to the enlargement in the cross-section area from the neck to AAA. In contrast, the blue colour zero (1/Pa) refers that the fluid particles leave that region quickly. Insignificant variations can be observed in the RRT distributions and profiles between the two sets of boundary conditions, see **Figure *7.4*** and **Figure *7.5***. TAWSS, OSI, and RRT profiles in **Figure *7.5*** are observed to follow the same trend with relatively inconsistent variation between both sets of boundary conditions.

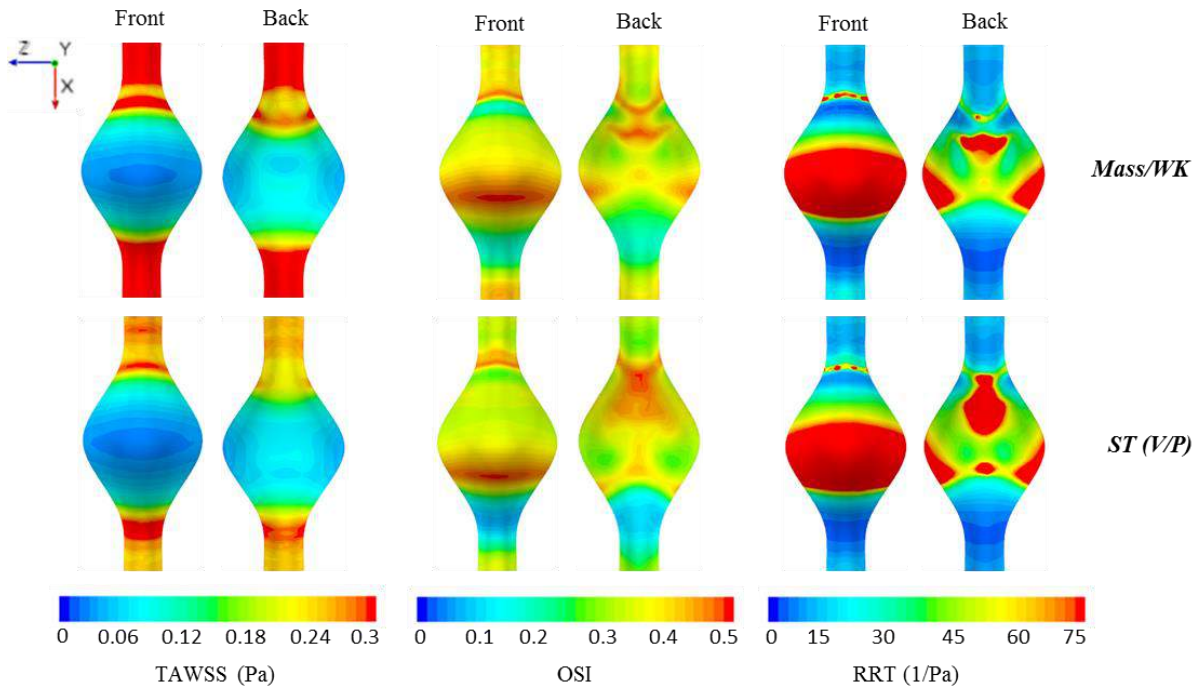

Figure 7.4: Comparison of hemodynamic parameters in idealised AAA: (**mass flow/Windkessel** against **Standard velocity/pressure** boundary conditions).

Further quantitative comparison between hemodynamic profiles is carried out for both boundary conditions, where the Mass/WK B.Cs is proposed to be the reference. At the left of **Figure *7.5***, it can be seen that the TAWSS values start fluctuating and varying at the proximal neck with a value of (0.26 and 0.38 Pa) in Standard and Mass/WK boundary conditions, respectively with 31.5 % difference. Then followed by a considerable increase over 0.4 Pa in Mass/WK boundary conditions. The TAWSS profiles in both sets of boundary conditions experience a drop to meet at a TAWSS value of 0.25 Pa, followed by a small peak between 0.3-0.35 Pa in Standard and Mass/WK, respectively, with 14.2% difference. At that point, blood particles enter the AAA region in which TAWSS encounters a sharp reduction to the lowest value of nearly zero at the mid-length of the AAAs in both sets of boundary conditions. Then, TAWSS gradually rises from the lowest value to another ultimate value between just above 0.3 in Standard conditions and over 0.5 Pa in the Mass/WK conditions (40 % variance). Once the fluid particles leave the AAA to the distal neck, which the TAWSS reaches a stable fluctuating value between 0.25-0.35 Pa in Standard and Mass/WK conditions, respectively (28.5% variance).

Profiles of OSI are also compared between the two sets of boundary conditions in the middle of **Figure *7.5***. Three peaks of OSI are observed in **Figure *7.5***; the main two peaks of

OSI correspond to 0.05 m and over 0.1 m positions that have same value and locations of OSI of just below 0.5 in both sets of boundary conditions. The third peak of OSI also occurs at the same position of 0.17 m in both boundary conditions with slight differences in the OSI values of 0.38 and 0.43 (11.6 % difference) in Standard and Mass/WK boundary conditions, respectively. The peaks of OSI in both boundary conditions correspond to the accumulative effect of the recirculation area and its intensity at the proximal neck pre-entering the AAA zone, middle of the AAA region, and the distal, see **Figure *7.3***.

Finally, a comparison of RRT trends for the two sets of boundary conditions is observed in the right hand of **Figure *7.5***. The first peak of the RRT occurs at 0.05 m position with a different range between 100 to 200 (1/Pa) (1% difference) in the Mass/WK and Standard B.Cs, which means the fluid particles need relatively low time to leave the zone due to less effect of the recirculation at this position. At just over the middle of the AAA, a sharp increase in RRT value varies from 1700 1/Pa in Standard boundary conditions profile to 1200 1/Pa in the Mass/WK boundary conditions profile is observed with (29.4 % difference). Then, both RRT profiles are shown to follow very low RRT when the blood enters the distal neck.

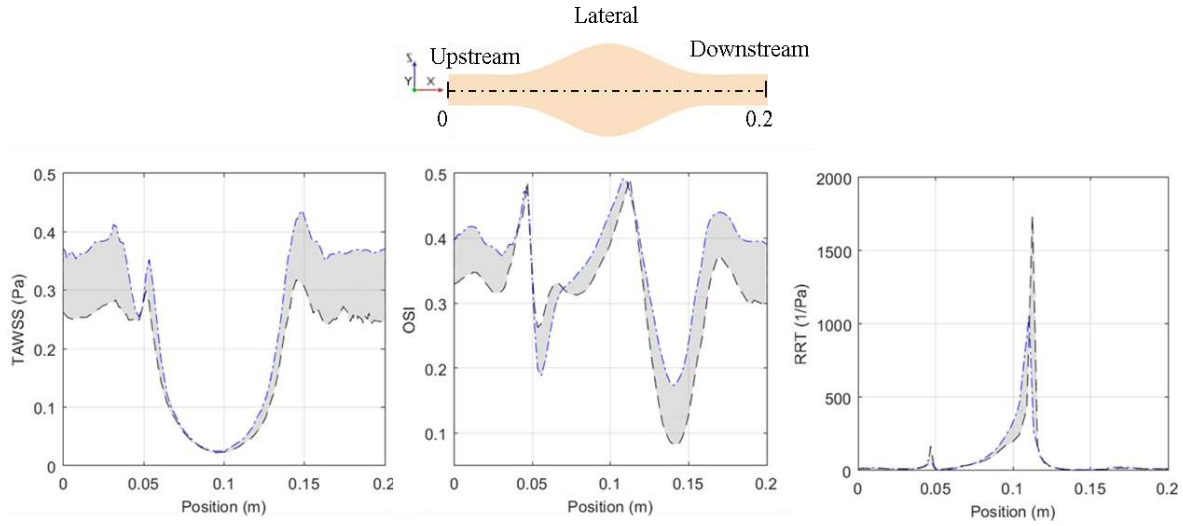

Figure 7.5: Comparison of hemodynamic profiles in a sagittal plane in the front of idealised AAA: mass flow/Windkessel (dashed-dot blue curves) against Standard velocity/pressure B.Cs (dashed black curves).

7.3.3 Idealised AAA: comparison of Stress patterns (mass flow/Windkessel **[Mass/WK] vs.** Standard velocity/pressure B.Cs **[ST (V/P)])**

The influence of using different boundary conditions on the maximum wall stress distribution is studied and presented for half geometry due to symmetric along the axial axis, see **Figure *7.6***. The dashed solid arrow refers to the original (un-deformed) AAA, while the solid black arrow indicates the deformed geometry. From **Figure *7.6***, it can be observed that the maximum wall stress of 0.5 MPa occurs at both laterals and inflection points (proximal and distal) for both sets of boundary conditions with noticeable differences in the distribution. The stress distributions in the upstream and downstream neck regions are observed to have insignificant variations in both sets of boundary conditions.

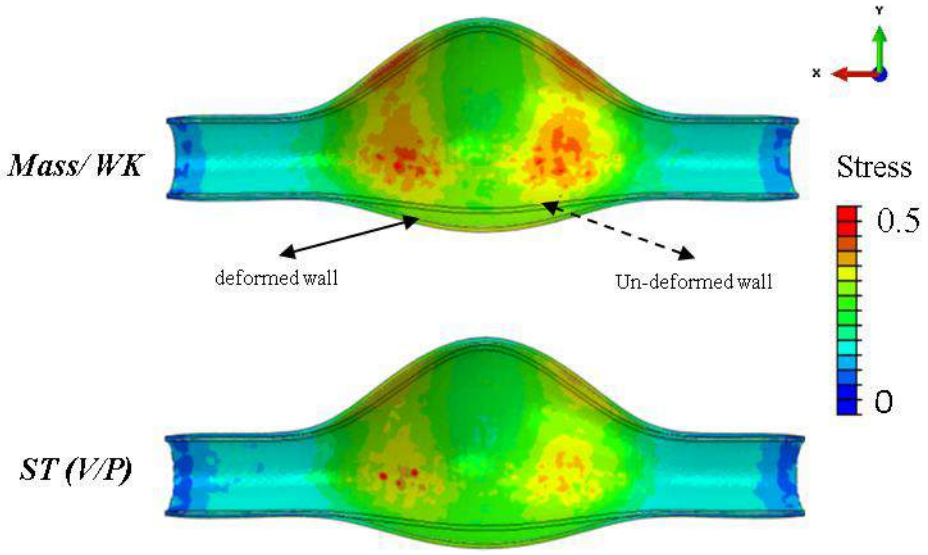

Figure 7.6: Comparison of maximum wall stress in idealised AAA: (mass flow/Windkessel against Standard velocity/pressure boundary conditions).

7.3.4 Patient-specific AAA models: comparison of the time-averaged velocity of mass flow/Windkessel against Standard velocity/pressure boundary conditions (Mass/WK vs. ST (V/P)

A sagittal plane along the AAA region was created to demonstrate and compare the patterns of time-averaged velocity within the AAA zone between Mass/WK and Standard velocity/pressure boundary conditions in all patients, see **Figure *7.7***. A navigation compass at the left side of the figure shows the orientation of the sagittal plane, where the *left side* of the sagittal plane refers to the *front view*, *right* refers to *back view* and *upstream/ downstream* refers to the *proximal* and *distal* respectively. The time-averaged velocity range varies from

zero to a maximum value of 0.06 m/s. The general overview of **Figure *7.7*** reveals the huge influence of the boundary conditions on the time-averaged velocity patterns. Large areas of the maximum time-averaged velocity of 0.06 m/s are observed in the Standard B.Cs compared to Mass/WK distribution. In Patients 2, 3, 4, and 1, the distributions of high blood jet (Standard B.Cs) are seen to keep adjacent to the back and front of the AAA wall after departing the proximal neck of the AAA. However, blood jet distributions (red zone) in the Mass/WK are observed to be weaker than the Standard B.Cs. In addition, Mass/WK time-averaged velocity experiences low-velocity zones in the middle of the AAA, more specifically in Patients 2 and 3 compared to Standard B.Cs.

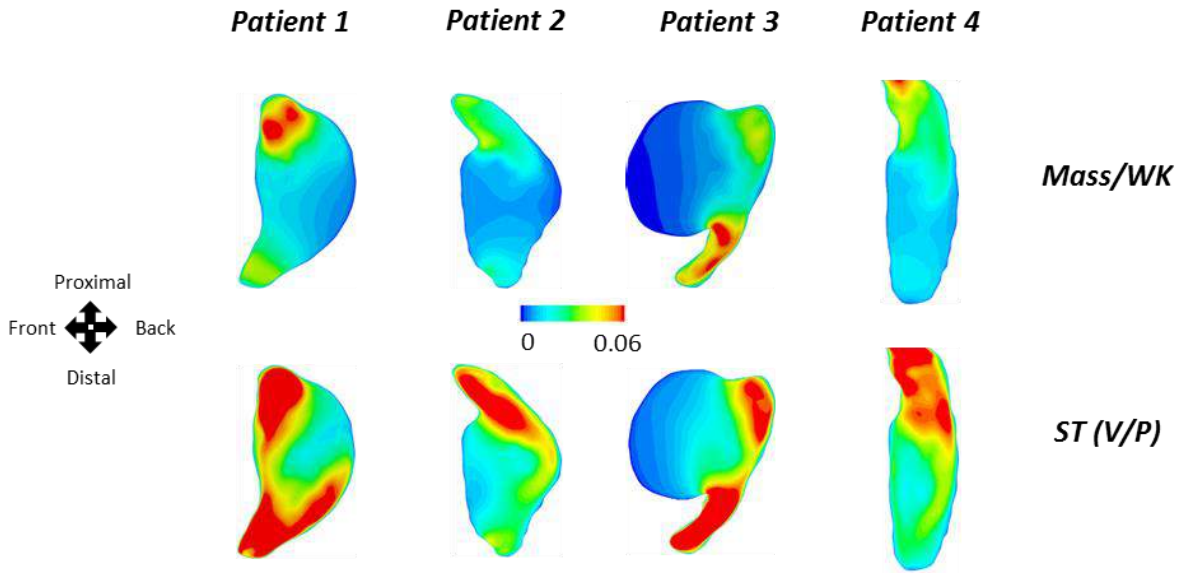

Figure 7.7: Comparison of time-averaged velocity in a vertical sagittal plane in all patients: (mass flow/Windkessel against Standard velocity/pressure relationship boundary conditions).

7.3.5 Patient-specific AAA models: comparison of hemodynamic parameters mass flow/Windkessel against Standard velocity/pressure boundary conditions (Mass/WK vs. ST (V/P)

Comparison of hemodynamic metrics contours and profiles between Mass/WK and standard B.Cs are illustrated in **Figure *7.8*** and **Figure *7.9***. TAWSS distributions can be presented in all patients on the left hand of **Figure *7.8*,** where areas of high TAWSS of up to 1 Pa can be observed in the common iliac branches due to high wall shear stress. On the other hand, AAA zones are always observed subjected to relatively low TAWSS of zero Pa or slightly above. The dissimilarities in TAWSS patterns are clearly observed between

Mass/WK and standard B.Cs. In all Patients, large regions of low TAWSS in Mass/WK AAAs are observed compared to the standard B.Cs AAAs.

Let's turn the attention to the OSI parameter, which identifies the total oscillation (change) in the wall shear stress vector during the cardiac cycle. The scale of OSI has two main values: low OSI of 0 means the wall shear stress is uniform due to uniform velocity patterns. In contrast, a high value of OSI means the wall shear stress changes the direction due to high recirculation flow, see **Figure *7.8*** in the mid column. Overall, noticeable variations in OSI distribution between Mass/WK and Standard B.Cs are apparent, see **Figure *7.8***. Generally, it is observed from **Figure *7.8*** that high OSI values mostly happen in the bulge area due to the flow disturbance induced from changing in the AAA cross-section areas and variation time period of systole and diastole in both boundary conditions sets. Mass/WK AAAs are observed to produce higher OSI (red zones) of 0.4 in all patients compared to the Standard B.Cs; see Patient 3 in **Figure *7.8*** for instance. In addition, comparing high and low locations in the OSI patterns in the Mass/WK AAAs does not deem to identically matching the OSI of Standard B.Cs. For example, Mass/WK of Patient1encounters low OSI value of zero at the left centre side of AAA while standard AAA shows low OSI at the backside from the centre towards the bifurcation area. Likewise, evident differences in high OSI distribution is observed in Mass/WK and standard AAAs of Patient1; in which high OSI of 0.4 is noticed at the back proximal curvature/ middle front of the Standard B.Cs AAA. However, the Mass/WK B.Cs part shows high OSI at the right side propagating to the front of the AAA.

Figure *7.8* left-hand column illustrates and compares the distribution of the RRT parameter between Mass/WK and standard B.Cs parts. Red areas of RRT=50 1/Pa mean that blood particles spend a long time in these zones due to the recirculation in the flow. Most of the high RRT areas happen in the AAA domain only. On the other hand, blue areas of low RRT of zero magnitudes indicate that the blood particles are rapidly leaving that part because no disturbance happens in the flow at these zones. Again, parts of Mass/WK B.Cs are observed to produce high RRT zones compared to Standard B.Cs parts, which produce a significant deviation in the RRT patterns.

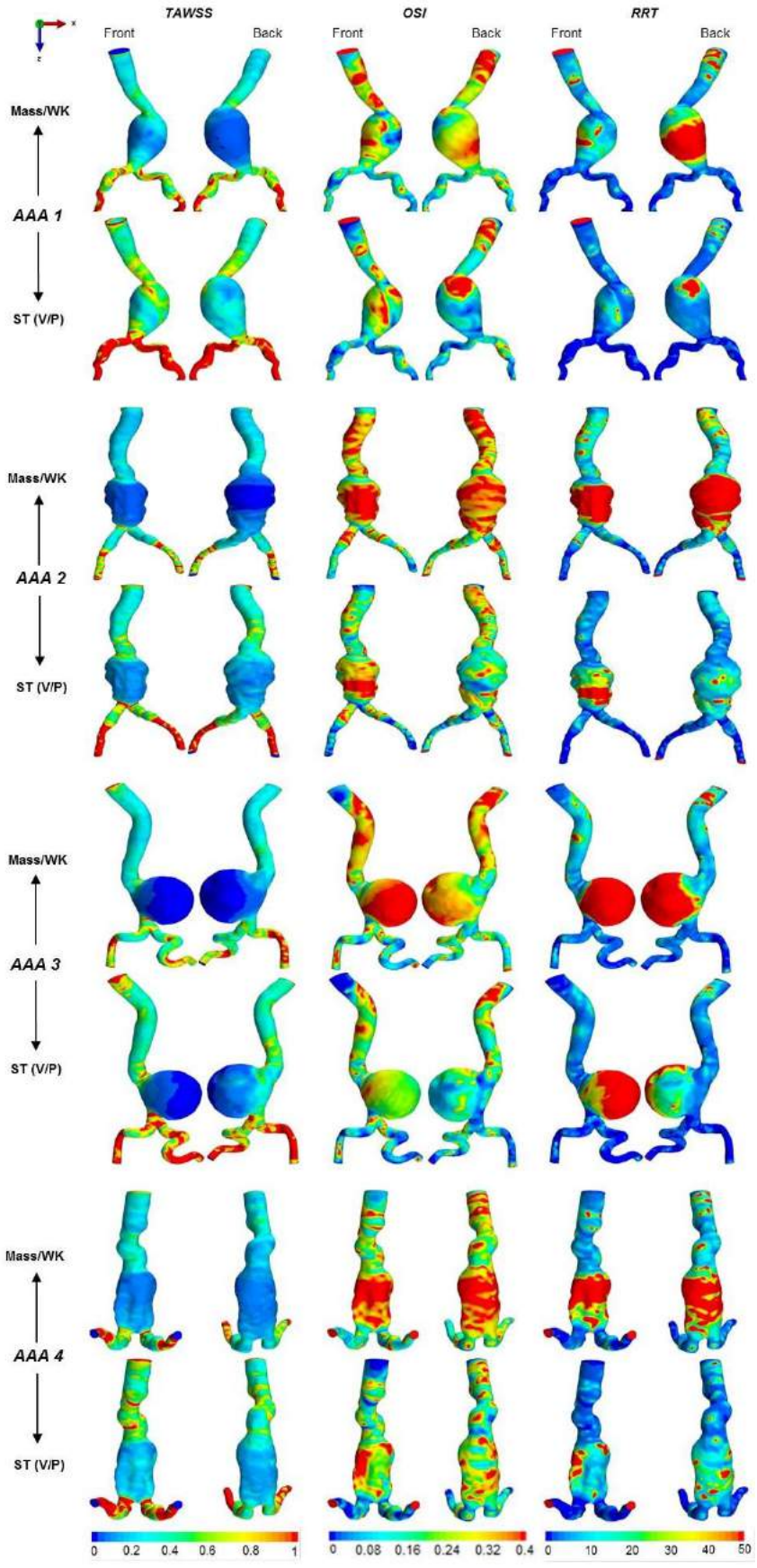

Figure 7.8: Comparison of hemodynamic parameters in all patients: (mass flow/Windkessel against Standard velocity/pressure relationship boundary conditions).

The differences in the hemodynamic profiles due to using two sets of boundary conditions can be further examined and compared by extracting the trends of TAWSS, OSI, and RRT metrics along a sagittal-plane in the front view, see **Figure *7.9***. The black dashed and blue dashed-dotted curves refer to hemodynamic profiles of Standard and Mass/WK B.Cs, respectively. Overall, values and trends of the hemodynamic metrics profiles are mostly observed to vary significantly, relying on the used set of boundary conditions. Insignificant differences are observed in the TAWSS trends between Standard and Mass/WK B.Cs in Patients 2 and 3 are noticed. At the same time, noticeable variations (a grey area) in the TAWSS profiles and the maximum TAWSS magnitudes can be seen in Patient 1 and 4, see **Figure *7.9***.

Figure *7.9* also provides a comparison of OSI profiles between Mass/WK and standard B.Cs AAAs. In general, OSI trends fluctuating up and down and are correlated with the intensity of recirculation regions in the AAA zone during the cardiac cycle. The lowest OSI value of below 0.1 is observed in the neck and bifurcation regions; however, the complexity and intensity of OSI escalate extremely in the AAA region to reach the highest value of 0.5 in both sets of boundary conditions. Noticeable dis-similarities between the OSI patterns of Mass/WK and Standard B.Cs AAAs can be observed in Patient1, see the grey area in **Figure *7.9***. The Mass/WK AAAs are observed to experience high oscillation compared to the Standard AAAs. The comparison of OSI profiles between Mass/WK and ST boundary conditions in Patient 2 is observed to repeatedly fluctuate with a slight deviation marked in grey colour, see **Figure *7.9***. Most interestingly, OSI trends of Patient 3 follow the same style, but with a significant deviation between the two profiles. Lastly, OSI patterns in Patient 4 are observed to show significant variations in terms of fluctuation and value between Mass/WK and Standard parts.

Finally, a comparison of RRT patterns between the two sets of B.Cs in **Figure *7.9*** shows a wavy distribution, specifically in the region of the AAA zone. Significant differences marked in the grey colour are observed in all Patients. Values and locations of the RRT peaks vary corresponding to the deviations in the TAWSS and OSI profiles. In Patinet1, the RRT profile of Mass/WK boundary conditions jumps rapidly to reach the maximum value of 117 (1/Pa) at just over the mid-length of the sagittal plane, while RRT values of Standard B.Cs are observed to be below 20 (1/Pa) with (82.9 % difference).

Comparison of RRT trends in Patient 2 in **Figure *7.9*** is observed to grow to the ultimate RRT value of 395 (1/Pa) Standard and 785 (1/Pa) Mass/WK boundary conditions of (49.6 % difference) with a considerable alteration in the position of 0.55 Standard and 0.45 Mass/WK. Patient 3 trends RRT are shown significant deviation (a grey area) in the ultimate value and distribution style between the two sets of boundary conditions, see in **Figure *7.9***. RRT trend of Mass/WK is observed to increase sharply from the zero (1/Pa) at the entrance to the highest value of at around 1250 (1/Pa), while Standard RRT profile encounters slight growth from zero to 100 (1/Pa) and keep almost the same value along the sagittal-plane to the end. In Patient4 **Figure *7.9***, RRT patterns, values and locations are clearly influenced by the type of the boundary conditions. Noticeable deviations are observed in the maximum value of RRT (Standard 25 (1/Pa) and Mass/WK 430 (1/Pa)) with (94.1% variance).

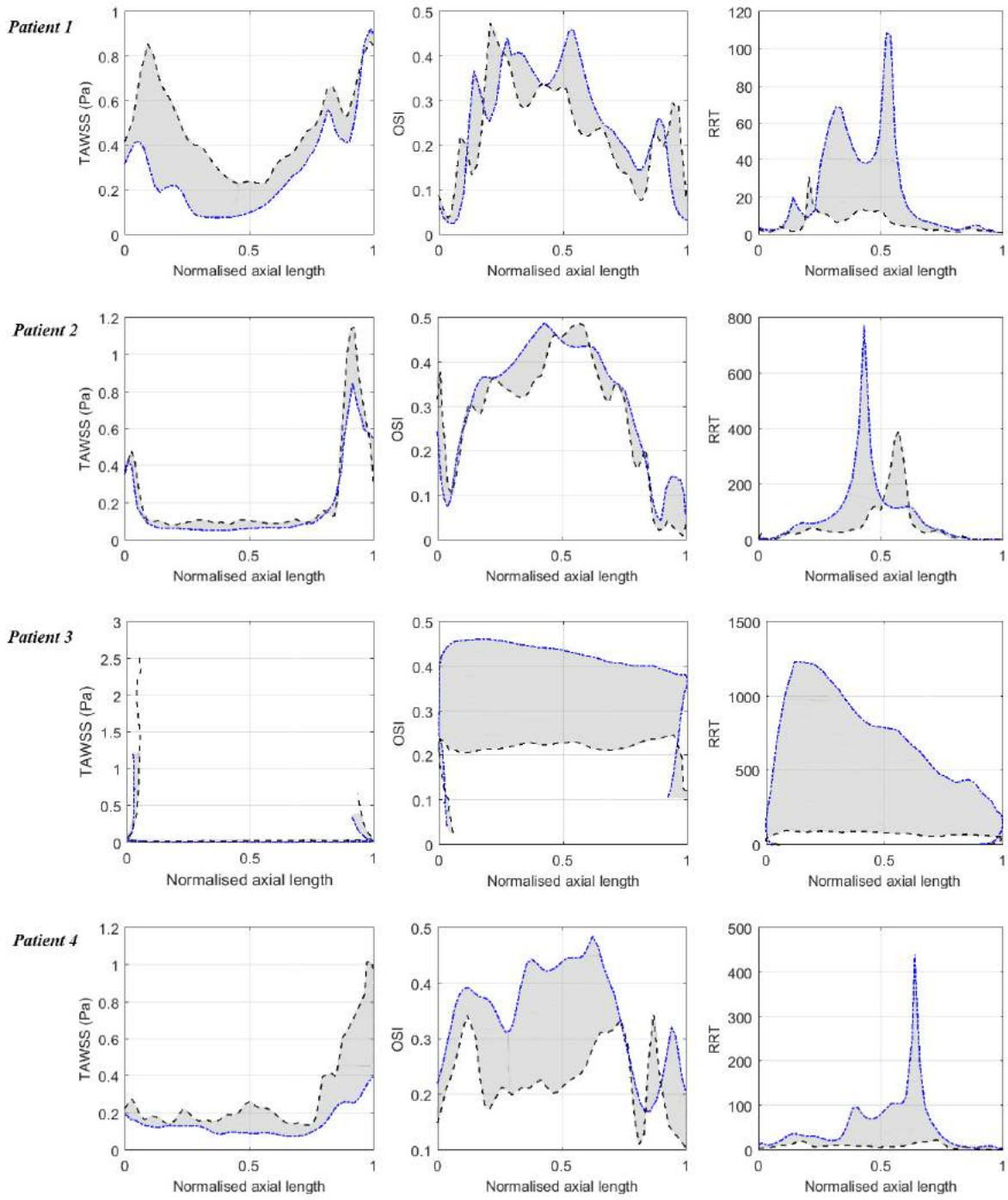

Figure 7.9: Comparison of hemodynamic parameters profiles along the sagittal plane explained in figure 7.5: mass flow/Windkessel (dashed-dotted blue curves) against Standard velocity/pressure relationship (dashed black curves).

7.3.6 Patient-specific AAA models: comparison of Stress and displacement patterns (Mass/WK vs. ST (V/P)

The influence of using two different boundary conditions on the maximum wall stress and displacement distribution is compared at peak systolic pressure in **Figure *7.10*.**

In general, high value and large areas of maximum wall stress/displacement are observed in Mass/WK boundary conditions compared to Standard B.Cs. However, sites of maximum wall stress and displacement are identified fairly similar. In **Figure *7.10*,** the maximum wall stress magnitude varies among the patients of 0.28, 0.28, 0.3, and 0.25 MPa in Patients 1, 2, 3, and 4, respectively. Significant variation in wall stress distribution of Patient1 in **Figure *7.10*** is observed, where the ST (V/P) AAA produces less wall stress magnitude compared to the WK B.Cs. In contrast, the location is almost identical in the front view at the distal curvature in both sets. Similarly, Patients 2, 3, and 4 produce wider areas of high stress in the Mass/WK boundary conditions compared to the ST (V/P) boundary conditions. Noticeable differences in the high wall stress distribution, especially at the back of Patient 4 and front of Patient 3, are observed.

The patterns of maximum wall stress in Patient1 and 3 are observed not to have zero stress magnitude because of the absence of the intraluminal thrombus. Moreover, shear forces induced by the recirculation of blood flow act directly on the aneurysmal wall. On the other hand, the presence of the intraluminal thrombus is observed to affect the stress patterns (zero value) in the whole perimeter of Patient 2 and the front of Patient 4 with a visible difference between Mass/WK and Standard B.Cs, see **Figure *7.10***.

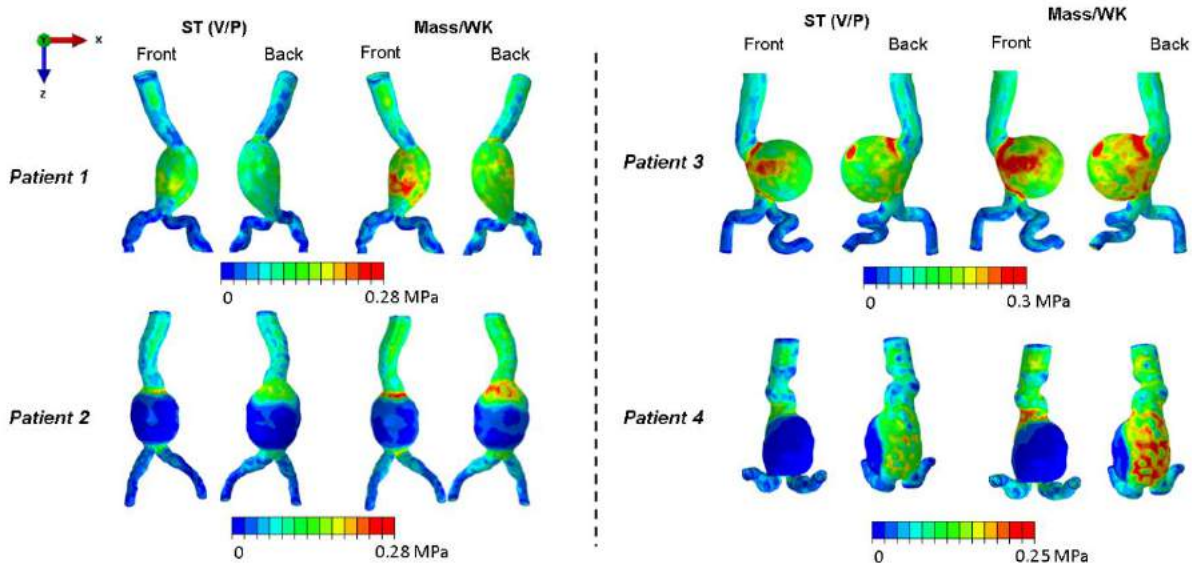

Figure 7.10: Comparison of maximum wall stress in all patients: (mass flow/Windkessel against Standard velocity/pressure relationship boundary conditions).

7.4 Discussion

The current work studied the differences introduced into the hemodynamic metrics and rupture indicators such as maximum wall stress in AAA as a result of selecting different inlet/outlet boundary conditions.

Standard velocity-pressure waves and mass flow rate/3-element Windkessel model boundary conditions were described at the inlets and outlets of AAAs and the resulting time-averaged velocity, time-averaged wall shear stress TAWSS, oscillatory shear index OSI, relative residence time RRT and maximum wall stress patterns were compared to examine the influence of using a different configuration of boundary conditions. Other parameters, such as the source of AAA geometries, segmentation, mechanical properties of wall/thrombus, and blood properties, were identical in all patients. In terms of time-averaged velocity, see **Figure *7.3***, both boundary conditions sets show noticeable variation in the general trends of secondary flow and jet flow in the idealised AAAs. Despite the duration of systole and systole were different in both sets of boundary conditions, slight deviations in the distribution and trends of hemodynamic metrics between standard (V/P) and Mass/WK boundary conditions were observed in idealised AAA. TAWSS profiles in idealised AAA revealed a noticeable gap (shaded area) between Mass/WK and Standard profiles at the upstream and downstream neck due to unchanging in the wall shear stress vectors, see **Figure *7.5***. However, insignificant variation in the TAWSS profiles at the AAA zone with slight shifting in the location due to changing in the time-averaged velocity profiles was observed in both

sets of boundary conditions. OSI profiles in idealised AAA were slightly affected by the boundary conditions, in which both sets of boundary conditions produced sufficiently large averaged OSI magnitude of (0.4) which is a key factor in interpreting the formation of thrombus[256]. RRT trends and distribution of idealised AAA revealed that blood particles in the Standard B.Cs spent a long time (RRT=1700 (1/Pa)) in the AAA domain compared to Mass/WK (1200 (1/Pa)) boundary conditions. The justification for higher RRT is due to producing higher recirculation region in the Standard B.Cs AAA, unlike the Mass/WK that shows lower recirculation because of the differences in the length of diastole and systole phase.

For patient-specific AAAs, comparison of time-averaged velocity between both B.Cs was observed in different deviations compared to the idealised AAA. Considerable differences were observed in the computed time-averaged velocity distributions between Standard and Mass/WK boundary conditions in terms of the maximum magnitude and the complexity of flow patterns, see **Figure *7.7***. Almost zero velocity zones at the sagittal-plane in all AAAs were observed in both sets of B.Cs in variant places; however, they are not identical. The jet flow of a high time-averaged velocity of 0.06 (m/s) was observed to be stronger and adjacent to the AAA wall in the Standard B.Cs opposite to the Mass/WK. The changes in the time-averaged patterns are attributed to the differences in the inlet and outlet trends (systole and diastole phase length) of the velocity and pressure see **Figure *6.3*** and **Figure *7.1*.**

Similarly, the effects of using these two B.Cs sets were observed on the hemodynamic and on the maximum wall stress distributions in all AAAs, see **Figure *7.8***, **Figure *7.9*,** and **Figure *7.10***. The comparison of the measured TAWSS, OSI, and RRT from both sets of boundary conditions revealed the effects of differences in the recirculation regions that reflected substantially on the distributions and trends of the hemodynamic metrics. The OSI contours and trends show that Mass/WK AAAs encountered higher oscillation values and areas due to changing in the wall shear stress vector during the cardiac cycle compared to the Standard B.Cs trends. Moreover, the comparisons of maximum oscillation locations in Mass/WK and Standard AAAs were not in corresponding, which alters the location of the thrombus formation[256]. The RRT parameter was higher in Mass/WK AAAs compared to Standard AAAs due to producing large recirculation areas in Mass/WK AAAs, as shown in time-averaged velocity distribution in **Figure *7.7***. For example, the difference between the high RRT values of Mass/WK and standard (V/P) in Patient 1 [117/30 (1/Pa)], Patient 2

[785/395 (1/Pa)], Patient 3 [1250/100 (1/Pa)] and Patient 4 [430/25 (1/Pa)]. The differences between RRT trends at the sagittal plane were presented by the grey shaded area.

The resultant maximum wall stress of range from 0.25-0.3 MPa in all patients was influenced by the changing of the flow patterns, **Figure *7.7*,** and **Figure *7.10***. Areas of red colour representing the maximum wall stress were clearly observed in variant places in the Mass/WK AAAs, while they can be barely recognised in the Standard (V/P) AAAs. The generation of the higher value of maximum wall stresses again back to the intensity of the frictional forces acting on the aortic wall induced by the low-velocity zones. Interestingly, the presence of thrombus decreases the level of wall stress incredibly to a value of almost/or zero, which in good agreement with the literature[257], see Patients 2 and 4 in **Figure *7.10*.**

This study has few limitations, such as using the Newtonian fluid model, assuming laminar flow, constant aortic wall thickness, and assigning linear material properties to the thrombus. Despite blood is non-Newtonian fluid, it is assumed to behave as a Newtonian fluid in big blood vessels who their diameter larger than 0.5 mm, as well as the viscosity is treated relatively constant in the large vessels because of high shear rates[125]. The flow at the inlet was classified as laminar based on the ***RE*** number and the diameter of the neck at the proximal, which was ≤ 2100. In terms of imposing a constant wall thickness returns to the fact that the aortic wall thickness is difficult to be captured from CT images. Intra-luminal thrombus is assumed to reduce the wall stress [209, 247] regardless of the constitutive model used to represent the mechanical properties of the thrombus.

7.5 Conclusion

Based on the findings of the current work, it can be concluded that using different configurations of inlet and outlet boundary conditions in idealised AAA were observed not to significantly influence the hemodynamic metrics. However, significant variations in the flow patterns within the Patient-Specific AAA were noticed. The hemodynamic metrics distributions, trends, values and maximum wall stress trends in the Patient-Specific AAA models were affected by the applied boundary conditions. Thus, the resultant variations in the predicted biomechanics of AAA due to using different boundary conditions should be taken into consideration. Ignoring such effects may lead to life-threating decisions for the AAA patients in case of repairing, especially when the AAA need for urgent repair but the indicators of rupture do not reveal the risk of rupture. Therefore, it is highly recommended to obtain and use patient-specific boundary conditions in conducting numerical simulations of

AAA in order to reduce the potential error induced by using non-patient-specific B.Cs on predicting the biomechanical factors of AAA.

8 Chapter Eight: Investigating the effect of surrounding organs on the AAA wall stress patterns: a pilot study

8.1 Introduction

Stress analysis (FEA) can be conducted to predict the maximum wall stress in the AAA wall, which can be considered as a good threshold to predict potential rupture than the maximum transverse diameter of AAA [84, 85]. FEA analysis requires the construction of patient-specific geometry of the AAA wall derived from computed-tomography images (CT), as well as appropriate boundary conditions and material properties. CT data with high-resolution has proven to provide a highly detailed model of any internal organs, for instance, AAA, including the intra-luminal thrombus (ILT) and lumen [160, 161]. The previous FEA works on AAA have limitations such as most of them ignored the influence of thrombus, and almost none of them included the effect of the internal organs on the stress distribution of AAA. Commonly, thrombus can be found in most AAAs that have a huge volume [265, 266]; and its role was studied in terms of thickness and growth rate and its major impact on the potential risk of rupture [56, 163]. On the other hand, Józsa and Paál [129] studied the impact of the spine on the flow patterns of AAA, in which they reached to a conclusion that the spine does not significantly influence the flow inside the AAA. In addition, Farsad et al.[131] conducted an FEA analysis to study the interaction between the spine and the AAA. It was found that the spine has a significant role in the growth rate and remodelling of AAA. However, the impact of Spine and soft organs (Intestine and Colon) all together on the AAA wall stress distribution has not been addressed yet. The question arises here; do the internal organs change the stress distribution of AAA significantly? This will be subject of investigation of this chapter, and the outcome would potentially improve the predictions of AAA maximum wall stress.

The aim of this pilot work was to investigate if the AAA model without including the surrounding organs predicts a higher potential of rupture (maximum wall stress). In addition, a comparison was carried out, showing the impact of the surrounding organs on the location and value of wall stress.

8.2 Methodology

A patient with AAA was selected in order to demonstrate the effects of involving the surrounding organs on the stress patterns and its value using FEA analysis. The patient had

undergone CT for the planning of AAA repair at University Hospital South Manchester and was identified via the radiology department records. The patient gave informed consent, and ethical approval was granted by the National Research Ethics Committee (13/NW/0468).

8.2.1 3D Reconstruction and geometry preparation

CT images for AAA patients were imported into Mimics v.18[43] research software to construct a 3D model of AAA, Spine, Intestine, and Colon. The construction process of an AAA alongside the internal organs starts with using a global thresholding technique, dynamic region growing, and manual or semiautomatic editing for masks. The first step to build an organ is producing initial 3d masks of the desired organ by assigning a suitable global threshold to capture the region of the organ on the CT images. Threshold values can be carefully set by using Mimics v.18 [43] predefined threshold values, which can be adjusted manually to capture the boundaries of the organ. However, in some cases, for instance, the threshold intensity of the AAA could be similar to the adjacent organs such as the spine which can be problematic. Hence; further manual intervention by the user was needed to split the spine out of the AAA.

In order to carry out the separation between the spine and AAA masks, morphology operations tools such as eroding, dilation, etc. were employed. Firstly, erode operation was applied to remove any pixels connecting the AAA mask and any unwanted adjacent organs. At that point, a "region growing" tool was used to create a new separated AAA mask without the spine and vice versa. After doing the separation of AAA and Spine masks, it is necessary here to compensate the pixels that have been removed by the user. Therefore, dilation operation was set to compensate for a similar number of pixels that were removed by the eroding process for all masks. The final AAA, Spine, Intestine, and Colon masks were recreated to rebuild the original boundaries of the organs as well as to fill the gaps automatically to obtain precise and homogeneous masks that match the boundary of each organ. Now, the masks of each organ, including AAA are ready to calculate a 3D model of the aorta and the surrounding organs where the final shape of the created 3D model is shown in **Figure *8.1***.

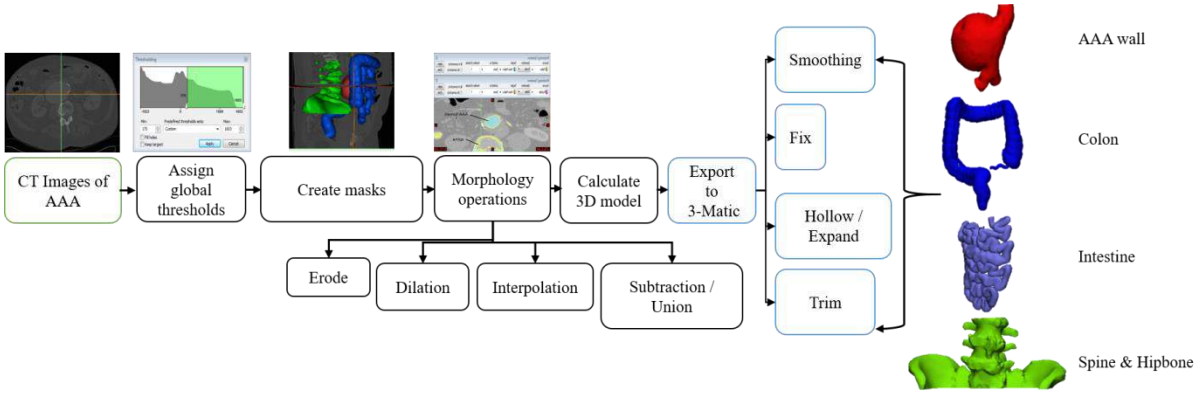

Figure 8.1: Steps used to construct the 3d computational models of the internal organs: AAA wall, Colon, Spine and Intestine

The STL files were then imported into 3-Matic, version 10 (Materialise, Belgium), which is able to combine CAD tools with pre-processing (meshing) capabilities. Any obvious unimportant points in all 3D geometries of the AAA and the surrounding organs were smoothed using the 'local smoothing' tool. In order to create the aneurysmal wall, the outer surface of blood geometry was expanded inwards by 2 mm using the 'hollow' operation. This is owing to the fact that the CT scans capture the outer boundaries of the AAA wall. A final operation had to be conducted to trim the inlet and outlets of AAA at the bifurcations to obtain a smooth plane surface. The proposed wall thickness of 2 mm was taken from the literature as no imaging modality has yet been proven to be able to accurately measure AAA wall thickness[42]. Moreover, no presence of thrombus within the AAA comprised in this study was observed. **Figure *8.2*** illustrates the differences in the geometrical configurations between the supported and non-supported AAA.

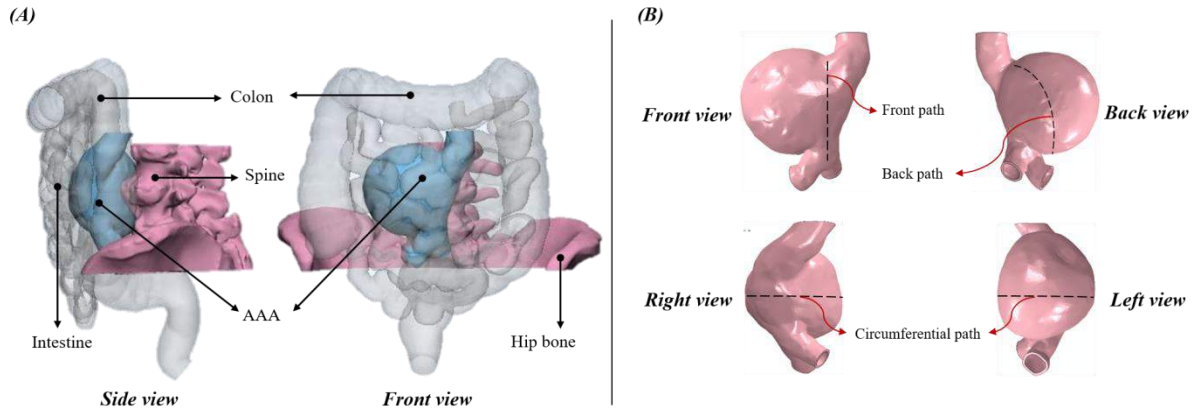

Figure 8.2: illustrates (A) AAA geometry, including the surrounding organs Colon, Intestine, and Spine; (B) AAA geometry without surrounding organs.

8.2.2 Boundary conditions

Similar assumptions of AAA wall (nonlinear, homogenous, isotropic, hyperplastic, and incompressible) that used in Chapter Four were used in this chapter. AAA wall was pressurised applying a static uniform blood pressure of (120 mmHg) [150]. These properties have been used in a number of previous studies [25, 73, 85, 118, 166]. The bone of the spine was modelled for just the cortical layer with Young's modulus of 18 GPa, Poisson's ratio of 0.2 and a density of 2000 Kg/m^3 [267, 268]. The mechanical properties of intestine and colon were extracted under compression load adopted from the literature [269], see **Figure *8.3***.

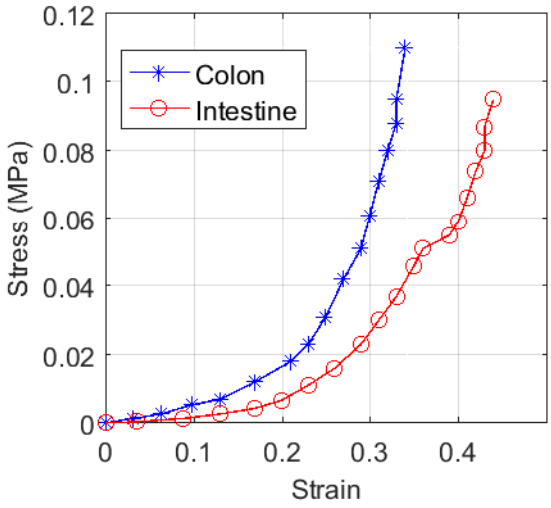

Figure 8.3: Material properties of the Colon and intestine used in this study.

The AAA wall and Spine were constrained in the proximal and distal locations to simulate the fixation of the aorta at the renal arteries and aortic bifurcation, as well as upper and down the spine. On the other hand, both intestine and colon were constrained at the connection points near the stomach and the end of the rectum, respectively. The internal organs interact with each other throughout contact points at their surfaces; these interaction points were detected by the user from the CT scan during the segmentation process. Then, a general contact surface was used to simulate the interaction between the nearby organs and AAA, in which the outer surfaces of the Intestine, Spine, and Colon is represented as master surfaces. In contrast, AAA outer surface is represented as a slave surface. Moreover, the interaction properties between the surface and surface were assumed to be frictionless [129].

8.2.3 Mesh generation

Once the parts of the AAA, Intestine, Colon, and Spine were cleaned and fixed, they were imported into Abaqus 2016 [44] for stress analysis. However, these STL parts must be converted into finite element models by assigning suitable mesh for all geometries. Thus, 'Mesh to Geometry' plug-in within Abaqus 2016 was used to convert the STL models into native Abaqus parts in order to mesh them utilising mesh module and reducing the pre-processing time. A mesh refinement procedure was conducted for AAA without supporting the surrounding organs to create a hybrid tetrahedral (C3D4H) volume mesh on the AAA part, as well as, to determine the optimal number of elements by doubling the seeds point at each mesh to increase the number of elements. The maximum wall stress values at a certain element were calculated and examined by increasing the number of elements incrementally; in order to obtain a suitable mesh size, see **Table *8.1***. The second mesh was chosen as stress values did not grow by more than 3.5% compared to the third mesh.

Table 8.1: Details of the mesh refinement study conducted on AAA without the presence of the surrounding organs.

Non-supported AAA geometry	
Number of elements	**Max wall stress values (MPa)**
96382	0.733
187203	1.435
257503	1.491

8.3 Results

Three paths at the front, back, and circumferential of the AAA wall with/without surrounding organs were created, in order to measure stress profiles for comparison, as shown by the dashed lines in **Figure *8.2* (B).** In addition, to easily present the differences in the wall stress patterns in the AAA pair, contours of maximum principal stress were extracted and compared. The FEA simulation and post-processing were performed in Abaqus 2016 [44] to produce detailed stress distributions on the AAA wall. In this study, maximum principal stress was considered first for comparison, similar to other research in the literature [167-171].

8.3.1 Wall stress analysis

Stress distribution in the AAA wall is considered to play a vital role as a potential rupture index, especially maximum wall stress value and location, as mentioned in the literature [24, 84, 150]. The most challenging limitation that faced almost all previous studies of AAA stress analysis is the absence of surrounding organs and ignoring their impact on the stress distribution of the AAA wall. Therefore, this work addressed the impact of involving these organs on the AAA wall stress for a single patient. **Figure *8.4*** exhibits a comparison of wall stress patterns between AAA supported and non-supported by surrounding organs. Areas of red colour are observed in various locations indicating locations of high wall stress whilst the blue regions in the wall represent locations of the lowest wall stress. The values of maximum wall stress were found as follows: 1.435 MPa and 0.94 MPa in AAA without and with the presence of surrounding organs, respectively. For better comparison, the stress ranges of both AAAs contours were unified to the maximum value of 0.3 MPa. Initially, it was observed that the location of maximum wall stress in both models witnesses slight shifting at the distal curvature in front view almost near the bifurcation area. Furthermore, differences in stress distributions, especially at the back of AAA, are quite evident due to the surrounding organs in the stress analysis. AAA model, in the case of the surrounding organ's absence, shows a high number of red patches (0.3 MPa) at different locations in addition to the area of peak wall stress. In contrast, the AAA model with support of surrounding organs encounters few red patches, which can be observed in the front and back of the AAA. The impact of the spine on the stress is clearly apparent by decreasing the stress to almost zero, particularly at the contact area, see **Figure *8.4*** back view. Likewise, the intestine and colon reduce and affect the stress distribution on the AAA wall notably, see **Figure *8.4*** front view.

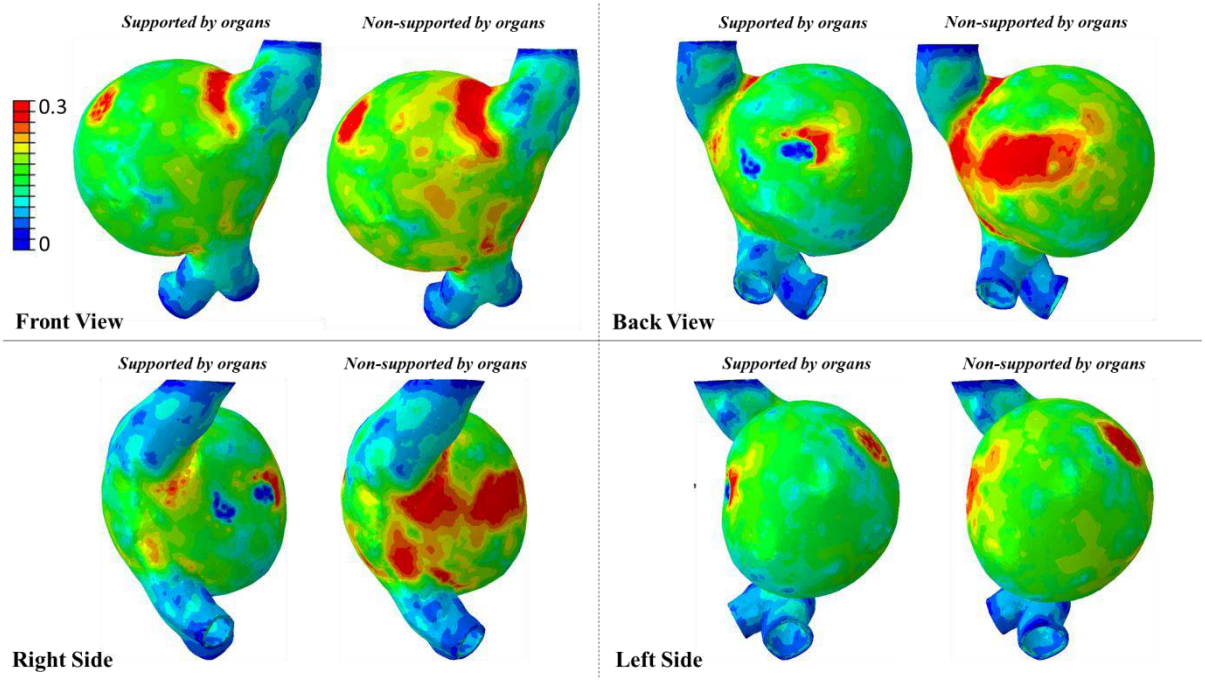

Figure 8.4: Front, right, left, and back view of wall stress distribution of AAA supported and non-supported by surrounding organs.

8.3.2 Comparison of wall stress trends

Although the difference in wall stress patterns due to surrounding organs is evident from the coloured contours plots, the profiles of wall stress are extracted from three different planes to investigate the impact of the organs further. **Figure *8.5*** presents a comparison of stress profiles obtained from the front plane that was previously created on the AAA, see **Figure *8.2***(B). In general, the comparison of stress profiles approximately follows the same trend in both AAA models with notable differences. The effect of Intestine and Colon on the stresses can be illustrated by the gap between the two trends where the values of stress decreased significantly owing to the presence of surrounding organs. Values of stress at four locations (0.2, 0.4, 0.6, and 0.8) along the front path were compared between AAA supported and non-supported, see **Table *8.2***. The deviation between the stresses of supported and non-supported varies from 26% to 30%, depending on the location of the stress specified at the path.

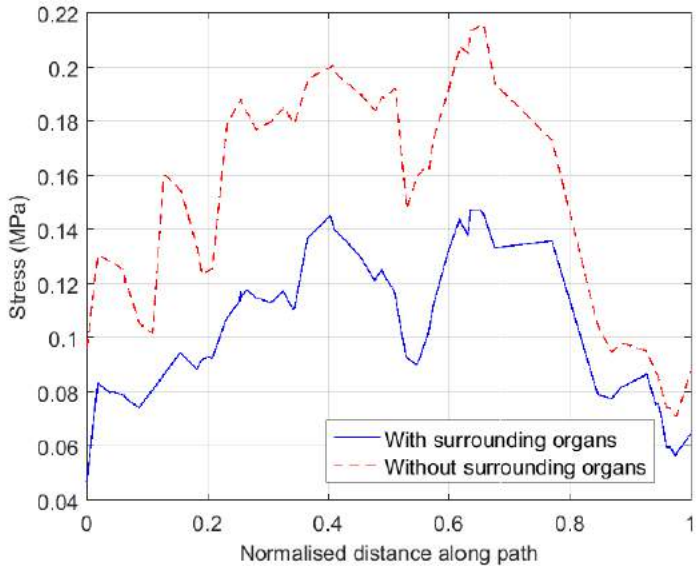

Figure 8.5: Comparison of wall stress profiles in AAA extracted from **front-path** that corresponds to the Intestine, Colon.

Table 8.2: A quantitative comparison between the stress of AAA supported and non-supported obtained at four instances at the **front path**.

Location at the path	Stress in AAA supported (MPa)	Stress in AAA Non-supported (MPa)	Percentage of deviation
0.2	0.092	0.125	26%
0.4	0.145	0.2	28%
0.6	0.134	0.19	30%
0.8	0.114	0.145	27%

Figure *8.6* shows a comparison of stress profiles obtained from a path created on the AAA at a position opposite to the Spine see **Figure *8.2***. The purpose of this comparison is to reveal the direct impact of the Spine on the stress distribution at the back of the AAA wall. The plots of stress distribution show a significant decrease in the stress value and trends for the supported AAA compared to non-supported. It can be observed a dramatic fall of stress value to almost zero, between 0.2 and 0.5 on the path length, in the AAA supported in which the spine is trying to obstruct the growth of the AAA wall due to the internal pressure, see **Figure *8.2*** and **Figure *8.4***. Moreover, the gap between the two profiles symbolizes the role of the Spine on the wall stress. A quantitative comparison of stress values in AAA supported and non-supported at four locations (0.2, 0.4, 0.6, and 0.8) along the back path were

examined, see **Table *8.3***. The deviation between the stresses of supported and non-supported varies from 28% to 96%, depending on the location of the stress specified at the path.

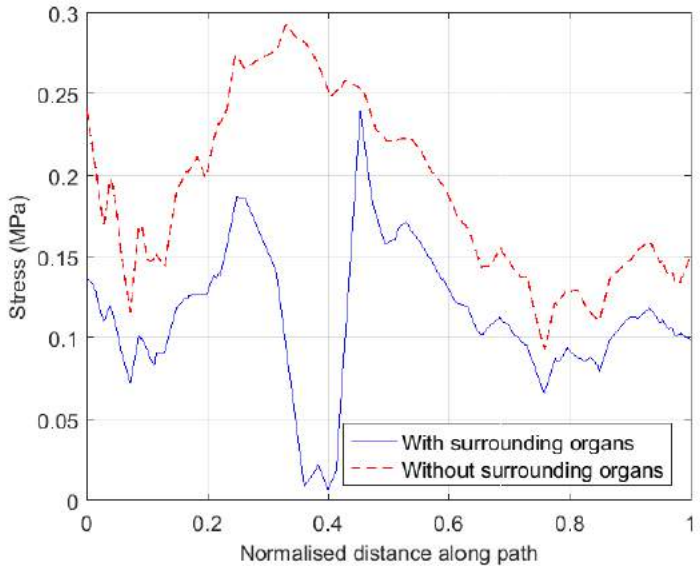

Figure 8.6: Comparison of wall stress profiles in AAA extracted from **back-path** that corresponds to the Spine.

Table 8.3: A quantitative comparison between the stress of AAA supported and non-supported obtained at four instances at **the back path**.

Location at the path	Stress in AAA supported (MPa)	Stress in AAA Non-supported (MPa)	Percentage of deviation
0.2	0.13	0.2	35%
0.4	0.009	0.25	96%
0.6	0.13	0.19	32%
0.8	0.09	0.125	28%

The effect of the combination of all organs on the stress profiles was studied by measuring the stress along a circumferential path at the mid of both AAAs, see **Figure *8.7***. As expected, the support induced by the Spine on the AAA wall stress evolution is evident, especially in the location between 0.1 and 0.3 on the circumferential path, where the stress dramatically dropped to negative values (compression) of just below -0.05 MPa. However, the stress of non-supported AAA at the same location reveals the high value of almost 0.3 MPa. Then, the stress of the supported AAA wall rapidly grows to a maximum value of up to 0.35 MPa at almost 0.3 at the path. After this point, the trends of supported and non-

supported stress profiles are, to some extent, similar with notable deviation in terms of the values. It also can be observed that the deviation in stress values and trends resulting from including Intestine and Colon are quite different from those arising from the Spine. Similarly, in order to show the variation in stress values due to the presence of all organs, a quantitative analysis was carried out to compare the values of stresses at four different locations (0.2, 0.4, 0.6, and 0.8) in the circumferential path, see **Table *8.4***. The deviation between the stresses of supported and non- supported varies from 17% to 72% depending on the location of the stress specified at the path, as shown by the dashed lines in **Figure *8.2*** (B).

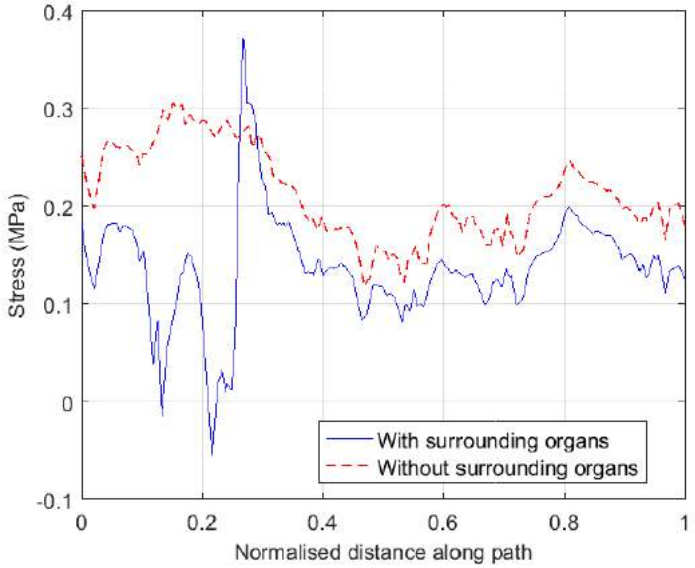

Figure 8.7: Comparison of wall stress profiles in AAA extracted from **circumferential mid-path** that corresponds to the Spine, Intestine, and Colon.

Table 8.4: A quantitative comparison between the stress of AAA supported and non-supported obtained at four instances at the **circumferential path**.

Location at the path	Stress in AAA supported (MPa)	Stress in AAA Non-supported (MPa)	Percentage of deviation
0.2	0.08	0.29	72%
0.4	0.12	0.19	37%
0.6	0.14	0.2	30%
0.8	0.2	0.24	17%

8.4 Discussion

The present work provides a comprehensive comparison of the stress distribution of AAA finite element models in the presence and absence of surrounding organs. 3D model construction of AAA wall, intestine, colon, and spine in addition to the stress analysis were implemented using Mimics v.18 [43] and Abaqus 2016 [44]. The encouraging finding of the variations in wall stress profiles showed the key role of the surrounding organs on the stress value and distribution.

The coloured contours of the stress of the AAA model without the internal organs show the higher value of wall stress, and the maximum stress locations also alter (red area). The results can be compared to those in AAA with the presence of the surrounding organs see **Figure *8.4***. The significant differences in stress distributions can be attributed to the support of the internal organs to the AAA wall, in which all organs provide constraint to AAA. Moreover, the reduction in the stress value would be significant at some location due to the support from relatively rigid organs such as the spine. Whereas the intestine and colon are soft tissue compared to the spine, however, they still affect the stress patterns that can be clearly seen in the front and back view in **Figure *8.4***. In addition, it was found in the literature that both sides and front of the AAA wall have more potential of rupture than the back due to the support of the spine which is in agreement with the finding of this work regarding the role of the spine[130]. Despite the differences in the AAA stress patterns, the region of high wall stress in both AAA models occurs in the external surface of the AAA wall, which signifies the maximum wall stress region mostly occurring adjacent to the inflection point of the wall surface curvature[77]. Generally, the predicted wall stress locations obtained from both AAA models were observed to be unrelated to the maximum diameter of the AAA, which is in agreement with many previous studies [73, 170, 183-185].

Although major differences in wall stress distribution are so apparent, a quantitative analysis was conducted to observe the deviations in the local stresses between the supported and the non-supported AAA. Stress profiles of supported and non-supported AAA were plotted in three positions front, back, and circumferential in order to examine the decrease in the local stress relying on the internal organs that correspond to each location. From **Figure *8.5***, it was noticed that a consistent deviation with noticeable differences between the stress profiles of AAA with organs and without organs owing to the presence of the intestine and colon. The local stresses were compared at the following locations 0.2, 0.4, 0.6, and 0.8 on the front path. The range of the deviation in the stress values varied from 26% to 30%, depending on the corresponding location. As mentioned earlier, fairly consistent variation was observed

and returned back to the soft tissue that adapted and re-formed with the growth of the AAA wall. While **Figure *8.6*** showed a comparison of stress profiles at the back path, which illustrated the significant role of the spine on the wall stress profiles and values.

Similarly, local stresses at four locations on the back path were compared to examine the deviation in wall stress. Interestingly, the deviation between the supported and non-supported local stresses was significant, as it was observed that the limit of deviation at the back path varied from 28% to 96 %. Finally, the combined effects of the spine, intestine, and colon were compared at the AAA wall by plotting the stress patterns at the circumferential path, see **Figure *8.7***. It was observed that the deviation between wall stress profiles of AAA supported and non-supported was highly dependent on the nature of the organs opposite to the AAA wall. For example, the fairly consistent deviation in the stress profiles was due to the presence of the soft organs (intestine and colon). On the other hand, the sharp drop and changes in the stress profiles are attributed to the spine. Therefore, it is important to consider the effect of the internal organs in assessing the risk of AAA rupture.

This study has some limitations, such as ignoring the influence of the ligaments and muscles that support the AAA with organs. Also, the applied internal pressure on the AAA wall was assumed constant with a uniform distribution based on the literature [183]. In terms of wall thickness, it was considered constant (2 mm); however, the AAA wall thickness is known to vary in different regions of AAAs and between patients [187]. Furthermore, the effects of flow forces were also ignored because this analysis did not comprise the blood in the computation of wall stress.

8.5 Conclusion

In summary, this study presented qualitative and quantitative results on the stress of the AAA wall in the presence and absence of the surrounding organs. When the surrounding internal organs were excluded from the simulation, it was observed high AAA wall stress value and large areas of the AAA encountered high stress. In contrast, including the surrounding organs in the computation of stress analysis of AAA significantly decreased the wall stress value and altered the stress distribution, especially in the area opposite to the spine. The stress in the front and sides of AAA also showed a reduction in magnitude and changes in its profiles. However, the reduction was comparatively less in the back region. The current results are preliminary due to comprising a single patient, analysing more AAA geometries are required to quantify the effect of the presence of the internal organs on the rupture risk assessment.

However, the preliminary analyses presented here demonstrate the importance of including the internal organs in the numerical simulation of AAA.

9 Chapter Nine: Conclusions and Future Research

The main objectives of this thesis were to study the suitability of using AAA models derived from 3D-US images instead of CT models that have the risk of ionising radiation and also to propose a new rupture indicator in order to overcome the overestimation in the predicted stress obtained from 3D-ultrasound models. Furthermore, this thesis also demonstrates the capability of fracture mechanics based finite element method, XFEM, to assess the rupture risk of AAA.

The effect of minor geometrical variations in the AAA computational models arising from different segmentation process on the predictions of the hemodynamic metrics of AAA was investigated. In addition, the effect of using various boundary conditions in the simulation was examined. The results provide a useful perspective in improving the accuracy of numerical rupture evaluation.

The role of the surrounding organs on the distribution of AAA wall stress was also investigated. The results show the significant effect of the presence of the surrounding organs on the wall stress patterns, which can have a significant impact on the potential rupture assessment of AAA.

This chapter provides the main conclusions based on the findings of the current thesis, followed by a few ideas for future research.

9.1 Conclusions

9.1.1 Suitability of using computational AAA models derived from 3D-ultrasound images

A comparative FEA analysis of computational models obtained from CT and 3D-US was conducted to examine the effect of imaging methods on the peak values and distribution of AAA wall stress/strain. The results showed that wall stress/strain distributions are largely independent of the imaging methods. In contrast, the peak values are different for the two imaging methods as the peak stress/strain values are highly influenced by small changes in the geometrical features. Therefore, two new parameters: weighted mean wall stress and characteristic wall stress are proposed in this study, which has been observed to be independent of small unavoidable geometric differences. Therefore, the prediction of rupture of abdominal aortic aneurysm (AAA) can be reliably obtained by evaluating the characteristic wall stress rather than the peak wall stress.

9.1.2 XFEM numerical model to predict the rupture initiation/propagation in AAA

XFEM, being based on the principles of fracture mechanics, has been shown to be suitable for the assessment of rupture potential in the abdominal aortic aneurysm. A good agreement of rupture predictions between the XFEM method and the experimental work in the abdominal aortic aneurysm was observed. The outcome of this method provides detailed information about the rupture such as stress distribution on the aneurysmal wall, length of rupture, site of rupture and potential of blood leakage, unlike the conventional FEA method that only indicate the possible rupture sites to be formed at the sites of peak stress. The XFEM approach, on the other hand, highlights the initiation and propagation of rupture, and the initiation may not always occur at positions the maximum wall stress.

In terms of using 3D-US images instead of CT in rupture analysis, it is found that the 3D-US models of AAA have the capability to predict the rupture site. Hence, 3D-US can be used for periodic rupture assessment analysis during the monitoring process of AAA patients due to minimal radiation risk and relative ease of affordability. The approach presented here can be developed as a diagnostic tool for surgeons that may help them to determine if the AAAs require surgical interventions.

9.1.3 Effects of geometrical differences due to segmentation process on the hemodynamics of AAA

This work highlighted deviations in the hemodynamic metrics distributions, maximum wall stress, and deformation patterns in AAAs induced by the minor geometrical variations due to the construction process using ImFusion suite and Mimics v.18 software. It was found that the segmentation process in Mimics v.18 can capture even the small details in the AAA to produce high-quality AAA geometry, in contrast to the ImFusion suite that fails to capture minor details of the AAA that negatively influence the blood flow patterns. It was observed that variations of ±10% of the idealised AAA default dimensions profoundly affected the velocity streamline especially in the AAA +10% model compared to the AAA default and AAA -10%, where dynamic recirculation and flow separation were increased and generated with the increase of the AAA dimensions by 10% and vice versa. The values and patterns of hemodynamic metrics in AAA +10% show lower TAWSS, higher OSI, and RRT compared to the AAA default and AAA -10%. Moreover, it is observed that making minor modifications to the idealised AAA dimensions will significantly increase or decrease the value and area of peak wall stress and deformation.

In terms of the patient-specific AAA models, Mimics AAAs are observed to produce a large number of dynamic vortices compared to the ImFusion AAAs. These changes in the flow patterns are noticeably reflected on the hemodynamic metrics and wall stress and deformation distribution, where lowest TAWSS, higher OSI, and RRT are observed in Mimics AAA parts rather than ImFusion AAA models. Moreover, maximum wall stress and deformation in Mimics AAAs are of higher magnitudes, wider in areas and occur in different locations, in contrary to ImFusion. These variations in the hemodynamic metrics and wall stress/displacement patterns, values, and locations in the AAA should be addressed thoroughly, which may mislead the understanding of the rupture potential, thrombus formation, and AAA growth mechanism.

9.1.4 Effects of the inlet and outlet boundary conditions

Using different configurations of inlet and outlet boundary conditions in idealised AAA were observed not to significantly influence the hemodynamic metrics. However, significant variations in the flow patterns within the patient-specific AAA were noticed. The hemodynamic metrics distributions, trends, values, and maximum wall stress trends in the patient-specific AAA models were affected by the applied boundary conditions. Thus, the resultant variations in the predicted biomechanics of AAA due to using different boundary conditions should be taken into consideration. Ignoring such effects may lead to incorrect decisions being made for the AAA patients in the threshold of repairing. Therefore, it is highly recommended to obtain and use patient-specific boundary conditions in conducting numerical simulations of AAA.

9.1.5 The effect of surrounding organs on the AAA wall stress patterns

Qualitative and quantitative results were conducted on the stress of the AAA wall in the presence and absence of the surrounding organs. When the surrounding internal organs were excluded from the simulation, it was observed high AAA wall stress value and large areas of the AAA encountered high stress. In contrast, including the surrounding organs in the computation of stress analysis of AAA significantly decreased the wall stress value and altered the stress distribution, especially in the area opposite to the spine. The stress in the front and sides of AAA also showed a reduction in magnitude and changes in its profiles. However, the reduction was comparatively less in the back region. The current results are preliminary in their nature due to comprising of a single patient, more cases of AAA geometries are needed to be analysed to quantify the effect of the presence of the internal organs on the rupture risk assessment. However, the preliminary analyses presented here

demonstrate the importance of including the internal organs in the numerical simulation of AAA.

In summary, the current work would be useful to practitioners if attention paid when 3D-US models are used in the analysis of rupture by using 95% characteristic stress instead of maximum stress to overcome the overestimation of stress values produced in the 3D-US models of AAA. Scanning schedules should be arranged at least every 2-3 months, depending on the progression of the AAA. CT scanning also is highly recommended if the AAA has a rapid growth rate to compare the stresses trends between 3D-US and CT models. In addition, hemodynamic parameters (TAWSS, OSI, and RRT) are sensitive to boundary conditions in the models, therefore, extracting instantaneous velocity and pressure waves for each patient at the same time of undertaking scanning is crucial to reduce the likelihood of rupture and to take the right decision. Choosing carefully of image segmentation software such as Mimics is very important in evaluating the risk of rupture as it showed chapter Three. The use of a good scanner to produce high definition images of AAA is required because of higher accuracy in the obtained AAA geometry.

9.2 Future work

Based on the findings from the research presented in this thesis, the following future works are recommended:

- Conducting frequent 3D-US scan for large groups of AAA patients to extract patient-specific images and velocity/pressure waves to improve the stress analysis, which may reach an accurate solution.
- Study the effect of the time gap between scanning periods on the rupture analysis by using the extracted AAA geometries and boundary conditions (velocity /pressure) with various time intervals. Furthermore, conducting error analysis to reduce the likelihood of rupture in AAA.
- Develop a statistical model to track any changes in the trends of stress obtained from 3D-US against those from CT models.
- The whole aorta, including branches, thrombus, and calcifications, were ignored in the stress analysis of AAA. The mechanical properties of the AAA wall vary locally and depend on the longitudinal and circumferential orientation. Thus, involving these parameters in a comprehensive stress analysis (FEA or XFEM) would be more realistic in order to possibly increase the accuracy of predicted wall stress patterns.

- The local variation in the AAA wall thickness is a major limitation in all rupture studies. In addition, capturing patient-Specific boundary conditions (velocity and pressure) at the same time as the imaging process is likely to increase the reliability of the potential rupture results

- Automating the numerical simulations of AAA by developing a code that deals with the following tasks:
  - Importing the AAA geometry into the code.
  - Assign appropriate mesh type and conducting mesh refinement study to satisfy the accuracy of the solution.
  - Assign appropriate material properties for each part in the AAA (wall, thrombus, lumen, and calcification).
  - Defining the interaction surfaces and constraints.
  - Post-processing of the results.
  - Provide different parameters to aid clinical decision making.

  This code would be beneficial for clinicians who may not have the necessary background of stress analysis.

References:

1. Li, Z. and C. Kleinstreuer, *A comparison between different asymmetric abdominal aortic aneurysm morphologies employing computational fluid–structure interaction analysis.* European Journal of Mechanics - B/Fluids, 2007. **26**(5): p. 615-631.
2. Scotti, C.M., et al., *Fluid-structure interaction in abdominal aortic aneurysms: effects of asymmetry and wall thickness.* Biomed Eng Online, 2005. **4**: p. 64-64.
3. Ramirez, F. and M. Lewkowicz, *Albert Einstein and Aortic Aneurysm.* Argentine Journal of Cardiology; Vol 82, No 3 (2014), 2014.
4. Gordon, P.A. and B. Toursarkissian, *Treatment of Abdominal Aortic Aneurysms: The Role of Endovascular Repair.* AORN Journal, 2014. **100**(3): p. 241-259.
5. Truijers, M., et al., *In Vivo Imaging of Abdominal Aortic Aneurysms: Increased FDG Uptake Suggests Inflammation in the Aneurysm Wall.* Journal of Endovascular Therapy, 2008. **15**(4): p. 462-467.
6. Chew, H.F., et al., *Mortality, Morbidity, and Costs of Ruptured and Elective Abdominal Aortic Aneurysm Repairs in Nova Scotia, Canada.* Annals of Vascular Surgery, 2003. **17**(2): p. 171-179.
7. Larsson, E., et al., *Analysis of aortic wall stress and rupture risk in patients with abdominal aortic aneurysm with a gender perspective.* Journal of vascular surgery, 2011. **54**(2): p. 295-299.
8. MacSweeney, S.T.R., et al., *Smoking and growth rate of small abdominal aortic aneurysms.* The Lancet, 1994. **344**(8923): p. 651-652.
9. Brown, L.C. and J.T. Powell, *Risk factors for aneurysm rupture in patients kept under ultrasound surveillance.* Annals of surgery, 1999. **230**(3): p. 289.
10. Crawford, C.M., et al., *Abdominal aortic aneurysm: an illustrated narrative review.* Journal of Manipulative and Physiological Therapeutics, 2003. **26**(3): p. 184-195.
11. Collin, J., *UK small aneurysms trial.* The Lancet, 1999. **353**(9150): p. 407-408.
12. Tsamis, A., J.T. Krawiec, and D.A. Vorp, *Elastin and collagen fibre microstructure of the human aorta in ageing and disease: a review.* Journal of the Royal Society, Interface. **10**(83): p. 20121004-20121004.
13. Wills, A., et al., *Pathogenesis of abdominal aortic aneurysms — Cellular and biochemical mechanisms.* European Journal of Vascular and Endovascular Surgery, 1996. **12**(4): p. 391-400.
14. Bluestein, D., et al., *Steady Flow in an Aneurysm Model: Correlation Between Fluid Dynamics and Blood Platelet Deposition.* Journal of Biomechanical Engineering, 1996. **118**(3): p. 280-286.
15. Vorp, D.A., et al., *Association of intraluminal thrombus in abdominal aortic aneurysm with local hypoxia and wall weakening.* Journal of Vascular Surgery, 2001. **34**(2): p. 291-299.
16. http://thumbs.dreamstime.com/z/abdominal-aortic-aneurysm-21361846.jpg. 2015 [cited 2015 20/11/2015].
17. Costantino, T.G., et al., *Accuracy of emergency medicine ultrasound in the evaluation of abdominal aortic aneurysm.* The Journal of Emergency Medicine, 2005. **29**(4): p. 455-460.
18. Kuhn, M., et al., *Emergency department ultrasound scanning for abdominal aortic aneurysm: accessible, accurate, and advantageous.* Ann Emerg Med, 2000. **36**(3): p. 219-223.

19. Brewster, D.C., et al., *Guidelines for the treatment of abdominal aortic aneurysms: report of a subcommittee of the Joint Council of the American Association for Vascular Surgery and Society for Vascular Surgery.* Journal of vascular surgery, 2003. **37**(5): p. 1106-1117.
20. Starr, J.E. and V. Halpern, *Abdominal aortic aneurysms in women.* Journal of Vascular Surgery, 2013. **57**(4, Supplement): p. 3S-10S.
21. Katz, D.A., B. Littenberg, and J.L. Cronenwett, *Management of small abdominal aortic aneurysms: Early surgery vs watchful waiting.* JAMA, 1992. **268**(19): p. 2678-2686.
22. Engellau, L., et al., *Measurements Before Endovascular Repair Of Abdominal Aortic Aneurysms: MR imaging with MRA vs. angiography and CT.* Acta Radiologica, 2003. **44**(2): p. 177-184.
23. Brown, P.M., D.T. Zelt, and B. Sobolev, *The risk of rupture in untreated aneurysms: the impact of size, gender, and expansion rate.* J Vasc Surg, 2003. **37**(2): p. 280-284.
24. Scotti, C.M., et al., *Wall stress and flow dynamics in abdominal aortic aneurysms: finite element analysis vs. fluid-structure interaction.* Comput Methods Biomech Biomed Engin, 2008. **11**(3): p. 301-322.
25. Raghavan, M.L., et al., *Wall stress distribution on three-dimensionally reconstructed models of human abdominal aortic aneurysm.* J Vasc Surg, 2000. **31**(4): p. 760-769.
26. Truijers, M., et al., *Wall Stress Analysis in Small Asymptomatic, Symptomatic and Ruptured Abdominal Aortic Aneurysms.* European Journal of Vascular and Endovascular Surgery, 2007. **33**(4): p. 401-407.
27. Erhart, P., et al., *Prediction of Rupture Sites in Abdominal Aortic Aneurysms After Finite Element Analysis.* Journal of Endovascular Therapy, 2015. **23**(1): p. 115-120.
28. Dua, M.M. and R.L. Dalman, *Hemodynamic influences on abdominal aortic aneurysm disease: Application of biomechanics to aneurysm pathophysiology.* Vascular pharmacology, 2010. **53**(1-2): p. 11-21.
29. Lin, S., et al., *Fluid-Structure Interaction in Abdominal Aortic Aneurysm: Effect of Modeling Techniques.* BioMed Research International, 2017. **2017**: p. 10.
30. Breeuwer, M., et al., *Assessment of the rupture risk of abdominal aortic aneurysms by patient-specific hemodynamic modeling—initial results.* International Congress Series, 2004. **1268**: p. 1090-1095.
31. Finol, E.A., K. Keyhani, and C.H. Amon, *The Effect of Asymmetry in Abdominal Aortic Aneurysms Under Physiologically Realistic Pulsatile Flow Conditions.* Journal of Biomechanical Engineering, 2003. **125**(2): p. 207-217.
32. Xenos, M., et al., *The effect of angulation in abdominal aortic aneurysms: fluid–structure interaction simulations of idealized geometries.* Medical & Biological Engineering & Computing, 2010. **48**(12): p. 1175-1190.
33. Drewe, C.J., et al., *Haemodynamics and stresses in abdominal aortic aneurysms: A fluid-structure interaction study into the effect of proximal neck and iliac bifurcation angle.* Journal of Biomechanics, 2017. **60**: p. 150-156.
34. Madhavan, S. and E.M.C. Kemmerling, *The effect of inlet and outlet boundary conditions in image-based CFD modeling of aortic flow.* BioMedical Engineering OnLine, 2018. **17**(1): p. 66.
35. Raghavan, M.L., et al., *Regional distribution of wall thickness and failure properties of human abdominal aortic aneurysm.* J Biomech, 2006. **39**(16): p. 3010-3016.

36. Raghavan, M.L., M.W. Webster, and D.A. Vorp, *Ex vivo biomechanical behavior of abdominal aortic aneurysm: assessment using a new mathematical model.* Annals of biomedical engineering, 1996. **24**(5): p. 573-582.
37. Thubrikar, M.J., et al., *Mechanical properties of abdominal aortic aneurysm wall.* Journal of Medical Engineering & Technology, 2001. **25**(4): p. 133-142.
38. Vande Geest, J.P., et al., *A biomechanics-based rupture potential index for abdominal aortic aneurysm risk assessment.* Ann N Y Acad Sci, 2006. **1085**: p. 11-21.
39. McGloughlin, T., et al., *A Finite Element Analysis Rupture Index (FEARI) as an Additional Tool for Abdominal Aortic Aneurysm Rupture Prediction*. Vol. 6. 2009.
40. Doyle, B.J., et al. *A Finite Element Analysis Rupture Index (FEARI) Assessment of Electively Repaired and Symptomatic/Ruptured Abdominal Aortic Aneurysms*. in *6th World Congress of Biomechanics (WCB 2010). August 1-6, 2010 Singapore*. 2010. Berlin, Heidelberg: Springer Berlin Heidelberg.
41. Owen, B., et al., *Computational hemodynamics of abdominal aortic aneurysms: Three-dimensional ultrasound versus computed tomography.* Proceedings of the Institution of Mechanical Engineers, Part H: Journal of Engineering in Medicine, 2016. **230**(3): p. 201-210.
42. Kok, A.M., et al., *Feasibility of wall stress analysis of abdominal aortic aneurysms using three-dimensional ultrasound.* J Vasc Surg, 2015. **61**(5): p. 1175-1184.
43. *Mimics*, in *3D Medical Image Processing Software*. 2016, Materialise UK.
44. *ABAQUS*. 2016, Simulia, Dassault Systèmes: UK.
45. *STAR CCM+* 2018, CD-adapco UK.
46. *ImFusion suite*. 2015, ImFusion GmbH: München, Germany.
47. Wolters, B.J.B.M., et al., *A patient-specific computational model of fluid–structure interaction in abdominal aortic aneurysms.* Medical Engineering & Physics, 2005. **27**(10): p. 871-883.
48. Durieux, R., et al., *High prevalence of abdominal aortic aneurysm in patients with three-vessel coronary artery disease.* Eur J Vasc Endovasc Surg, 2014. **47**(3): p. 273-278.
49. Darling, R.C., et al., *Autopsy study of unoperated abdominal aortic aneurysms. The case for early resection.* Circulation, 1977. **56**(3 Suppl): p. II161-4.
50. Hall, A.J., et al., *Aortic wall tension as a predictive factor for abdominal aortic aneurysm rupture: improving the selection of patients for abdominal aortic aneurysm repair.* Annals of Vascular Surgery, 2000. **14**(2): p. 152-157.
51. Choksy, S.A., A.B. Wilmink, and C.R. Quick, *Ruptured abdominal aortic aneurysm in the Huntingdon district: a 10-year experience.* Annals of the Royal College of Surgeons of England, 1999. **81**(1): p. 27.
52. Galland, R.B., M.S. Whiteley, and T.R. Magee, *The fate of patients undergoing surveillance of small abdominal aortic aneurysms.* European Journal of Vascular and Endovascular Surgery, 1998. **16**(2): p. 104-109.
53. Nicholls, S.C., et al., *Rupture in small abdominal aortic aneurysms.* Journal of Vascular Surgery, 1998. **28**(5): p. 884-888.
54. Heikkinen, M., J.P. Salenius, and O. Auvinen, *Ruptured abdominal aortic aneurysm in a well-defined geographic area.* Journal of vascular surgery, 2002. **36**(2): p. 291-296.
55. Martufi, G. and T.C. Gasser, *the role of biomechanical modeling in the rupture risk assessment for abdominal aortic aneurysms.* Journal of biomechanical engineering, 2013. **135**(2): p. 021010.

56. Stenbaek, J., B. Kalin, and J. Swedenborg, *Growth of thrombus may be a better predictor of rupture than diameter in patients with abdominal aortic aneurysms.* Eur J Vasc Endovasc Surg, 2000. **20**(5): p. 466-469.
57. Limet, R., N. Sakalihassan, and A. Albert, *Determination of the expansion rate and incidence of ruptur of abdominal aortic aneurysms.* Journal of Vascular Surgery, 1991. **14**(4): p. 540-548.
58. Brown, P.M., D.T. Zelt, and B. Sobolev, *The risk of rupture in untreated aneurysms: the impact of size, gender, and expansion rate.* Journal of vascular surgery, 2003. **37**(2): p. 280-284.
59. Cronenwett, J.L., *Variables That Affect the Expansion Rate and Rupture of Abdominal Aortic Aneurysms.* Annals of the New York Academy of Sciences, 1996. **800**(1): p. 56-67.
60. Speelman, L., et al., *The mechanical role of thrombus on the growth rate of an abdominal aortic aneurysm.* J Vasc Surg, 2010. **51**(1): p. 19-26.
61. Georgakarakos, E., et al., *The role of geometric parameters in the prediction of abdominal aortic aneurysm wall stress.* Eur J Vasc Endovasc Surg, 2010. **39**(1): p. 42-48.
62. Graham, M. and A. Chan, *Ultrasound screening for clinically occult abdominal aortic aneurysm.* CMAJ: Canadian Medical Association Journal, 1988. **138**(7): p. 627.
63. Guirguis-Blake, J.M., et al., *Ultrasonography screening for abdominal aortic aneurysms: A systematic evidence review for the u.s. preventive services task force.* Annals of Internal Medicine, 2014. **160**(5): p. 321-329.
64. Lamah, M. and S. DarkeM.S, *Value of Routine Computed Tomography in the Preoperative Assessment of Abdominal Aneurysm Replacement.* World Journal of Surgery, 1999. **23**(10): p. 1076-1080.
65. Singh, K., et al., *The Difference Between Ultrasound and Computed Tomography (CT) Measurements of Aortic Diameter Increases with Aortic Diameter: Analysis of Axial Images of Abdominal Aortic and Common Iliac Artery Diameter in Normal and Aneurysmal Aortas. The Tromsø Study, 1994–1995.* European Journal of Vascular and Endovascular Surgery, 2004. **28**(2): p. 158-167.
66. Sparks, A.R., P.L. Johnson, and M.C. Meyer, *Imaging of abdominal aortic aneurysms.*
67. Cheng, C.P., R.J. Herfkens, and C.A. Taylor, *Abdominal aortic hemodynamic conditions in healthy subjects aged 50–70 at rest and during lower limb exercise: in vivo quantification using MRI.* Atherosclerosis, 2003. **168**(2): p. 323-331.
68. Sakalihasan, N., R. Limet, and O.D. Defawe, *Abdominal aortic aneurysm.* The Lancet, 2005. **365**(9470): p. 1577-1589.
69. Fillinger, M., *Who should we operate on and how do we decide: predicting rupture and survival in patients with aortic aneurysm.* Semin Vasc Surg, 2007. **20**(2): p. 121-127.
70. Xenos, M., et al., *Progression of abdominal aortic aneurysm towards rupture: refining clinical risk assessment using a fully coupled fluid-structure interaction method.* Ann Biomed Eng, 2015. **43**(1): p. 139-153.
71. Hollier, L.H., L.M. Taylor, and J. Ochsner, *Recommended indications for operative treatment of abdominal aortic aneurysms.* Journal of Vascular Surgery, 1992. **15**(6): p. 1046-1056.
72. Bargellini, I., et al., *Type II lumbar endoleaks: Hemodynamic differentiation by contrast-enhanced ultrasound scanning and influence on aneurysm enlargement*

after endovascular aneurysm repair. Journal of Vascular Surgery, 2005. **41**(1): p. 10-18.

73. Fillinger, M.F., et al., *Prediction of rupture risk in abdominal aortic aneurysm during observation: wall stress versus diameter.* J Vasc Surg, 2003. **37**(4): p. 724-732.
74. Peppelenbosch, N., et al., *Diameter of abdominal aortic aneurysm and outcome of endovascular aneurysm repair: does size matter? A report from EUROSTAR.* Journal of Vascular Surgery, 2004. **39**(2): p. 288-297.
75. https://www.vascularweb.org/vascularhealth/Pages/surgical-aneurysm-repair.aspx.
76. Stringfellow, M.M., P.F. Lawrence, and R.G. Stringfellow, *The influence of aorta-aneurysm geometry upon stress in the aneurysm wall.* Journal of surgical research, 1987. **42**(4): p. 425-433.
77. Elger, D.F., et al., *The influence of shape on the stresses in model abdominal aortic aneurysms.* J Biomech Eng, 1996. **118**(3): p. 326-32.
78. Inzoli, F., et al., *Biomechanical Factors in Abdominal Aortic Aneurysm Rupture.* Eur J Vasc Surg, 1993. **7**: p. 667-667.
79. Mower, W.R., L.J. Baraff, and J. Sneyd, *Stress Distributions in Vascular Aneurysms: Factors Affecting Risk of Aneurysm Rupture.* Journal of Surgical Research, 1993. **55**(2): p. 155-161.
80. Mower, W.R., W.J. Quinones, and S.S. Gambhir, *Effect of intraluminal thrombus on abdominal aortic aneurysm wall stress.* Vasc Surg, 1997. **26**(4): p. 602-608.
81. Di Martino, E., et al., *Biomechanics of abdominal aortic aneurysm in the presence of endoluminal thrombus: Experimental characterisation and structural static computational analysis.* European Journal of Vascular and Endovascular Surgery, 1998. **15**(4): p. 290-299.
82. Vorp, D.A., *Biomechanics of abdominal aortic aneurysm.* Journal of Biomechanics, 2007. **40**(9): p. 1887-1902.
83. Raghavan, M.L. and D.A. Vorp, *Toward a biomechanical tool to evaluate rupture potential of abdominal aortic aneurysm: identification of a finite strain constitutive model and evaluation of its applicability.* Journal of biomechanics, 2000. **33**(4): p. 475-482.
84. Venkatasubramaniam, A.K., et al., *A comparative study of aortic wall stress using finite element analysis for ruptured and non-ruptured abdominal aortic aneurysms.* Eur J Vasc Endovasc Surg, 2004. **28**(2): p. 168-176.
85. Fillinger, M.F., et al., *In vivo analysis of mechanical wall stress and abdominal aortic aneurysm rupture risk.* J Vasc Surg, 2002. **36**(3): p. 589-597.
86. Vande Geest, J.P., et al., *The Effects of Anisotropy on the Stress Analyses of Patient-Specific Abdominal Aortic Aneurysms.* Annals of Biomedical Engineering, 2008. **36**(6): p. 921-932.
87. Gasser, T.C., et al., *Biomechanical rupture risk assessment of abdominal aortic aneurysms: model complexity versus predictability of finite element simulations.* Eur J Vasc Endovasc Surg, 2010. **40**(2): p. 176-185.
88. Gasser, T.C., et al., *A novel strategy to translate the biomechanical rupture risk of abdominal aortic aneurysms to their equivalent diameter risk: method and retrospective validation.* Eur J Vasc Endovasc Surg, 2014. **47**(3): p. 288-295.
89. Erhart, P., et al., *Finite Element Analysis in Asymptomatic, Symptomatic, and Ruptured Abdominal Aortic Aneurysms: In Search of New Rupture Risk Predictors.* European Journal of Vascular and Endovascular Surgery, 2015. **49**(3): p. 239-245.

90. Maier, A., et al., *A comparison of diameter, wall stress, and rupture potential index for abdominal aortic aneurysm rupture risk prediction.* Ann Biomed Eng, 2010. **38**(10): p. 3124-3134.
91. Heng, M.S., et al., *Peak wall stress measurement in elective and acute abdominal aortic aneurysms.* J Vasc Surg, 2008. **47**(1): p. 17-22; discussion 22.
92. Shang, E.K., et al., *Local wall thickness in finite element models improves prediction of abdominal aortic aneurysm growth.* Journal of Vascular Surgery, 2015. **61**(1): p. 217-223.
93. Raghavan, M.L., et al., *Automated Methodology for Determination of Stress Distribution in Human Abdominal Aortic Aneurysm.* Journal of Biomechanical Engineering, 2005. **127**(5): p. 868-871.
94. Vande Geest, J.P., et al., *Towards A Noninvasive Method for Determination of Patient-Specific Wall Strength Distribution in Abdominal Aortic Aneurysms.* Annals of Biomedical Engineering, 2006. **34**(7): p. 1098-1106.
95. Xenos, M., et al., *Patient-Based Abdominal Aortic Aneurysm Rupture Risk Prediction with Fluid Structure Interaction Modeling.* Annals of Biomedical Engineering, 2010. **38**(11): p. 3323-3337.
96. Maier, A., et al., *A Comparison of Diameter, Wall Stress, and Rupture Potential Index for Abdominal Aortic Aneurysm Rupture Risk Prediction.* Annals of Biomedical Engineering, 2010. **38**(10): p. 3124-3134.
97. Indrakusuma, R., et al., *Biomechanical Imaging Markers as Predictors of Abdominal Aortic Aneurysm Growth or Rupture: A Systematic Review.* European Journal of Vascular and Endovascular Surgery, 2016. **52**(4): p. 475-486.
98. Dalman, R.L., et al., *AAA Disease: Mechanism, Stratification, and Treatment.* Annals of the New York Academy of Sciences, 2006. **1085**(1): p. 92-109.
99. Suh, G.-Y., et al., *Hemodynamic changes quantified in abdominal aortic aneurysms with increasing exercise intensity using mr exercise imaging and image-based computational fluid dynamics.* Annals of biomedical engineering, 2011. **39**(8): p. 2186-2202.
100. Les, A.S., et al., *Quantification of hemodynamics in abdominal aortic aneurysms during rest and exercise using magnetic resonance imaging and computational fluid dynamics.* Annals of biomedical engineering, 2010. **38**(4): p. 1288-1313.
101. Fry, D.L., *certain hemorheologic considerations regarding the blood vascular interface with particular reference to coronary artery disease.* Circulation, 1969. **40**: p. 38-57.
102. Caro, C.G., J.M. Fitz-Gerald, and R.C. Schroter, *Atheroma and arterial wall shear-Observation, correlation and proposal of a shear dependent mass transfer mechanism for atherogenesis.* Proc. R. Soc. Lond. B, 1971. **177**(1046): p. 109-133.
103. Ku, D.N., et al., *Pulsatile flow and atherosclerosis in the human carotid bifurcation. Positive correlation between plaque location and low oscillating shear stress.* Arteriosclerosis, thrombosis, and vascular biology, 1985. **5**(3): p. 293-302.
104. Tarbell, J.M., et al., *Fluid mechanics, arterial disease, and gene expression.* Annual review of fluid mechanics, 2014. **46**.
105. He, X. and D.N. Ku, *Pulsatile flow in the human left coronary artery bifurcation: average conditions.* Journal of biomechanical engineering, 1996. **118**(1): p. 74-82.

106. Peiffer, V., S.J. Sherwin, and P.D. Weinberg, *Computation in the rabbit aorta of a new metric–the transverse wall shear stress–to quantify the multidirectional character of disturbed blood flow.* Journal of biomechanics, 2013. **46**(15): p. 2651-2658.
107. Boyd, A.J., et al., *Low wall shear stress predominates at sites of abdominal aortic aneurysm rupture.* Journal of Vascular Surgery, 2016. **63**(6): p. 1613-1619.
108. Papaharilaou, Y., et al., *A decoupled fluid structure approach for estimating wall stress in abdominal aortic aneurysms.* Journal of Biomechanics, 2007. **40**(2): p. 367-377.
109. Chisci, E., et al., *Grading Abdominal Aortic Aneurysm Rupture Risk.* Journal of Vascular Surgery, 2013. **57**(5): p. 43S.
110. Doyle, B.J., et al. *From Detection to Rupture: A Serial Computational Fluid Dynamics Case Study of a Rapidly Expanding, Patient-Specific, Ruptured Abdominal Aortic Aneurysm*. in *Computational Biomechanics for Medicine*. 2014. New York, NY: Springer New York.
111. Scotti, C.M., et al., *Fluid-structure interaction in abdominal aortic aneurysms: effects of asymmetry and wall thickness.* BioMedical Engineering OnLine, 2005. **4**: p. 64-64.
112. Scotti, C.M., et al., *Wall stress and flow dynamics in abdominal aortic aneurysms: finite element analysis vs. fluid–structure interaction* Computer Methods in Biomechanics and Biomedical Engineering, 2008. **11**(3): p. 301-322.
113. Vorp, D.A., M.L. Raghavan, and M.W. Webster, *Mechanical wall stress in abdominal aortic aneurysm: Influence of diameter and asymmetry.* Journal of Vascular Surgery, 1998. **27**(4): p. 632-639.
114. Doyle, B.J., et al., *Vessel asymmetry as an additional diagnostic tool in the assessment of abdominal aortic aneurysms.* Journal of Vascular Surgery, 2009. **49**(2): p. 443-454.
115. Giannoglou, G., et al., *Predicting the Risk of Rupture of Abdominal Aortic Aneurysms by Utilizing Various Geometrical Parameters: Revisiting the Diameter Criterion.* Angiology, 2006. **57**(4): p. 487-494.
116. Doyle, B.J. and T.M. McGloughlin, *Computer-Aided Diagnosis of Abdominal Aortic Aneurysms*, in *Biomechanics and Mechanobiology of Aneurysms*, T. McGloughlin, Editor. 2011, Springer Berlin Heidelberg: Berlin, Heidelberg. p. 119-138.
117. Wang, D.H.J., M. Sacks, and D.A. Vorp, *Modification of a 3-D reconstruction technique for abdominal aortic aneurysm that includes intraluminal thrombus*. Vol. 28. 2000. S-64.
118. Wang, D.H., et al., *Effect of intraluminal thrombus on wall stress in patient-specific models of abdominal aortic aneurysm.* J Vasc Surg, 2002. **36**(3): p. 598-604.
119. Bluestein, D., et al., *Intraluminal thrombus and risk of rupture in patient specific abdominal aortic aneurysm - FSI modelling*. Vol. 12. 2009. 73-81.
120. Speelman, L., et al., *Effects of Wall Calcifications in Patient-Specific Wall Stress Analyses of Abdominal Aortic Aneurysms.* Journal of Biomechanical Engineering, 2006. **129**(1): p. 105-109.
121. Vignon-Clementel, I.E., et al., *Outflow boundary conditions for three-dimensional finite element modeling of blood flow and pressure in arteries.* Computer Methods in Applied Mechanics and Engineering, 2006. **195**(29): p. 3776-3796.
122. Alastruey, J., et al., *On the impact of modelling assumptions in multi-scale, subject-specific models of aortic haemodynamics.* Journal of the Royal Society, Interface, 2016. **13**(119): p. 20160073.

123. Perktold, K. and G. Rappitsch, *Computer simulation of local blood flow and vessel mechanics in a compliant carotid artery bifurcation model.* Journal of Biomechanics, 1995. **28**(7): p. 845-856.
124. Arzani, A., et al., *Effect of exercise on patient specific abdominal aortic aneurysm flow topology and mixing.* International journal for numerical methods in biomedical engineering, 2014. **30**(2): p. 280-295.
125. Scotti, C.M. and E.A. Finol, *Compliant biomechanics of abdominal aortic aneurysms: A fluid–structure interaction study.* Computers & Structures, 2007. **85**(11): p. 1097-1113.
126. J Mills, C., et al., *Pressure flow relationship and vascular impedance in man*. Vol. 4. 1970. 405-17.
127. Mohiaddin, R.H., et al., *Magnetic resonance volume flow and jet velocity mapping in aortic coarctation.* Journal of the American College of Cardiology, 1993. **22**(5): p. 1515-1521.
128. Di Martino, E., M. D Gasbarro, and K. Shimada, *Explicit finite element method for in-vivo mechanics of abdominal aortic aneurysm*. Vol. 16. 2007. 337-363.
129. Józsa, T.I. and G. Paál, *Boundary conditions for flow simulations of abdominal aortic aneurysms.* International Journal of Heat and Fluid Flow, 2014. **50**: p. 342-351.
130. Kwon, S.T., et al., *Interaction of expanding abdominal aortic aneurysm with surrounding tissue: Retrospective CT image studies.* Journal of nature and science, 2015. **1**(8): p. e150-e150.
131. Farsad, M., et al., *Computational Growth and Remodeling of Abdominal Aortic Aneurysms Constrained by the Spine.* Journal of biomechanical engineering, 2015. **137**(9): p. 0910081-09100812.
132. Moayeri, M. and G.J.J.o.B. Zendehbudi, *Effects of elastic property of the wall on flow characteristics through arterial stenoses.* 2003. **36**(4): p. 525-535.
133. Salsac, A.-V., et al., *Evolution of the wall shear stresses during the progressive enlargement of symmetric abdominal aortic aneurysms.* 2006. **560**: p. 19-51.
134. Pedley, T.J., *The Fluid Mechanics of Large Blood Vessels*. Cambridge Monographs on Mechanics. 1980, Cambridge: Cambridge University Press.
135. Berger, S. and L.-D.J.A.r.o.f.m. Jou, *Flows in stenotic vessels.* 2000. **32**(1): p. 347-382.
136. Papaioannou, T.G. and C. Stefanadis, *Vascular wall shear stress: basic principles and methods.* Hellenic journal of cardiology : HJC = Hellenike kardiologike epitheorese, 2005. **46**(1): p. 9-15.
137. Fung, Y.C., *Biomechanics, Circulation*. Vol. 2. 1997, Springer Science+Business Media New York: Springer-Verlag New York. 572.
138. Perktold, K., M. Resch, and H. Florian, *Pulsatile non-Newtonian flow characteristics in a three-dimensional human carotid bifurcation model.* 1991.
139. Gijsen, F.J.H., et al., *The influence of the non-Newtonian properties of blood on the flow in large arteries: unsteady flow in a 90° curved tube.* Journal of Biomechanics, 1999. **32**(7): p. 705-713.
140. Oliveira, C., et al., *Numerical Study of Non-Newtonian Blood Behavior in the Abdominal Aortic Bifurcation of a Patient-Specific at Rest.* The Open Sports Sciences Journal, 2017. **10**(Suppl-2, M9): p. 279-285.
141. Kumar, D., R. Vinoth, and V.S. Raviraj Adhikari, *Non-Newtonian and Newtonian blood flow in human aorta: a transient analysis.* 2017.

142. Meyer, C.A., et al., *Stereoscopically Observed Deformations of a Compliant Abdominal Aortic Aneurysm Model.* Journal of Biomechanical Engineering, 2011. **133**(11): p. 111004-111004-8.
143. Deplano, V., et al., *Flow behaviour in an asymmetric compliant experimental model for abdominal aortic aneurysm.* Journal of Biomechanics, 2007. **40**(11): p. 2406-2413.
144. Finol, E.A., et al., *Fluid-structure interaction and structural analysis of an aneurysm model.*, in *Summer Bioengineering Conference*, A.S.o.M. Engineers, Editor. 2003, American Society of Mechanical Engineers: Sonesta Beach Resort in Key Biscayne, Florida p. 75–76.
145. Hua, J. and W.R. Mower, *Simple geometric characteristics fail to reliably predict abdominal aortic aneurysm wall stresses.* J Vasc Surg, 2001. **34**(2): p. 308-315.
146. Yu, S.C.M., *Steady and pulsatile flow studies in Abdominal Aortic Aneurysm models using Particle Image Velocimetry.* International Journal of Heat and Fluid Flow, 2000. **21**(1): p. 74-83.
147. Sacks, M.S., et al., *In Vivo Three-Dimensional Surface Geometry of Abdominal Aortic Aneurysms*. Vol. 27. 1999. 469-79.
148. *ABAQUS*. 2014, Simulia, Dassault Systèmes: UK.
149. Finol, E.A., et al. *Biomechanics of patient specific abdominal aortic aneurysms: computational analysis of fluid flow*. in *Proceedings of the IEEE 28th Annual Northeast Bioengineering Conference (IEEE Cat. No.02CH37342)*. 2002.
150. Thubrikar, M.J., J. Al-Soudi, and F. Robicsek, *Wall stress studies of abdominal aortic aneurysm in a clinical model.* Ann Vasc Surg, 2001. **15**(3): p. 355-366.
151. Lowe, C., *Three-dimensional ultrasound in the management of abdominal aortic aneurysm*, in *Cardiovascular*. 2016, The University of Manchester: Manchetser. p. 243.
152. Boykov, Y.Y. and M.P. Jolly, *Interactive Graph Cuts for Optimal Boundary & Region Segmentation of Objects in N-D Images.* Proceedings of "Internation Conference on Computer Vision", 2001. **1**: p. 105-112.
153. Criminisi, A., T. Sharp, and A. Blake. *GeoS: Geodesic Image Segmentation*. in *Computer Vision – ECCV 2008*. 2008. Berlin, Heidelberg: Springer Berlin Heidelberg.
154. Couprie, C., et al., *Power Watershed: A Unifying Graph-Based Optimization Framework.* IEEE Transactions on Pattern Analysis and Machine Intelligence, 2011. **33**(7): p. 1384-1399.
155. Lorensen, W.E. and H.E. Cline, *Marching cubes: A high resolution 3D surface construction algorithm.* SIGGRAPH Comput. Graph., 1987. **21**(4): p. 163-169.
156. *MATLAB* 2015, MathWorks: UK.
157. Sonesson, B., T. Sandgren, and T. La¨ nne, *Abdominal Aortic Aneurysm Wall Mechanics and their Relation to Risk of Rupture.* Eur J Vasc Endovasc Surg, 1999. **18**: p. 487-493.
158. Sprouse, L.R., et al., *Is ultrasound more accurate than axial computed tomography for determination of maximal abdominal aortic aneurysm diameter?* Eur J Vasc Endovasc Surg, 2004. **28**(1): p. 28-35.
159. Vidakovic, R., et al., *Comparison With Computed Tomography of Two Ultrasound Devices for Diagnosis of Abdominal Aortic Aneurysm.* The American Journal of Cardiology, 2007. **100**(12): p. 1786-1791.
160. Reeps, C., et al., *The impact of model assumptions on results of computational mechanics in abdominal aortic aneurysm.* J Vasc Surg, 2010. **51**(3): p. 679-688.

161. Hirose, Y. and M. Takamiya, *Growth curve of ruptured aortic aneurysm.* J. Cardiovasc. Surg, 1998. **39**(1): p. 9-13.
162. Schurink, G.W., et al., *Thrombus within an aortic aneurysm does not reduce pressure on the aneurysmal wall.* J Vasc Surg, 2000. **31**(3): p. 501-506.
163. Wolf, Y.G., et al., *Computed tomography scanning findings associated with rapid expansion of abdominal aortic aneurysms.* J Vasc Surg, 1994. **20**(4): p. 529-35.
164. Di Martino, E., et al., *Biomechanics of abdominal aortic aneurysm in the presence of endoluminal thrombus: experimental characterisation and structural static computational analysis.* Eur J Vasc Endovasc Surg, 1998. **15**: p. 290-299.
165. Doyle, B.J., et al., *Identification of rupture locations in patient-specific abdominal aortic aneurysms using experimental and computational techniques.* J Biomech, 2010. **43**(7): p. 1408-1416.
166. Mcgloughlin, T.M., et al., *A Finite Element Analysis Rupture Index (FEARI) as an Additional Tool for Abdominal Aortic Aneurysm Rupture Prediction.* Vascular Disease Prevention, 2009. **9**: p. 114-121.
167. Sheidaei, A., et al., *Simulation of abdominal aortic aneurysm growth with updating hemodynamic loads using a realistic geometry.* Med Eng Phys, 2011. **33**: p. 80-88.
168. Pérez, E.A., L.R. Rojas-Solórzano, and E. Finol, *Geometric Predictors of Abdominal Aortic Aneurysm Maximum Wall Stress.* Chemical Engineering Transactions, 2016. **49**: p. 73-78.
169. Geest, V. and J. Pieter, *Towards an improved rupture potential index for abdominal aortic aneurysms: Anisotropic constitutive modeling and noninvasive wall strength estimation*. 2005, University of Pittsburgh.
170. Raut, S.S., et al. *The Effect of Uncertainty in Vascular Wall Material Properties on Abdominal Aortic Aneurysm Wall Mechanics*. 2014. New York, NY: Springer New York.
171. Raut, S.S., et al., *The Importance of Patient-Specific Regionally Varying Wall Thickness in Abdominal Aortic Aneurysm Biomechanics.* Journal of Biomechanical Engineering, 2013. **135**(8): p. 081010.
172. *Origin*. 2016, OriginLab Corporation: Northampton, MA, USA.
173. Chung, M., et al., *On the optimization of low-cost FDM 3D printers for accurate replication of patient-specific abdominal aortic aneurysm geometry.* 3D Printing in Medicine, 2018. **4**(1): p. 2.
174. Doyle, B.J., et al., *Experimental modelling of aortic aneurysms: novel applications of silicone rubbers.* Med Eng Phys, 2009. **31**(8): p. 1002-1012.
175. Corbett, T.J., et al., *Engineering Silicone Rubbers for In vitro Studies: Creating AAA Models and ILT Analogues with Physiological Properties.* Journal of biomechanical engineering, 2010. **132**(1): p. 011008-011008.
176. Doyle, B.J., et al., *3D Reconstruction and Manufacture of Real Abdominal Aortic Aneurysms: From CT Scan to Silicone Model.* Journal of Biomechanical Engineering, 2008. **130**(3): p. 034501-5.
177. Doyle , B.J., et al., *The use of silicone materials to model abdominal aortic aneurysm behaviour.*, in *SPE 1st European Conference on Medical Polymers*. 2008: Northern Ireland, Belfast.
178. Doyle, B.J., et al., *An Experimental and Numerical Comparison of the Rupture Locations of an Abdominal Aortic Aneurysm.* Journal of Endovascular Therapy, 2009. **16**(3): p. 322-335.

179. *Solidworks*. 2016, Dassault Systemes: UK.
180. Laheij, R., C.V. Marrewijk, and J. Buth, *EUROSTAR Data Registry Centre*. 2001.
181. Bartko, J.J., *Measurement and reliability: statistical thinking considerations.* Schizophr Bulletin, 1991. **17**(3): p. 483-489.
182. Siika, A., et al., *AAA Rupture Often Occurs Outside the Maximal Diameter Region and is Preceded by Rapid Local Growth and an Increased Biomechanical Rupture Risk Index*. Vol. 50. 2015. 390.
183. Giannoglu, G., et al., *Predicting the risk of rupture of abdominal aortic aneurysms by utilizing various geometrical parameters: revisiting the diameter criterion.* Angiology, 2006. **57**(4): p. 487-494.
184. Khosla, S., D.R. Morris, and J.V. Moxon, *Meta-Analysis of Peak Wall Stress in Ruptured, Symptomatic, and Intact Abdominal Aortic Aneurysms.* Journal of Vascular Surgery, 2015. **61**(3): p. 836-837.
185. Doyle, B., J., et al., *From Detection to Rupture: A Serial Computational Fluid Dynamics Case Study of a Rapidly Expanding, Patient-Specific, Ruptured Abdominal Aortic Aneurysm.* Computational Biomechanics for Medicine: Fundamental Science and Patient-specific Applications, 2014: p. 53-68.
186. Doyle, B.J., et al., *3D Reconstruction and Manufacture of Real Abdominal Aortic Aneurysms: From CT Scan to Silicone Model.* Journal of biomechanical engineering, 2008. **130**.
187. Georgakarakos, E., et al., *Peak wall stress does not necessarily predict the location of rupture in abdominal aortic aneurysms.* Eur J Vasc Endovasc Surg, 2010. **39**(3): p. 302-304.
188. Doyle, B.J., P.R. Hoskins, and T.M. McGloughlin, *Computational Rupture Prediction of AAAs: What Needs to Be Done Next?* Journal of Endovascular Therapy, 2011. **18**(2): p. 226-229.
189. Larsson, E., et al., *Analysis of aortic wall stress and rupture risk in patients with abdominal aortic aneurysm with a gender perspective.* J Vasc Surg, 2011. **54**(2): p. 295-299.
190. Samarth, S.R., et al., *Biological, Geometric and Biomechanical Factors Influencing Abdominal Aortic Aneurysm Rupture Risk: A Comprehensive Review.* Recent Patents on Medical Imaging (Discontinued), 2013. **3**(1): p. 44-59.
191. Piechota-Polanczyk, A., et al., *The Abdominal Aortic Aneurysm and Intraluminal Thrombus: Current Concepts of Development and Treatment.* Frontiers in Cardiovascular Medicine, 2015. **2**.
192. Moll, F.L., et al., *Management of abdominal aortic aneurysms clinical practice guidelines of the European society for vascular surgery.* Eur J Vasc Endovasc Surg, 2011. **41 Suppl 1**: p. S1-S58.
193. Imray, C., *Managing an abdominal aortic aneurysm. Practical cardiovascular risk management.* 2006. **4**(2): p. 9-11.
194. Nicholls, S.C., et al., *Rupture in small abdominal aortic aneurysms.* J Vasc Surg, 1998. **28**(5): p. 884-888.
195. Taylor, C.A., T.J.R. Hughes, and C.K. Zarins, *Finite Element Modeling of Three-Dimensional Pulsatile Flow in the Abdominal Aorta: Relevance to Atherosclerosis.* Annals of Biomedical Engineering, 1998. **26**(6): p. 975-987.

196. Li, Z. and C. Kleinstreuer, *Effects of blood flow and vessel geometry on wall stress and rupture risk of abdominal aortic aneurysms.* Journal of Medical Engineering & Technology, 2006. **30**(5): p. 283-297.
197. Younis, H.F., et al., *Hemodynamics and wall mechanics in human carotid bifurcation and its consequences for atherogenesis: investigation of inter-individual variation.* Biomech Model Mechanobiol, 2004. **3**(1): p. 17-32.
198. Finol, E.A. and C.H. Amon, *Flow-induced wall shear stress in abdominal aortic aneurysms: Part I--steady flow hemodynamics.* Comput Methods Biomech Biomed Engin, 2002. **5**(4): p. 309-318.
199. Owen, B., et al., *Computational hemodynamics of abdominal aortic aneurysms: Three-dimensional ultrasound versus computed tomography.* Proc Inst Mech Eng H, 2016. **230**(3): p. 201-210.
200. Leung, J.H., et al., *Fluid structure interaction of patient specific abdominal aortic aneurysms: a comparison with solid stress models.* Biomed Eng Online, 2006. **5**: p. 33-33.
201. Hoskins, P.R., et al., *Fluid–structure interaction in axially symmetric models of abdominal aortic aneurysms.* Proceedings of the Institution of Mechanical Engineers, Part H: Journal of Engineering in Medicine, 2009. **223**(2): p. 195-209.
202. Gao, F., O. Ohta, and T. Matsuzawa, *Fluid-structure interaction in layered aortic arch aneurysm model: assessing the combined influence of arch aneurysm and wall stiffness.* Australasian Physics & Engineering Sciences in Medicine, 2008. **31**(1): p. 32.
203. Du, Z.-Z. *eXtended Finite Element Method (XFEM) in Abaqus*. 2009 [cited 2016 10th of March]; Available from: http://www.simulia.com/download/rum11/UK/Advanced-XFEM-Analysis.pdf
204. Di Martino, E.S., et al., *Fluid–structure interaction within realistic three-dimensional models of the aneurysmatic aorta as a guidance to assess the risk of rupture of the aneurysm.* Medical Engineering & Physics, 2001. **23**(9): p. 647-655.
205. Kobielarz, M. and L. Jankowski, *Experimental characterization of the mechanical properties of the abdominal aortic aneurysm wall under uniaxial tension*. Vol. 51. 2013. 949-958.
206. Dassault Systèmes, S.A.C.A.E. *Analysis user's manual volume number ii, analysis procedures, solution, and control*. 2016 [cited 2016 May].
207. Natarajan, S., D. RoyMahapatra, and S.P.A. Bordas, *A simple integration technique for strong and weak discontinuities in GFEM/XFEM.* Int. J. Numer. Meth. Engng, 2009.
208. Singh, K., K. Keswani, and M. Vaggar, *Crack growth simulation of stiffened fuselage panels using XFEM techniques*. Vol. 21. 2014. 418-428.
209. Georgakarakos, E., et al., *The influence of intraluminal thrombus on abdominal aortic aneurysm wall stress.* International Union of Angiology, 2009. **28**(4): p. 325-333.
210. Wolters, B.J.B.M., et al., *A patient-specific computational model of fluid–structure interaction in abdominal aortic aneurysms.* Med Eng Phys, 2005. **27**(10): p. 871-883.
211. Vande Geest, J.P., M.S. Sacks, and D.A. Vorp, *The effects of aneurysm on the biaxial mechanical behavior of human abdominal aorta.* J Biomech, 2006. **39**(7): p. 1324-1334.
212. de Putter, S., et al., *Patient-specific initial wall stress in abdominal aortic aneurysms with a backward incremental method.* Journal of Biomechanics, 2007. **40**(5): p. 1081-1090.

213. Lederle, F.A., et al., *Prevalence and associations of abdominal aortic aneurysm detected through screening.* Annals of Internal Medicine, 1997. **126**(6): p. 441-449.
214. Doyle , B.J., et al., *Regions of High Wall Stress Can Predict the Future Location of Rupture of Abdominal Aortic Aneurysm.* Cardiovasc Intervent Radiol, 2014. **37**(3): p. 815-818.
215. Helderman, F., et al., *A numerical model to predict abdominal aortic aneurysm expansion based on local wall stress and stiffness.* Med Biol Eng Comput, 2008. **46**(11): p. 1121-1127.
216. Zelaya, J.E., et al., *Improving the Efficiency of Abdominal Aortic Aneurysm Wall Stress Computations.* PLoS ONE, 2014. **9**(7): p. e101353.
217. Raut, S.S., et al., *The role of geometric and biomechanical factors in abdominal aortic aneurysm rupture risk assessment.* Ann Biomed Eng, 2013. **41**(7): p. 1459-1477.
218. Vardulaki, K.A., et al., *Quantifying the risks of hypertension, age, sex and smoking in patients with abdominal aortic aneurysm.* British Journal of surgery, 2000. **87**: p. 195-200.
219. Doyle , B.J., et al., *From Detection to Rupture: A Serial Computational Fluid Dynamics Case Study of a Rapidly Expanding, Patient-Specific, Ruptured Abdominal Aortic Aneurysm.*, in *Computational Biomechanics for Medicine*, M.K. Doyle B., Wittek A., Nielsen P., Editor. 2014, Springer: New York, NY.
220. Maier, A., et al. *Impact of Model Complexity on Patient Specific Wall Stress Analyses of Abdominal Aortic Aneurysms*. in *World Congress on Medical Physics and Biomedical Engineering, September 7 - 12, 2009, Munich, Germany*. 2010. Berlin, Heidelberg: Springer Berlin Heidelberg.
221. Lasheras, J.C., *Haemodynamic stresses and the onset and progression of vascular diseases.* Journal of Fluid Mechanics, 2010. **664**: p. 1-4.
222. Malek, A.M., S.L. Alper, and S. Izumo, *Hemodynamic shear stress and its role in atherosclerosis.* JAMA, 1999. **282**(21): p. 2035-2042.
223. Retarekar, R., et al., *Stratification of a Population of Intracranial Aneurysms Using Blood Flow Metrics.* Computer methods in biomechanics and biomedical engineering, 2015. **18**(10): p. 1072-1082.
224. Tarbell, J.M., et al., *Fluid Mechanics, Arterial Disease, and Gene Expression.* Annual review of fluid mechanics, 2014. **46**: p. 591-614.
225. Stevens, R.R.F., et al., *Biomechanical changes during abdominal aortic aneurysm growth.* PLOS ONE, 2017. **12**(11): p. e0187421.
226. Arzani, A., et al., *A longitudinal comparison of hemodynamics and intraluminal thrombus deposition in abdominal aortic aneurysms.* American journal of physiology. Heart and circulatory physiology, 2014. **307**(12): p. H1786-H1795.
227. *Simpleware*. 2018, Synopsys: UK.
228. Çengel, Y.A. and J.M. Cimbala, *Fluid mechanics: Fundamentals and applications*. 7th ed. ed. 2006, Boston: McGraw-HillHigher Education.
229. Hardman, D., et al., *On the prediction of monocyte deposition in abdominal aortic aneurysms using computational fluid dynamics.* Proceedings of the Institution of Mechanical Engineers, Part H: Journal of Engineering in Medicine, 2013. **227**(10): p. 1114-1124.
230. Wood, N.B., *Aspects of Fluid Dynamics Applied to the Larger Arteries.* Journal of Theoretical Biology, 1999. **199**(2): p. 137-161.

231. Chaikof, E.L., et al., *SVS practice guidelines for the care of patients with an abdominal aortic aneurysm: Executive summary.* Journal of Vascular Surgery, 2009. **50**(4): p. 880-896.
232. Humphrey, J.D. and C.A. Taylor, *Intracranial and Abdominal Aortic Aneurysms: Similarities, Differences, and Need for a New Class of Computational Models.* Annual review of biomedical engineering, 2008. **10**: p. 221-246.
233. Keshmiri, A. and K. Andrews, *Vascular Flow Modelling Using Computational Fluid Dynamics*, in *Handbook of Vascular Biology Techniques*, M. Slevin and G. McDowell, Editors. 2015, Springer Netherlands: Dordrecht. p. 343-361.
234. Peiffer, V., S.J. Sherwin, and P.D. Weinberg, *Computation in the rabbit aorta of a new metric – the transverse wall shear stress – to quantify the multidirectional character of disturbed blood flow().* Journal of Biomechanics, 2013. **46**(15): p. 2651-2658.
235. Boussel, L., et al., *Aneurysm growth occurs at region of low wall shear stress: Patient-specific correlation of hemodynamics and growth in a longitudinal study.* Stroke; a journal of cerebral circulation, 2008. **39**(11): p. 2997-3002.
236. Ku, D., et al., *Pulsatile flow and atherosclerosis in the human carotid bifurcation: Positive correlation between plaque location and low and oscillating shear stress.* Arteriosclerosis, 1985. **3**(5): p. 293-302.
237. HERTOUT, A., *How to improve Implicit Co-Simulation between STAR-CCM+ and Abaqus*. 2017, Siemens PLM Software.
238. Field, A., *How can I equate coupled solver CFL to under-relaxation factors?* 2017, Siemens PLM Software.
239. Field, A., *How to define a Courant number dependent time-step*. 2017, Siemens PLM Software.
240. Magdalena, K. and J.J. Ludomir, *EXPERIMENTAL CHARACTERIZATION OF THE MECHANICAL PROPERTIES OF THE ABDOMINAL AORTIC ANEURYSM WALL UNDER UNIAXIAL TENSION.* JOURNAL OF THEORETICAL AND APPLIED MECHANICS, 2013. **51**(4): p. 949-958.
241. Küttler, U. and W. Wall, *Fixed-point fluid-structure interaction solvers with dynamic relaxation*. Vol. 43. 2008. 61-72.
242. Wilensky, S., *Adding additional convergence criterion to a transient simulation*. 2017, Siemens PLM Software.
243. *http://macrohut.cdadapco.com/phpBB3/viewtopic.php?f=4&t=321*. 2017 [cited 2017.
244. Brown, A.G., et al., *Accuracy vs. computational time: Translating aortic simulations to the clinic.* Journal of Biomechanics, 2012. **45**(3): p. 516-523.
245. Kung, E.O., et al., *In Vitro Validation of Finite Element Analysis of Blood Flow in Deformable Models.* Annals of biomedical engineering, 2011. **39**(7): p. 1947-1960.
246. Segers, P., et al., *Three-and-four-element Windkessel models: Assessment of their fitting performance in a large cohort of healthy middle-aged individuals*. Vol. 222. 2008. 417-28.
247. Wilson, J.S., et al., *Biochemomechanics of intraluminal thrombus in abdominal aortic aneurysms.* Journal of biomechanical engineering, 2013. **135**(2): p. 021011-021011.
248. Vorp, D.A., *Biomechanics of abdominal aortic aneurysm.* J Biomech, 2007. **40**(9): p. 1887-1902.
249. Upchurch Gr, S.T.A., *Abdominal aortic aneurysm.* Am Family Phys, 2006. **73**(7): p. 1198-1204.

250. Amit Gefen, R.A., *Biomechanics and Mechanobiology of Aneurysms.* Springer Heidelberg Dordrecht London New York, 2011. **7**.
251. Peppelenbosch N Harris L, V.m.C.F.G.B.J., *Diameter of abdominal aortic aneurysm and outcome of endovascular aneurysm repair: does size matter? A report from eurostar.* J Vasc Surg, 2004: p. 39: 288-39: 288.
252. Khanafer, K.M., J.L. Bull, and R. Berguer, *Fluid–structure interaction of turbulent pulsatile flow within a flexible wall axisymmetric aortic aneurysm model.* European Journal of Mechanics B/Fluids, 2009. **28**: p. 88–102.
253. Algabri, Y.A., S. Rookkapan, and S. Chatpun, *Three-dimensional finite volume modelling of blood flow in simulated angular neck abdominal aortic aneurysm.* IOP Conference Series: Materials Science and Engineering, 2017. **243**(1): p. 012003.
254. Ruiz de Galarreta, S., et al., *INFLUENCE OF THE LOCAL MEAN CURVATURE ON THE ABDOMINAL AORTIC ANEURYSM STRESS DISTRIBUTION*. Vol. 17. 2017. 1750106.
255. de Galarreta, S.R., et al., *The Relationship Between Surface Curvature and Abdominal Aortic Aneurysm Wall Stress.* Journal of Biomechanical Engineering, 2017. **139**(8): p. 081006-081006-7.
256. Basciano, C., et al., *A relation between near-wall particle-hemodynamics and onset of thrombus formation in abdominal aortic aneurysms.* Annals of biomedical engineering, 2011. **39**(7): p. 2010-2026.
257. Speelman, L., et al., *The mechanical role of thrombus on the growth rate of an abdominal aortic aneurysm.* Journal of Vascular Surgery, 2010. **51**(1): p. 19-26.
258. Taylor, C.A. and M.T. Draney, *Experimental and computational methods in cardiovascular fluid mechanics*, in *Annual Review of Fluid Mechanics*. 2004. p. 197-231.
259. Taylor, C.A., et al., *Predictive medicine: Computational techniques in therapeutic decision- making.* Computer Aided Surgery, 1999. **4**(5): p. 231-247.
260. Lenfant, C., *Report of the Task Force on Research in Pediatric Cardiovascular Disease.* Circulation, 2002. **106**(9): p. 1037-1042.
261. Meng, H., et al., *High WSS or Low WSS? Complex Interactions of Hemodynamics with Intracranial Aneurysm Initiation, Growth, and Rupture: Toward a Unifying Hypothesis.* American Journal of Neuroradiology, 2014. **35**(7): p. 1254.
262. Watton, P.N., et al., *Modelling evolution and the evolving mechanical environment of saccular cerebral aneurysms.* Biomechanics and Modeling in Mechanobiology, 2011. **10**(1): p. 109-132.
263. Ku, D.N., et al., *Pulsatile flow and atherosclerosis in the human carotid bifurcation positive correlation between plaque location and low and oscillating shear stress.* Arteriosclerosis, 1985. **5**(3): p. 293-302.
264. Rikhtegar, F., et al., *Choosing the optimal wall shear parameter for the prediction of plaque location—A patient-specific computational study in human left coronary arteries.* Atherosclerosis, 2012. **221**(2): p. 432-437.
265. Hans, S.S., et al., *Size and location of thrombus in intact and ruptured abdominal aortic aneurysms.* J Vasc Surg, 2005. **41**(4): p. 584-588.
266. Yasuhara, H., N. Ohara, and H. Nagawa, *Influence of gender on intraluminal thrombus of abdominal aortic aneurysms.* The American Journal of Surgery, 2001. **182**(1): p. 89-92.

267. Gíslason, M.K., B. Stansfield, and D.H. Nash, *Finite element model creation and stability considerations of complex biological articulation: The human wrist joint.* Medical Engineering & Physics, 2010. **32**(5): p. 523-531.
268. Gislason, M.K., et al., *A three-dimensional finite element model of maximal grip loading in the human wrist.* Proceedings of the Institution of Mechanical Engineers, Part H: Journal of Engineering in Medicine, 2009. **223**(7): p. 849-861.
269. Rosen, J., et al., *Biomechanical Properties of Abdominal Organs In Vivo and Postmortem Under Compression Loads.* Journal of Biomechanical Engineering, 2008. **130**(2): p. 021020-021020-17.
270. Prasad, S., et al. *Co-Simulation and Multiphysics Technologies for Coupled Fluid-Structure Interaction Problems*.
271. White, F.M., *Fluid Mechanics*. McGraw-Hill series in mechanical engineering. 2011: McGraw Hill.
272. Owen B; Lowe C, A.N., Mandal1 P, Rogers S, Wein W, McCollum CN, Revell A, *Computational hemodynamics of abdominal aortic aneurysms: 3D ultrasound versus computerised tomography.* European Journal of Vascular and Endovascular Surgery, 2015.

Appendix A

Comparison of characteristic stress values above and below 95%.

Stress (MPa)	Patient1		Patient2		Patient3		Patient4	
	CT	US	CT	US	CT	US	CT	US
Maximum	0.6	1.2	0.39	0.54	0.41	0.5	0.46	0.58
Mean (50%)	0.22	0.24	0.15	0.15	0.15	0.14	0.14	0.14
Characteristic (99%)	0.58	1.1	0.37	0.51	0.39	0.48	0.44	0.56
Characteristic (98%)	0.51	0.9	0.33	0.47	0.35	0.41	0.4	0.51
Characteristic (97%)	0.48	0.78	0.3	0.42	0.31	0.37	0.35	0.45
Characteristic (96%)	0.4	0.6	0.27	0.35	0.27	0.32	0.29	0.4
Characteristic (95%)	***0.38***	***0.4***	***0.25***	***0.25***	***0.26***	***0.25***	***0.25***	***0.25***
Characteristic (94%)	0.38	0.39	0.23	0.23	0.25	0.24	0.23	0.23
Characteristic (93%)	0.32	0.33	0.22	0.22	0.23	0.23	0.22	0.21
Characteristic (92%)	0.3	0.31	0.22	0.22	0.22	0.22	0.21	0.21
Characteristic (91%)	0.3	0.3	0.2	0.2	0.22	0.2	0.21	0.21

Appendix B

CFD modelling of an idealised aorta and Patient-Specific AAA (3D-US vs. CT models) and (Mimics vs. ImFusion models):

A simplified healthy abdominal aorta of 2 cm diameter and patient-specific AAA geometries extracted from CT and 3D-US images using ImFusion suit [46] and Mimics v.18 [43] were modelled numerically and validated analytically using CFD approach.

B.1. Methodology:

The simplified abdominal artery represented as a straight pipe of diameter = 20 mm and of 150 mm length was created in Abaqus/CAE. CT images were exported into ImFusion suite and Mimics v.18 to construct AAA blood geometries; for full details, see Chapter three. However, Mimics v.18 is not supporting the output format of the 3D-Ultrasound images that have been obtained from the clinicians; therefore, 3D-US models of AAA were segmented in ImFusion only, see **Figure (B-1)**.

Figure (B-1) : shows (a) AAA1 lumen segmented in ImFusion suit (CT vs 3D-US)[41] ; AAA1 (b) segmented in Mimics v.18 (CT).

The blood flow was assumed to behave as a steady, incompressible, Newtonian, and laminar flow with a Re number of 660 based on the average inlet flow velocity and diameter of the aorta. The blood has a density = 1050 Kg/m^3 and dynamic viscosity = 0.004 Pa.s [41, 270] . The flow at the inlet was assumed to be a Poiseuille Flow (**Equation (B.1)**[271]) representing more realistic blood flow :

$$V_z = V_{max}\left(1-\frac{r^2}{R^2}\right) \qquad \textbf{(B.1)}$$

Where: V_{max} = 2 times the V_Z (average inlet velocity), r = the radial coordinate and R = the artery radius. The pressure set to be zero at the outlet boundary condition and a no-slip

boundary conditions were performed on the wall surface of the fluid model. The no-slip boundary condition at the wall region means that the velocity is zero at the wall.

B.2 Computational Mesh:

All computational grids were created within Abaqus/CAE and can be illustrated in **Figure (B-2)** for the simplified Aorta. Five different grids of elements number ranging from 2200 to 138400 and of type a fully integrated hexahedral element (FC3D8) were investigated to reach the desired density **Figure (B-2)/ (A)**. The difference between the analytical velocity at the centre of simplified aorta= 180 mm/s and the numerical solution = 178 mm/s is considered acceptable. A similar procedure was performed for the AAA parts as follows: three meshes were used (532815, 717247, 1665814 and 2709552)/ (253916, 369907,741649 and 1169247) for ImFusion and Mimics models respectively. It was found the meshes of (1665814 elements) ImFusion / (741649 elements) Mimics satisfy the desired convergence.

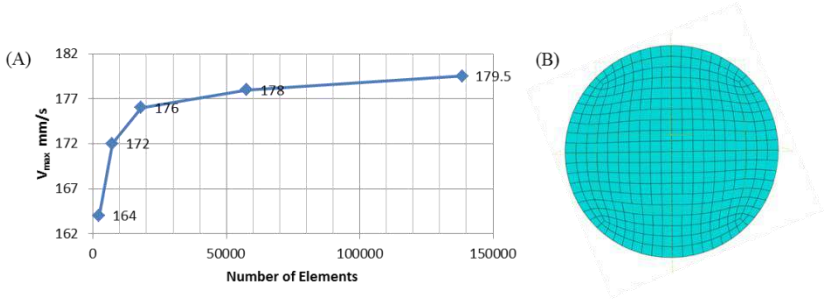

Figure (B-2): shows (A) mesh Sensitivity study (V_{max} against Number of elements), (B) mesh appearance in the fluid part.

B.3 Analytical solution:

As mentioned earlier, the flow is assumed to be steady, laminar, fully developed, and incompressible. The Hagen–Poiseuille law can be derived from the Navier–Stokes equations for a pipe of 20 mm diameter by applying the above assumptions. In this case, despite the fluid is moving, it is not accelerating, so that $\frac{\partial(.....)}{\partial t}=0$ and the velocity components in (r and θ) directions are zero[271]. The first momentum equation shrinks to $\frac{\partial p}{\partial r}=0$, which means the pressure is a function of the axial flow coordinate Z only. While the third momentum equation will be reduced and solved in the form below:

$$\frac{1}{r}\frac{\partial}{\partial r}\left(r\frac{\partial V_z}{\partial r}\right)=\frac{1}{\mu}\frac{\partial p}{\partial z}$$

$$V_z = \frac{1}{4\mu}\frac{\partial p}{\partial z} r^2 + c_1 \ln r + c_2$$

As $\boldsymbol{V_z}$ should be finite at $\boldsymbol{r = 0}$, $\boldsymbol{c_1 = 0}$. Using the no-slip condition at the wall means that $V_z = 0\ at\ R = 0$ at the wall, that leads to:

$$c_2 = -\frac{1}{4\mu}\frac{\partial p}{\partial z} R^2$$

Consequently, the final parabolic velocity profile will be:

$$V_{(r)} = 2\ V_z \left(1 - \left(\frac{r^2}{R^2}\right)\right)$$

The maximum velocity occurs at the centreline (r =0):

$$V_{zmax} = 2\ V_z$$

The Hagen–Poiseuille equation can calculate the pressure gradient Δp through a circular tube of (L= length, V_Z = the average flow velocity) and other parameters. Using the assumption that the pressure is decreasing linearly along the flow axis, due to that, the term $-\frac{\partial p}{\partial z} = \frac{\Delta p}{L}$ is constant. The final equation will be Hagen–Poiseuille equation:

$$\Delta p = \frac{32\ \mu\ L\ V_z}{D^2} \qquad \textbf{(B.2)}$$

The shear stress at the wall can be determined from the basic principles **Figure (B-3).** For a wall segment of length L; the pressure difference ΔP multiplied by the cross-section area = 2πr should be equivalent to the opposite force created due to friction. This viscous (frictional) force acting on the wall equals to the shear stress multiplying by the lateral surface area= 2πrL. So the final equation will be given: $\tau = \frac{\Delta p\ R}{2L}$

(B.3)

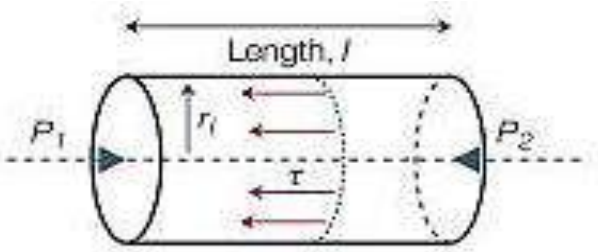

Figure (B-3): illustrates a wall segment shows the balance between the pressure difference force and frictional force.[271]

B.4. CFD results of the simplified aorta:

Velocity distributions in vertical and cross-sectional planes in the simplified aorta are presented in **figure (B-4)/A, B.** The maximum velocity of 178 mm/s is observed at the centre line of the aorta because the flow is fully developed, as well as, the velocity magnitude is observed to equal zero at the wall due to the viscosity effect near the wall. **Figure (B-4)/C** also illustrates the distribution of pressure in the simplified aorta wall obtained from the CFD simulation. There are two conditions for Poiseuille flow; the flow is laminar and fully developed. The Reynolds number of the current flow is 660, it is less than the critical value for the transition to turbulence Re=2300. Therefore, the condition of laminar flow is achieved. Compute the pressure drop between the inlet and outlet of the pipe from the CFD results and for a similar Poiseuille flow to compare them. It is found the pressure drop is the same analytically and numerically see **table (B-1)**.

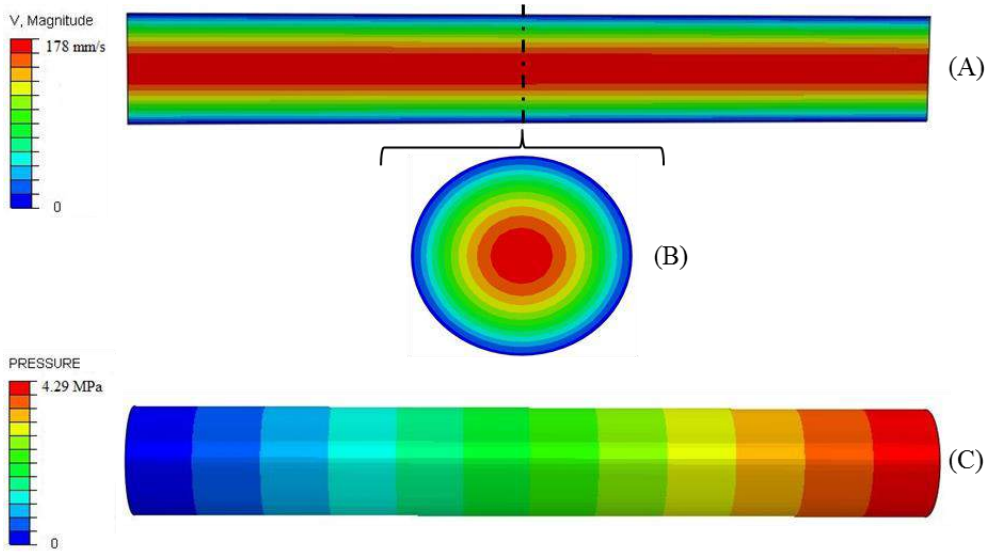

Figure (B-4): illustrates (A) velocity profiles in longitudinal section, (B) velocity profiles in cross-section of a simplified aorta; and (C) pressure contour.

Table (B-1) shows Pressure drop, Centreline velocity, and Shear stress (CFD results VS analytical results).

Centreline velocity (mm/s)		Pressure drop (MPa)		Shear stress (MPa)	
CFD results	Analytical results	CFD results	Analytical results	CFD results	Analytical results
178.3	180	4.29	4.32	0.144	0.144

Velocity profiles along the diameter of the artery were plotted at three different positions inlet, middle, and outlet (L=0, L=75 mm, and L=150 mm) see **figure (B-5)**. It can be seen that the velocity profiles are almost identical with insignificant deviation compared to the analytical solution. It is observed that velocity profile at L=0 where the velocity magnitude near or at the wall is not equal to zero owing to the formation boundary layer.

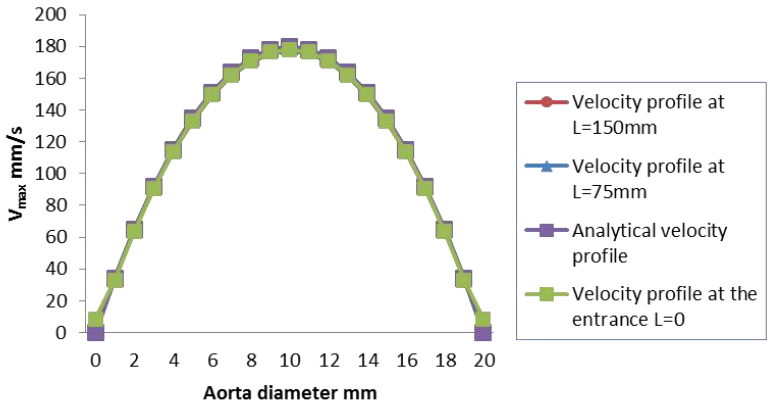

Figure (B-5) shows that the analytical velocity profile is matched with numerical profiles.

The wall shear stress in a healthy artery is measured numerically at the wall, see **Figure (B-6)**. The distribution of wall shear stress is observed to be almost consistently distributed along the artery because the velocity profile is parabolic. Very good agreement is observed between the analytical and numerical solution see **table (B-1)**.

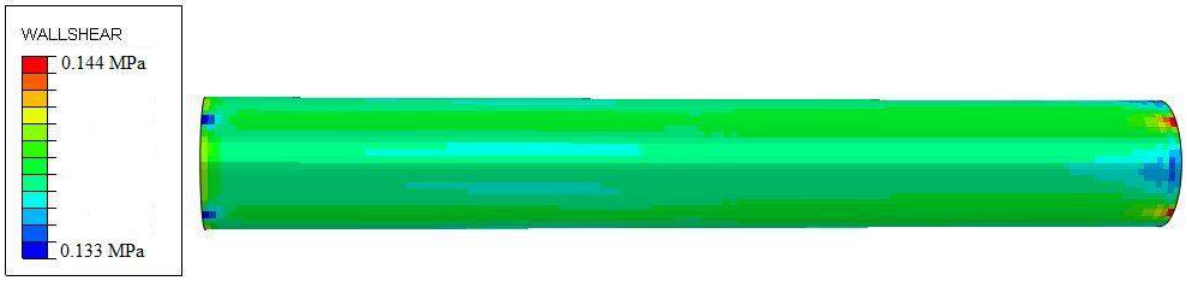

Figure (B-6): wall shear stress (MPa) distribution in a simplified aorta.

B.5. CFD results of AAA:

Figure (B-7) shows a comparison of wall shear stress (WSS) distribution for (CT and 3D US) AAA models segmented in ImFusion and solved in STAR CCM+ and Abaqus, respectively. It can be observed that the predicted wall shear stress distributions in CT and 3D

US AAA models are fairly similar, as well as the results of two solvers have almost the same distributions. Regions of low wall shear stress measured in (Pa) are spotted in similar sites for both imaging methods (CT and 3D US).

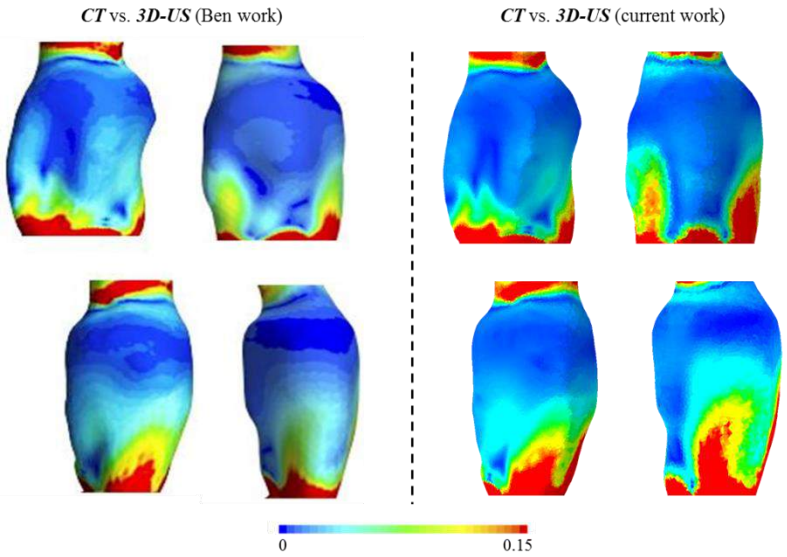

Figure (B-7) comparison of wall shear stress distributions (Pa) for CT and 3D US AAA models: (Left) Ben work used STAR CCM+ solver [272]; (Right) current work used Abaqus solver.

Figure (B-8) shows a comparison of wall shear stress (WSS) distribution for the same patient using in ImFusion and Mimics. It is observed from **Figure (B-8)** that WSS distribution in the Mimics model is totally different compared to the ImFusion model. Variations of wss distribution are influenced by the differences induced from the segmentation process.

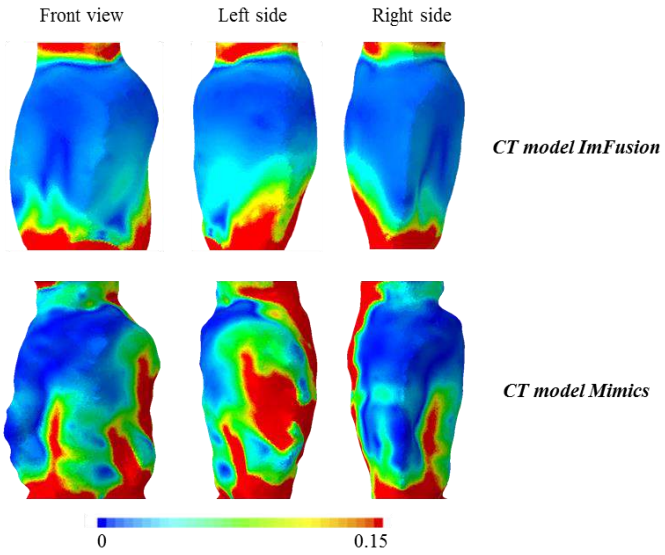

Figure (B-8) comparison of wall shear stress distribution (Pa) for CT models of AAA segmented in ImFusion suite and Mimics v.18 using Abaqus commercial code.

Figure (B-9)/a demonstrates velocity streamlines in CT, and 3D-US AAA segmented in ImFusion, simulated in STAR CCM+, and Abaqus/CFD. It can be observed that flow streamlines for both AAA geometries and solutions are fairly comparable with noticeable differences in the low-velocity streamlines due to the geometric irregularities. **Figure (B-9)/b** shows a comparison of velocity streamlines in AAA segmented in Mimics v.18 and ImFusion suite package, and both simulated in Abaqus/CFD. The circulation zone in the Mimics model is observed to be stronger than the ImFusion model.

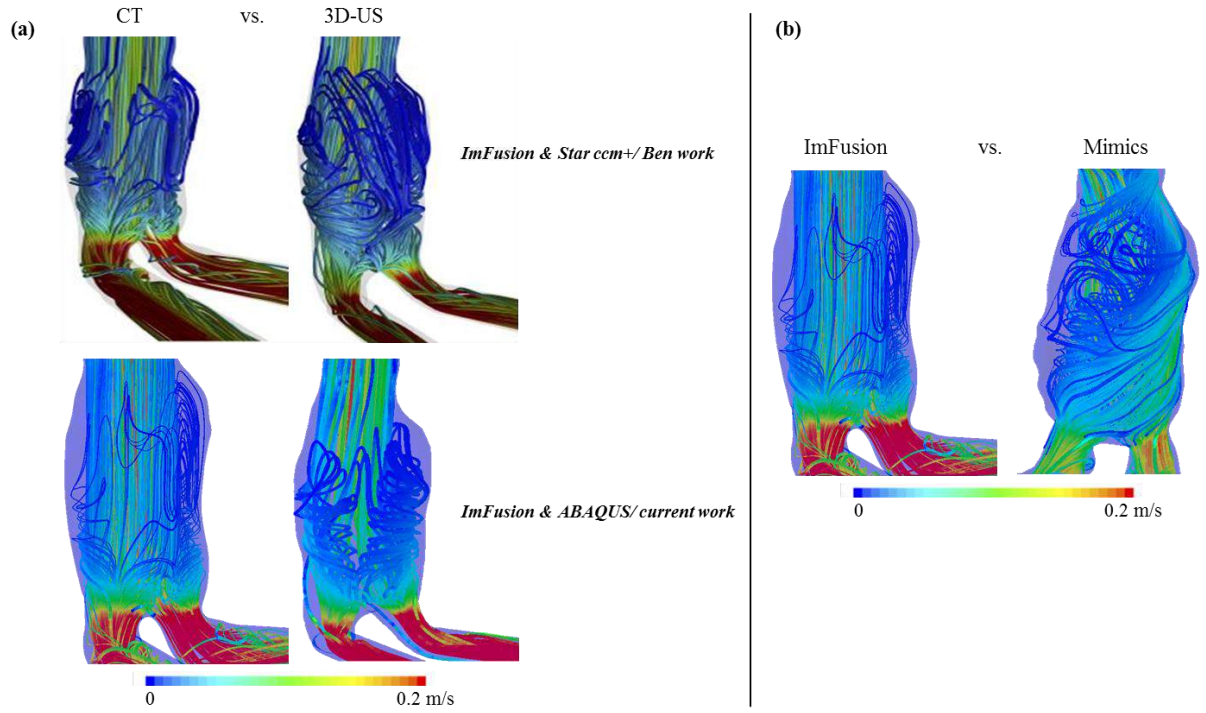

Figure (B-9) illustrates a comparison of **(a)** velocity streamlines (CT vs. 3D-US) AAA geometries using different solvers; **(b)** velocity streamlines between CT AAA geometries segmented in ImFusion suite and Mimics v.18.

In summary, wall shear stresses and velocity streamlines obtained in AAAs were depending on imaging source and segmentation techniques. The geometric differences between the CT and 3D-US models produced in ImFusion were not huge to cause a significant influence in the distribution of WSS. Despite the source of imaging is CT, the AAA model segmented in Mimics v.18 differs significantly from the AAA produced by the ImFusion suite, which led to the different WSS distributions and velocity streamlines.

Appendix C

3-Elements Windkessel Java script described at the outlets of AAA. Adopted from[243, 244]

```
====================     ====================  ====================

package windkessel;

/* This macro currently requires that the Region is called "Fluid",
 * the outlets are named "Outlet1", "Outlet2" etc. and all the
Inlets
 * are called "Inlet1", "Inlet2" etc
 *
 * The macro interacts with STAR-CCM+ at the end of every time-step
and so is
 * an explicit coupling between the lumped parameter model and the
3D simulation.
 * The macro will find all the inlets and outlets in the model
 * (based on the naming convention above) and setup local coordinate
systems,
 * reports, monitors and plots of volume flow and pressure. It will
also extract
 * information on the time-step and end time from the simulation to
start and
 * stop at the correct instance.
 *
 * The Windkessel parameters are defined on lines 54-56 of this
macro.
 * If multiple outlets are present in the model then the macro will
use the
 * first set of entries in the Windkessel parameter vector for the
 * outlet named "Outlet1" and the second set of entries for
"Outlet2" etc.
 *
 */
import java.util.*;
import star.base.neo.DoubleVector;
import star.base.neo.IntVector;
import star.common.*;
import star.base.report.*;
import star.flow.StaticPressureProfile;

/**
 *
 * @author abrown
 */
public class Windkessel_v1 extends StarMacro {

    @Override
    public void execute() {
        execute0();
    }

    private void execute0() {
```

```
        Simulation simu = getActiveSimulation();
        Region fluidregion =
                simu.getRegionManager().getRegion("Fluid");

        // Count the number of outlet boundaries in model and set
then as "Pressure Outlets"
        int outCount = getBoundaryCount(simu);

        // Count the number of Inlet boundaries in model
        int inCount = getInBoundaryCount(simu);

        // Windkessel Variables
        double[] R = new double[]{1.45e8};      // kg m^-4 s^-1
        double[] C = new double[]{1.45e-8};     // m^4 s^2 kg^-1
        double[] Z = new double[]{1.1e7};       // kg m^-4 s^-1

        // Primitive Field Functions
        PrimitiveFieldFunction FFpressure =
((PrimitiveFieldFunction)
simu.getFieldFunctionManager().getFunction("Pressure"));
        PrimitiveFieldFunction FFvelocity =
((PrimitiveFieldFunction)
simu.getFieldFunctionManager().getFunction("Velocity"));

        // Inialise flow field
        simu.getSolution().initializeSolution();

        // Initialise Variable Arrays
        double[] P_ini = new double[outCount];
        double[] Q_ini = new double[outCount];
        double[] P_old = new double[outCount];
        double[] Q_old = new double[outCount];
        double[] Pm_old = new double[outCount];
        double[] Pm_new = new double[outCount];
        double[] P_new = new double[outCount];
        double[] Q_new = new double[outCount];

        // This will setup local co-ordinate systems at the outlets
and construct
        //reports, monitors and plots for pressure and flow at each
outlet.
        createRepMonPlots("Outlet", outCount, fluidregion, simu,
FFpressure, FFvelocity);

        // This will setup local co-ordinate systems at the inlets
and construct
        //reports, monitors and plots for pressure and flow at each
inlet.
        createRepMonPlots("Inlet", inCount, fluidregion, simu,
FFpressure, FFvelocity);

        // Populate P_ini and Q_ini arrays from initial conditions
        for (int i = 1; i < (outCount + 1); i++) {
            Boundary outlet =
fluidregion.getBoundaryManager().getBoundary("Outlet" + i);
```

```
            // Pressure array
            AreaAverageReport pReport =
                    ((AreaAverageReport)
simu.getReportManager().getReport("Av Pressure Outlet" + i));
            P_ini[i - 1] = pReport.getValue();
            //simu.println("P out"+i+"="+P_ini[i-1]);
            // Flow array
            SurfaceIntegralReport qReport =
                    (SurfaceIntegralReport)
simu.getReportManager().getReport("Flow Outlet" + i);
            Q_ini[i - 1] = qReport.getValue();
            //simu.println("Q out"+i+"="+Q_ini[i-1]);
        }

        // Get solution duration from simulation and deactivate max
steps stopping criteria
        double[] time = getTimeInfo(simu);
        double dt = time[1];
/*****************************SOLVE*********************************
************
        // Begin solution with an explicit coupling to a three
element Windkessel model
        for (int j = 1; j < time.length; j++) {
            if (j + 1 == time.length) {
                simu.println("Maximum Physical Time
Reached.....Macro Stopping");
            } else {
                for (int i = 1; i < (outCount + 1); i++) { //Loop
through outlet boundaries
                    Boundary outlet =
fluidregion.getBoundaryManager().getBoundary("Outlet" + i);
                    // Check if at first time-step
                    if (j == 1) {
                        //Initialise variables
                        Q_old[i - 1] = Q_ini[i - 1];
                        Q_new[i - 1] = Q_ini[i - 1];
                        P_old[i - 1] = P_ini[i - 1];
                        Pm_old[i - 1] = P_old[i - 1] - (Q_old[i - 1]
* Z[i - 1]);
                    } else {
                        //Extract Pressure information
                        AreaAverageReport pReport =
                                ((AreaAverageReport)
simu.getReportManager().getReport("Av Pressure Outlet" + i));
                        P_old[i - 1] = pReport.getValue();
                        //Extract Flow information
                        SurfaceIntegralReport qReport =
                                (SurfaceIntegralReport)
simu.getReportManager().getReport("Flow Outlet" + i);
                        Q_new[i - 1] = qReport.getValue();
                    }
                    //Calculate the new Windkessel Pressure
                    Pm_new[i - 1] = ((R[i - 1] * dt * Q_new[i - 1])
+ (R[i - 1] * C[i - 1] * Pm_old[i - 1])) / (R[i - 1] * C[i - 1] +
dt);
```

```
                    P_new[i - 1] = Pm_new[i - 1] + (Z[i - 1] *
Q_new[i - 1]);
                    // Check for negative pressures from Windkessel
                    if (P_new[i-1] <= 0){
                        P_new[i-1]=1;
                        simu.println("Negative pressure computed by
Windkessel - Limiting pressure to 1Pa on Outlet" + i);
                    }
                    // Apply Windkessel Pressure to STAR-CCM+
boundary
                    StaticPressureProfile pressureProfile =
outlet.getValues().get(StaticPressureProfile.class);

pressureProfile.getMethod(ConstantScalarProfileMethod.class).getQuan
tity().setValue(P_new[i - 1]);
                    //
                    if (j < time.length) {
                        // Update pressure data for next time-step,
unless the simulation has finished.
                        Pm_old[i - 1] = Pm_new[i - 1];
                    }
                }
                simu.getSimulationIterator().run(1);
            }

        }

        simu.println("Solution Complete!");
    }

    private double[] getTimeInfo(Simulation simu) {
        ImplicitUnsteadySolver impUS = ((ImplicitUnsteadySolver)
simu.getSolverManager().
                getSolver(ImplicitUnsteadySolver.class));
        double dt = impUS.getTimeStep().getValue();
        double endtime = ((PhysicalTimeStoppingCriterion)
simu.getSolverStoppingCriterionManager().
                getSolverStoppingCriterion("Maximum Physical
Time")).getMaximumTime().getValue();
        ((StepStoppingCriterion)
simu.getSolverStoppingCriterionManager().
                getSolverStoppingCriterion("Maximum
Steps")).setIsUsed(false);
        //Variables
        int steps = (int) (endtime / dt);
        double[] time = new double[steps + 2];
        time[0] = 0;
        // Time array
        for (int j = 0; j < time.length; j++) {
            if (j + 1 == time.length) {
                //simu.println("End");
            } else {
                time[j + 1] = time[j] + dt;
                //simu.println(time[j]);
            }
        }
```

```
        return time;

    }

      private void createRepMonPlots(String name, int outCount,
Region fluidregion, Simulation simu, FieldFunction FFpressure,
FieldFunction FFvelocity) {
        for (int i = 1; i < (outCount + 1); i++) {
            Boundary outlet =
fluidregion.getBoundaryManager().getBoundary(name + i);
            // Setup local coordinate system
            setupCoordinate(name + i, fluidregion, simu);
            //simu.println(outlet);
            // Pressure report
            AreaAverageReport pReport =
simu.getReportManager().createReport(AreaAverageReport.class);
            pReport.setPresentationName("Av Pressure " + name + i);
            pReport.getParts().setObjects(outlet);
            pReport.setScalar(FFpressure);
            //P_ini[i - 1] = pReport.getValue();
            ReportMonitor monitor = pReport.createMonitor();
            monitor.setPresentationName("Av Pressure Monitor " +
name + i);
            MonitorPlot plot =
simu.getPlotManager().createMonitorPlot();
            plot.setPresentationName("Av Pressure Plot " + name +
i);
            plot.getMonitors().addObjects(monitor);
            plot.getAxes().getXAxis().getTitle().setText("Time");

plot.getAxes().getYAxis().getTitle().setText("Pressure");
            // Volume flow report
            SurfaceIntegralReport qReport =
simu.getReportManager().createReport(SurfaceIntegralReport.class);
            qReport.setPresentationName("Flow " + name + i);
            qReport.getParts().setObjects(outlet);
            // set coordinate system
            CylindricalCoordinateSystem localCo =
(CylindricalCoordinateSystem) simu.getCoordinateSystemManager().

getLabCoordinateSystem().getLocalCoordinateSystemManager().getObject
(name + i);
            VectorComponentFieldFunction localVel =
(VectorComponentFieldFunction) FFvelocity.

getFunctionInCoordinateSystem(localCo).getComponentFunction(2);
            qReport.setScalar(localVel);
            //Q_ini[i - 1] = qReport.getValue();
            ReportMonitor monitor2 = qReport.createMonitor();
            monitor2.setPresentationName("Flow Monitor " + name +
i);
            MonitorPlot plot2 =
simu.getPlotManager().createMonitorPlot();
            plot2.setPresentationName("Flow Plot "+ name + i);
            plot2.getMonitors().addObjects(monitor2);
            plot2.getAxes().getXAxis().getTitle().setText("Time");
```

```
            plot2.getAxes().getYAxis().getTitle().setText("Volume
Flow");
        }
    }

    private int getBoundaryCount(Simulation simu) {
        Collection<Boundary> boundColl =

simu.getRegionManager().getRegion("Fluid").getBoundaryManager().getB
oundaries();
        int outCount = 0;
        for (Boundary bound : boundColl) {
            String boundName = bound.getPresentationName();
            if (boundName.contains("Outlet")) {
                bound.setBoundaryType(PressureBoundary.class);
                outCount++;
            }
        }
        return outCount;
    }

    private int getInBoundaryCount(Simulation simu) {
        Collection<Boundary> boundColl =

simu.getRegionManager().getRegion("Fluid").getBoundaryManager().getB
oundaries();
        int inCount = 0;
        for (Boundary bound : boundColl) {
            String boundName = bound.getPresentationName();
            if (boundName.contains("Inlet")) {
                inCount++;
            }
        }
        return inCount;
    }

    private void setupCoordinate(String bndName, Region reg,
Simulation sim) {
        MaxReport maxReport_0 =

sim.getReportManager().createReport(MaxReport.class);

        PrimitiveFieldFunction primitiveFieldFunction_0 =
                ((PrimitiveFieldFunction)
sim.getFieldFunctionManager().getFunction("Centroid"));

        VectorComponentFieldFunction vectorComponentFieldFunction_0
=
                ((VectorComponentFieldFunction)
primitiveFieldFunction_0.getComponentFunction(0));


        //Get max and min values around the circle
        maxReport_0.setScalar(vectorComponentFieldFunction_0);
```

```
        Boundary boundary_0 =
                reg.getBoundaryManager().getBoundary(bndName);

        maxReport_0.getParts().setObjects(boundary_0);

        double Max_i = maxReport_0.getValue();


        VectorComponentFieldFunction vectorComponentFieldFunction_1
=
                ((VectorComponentFieldFunction)
primitiveFieldFunction_0.getComponentFunction(1));

        maxReport_0.setScalar(vectorComponentFieldFunction_1);

        double Max_j = maxReport_0.getValue();


        VectorComponentFieldFunction vectorComponentFieldFunction_2
=
                ((VectorComponentFieldFunction)
primitiveFieldFunction_0.getComponentFunction(2));

        maxReport_0.setScalar(vectorComponentFieldFunction_2);

        double Max_k = maxReport_0.getValue();


        MinReport minReport_0 =

sim.getReportManager().createReport(MinReport.class);

        minReport_0.setScalar(vectorComponentFieldFunction_0);

        minReport_0.getParts().setObjects(boundary_0);

        double Min_i = minReport_0.getValue();


        minReport_0.setScalar(vectorComponentFieldFunction_1);

        double Min_j = minReport_0.getValue();


        minReport_0.setScalar(vectorComponentFieldFunction_2);

        double Min_k = minReport_0.getValue();

//      Get the area and area vector of the inlet surface
        SumReport sumReport_1 =

sim.getReportManager().createReport(SumReport.class);

        PrimitiveFieldFunction primitiveFieldFunction_1 =
                ((PrimitiveFieldFunction)
sim.getFieldFunctionManager().getFunction("Area"));
```

```
        VectorMagnitudeFieldFunction vectorMagnitudeFieldFunction_0
=
                ((VectorMagnitudeFieldFunction)
primitiveFieldFunction_1.getMagnitudeFunction());

        sumReport_1.setScalar(vectorMagnitudeFieldFunction_0);

        sumReport_1.getParts().setObjects(boundary_0);

        double Area_mag = sumReport_1.getValue();


        VectorComponentFieldFunction vectorComponentFieldFunction_3
=
                ((VectorComponentFieldFunction)
primitiveFieldFunction_1.getComponentFunction(0));

        sumReport_1.setScalar(vectorComponentFieldFunction_3);

        double Area_i = sumReport_1.getValue();


        VectorComponentFieldFunction vectorComponentFieldFunction_4
=
                ((VectorComponentFieldFunction)
primitiveFieldFunction_1.getComponentFunction(1));

        sumReport_1.setScalar(vectorComponentFieldFunction_4);

        double Area_j = sumReport_1.getValue();


        VectorComponentFieldFunction vectorComponentFieldFunction_5
=
                ((VectorComponentFieldFunction)
primitiveFieldFunction_1.getComponentFunction(2));

        sumReport_1.setScalar(vectorComponentFieldFunction_5);

        double Area_k = sumReport_1.getValue();

//      no longer need reports, remove
        sim.getReportManager().removeObjects(sumReport_1);
        sim.getReportManager().removeObjects(minReport_0);
        sim.getReportManager().removeObjects(maxReport_0);

        Units units_0 =
                sim.getUnitsManager().getPreferredUnits(new
IntVector(new int[]{0, 1, 0, 0, 0, 0, 0, 0, 0, 0, 0, 0, 0, 0, 0,
0, 0, 0, 0, 0}));

//      create a local coordinate system
        LabCoordinateSystem labCoordinateSystem_0 =
                ((LabCoordinateSystem)
sim.getCoordinateSystemManager().getCoordinateSystem("Laboratory"));
```

```
        //getObject("Laboratory"));

        CylindricalCoordinateSystem cylindricalCoordinateSystem_0 =

labCoordinateSystem_0.getLocalCoordinateSystemManager().createLocalC
oordinateSystem(CylindricalCoordinateSystem.class, "Cylindrical");

        Coordinate coordinate_0 =
                cylindricalCoordinateSystem_0.getOrigin();

        coordinate_0.setCoordinate(units_0, units_0, units_0, new
DoubleVector(new double[]{0.0, 0.0, 0.0}));

//      get center of the cirlce
        double Xc = 0.5 * (Max_i + Min_i);
        double Yc = 0.5 * (Max_j + Min_j);
        double Zc = 0.5 * (Max_k + Min_k);
        coordinate_0.setValue(new DoubleVector(new double[]{Xc, Yc,
Zc}));

//      if you understand this, cool for you
        double Anx = Area_i / Area_mag;
        double Any = Area_j / Area_mag;
        double Anz = Area_k / Area_mag;


        double xlabx = Max_i - Xc;
        double xlaby = Max_j - Yc;
        double xlabz = Max_k - Zc;


        double xdotBasis = (xlabx * Anx + xlaby * Any + xlabz *
Anz);

        double erx = xlabx - xdotBasis * Anx;
        double ery = xlaby - xdotBasis * Any;
        double erz = xlabz - xdotBasis * Anz;

        double ermag = Math.sqrt(erx * erx + ery * ery + erz * erz);
//       the is the radial direction vector
        double erx_u = erx / ermag;
        double ery_u = ery / ermag;
        double erz_u = erz / ermag;
//      this is the theta direction vector
        double etheta_x = Any * erz_u - Anz * ery_u;
        double etheta_y = Anz * erx_u - Anx * erz_u;
        double etheta_z = Anx * ery_u - Any * erx_u;

        // now assign values to the new coordinate system
        cylindricalCoordinateSystem_0.setBasis0(new DoubleVector(new
double[]{erx_u, ery_u, erz_u}));
        cylindricalCoordinateSystem_0.setBasis1(new DoubleVector(new
double[]{etheta_x, etheta_y, etheta_z}));
        cylindricalCoordinateSystem_0.setPresentationName(bndName);
    }
```